2022

Buckling behaviour of cold-formed steel beams with web perforations

Yu, Nanting

http://hdl.handle.net/10026.1/18585

http://dx.doi.org/10.24382/1046
University of Plymouth

COPYRIGHT STATEMENT

Buckling behaviour of cold-formed steel beams with web perforations

By

Nanting Yu, BEng, MSc

A thesis submitted to the University of Plymouth in partial fulfilment
for the degree **DOCTOR OF PHILOSOPHY**

School of Engineering, Computing and Mathematics

January 2022

ACKNOWLEDGEMENTS

First and foremost, I wish to express my sincere gratitude to my Director of Studies, Dr. Boksun Kim who directed me into this interesting research field and provided me an excellent working opportunity. Her constructive advice and help on my English writing have been beneficial for this thesis. I would also like to thank my second supervisor Prof. Long-yuan Li, who provided plenty of helpful comments for my published papers in his valuable time. His patience, energetic working style have a great influence on my research. Without their help this research work would never been completed.

Many thanks to School of Engineering, Computing and Mathematics, University of Plymouth for providing me four-year PhD scholarship and such a fascinating academic environment. I would also like to give thanks to the technicians who have contributed to this research.

I am grateful to my colleagues working in Marine Building for their valuable advice and generous support during the past four years. Thanks also to my friends who helped me adapt the new life style in United Kingdom and made my PhD period more comfortable and memorable.

I would like to acknowledge the financial support provided by China Scholarship Council (No. 201708330276) for my PhD study in United Kingdom. The research findings described in this study are supported by the Natural Science Foundation of Zhejiang Province (No. LY19E080020).

Finally, massive thanks to my parents, Guo-hong Yu and Ming-feng Xia who brought me to this wonderful world, their endless support, encourage and love made me through the most difficult time. This thesis is dedicated to them.

AUTHOR’S DECLARATION

At no time during the registration for the degree of Doctor of Philosophy has the author been registered for any other University award without prior agreement of the Doctoral College Quality Sub-Committee.

Work submitted for this research degree at the University of Plymouth has not formed part of any other degree either at the University of Plymouth or at another establishment.

External contacts: yunanting@foxmail.com

Word counts of the main body of thesis: 50193 words

Signed: 余南霆

Date: 15/07/2021

Buckling behaviour of cold-formed steel beams with web perforations

Nanting Yu

ABSTRACT

Cold-formed steel (CFS) members are widely used in the constructional industry, because CFS has high strength-to-weight ratio and can be easily fabricated into different shapes. In order to accommodate services like electric wires and pipelines, perforations are commonly punched into the web of CFS beams. However, the appearance of web openings may reduce the properties of the cross section and hence change the stress distribution along the longitude axis. As a result, the perforated cold-formed steel (PCFS) beam is more susceptible to lateral-torsional buckling. For specific cross sections controlled by distortional buckling, the restraint of web on the flange weakens due to the web perforations and hence the PCFS beam may fail more easily than the CFS beam. Among all the current specifications, the design equations for determining the critical stress of PCFS beams are non-existent. In addition, the design guideline of CFS mainly concentrates on the loading conditions that the members subject to pure bending or compression, while the uniformly distributed load is more common in beams.

It is known that singly PCFS beams have low lateral stiffness and torsional rigidity about the weak axis which lead to them suffering from distortional or lateral-torsional buckling. To use PCFS sections with larger scale in structures, back-to-back built-up CFS beams with web perforations are commonly employed. They are connected by two individual PCFS studs using self-drilling screws. However, the application of built-up CFS beams with web perforations in practice is encountering challenges due to the lack of suitable design method. The researchers are prone to modify the design equations of hot-rolled I sections to predict the ultimate strength of built-up CFS sections, but this approach was found to be conservative.

This project aims to investigate the buckling behaviour of CFS beams with web perforations. Simplified analytical models based on energy method were proposed to predict the critical stress of distortional buckling of PCFS beams subject to pure bending and uniformly distributed load, and the effect of variant moment distribution along the longitude axis was examined. Li's model proposed in 2004 was modified for the calculation of the lateral-torsional buckling of PCFS beam subject to pure bending and uniformly distributed uplift load, and the influences of lateral and translational restraint provided by sheeting were discussed. Elastic finite element models were developed by using commercial software ANSYS to investigate the influence of hole sizes and cross-section dimensions on the buckling behaviour of PCFS beams. The results have shown a good agreement between the finite element analysis data and theoretical results.

In this study, non-linear finite element models including material, geometrical and contact non-linearity were performed to explore the structural behaviour of CFS built-up beams with web perforations subject to pure bending. The numerical results were verified against the existing experimental data in the literature. Afterwards, the validated finite element models were employed for the extensive parametric study. A total of 398 numerical simulations were conducted to examine the influence of hole sizes, hole spacing, beam slenderness and screw arrangements. The current direct strength method for PCFS beams was extended for the design rule of CFS built-up beams with web perforations subject to pure bending.

This thesis has contributed to improve the understanding of distortional and lateral-torsional buckling behaviour of PCFS beams subject to pure bending and uniformly distributed load, the data obtained from the numerical investigations provided a thorough grounding for further design of CFS built-up beams with web perforations.

KEY WORDS: cold-formed steel beams; web perforations; built-up sections; distortional buckling; lateral-torsional buckling; finite strip method; finite element method; pure bending; uniformly distributed load; stress gradient; energy method; built-up section; ultimate capacity; non-linear analysis; direct strength method

CONTENTS

ACKNOWLEDGEMENTS i

AUTHOR’S DECLARATION ii

ABSTRACT iii

CONTENTS v

LIST OF FIGURES xi

LIST OF TABLES xviii

NOMENCLAURE xx

Chapter 1 — Introduction 1

- 1.1 General introduction – cold-formed steel sections 1
- 1.2 Background of the project 3
- 1.3 Research aim and objectives 6
- 1.4 Outline of the project 7

Chapter 2 — Literature review 10

- 2.1 General 10
- 2.2 Analytical models for buckling behaviour of cold-formed steel members 11
  - 2.2.1 Local buckling 11
  - 2.2.2 Distortional buckling 12
  - 2.2.3 Lateral-torsional buckling 16
- 2.3 Design method of cold-formed steel members 18
  - 2.3.1 Generalised beam theory 18
  - 2.3.2 Finite element method 19
  - 2.3.3 Finite strip method 20
  - 2.3.4 Effective width method 21

2.3.5 Direct strength method 24

2.4 The buckling behaviour of perforated cold-formed steel sections 27

2.4.1 Experimental work 28

2.4.2 Numerical investigation 31

2.4.3 Theoretical study 35

2.5 The structural behaviour of cold-formed steel built-up sections 38

2.5.1 CFS built-up sections 38

2.5.2 CFS built-up sections with intermediate stiffeners 43

2.5.3 CFS built-up sections with perforations 44

2.6 Summary 46

Chapter 3 — Distortional buckling performance of perforated cold-formed steel channel beams 49

3.1 Introduction 49

3.2 Numerical investigation 50

3.2.1 Finite strip method 50

3.2.2 Elastic finite element analysis 53

3.2.3 Results and discussion 57

3.2.4 ANSYS-CUFSM results comparison 62

3.3 Analytical model for PCFS beams subject to pure bending 64

3.3.1 The analytical model by Hancock 64

3.3.2 Proposed analytical model 68

3.2.3 Comparison between the proposed model and FEA 72

3.4 Analytical model for PCFS beams subject to uniformly distributed load 74

3.4.1 The analytical model by Li and Chen 74

3.4.2 Proposed analytical model 78

3.4.3 Comparison between the proposed model and FEA 85

3.5 Summary...87

Chapter 4 — Lateral-torsional buckling performance of perforated cold-formed steel channel beams 89

4.1 Introduction 89

4.2 Numerical investigation..90

4.2.1 Finite strip method 90

4.2.2 Elastic finite element analysis 91

4.2.3 ANSYS-CUFSM results comparison..97

4.3 Analytical model for lateral-torsional buckling analysis of PCFS beams.................99

4.3.1 Li's model 99

4.3.2 Proposed analytical model 105

4.3.3 Comparison between the proposed analytical model and FEA......................115

4.4 Summary...122

Chapter 5 — Numerical investigation on cold-formed steel built-up channel beams with web perforations 124

5.1 Introduction 124

5.2 Evaluation of existing experimental data 125

5.3 Nonlinear finite element modelling in ANSYS...129

5.3.1 Geometry...129

5.3.2 Element type and mesh 130

5.3.3 Boundary and loading conditions..131

5.3.4 Contact of webs and constraint of screws 132

5.3.5 Initial geometric imperfections 133

5.3.6 Non-linear solution..134

5.4 Verification of the finite element models 135
5.4.1 CFS built-up beams with web perforations 135
5.4.2 CFS built-up beams 140
5.5 Summary 143
Chapter 6 — Proposed design rule for cold-formed steel built-up channel beams with web perforations 144
6.1 Introduction 144
6.2 Numerical examples 145
6.2.1 Specimen labelling 145
6.2.2 Results and discussion 146
6.3 Parametric study 149
6.3.1 Influence of screw arrangement 149
6.3.2 Influence of hole sizes 153
6.3.3 Influence of hole spacing 156
6.3.4 Influence of slenderness ratio 160
6.4 Modified direct strength method for CFS built-up beam with web perforations 161
6.4.1 Local buckling investigation 165
6.4.2 Distortional buckling investigation 170
6.4.3 Lateral-torsional buckling investigation 175
6.5 Summary 183
Chapter 7 — Conclusions and future work 185
7.1 Conclusions 185
7.2 Future work 188
REFERENCES 190
Appendix A - Mesh sensitivity analysis 204

A.1 Mesh sensitivity study for the distortional buckling of PCFS beams subject to pure bending 204

A.2 Mesh sensitivity study for the lateral-torsional buckling of PCFS beams subject to pure bending 205

Appendix B - Distortional buckling load of PCFS beams obtained from eigenvalue buckling analysis 206

B.1 PCFS beams with different hole sizes subject to pure bending 206

B.2 PCFS beams with different hole sizes subject to uniformly distributed load 209

Appendix C - Distortional half-wave lengths of CFS beams 210

Appendix D - Lateral-torsional buckling load of PCFS beams obtained from eigenvalue buckling analysis 211

D.1 Laterally unrestrained PCFS beams with different hole sizes subject to pure bending (k_z=0, k_ϕ=0) 211

D.2 Laterally restrained PCFS beams with different hole sizes subject to pure bending (k_z=∞, k_ϕ=0) 212

D.3 Laterally unrestrained PCFS beams with different hole sizes subject to uniformly distributed uplift load (k_z=0, k_ϕ=0) 213

D.4 Laterally restrained PCFS beams with different hole sizes subject to uniformly distributed uplift load (k_z=∞, k_ϕ=0) 214

Appendix E - Comparison of ultimate moment obtained from FEA with original and modified DSM prediction for CFS built-up beams with web perforations 215

E.1 Comparison of ultimate moment obtained from FEA with original and modified DSM prediction for CFS built-up beams with web perforations failed by local buckling 215

E.2 Comparison of ultimate moment obtained from FEA with original and modified DSM prediction for CFS built-up beams with web perforations failed by distortional buckling 218

E.3 Comparison of ultimate moment obtained from FEA with original and modified DSM prediction for CFS built-up beams with web perforations failed by lateral-torsional buckling 224

Publications 231

LIST OF FIGURES

Figure 1.1 Common used sections of CFS members (Copy from EN 1993-1-3 (2006))...2

Figure 1.2 Buckling modes of a CFS channel beam in bending (a) Local buckling, (b) Distortional buckling and (c) Lateral-torsional buckling 3

Figure 1.3 Buckling curves of CFS beams subject to pure bending..................................4

Figure 1.4 Castellated and cellular beams used in constructional industry........................5

Figure 1.5 Cold-formed steel built-up channel beams with web perforation 6

Figure 2.1 Distortional buckling model proposed by Lau and Hancock (1987) 12

Figure 2.2 Distortional buckling model proposed in EN-1993-1-3 (2006) 13

Figure 2.3 Distortional buckling model proposed by Li and Chen (2008).......................14

Figure 2.4 Distortional buckling model proposed by Zhu and Li (2016).........................15

Figure 2.5 Lateral-torsional buckling model proposed by Li (2004) 17

Figure 2.6 Effective cross-section of CFS channel members (a) column (b) beam (Copy from EN 1993-1-5 (2006)) 24

Figure 2.7 Setup and instrumentation of the column test (Moen and Schafer, 2008)......29

Figure 2.8 Four-point bending test rig (Zhao et al., 2019) 30

Figure 2.9 Buckling modes of PCFS columns obtained from eigenvalue buckling FEM analysis (Moen and Schafer, 2011) 34

Figure 2.10 Boundary and loading conditions of finite-element model (Moen and Schafer, 2011)...35

Figure 2.11 Local buckling shape of simply-supported plate with or without holes subject uniform compression (Moen and Schafer, 2009b)...36

Figure 2.12 ANSYS model for CFS built-up members (Li et al., 2014)..........................40

Figure 2.13 Ultimate stage of distortional and flexural buckling of CFS built-up beams with web perforation in the four-point bending tests. (Wang and Young, 2015c)...........45

Figure 2.14 ABAQUS model for CFS built-up beams with web perforation (Wang and Young, 2017) 45

Figure 2.15 Distorsional buckling of CFS built-up beams with web perforations in test and finite element simulation (Chen et al., 2021) 46

Figure 3.1 Cross section in CUFSM to obtain the distortional buckling stress of CFS beams subject to pure bending (Section B) 51

Figure 3.2 Typical distortional buckling modes of CFS beams in CUFSM 52

Figure 3.3 Distortional curves of selected CFS beams with plain web produced by CUFSM (σ_y=390 MPa, M_y is the yield moment) 53

Figure 3.4 Geometry of a PCFS beam with circular perforations in the web 54

Figure 3.5 Typical finite element mesh of a PCFS beam (Section B, h=200 mm, b=70 mm, c=20 mm, t=2.5 mm, d=100 mm, l=1256 mm) 55

Figure 3.6 Boundary and loading conditions of PCFS beams subject to pure bending ... 55

Figure 3.7 Boundary conditions of PCFS beams subject to uniformly distributed load .. 56

Figure 3.8 Loading conditions of PCFS beams subject to uniformly distributed load 57

Figure 3.9 Distortional buckling curves of PCFS beams with different hole sizes subject to pure bending (a) Section A (b) Section B (c) Section C (σ_y=390 MPa, M_y is the yield moment) 59

Figure 3.10 Distortional buckling modes of PCFS beams (Section A, d=h/2) subject to pure bending (a) 470 mm (b) 846 mm (c) 1316 mm 60

Figure 3.11 Distortional buckling modes of PCFS beams (Section B, d=h/2) subject to pure bending (a) 628 mm (b) 1256 mm (c) 1884 mm 60

Figure 3.12 Distortional buckling modes of PCFS beams (Section C, d=h/2) subject to pure bending (a) 785 mm (b) 1570 mm 61

Figure 3.13 Typical distortional buckling modes of PCFS beam subject to uniformly distributed load (h=200 mm, b=65 mm, c=20 mm and t=2.5 mm) 62

Figure 3.14 Distortional buckling modes of CFS beams with plain web subject to pure bending obtained from FSM and FEA (Section B, *h*=200 mm, *b*=70 mm, *c*=20 mm, *t*=2.5 mm, *l*=570 mm) 63

Figure 3.15 Analytical model proposed by Lau and Hancock (1987) 64

Figure 3.16 Web deformation of the CFS sections due to the distortional buckling (a) pure compression (b) pure bending 69

Figure 3.17 Notation and geometry of the PCFS beam in the longitudinal direction 69

Figure 3.18 Distortional buckling model proposed by Hancock (1997) (left) and proposed analytical model used to determine rotational spring stiffness (right) 71

Figure 3.19 Comparisons of critical moments of distortional buckling of PCFS beams subject to pure bending among the proposed analytical model, analytical model in Ref.[Yuan et al., 2017] and eigenvalue buckling analysis (a) Section A (b) Section B (c) Section C (σ_y=390 MPa, M_y is the yield moment) 74

Figure 3.20 Analytical model proposed by Li and Chen (2008) 75

Figure 3.21 Bending moment diagram for uniformly distributed load (left) and pure bending (right) 79

Figure 3.22 Model used to determine the stiffness of the vertical spring 80

Figure 3.23 Comparisons of critical distortional buckling stress of PCFS beams subject to uniformly distributed load and pure bending (σ_y=390 MPa, h=200 mm, b=65 mm, c= 20 mm and t=2 mm) 85

Figure 3.24 Comparison between the proposed model and eigenvalue buckling analysis of PCFS beams with different hole sizes subject to uniformly distributed load (σ_y=390 MPa, h=200 mm, b=65 mm, c= 20 mm and t=2.5 mm) 86

Figure 4.1 Cross section in CUFSM to obtain the critical moments of lateral-torsional buckling of CFS beams (without holes) subject to pure bending 90

Figure 4.2 Lateral-torsional buckling mode of a 3-meter-long CFS beam (without holes) in CUFSM. (h=200 mm, b=70 mm, c=20 mm, t=2 mm) 91

Figure 4.3 Geometry and notations used in the PCFS beam with circular holes in the web92

Figure 4.4 Typical finite element meshes of a PCFS beam in ANSYS (Section E, h=200 mm, b=70 mm, c=20 mm, t=2 mm, d=100 mm, l=3140 mm) 92

Figure 4.5 Boundary conditions of an unrestrained PCFS beam in ANSYS 93

Figure 4.6 Boundary conditions of a laterally restrained PCFS beam in ANSYS 94

Figure 4.7 Loading conditions of a PCFS beam subject to pure bending 94

Figure 4.8 Loading conditions of a PCFS beam subject to uniformly distributed uplift load 95

Figure 4.9 Typical lateral-torsional buckling modes of a PCFS beam subject to pure bending in ANSYS (h=200 mm, b=70 mm, c=20 mm, t=2 mm, d=100 mm, l=3140 mm) (a) with no lateral restraint (b) with lateral restraint at the tension flange 96

Figure 4.10 Typical lateral-torsional buckling modes of a PCFS beam subject to uniformly distributed uplift load in ANSYS (h=200 mm, b=70 mm, c=20 mm, t=2 mm, d=100 mm, l=3140 mm) (a) with no lateral restraint (b) with lateral restraint at the tension flange.. 97

Figure 4.11 Comparison of lateral-torsional buckling modes of CFS beams (without holes) subject to pure bending obtained from FSM and FEA (h=200 mm, b=70 mm, c=20 mm, t=2 mm, l=3000 mm) 98

Figure 4.12 Analytical model proposed by Li (2004) 100

Figure 4.13 Model used for lateral-torsional buckling analysis of PCFS beams subject to pure bending (a) Notation and geometry (b) Analytical model..................................... 106

Figure 4.14 Cross-section properties of the PCFS beam in different regions 107

Figure 4.15 Model used for lateral-torsional buckling analysis of PCFS beams subject to uniformly distributed uplift load (a) Practical case (b) Simplified model...................... 112

Figure 4.16 Comparison between critical moments of lateral-torsional buckling obtained from present model and FEA for PCFS beams with different hole sizes subject to pure bending. (a) d=100 mm (b) d=80 mm (c) d=66.7 mm (d) d=50mm (σ_y=390 MPa, h=200 mm, b=70 mm, c= 20 mm and t=2 mm).. 116

Figure 4.17 Comparisons of critical moments of lateral-torsional buckling of CFS beams (without holes) with PCFS beams (d=100 mm) subject to pure bending (σ_y=390 MPa, h=200 mm, b=70 mm, c= 20 mm, t=2 mm) 117

Figure 4.18 Comparison between critical moments of lateral-torsional buckling obtained from present model and FEA for PCFS beams with different hole sizes subject to uniformly distributed uplift load. (a) d=100 mm (b) d=80 mm (c) d=66.7 mm (d) d=50mm (σ_y=390 MPa, h=200 mm, b=70 mm, c=20 mm and t=2 mm) 119

Figure 4.19 Comparisons of critical moments of lateral-torsional buckling of PCFS beams subject to uniformly distributed uplift load and pure bending (h=200 mm, b=70 mm, c= 20 mm, t=2 mm, d=100 mm) 119

Figure 4.20 Comparisons of critical moments of lateral-torsional buckling for the laterally restrained and unrestrained PCFS beams subject to pure bending (k_ϕ=0, σ_y=390 MPa, h=200 mm, b=70 mm, c= 20 mm, t=2 mm and d=100 mm) 120

Figure 4.21 Influence of spring stiffness on the critical moments of lateral-torsional buckling of a 6-meter-long PCFS beam subject to uniformly distributed uplift load (σ_y=390 MPa, h=200 mm, b=70 mm, c= 20 mm, t=2 mm and d=100 mm) 121

Figure 5.1 Loading rig for CFS built-up open section beams by Wang and Young (2015)125

Figure 5.2 Geometry and notations in the CFS built-up beam with web perforations according to the four-point bending tests (Wang and Young, 2015) 130

Figure 5.3 Typical finite element meshes of the CFS built-up beam with web perforations (Specimen OH0.5T1.9-136) 131

Figure 5.4 Boundary and loading conditions of a CFS built-up beam with web perforations under four-point bending (Specimen OH0.5T1.9-136) 132

Figure 5.5 Comparisons of moment-curvature curves obtained from load-controlled method, displacement-controlled method and experimental data (Specimen OH0.5T1.2-86) 135

Figure 5.6 Comparisons of moment-curvature curves of CFS built-up beams with web perforations obtained from test, ABAQUS and ANSYS (Wang and Young, 2015) 138

Figure 5.7 Typical deformed shapes of CFS built-up beams with web perforations obtained from four-point bending tests (Wang and Young, 2015) and FEA 140

Figure 5.8 Comparisons of moment-curvature curves of CFS built-up beams obtained from test, ABAQUS and ANSYS (Specimen: OT1.9-136-S300) (Wang and Young, 2018) 142

Figure 5.9 Typical deformed shapes of CFS built-up beams obtained from four-point bending tests (Wang and Young, 2018) and FEA (Specimen OT1.9-136-S300) 142

Figure 6.1 Specimens in the parametric study (a) Labelling rule (b) Four-point bending load for local and distortional buckling (c) Pure bending for lateral-torsional buckling146

Figure 6.2 Nonlinear FEA results of the CFS built-up beam with web perforations controlled by local buckling (H200-L1200-T1.4-S200-A300(d/h0.25)) (a) moment-curvature curve (b) deformed shape 147

Figure 6.3 Nonlinear FEA results of the CFS built-up beam with web perforations controlled by distortional buckling (H300-L1200-T2.4-S300-A300(d/h0.5)) (a) moment-curvature curve (b) deformed shape 148

Figure 6.4 Nonlinear FEA results of the CFS built-up beam with web perforations controlled by lateral-torsional buckling (H150-L4000-T1.8-S150-A300(d/h0.65)) (a) moment-curvature curve (b) deformed shape.. 148

Figure 6.5 Ultimate moment curves of 1.2-meter-long CFS built-up beams with web perforations in different screw arrangements obtained from FEA 151

Figure 6.6 Ultimate moment curves of 4-meter-long CFS built-up beams with web perforations in different screw arrangements obtained from FEA 152

Figure 6.7 Ultimate moment curves of 1.2-meter-long CFS built-up beams with different hole sizes obtained from FEA 154

Figure 6.8 Ultimate moment curves of 4-meter-long CFS built-up beams with web perforations in different hole sizes obtained from FEA 156

Figure 6.9 Ultimate moment curves of 1.8-meter-long CFS built-up beams with web perforations in different hole spacing obtained from FEA.. 158

Figure 6.10 Ultimate moment curves of 4-meter-long CFS built-up beams with web perforations in different hole spacing obtained from FEA 159

Figure 6.11 Ultimate moment curves of CFS built-up beams with web perforations in different hole sizes and slenderness ratio obtained from FEA 161

Figure 6.12 Comparison of the modified DSM curves with FEA results for CFS built-up beams with web perforations controlled by local buckling 167

Figure 6.13 Comparison of the modified DSM curves with FEA results for CFS built-up beams with web perforations controlled by distortional buckling 173

Figure 6.14 Comparison of the original DSM curves with FEA results for CFS built-up beams with web perforations controlled by lateral-torsional buckling 175

Figure 6.15 Comparison of FEA results with design strength calculated by original DSM for CFS built-up beams with web perforations failed by lateral-torsional buckling in different slenderness ratio 178

Figure 6.16 Comparison of FEA results with different screw spacing for CFS built-up beams with web perforations failed by lateral-torsional buckling 179

Figure 6.17 Comparison of FEA results with design strength calculated by modified DSM for CFS built-up beams with web perforations failed by lateral-torsional buckling in different slenderness ratio 181

Figure A.1 Effect of mesh size on the distortional buckling of a PCFS beam (Section B: h=200 mm, b=70 mm, c=20 mm, t=2.5 mm, d=100 mm and l=1256 mm) 204

Figure A.2 Effect of mesh size on the lateral-torsional buckling of a PCFS beam (Section E: h=200 mm, b=70 mm, c=20 mm, t=2 mm, d=100 mm and l=3140 mm)................. 205

LIST OF TABLES

Table 2.1 Internal compression elements (copy from EN 1993-1-5 (2006)) 22

Table 2.2 Outstand compression elements (copy from EN 1993-1-5 (2006)) 23

Table 3.1 Cross-section dimensions of the selected CFS beams for numerical investigations in pure bending (unit: mm).. 51

Table 3.2 Comparison of critical moment of distortional buckling of the CFS beam with plain web obtained from FSM and FEA (Section selected from Albion Section) 63

Table 4.1 Comparison of the critical moments of lateral-torsional buckling of CFS beams (without holes) obtained from FSM and FEA (Section E, h=200 mm, b=70 mm, c=20 mm, t=2 mm) 99

Table 5.1 Summary of four-points bending tests for cold-formed steel built-up channel beam with web perforations by Wang and Young (2015)... 126

Table 5.2 Summary of four-points bending test for built-up cold-formed steel channel beam with web perforations by Chen et al. (2021)... 127

Table 5.3 Summary of four-points bending tests for cold-formed steel built-up channel beam (without web perforations) by Wang and Young (2018)..................................... 128

Table 5.4 Material properties obtained from the tensile coupon tests (Wang and Young, 2015).. 130

Table 5.5 Comparisons of FEA results against experimental data (Wang and Young, 2015) for CFS built-up beams with web perforations 136

Table 5.6 Comparisons of FEA results against experimental data (Wang and Young, 2018) for CFS built-up beams 141

Table 6.1 Comparison of ultimate moment obtained from FEA with original DSM prediction for selected specimens controlled by local buckling..................................... 162

Table 6.2 Comparison of ultimate moment obtained from FEA with original and modified DSM prediction for selected specimens controlled by distortional buckling . 163

Table 6.3 Comparison of ultimate moment obtained from FEA with original and modified DSM prediction for selected specimens controlled by lateral-torsional buckling164

Table 6.4 Comparison of ultimate moment obtained from FEA with original and modified DSM prediction for selected specimens controlled by local buckling............168

Table 6.5 Comparison of ultimate moment obtained from FEA with original and modified DSM prediction for selected specimens controlled by distortional buckling .174

Table 6.6 Comparison of ultimate moment obtained from FEA with original and modified DSM prediction for selected specimens controlled by lateral-torsional buckling182

NOMENCLAURE

All the symbols have been defined where they first appeared, the primary symbols used in this thesis are summarized below,

h	web depth of the cross section
b	flange width of the cross section
c	lip height of the cross section
t	thickness
d	diameter of the circular hole
l	beam length
n_h	total number of the holes in the web
A	cross-section area of the compressed flange and lip
E	Young's modulus
μ	Poisson's ratio
σ_y	yield stress
G	shear modulus
J	torsion constant of the compressed flange and lip
λ_d	critical half-wave length of distortional buckling
I_w	warping constant
I_x	moment of inertia of the compressed flange and lip to the shear center about the x-axis
I_y	moment of inertia of the compressed flange and lip to the shear center about the y-axis
I_{xy}	product of inertia of the compressed flange and lip about the shear center
k_ϕ	rotational spring stiffness
u	horizontal displacement of the compressed flange and lip at the shear center for distortional buckling
v	vertical displacement of the compressed flange and lip at the shear center for distortional buckling
ϕ	rotation of the compressed flange and lip about the shear center for distortional buckling
D	flexural rigidity of the unperforated strip

D_h	flexural rigidity of the perforated strip
α	reduction factor of the rotational spring stiffness for distortional buckling
k_y	vertical spring stiffness for distortional buckling
EI_1	bending stiffness of the plain web
EI_2	bending stiffness of the perforated web
β	reduction factor of the vertical spring stiffness for distortional buckling
M_{cr}	critical moment of the PCFS beam
M_{y}	yield moment of of gross cross-section
r_c	polar radius of gyration of the compressed flange and lip about the centroid
σ_{crdPB}	critical stress of distortional buckling of the PCFS beam subject to pure bending
M_{crdPB}	critical moment of distortional buckling of the PCFS beam subject to pure bending
σ_{crdUDL}	critical stress of distortional buckling of the PCFS beam subject to uniformly distributed load
M_{crdUDL}	critical moment of distortional buckling of the PCFS beam subject to uniformly distributed load
q_z	density of uniformly distributed load for distortional buckling
R_y	radii of curvature of neutral axis in the xz plane
R_z	radii of curvature of neutral axis in the xy plane
q_{y}	density of uniformly distributed uplift load for lateral-torsional buckling
$\sigma_x(x,y,z)$	pre-buckling longitudinal stress for lateral-torsional buckling
$\bar{u}(x,y,z)$	longitudinal deflection at point (x,y,z) during lateral-torsional buckling
k_{z}	horizontal spring stiffness for lateral-torsional buckling
w	horizontal displacement of the PCFS beam at the centroid for lateral-torsional buckling
v_1	vertical displacements of the PCFS beam at the centroid for lateral-torsional buckling
ϕ_1	rotation of the PCFS beam about the shear center for lateral-torsional buckling
I_{z1}	the moment of inertia of CFS beams (without holes) about the z-axis
I_y^*	moment of inertia of the PCFS channel section about the y-axis
I_z^*	moment of inertia of the PCFS channel section about the z-axis

J^*	torsion constant of the PCFS channel section
$M_{cr\lambda PB}$	critical moment of lateral-torsional buckling of the PCFS beam subject to pure bending
$M_{cr\lambda UDL}$	critical moment of lateral-torsional buckling of the PCFS beam subject to uniformly distributed uplift loads
a	distance between two adjacent holes
s	screw spacing
M_{ynet}	yield moment of net cross-section
M_{crlPB}	critical moment of local buckling of the PCFS beam subject to pure bending
λ_l	section slenderness for local buckling
λ_{d0}	section slenderness for distortional buckling
λ_c	section slenderness for lateral-torsional buckling
M_{ul}	ultimate moment of the CFS built-up beam with web perforations controlled by local buckling obtained from modified DSM curves
M_{ud}	ultimate moment of the CFS built-up beam with web perforations controlled by distortional buckling from modified DSM curves
$M_{ul\lambda}$	ultimate moment of the CFS built-up beam with web perforations controlled by lateral-torsional buckling from modified DSM curves
$M_{ul\lambda,o}$	ultimate moment of the CFS built-up beam with web perforations controlled by lateral-torsional buckling from original DSM curves
Φ_b	resistance factor
$C_{\Phi b}$	calibration coefficient
M_m	mean value of material factor
F_m	mean value of fabrication factor
P_m	mean value of professional factor
V_M	coefficient of variation of material factor
V_F	coefficient of variation of fabrication factor
V_P	coefficient of variation of test results
V_Q	coefficient of variation of load effect
C_P	correction factor
β_1	calculated reliability index
β_0	target reliability index

Chapter 1 — Introduction

1.1 General introduction – cold-formed steel sections

Cold-formed steel (CFS) sections are made by pressing, folding plates or rolling sheet steel at ambient temperature. The yield stress of CFS is increased due to the cold working processes, which can reach 550 MPa or higher, while the ductility of CFS may be decreased at the same time. The benefit of CFS is not only its high strength but also its lightness in weight. The thicknesses of the CFS usually range from 0.9 mm to 8 mm. Due to its unique material property, it is widely used in the construction industry. For example, CFS sections are usually employed as main structural members in the light steel prefabricated buildings. They are also used in storage racks, stadiums, bridges, transmission towers, etc.

CFS members first used in building construction began in the 1850s in America. No design standard about CFS existed at that time, for this reason, the usage of the CFS members was limited. The first specification for design of CFS sections was published in 1946 (AISI, 1946). Since then, some CFS design codes have been came out by other countries. America, Canada and Mexico use the North American Specification (AISI, 2016) to design the CFS members. European countries design the CFS members according to the Eurocode 3 (EN-1993-1-3, 2006). Other countries tend to utilize their own guidelines for CFS members, which were developed based on the American design code.

There are various types of CFS sections (see Figure 1.1), the most common sections are the channel, sigma and zed shapes. Lips are added to improve the efficiency against local buckling (Li and Chu, 2008). Compared with hot rolled steel sections, the thickness of CFS sections is relevantly thin which makes it tend to buckle under compression, generally it cannot reach the full strength of the material. Furthermore, CFS beams have low lateral stiffness and low torsional stiffness which give great flexural stiffness about one axis. This leads to CFS beams very prone to buckling. Hence, the stability is the key problem for the CFS structures.

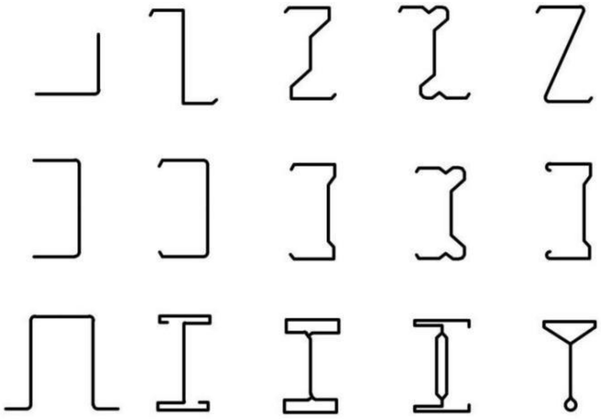

Figure 1.1 Common used sections of CFS members (Copy from EN 1993-1-3 (2006))

Normally, open cross-section CFS beams have three typical buckling modes, namely, local buckling, distortional buckling and lateral-torsional buckling (see Figure 1.2). The buckling mode of the CFS section mainly depends on the dimension of the section, the beam length and the support condition (Chen and Li, 2010).

The local buckling is a mode only involves plate flexure, no translation of the intersection lines of the adjacent plates appears (Ádány, 2004). In addition, the half-wave length of local buckling is similar to the cross section which is the shortest one among the three modes, as shown in Figure 1.2(a).

Distortional buckling is known as stiffener buckling which involves translation and rotation of the compressed flange and lip at the web-flange junction. The flange-lip system does not change in the cross-sectional shape during buckling (Teng et al., 2003). When the flange-lip system buckles, the web will suffer flexure at the same half-wavelength. The half-wavelength of distortional buckling is several times longer than the cross-section size which is between the local and lateral-torsional buckling, as shown in Figure 1.2(b).

Lateral-torsional buckling is a mode in which the whole member moves like rigid body, the whole cross section may rotate and translate, but the shape of the section will not change (Li, 2004). The half-wavelength of lateral-torsional buckling is equal to the beam length which is the longest one among the three modes, as shown in Figure 1.2(c).

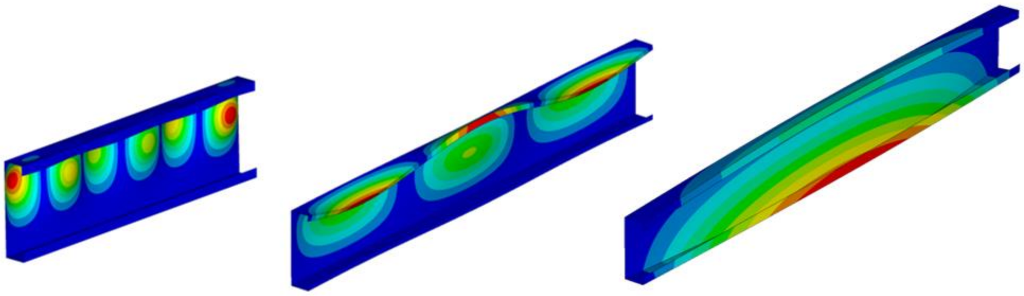

(a) (b) (c)

Figure 1.2 Buckling modes of a CFS channel beam in bending (a) Local buckling, (b) Distortional buckling and (c) Lateral-torsional buckling

Figure 1.3 illustrates the buckling curve of CFS channel beams with a typical section under bending which is generated by the program CUFSM (Shafer and Ádány, 2006), the web depth, flange width, lip length and thickness of cross section is selected as 200 mm, 70 mm, 20 mm and 2.5 mm, respectively. It can be found that local buckling occurs at the first minimal value in which the half-wavelength is 100 mm, the distortional buckling occurs at the second minimal value in which the half-wavelength is 550 mm. When the half-wavelength is greater than 2000 mm, lateral-torsional bucking is the dominant buckling mode.

1.2 Background of the project

The perforated cold-formed steel (PCFS) beams have been employed as bearing components in constructions. The web openings can not only create the space for serviceability of pipelines to pass across but also reduce the weight of the beam due to the economic benefit. Compared with castellated beams, PCFS beams are lighter and thinner so that the costs on the transport and erection of the construction are lower. Moreover, the web perforations can be done by hole punches directly during the beam manufacturing processes and it would not cause much extra labour work. Therefore, the PCFS beam could be a more economical choice for steel construction industry.

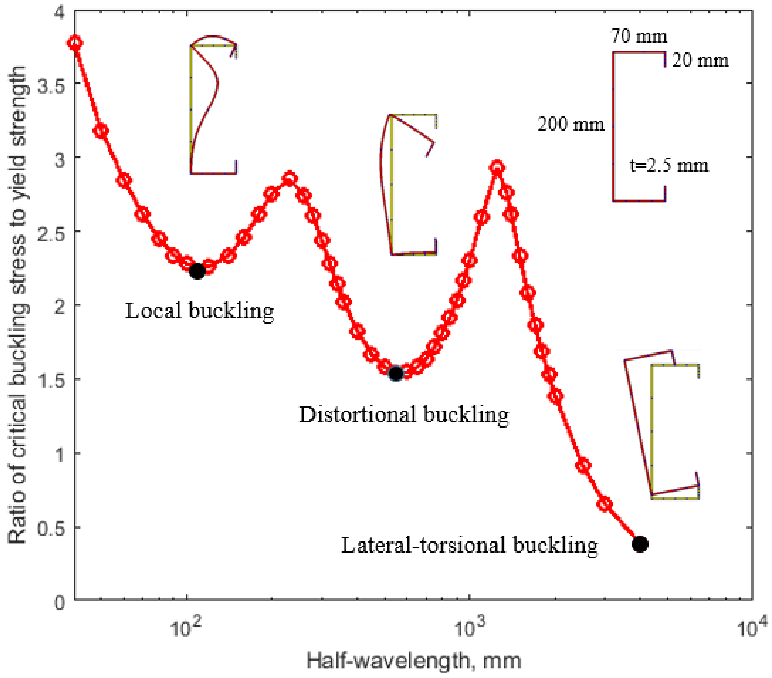

Figure 1.3 Buckling curves of CFS beams subject to pure bending

In the existing specifications (AISI, 2016; AS/NZS, 2005), there are some design rules for determining the ultimate strength of PCFS members. However, these design rules were proposed based on the experimental and numerical investigations, little information about the theoretical approaches were mentioned. The theoretical approaches for calculating the critical buckling stress are needed. In this thesis, new formulae based on Hancock's model proposed in 1987 and Li's model proposed in 2004 were presented for predicting the critical stress of distortional and lateral-torsional buckling of PCFS channel beams subject to pure bending, respectively.

Furthermore, the current design codes mainly focused on the situation that the sections are subject to pure bending or compression, but the uniformly distributed load is the most common force in practice. When the PCFS beam is subject to uniformly distributed load, the buckling behaviour could be different compared to pure bending. In this thesis, new formulae based on Li and Chen's model proposed in 2008 and Li's model proposed in 2004 were derived for determining the critical stress of distortional and lateral-torsional buckling of PCFS channel beams subject to uniformly distributed load, respectively. The influence of variant moment distributions along the longitudinal axis was also discussed.

Since 1950s, castellated and cellular beams have been used as structural members in constructional industry by engineers (see Figure 1.4). A castellated beam is fabricated from standard I-shape steel by cutting a zigzag pattern along the web. The two halves are welded back together to form the castellated section (AISC, 2016). A cellular beam is produced in the similar process, the only difference is that webs require twice cutting to form half circular patterns. These work increases the depth of the web without adding any material and hence strengthen the major axis bending strength and stiffness (Yuan et al., 2014; Kim et al., 2016).

Figure 1.4 Castellated and cellular beams used in constructional industry

Recently, cellular beams are made by just cutting holes directly from the web, which eliminates welding. There are already several books written for the design and analyses of castellated and cellular beams (Knowles, 1985; Harper, 1991; Fares et al., 2016), the corresponding design method is explicit. However, the castellated and cellular beams are made from hot-rolled steel, the yield strength cannot reach as high as 550 MPa. Furthermore, the processes of cutting and welding can increase the fabrication cost.

There is a trend that the CFS built-up channel beam with web perforations takes the place of castellated beams or cellular beams in practice. The CFS built-up channel beam with web perforations is connected by two PCFS sections using self-tapping screw, back to back (see Figure 1.5). Compared with single section, the built-up section has higher torsional rigidity and lateral stiffness which makes it have better performance against distortional and lateral-torsional buckling.

Figure 1.5 Cold-formed steel built-up channel beams with web perforation

The structural behaviour of built-up sections contains nonlinear problems due to the contact between two webs and discontinuous connections along the longitudinal axis. For these reasons, the theoretical analysis of built-up CFS channel beam is very complicated. Researchers tended to modify the equations of hot-rolled I sections for designing the built-up CFS sections even though this design rule may be conservative. In the current specifications, a suitable approach for predicting the failure strength of the CFS built-up beam with web perforations is limited. In this thesis, non-linear finite element analyses (FEA) were conducted for the parametric study to extend the direct strength method (DSM) equations for calculating the ultimate moment of CFS built-up beams with web perforations.

1.3 Research aim and objectives

The aim of this study is to investigate the distortional and lateral-torsional buckling behaviour of PCFS beams subject to pure bending and uniformly distributed load, new theoretical approaches to determine the critical buckling stress need to be presented. Meanwhile, the non-linear numerical investigations of built-up CFS beams with web perforations are performed to extend the DSM equations for predicting the ultimate failure strength. The specific objectives are listed as follows,

- To find suitable analytical approaches to predict the critical stress of distortional buckling of PCFS beams subject to pure bending and uniformly distributed load.

- To study the influence of web perforations on the buckling behaviour of PCFS beams subject to pure bending and uniformly distributed load by FEA.

- To investigate the effect of stress gradient along the beam longitudinal direction on the distortional buckling behaviour of PCFS beams.

- To develop analytical models for calculating the critical moment of lateral-torsional buckling of PCFS beams subject to pure bending and uniformly distributed uplift load.

- To explore the influence of horizontal and rotational restraint provided by the sheeting on the lateral-torsional buckling behaviour of PCFS beams subject to pure bending and uniformly distributed uplift load.

- To conduct nonlinear FE models to obtain the ultimate failure strength of built-up CFS beams with web perforations subject to pure bending.

- To investigate the effect of beam slenderness, screw arrangements, hole size and hole spacing on the structural behaviour of CFS built-up beams with web perforations subject to pure bending.

- To extend original DSM design equations for predicting the ultimate failure strength of CFS built-up beams with web perforations subject to pure bending.

1.4 Outline of the project

The objectives of this project are implemented through combination of numerical simulation experimental investigation and theoretical derivation. The results of elastic FEA were compared with finite strip method and the non-linear finite element models were validated against the data of existing test. This thesis is consistent of seven chapters and divided into three steps.

- Step I (Chapters 1-2)

Step I mainly focuses on illustrating the background of the project and reviewing the relevant literature. Chapter 1 comprises the general introduction of CFS sections, background of the project, objectives and outline of this thesis. Chapter 2 provides more detailed literature review, including the development of existing analytical models for buckling of CFS sections, design method for CFS sections, buckling behaviour of PCFS members and structural behaviour of CFS built-up beams with plain web, intermediate stiffeners and web perforations.

- Step II (Chapters 3-4)

Step II turns the point to investigate the buckling behaviour of PCFS beams. Chapter 3 conducted the theoretical and numerical investigation of distortional buckling. New analytical approaches were proposed to obtain the critical stresses of distortional buckling of PCFS beams subject to pure bending and uniformly distributed load. The influences of hole sizes, cross-section dimensions and stress gradient were examined in FEA. Chapter 4 studies the lateral-torsional buckling of PCFS beams subject to pure bending and uniformly distributed uplift load, the simplified formulae were put forward to determine the critical moment of lateral-torsional buckling. The effects of horizontal and rotational restraint provided by sheeting were investigated. The finite strip method (FSM) performed by CUFSM was used to validate against the results of the elastic finite element models with plain web.

- Step III (Chapter 5-6)

Step III concentrates on investigating the structural behaviour of CFS built-up beams with web perforations subject to pure bending. Chapter 5 reports the details of non-linear finite element including material non-linearity, geometric non-linearity and contact non-linearity. The existing experimental data of CFS built-up beams with or without web perforations was used to check the accuracy of numerical investigation. Chapter 6 presents the design rule of CFS built-up beams with web perforations, the current DSM design equations were extended according to the parametric study. The influences of hole size, hole spacing, screw arrangements and beam slenderness were also investigated.

Chapter 7 is the last part of this thesis, which summarizes the main findings of the project. The recommendations for future work on the PCFS beams and CFS built-up beams with web perforations were also presented.

Chapter 2 — Literature review

2.1 General

This chapter reviews the previous research on the buckling performance of CFS members including local buckling, distortional buckling and lateral-torsional buckling. Especially focusing on the former study on the buckling behaviour of PCFS sections and structural behaviour of CFS built-up beams with web perforations.

The first part summarizes the design method for CFS members, including the existing analytical approaches, the generalised beam theory, numerical method, effective width method and direct strength. The second part covers the existing literature on the buckling behaviour of single PCFS members including the development of experimental work, numerical investigation and theoretical study. The third part involves the recent research on the structural behaviour of the CFS built-up sections, CFS built-up sections with intermediate stiffeners and CFS built-up sections with perforations.

The relevant literatures are listed in each section of this chapter.

2.2 Analytical models for buckling behaviour of cold-formed steel members

2.2.1 Local buckling

Local buckling normally occurs in the compression flange of CFS beams in deep sections, it may also occur in the web (Li, 2011). The critical stress of the local buckling can be calculated using the formula of buckling of plates developed by Timoshenko and Gere (1961) as follows,

$$\sigma_{cr,l} = k_l \frac{\pi^2 E}{12(1-\mu^2)}\left(\frac{t}{b_c}\right)^2 \tag{2-1}$$

where $\sigma_{cr,l}$ is the critical stress of local buckling, E is the Young's modulus, k_l is the buckling coefficient, μ is the Poisson's ratio, t is the thickness of the element and b_c is the width of the compression element. When the element is subject to pure compression and the lip does not have enough stiffness, the buckling coefficient of flange and web can be taken as 4 and the buckling coefficient of lip can be taken as 0.43, respectively. When the element is subject to pure bending, the web buckling coefficient can be taken as 23.9, the flange buckling coefficient is considered as 4 and the lip buckling coefficient is about 0.43 (Li and Chu, 2007).

However, the critical stress obtained from Eq.2-1 is underestimated, because the interactions between the adjacent elements are not taken into account. Schafer and Peköz (1999) presented a semi-empirical interaction model to predict the local buckling stress of CFS members which considered interaction of the flange, web, and/or lip, the buckling coefficient can be expressed as follows,

flange/lip: $$k_{fl} = \left(8.85\xi_{lip} - 11.07\right)\left(\frac{c}{b}\right)^2 + (-1.59\xi_{lip} + 3.95)\left(\frac{c}{b}\right) + 4 \tag{2-2}$$

for $\xi_{lip} \le 1$ and $\left(\frac{c}{b}\right) \le 0.6$

flange/web: $$k_{fw} = 1.125\min\left\{4, \left(0.5\xi_{web}^3 + 4\xi_{web}^2 + 4\right)\left(\frac{c}{b}\right)^2\right\} \tag{2-3}$$

$$\xi = \frac{f_1 - f_2}{f_2} \tag{2-4}$$

where b is flange width and c is lip length. f_1 and f_2 is the stresses at the opposite edges of the element, respectively.

2.2.2 Distortional buckling

Compared with the local buckling in which the critical stress depends only on the ratio of the width to thickness of the plate, the distortional buckling is much more complicated. Because the distortional buckling stress is not only dependent on buckled part but also the other parts of the section (Chen and Li, 2010). Several analytical methods have been developed to determine the critical stress of distortional buckling of CFS members.

Lau and Hancock (1987) first presented an analytical model to predict the distortional buckling stress of CFS columns. The model considered the compression flange and lip alone and assumed that they were not distorted. The lateral and rotational spring were applied at the web-flange junction to represent the effects of web, as shown in Figure 2.1. Lau and Hancock found that the lateral restraint had very small influence on the critical stress and could be ignored. The stiffness of rotational spring was determined by the longitudinal compression stress and distributed bending stress along the longitudinal edges, meanwhile, the web was assumed to be simply supported along the edges. Later, Hancock (1997) extended this model to CFS beams. It was assumed that the compression end of the web was simply supported but the tension end of the web was fix supported for determining the rotational spring stiffness, the specific computational processes are illustrated in Section 3.3.1.

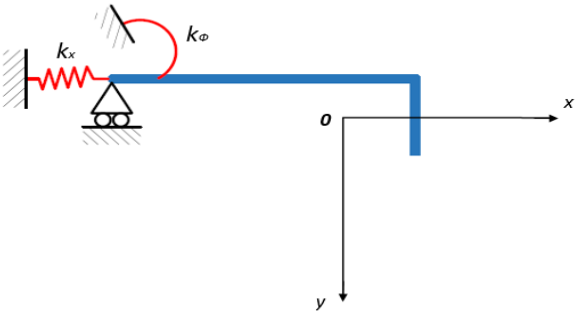

Figure 2.1 Distortional buckling model proposed by Lau and Hancock (1987)

Eurocode 3 (EN1993-1-3, 2006) recommended an analytical model which had simple expression for calculating the critical distortional buckling stress. In this model, the half flange and lip was on the elastic foundation which represented the buckling behaviour of the compression flange and lip system, see Figure 2.2. The spring stiffness could be determined by applying the unit load at the centroid of the stiffener, the two ends of the web were assumed to be simply supported. The design equation for calculating the critical stress of CFS members is given by,

$$\sigma_{cr,d} = \frac{2\sqrt{KEI_s}}{A_s} \tag{2-5}$$

where $\sigma_{cr,d}$ is the critical stress of distortional buckling, K is the spring stiffness per unit length, E is the Young's modulus, A_s is effective area of the stiffened element, I_s is the effective second moment of area of the stiffened element about the centroid axis, for channel sections, the relevant parameters are,

$$K = \frac{u}{\delta} = \frac{3D}{a^2(a+h)} \tag{2-6}$$

$$A_s = \left(\frac{b}{2}+c\right)t \tag{2-7}$$

$$I_s = \frac{bt^3}{24} + \frac{e^2bt}{2} + \frac{tc^3}{12} + ct(\frac{c}{2}-e)^2 \tag{2-8}$$

where b, c, h are the flange width, lip length and web height respectively. t is the thickness, $D= Et^3/12/(1-\mu^2)$ is the flexural rigidity of the web, $a=b-b^2/4/(b+2c)$ is the horizontal distance of the centroid of the stiffened element from the web and $e=c^2/(b+2c)$ is the vertical distance of the centroid of the stiffened element from the flange.

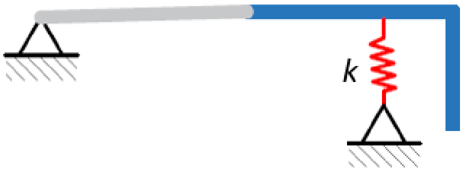

Figure 2.2 Distortional buckling model proposed in EN-1993-1-3 (2006)

According to the analytical model suggested by EN1993-1-3, Li (2009) used different support conditions at the tension and compression ends of the web to investigate their influence on the critical stress of distortional buckling of CFS sigma purlins. The results showed that the model with a fixed support at the tension end and a roller support at the compression end of the web had a better agreement with the finite strip method (FSM). To optimize the section dimensions, Ye et al. (2016) presented a methodology which can be used to develop more efficient cold-formed steel channel sections with maximum flexural strength for practical applications. The optimized sections were designed to comply with the Eurocode 3 geometrical requirements as well as with a number of manufacturing and practical constraints.

Li and Chen (2008) presented an analytical model to describe the distortional buckling of CFS sections which considered the flexure behaviour of the compression flange. It was very similar to Hancock's model (Lau and Hancock, 1987). The only difference was that they used the translational spring at the centroid of the compression flange and lip system to take the place of the rotational spring at the flange-web junction, as shown in Figure 2.3. It was shown that Li and Chen's model was as good as Hancock's model for most channel, zed and sigma sections. The details of the Li and Chen's model are shown in Section 3.4.1.

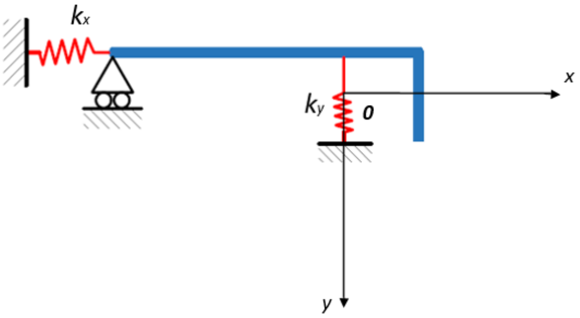

Figure 2.3 Distortional buckling model proposed by Li and Chen (2008)

Zhu and Li (2016) proposed a stiffened plate buckling model which assumed the compressive flange/lip system behaved like a rigid body to follow the movement of the compressive end of the web (see Figure 2.4). The web can be treated as a plate and the whole system can be treated as a plate with a stiffener. The analytical formula was derived for calculating the critical stress of distortional buckling of CFS beams based on the energy method. Later, Huang and Zhu (2016) extended this model to CFS columns, the web had both in-plane and out-plane bending deformations, the flange/lip systems were regarded as the stiffener at the two ends of the web subjected to asymmetric bending and torsion, good agreement of comparison between the theoretical model and FSM showed that the stiffened plate buckling model can be applied to the practical engineering. After that, they used the model for distortional buckling analysis of CFS sections with stiffened web and web stiffened by longitudinal ribs subject to compression or pure bending (Huang et al., 2018; Huang et al., 2019).

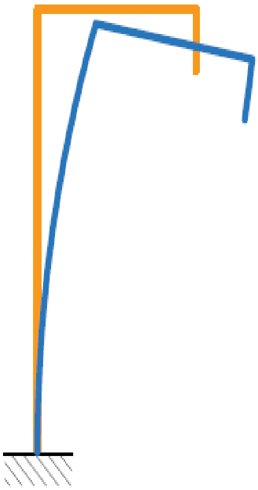

Figure 2.4 Distortional buckling model proposed by Zhu and Li (2016)

It should be pointed out that all the analytical models mentioned above can only be applied to members subjected to compression or pure bending. This is because these models did not consider the variation of pre-stresses along the longitudinal axis of the compressed flange/lip system. Chen and Li (2010) extended their former model (Li and Chen, 2008) to analysis the distortional buckling of CFS beams subjected to uniformly distributed load. The influence of stress gradient which was highly dependent on the beam length was investigated. For the very long beams, the effect of stress gradient could be ignored. Zhu and Li (2018) investigated the effect of shear stress on distortional buckling of CFS beams subjected to uniformly distributed load. It seemed that the shear stress gradient might reduce the critical stress of distortional buckling of short beams. But for the long beams, the shear stress effect could be ignored.

2.2.3 Lateral-torsional buckling

Unlike local and distortional buckling, the research on the lateral-torsional buckling of CFS members is limited. This is because the CFS members usually work with metal sheeting or cladding in which the lateral movement of upper flange is completely restrained. Normally the lateral-torsional buckling occurs in the long CFS beams with low lateral and torsional rigidity.

The calculation approaches for determining the critical moment of lateral-torsional buckling of unrestrained, simply supported CFS beams subject to different loading conditions have been described in some books (Timoshenko and Gere, 1961; Yoo and Lee, 2011). It can be expressed as follows,

$$M_{cr,l} = \alpha \frac{\pi}{l} \sqrt{EI_y (GJ + \frac{EI_w \pi^2}{l^2})} \tag{2-9}$$

where $M_{cr,l}$ is the critical moment of distortional buckling, α is the loading coefficient (α=1 for pure bending, α=1.13 for uniformly distributed load and α=1.39 for one concentrated load applied at mid-span), l is the length of the beam, E is the Young's modulus, I_y is the moment of inertia about the y-axis, G is the shear modulus, J is the torsion constant and I_w is the warping constant.

Seah and Khong (1990) proposed semi-analytical, semi-numerical method to predict the critical moment of lateral-torsional buckling of channel beams with unbraced longitudinal edge stiffeners. In theoretical study, quintic polynomial function was used to represent the deformation of plate component in transverse direction and single term trigonometric function was used to represent the deformation of plate component in longitudinal direction, meanwhile, the classical energy method was employed in matric structural analysis. Four-point loading experiments were conducted to validate the proposed method.

Cheng et al. (2013) presented an analytical solution for the flexural and lateral-torsional buckling of CFS beams subject to combined compression and bending. The interactive effect of compression load and bending moment has been investigated. They found that when the member was subjected combined compression and the major-axis bending, the bending moment would decrease the critical compressed load; when the member was subjected to combined compression and the minor-axis bending, the influence of bending moment depended on the direction of bending applied.

Li (2004) originally presented a model for analyzing the lateral-torsional buckling of CFS zed-purlin beams partially restrained by metal sheeting subjected to transverse loads which was built for practical cases. In Li's model, the restraint of sheeting was simplified by one rotational spring and translational spring, see Figure 2.5. The energy method was used for determining the critical load. The effects of interval anti-sag bar, the moment distribution and boundary conditions were investigated. Some details of Li's analytical model can be found in Section 4.4.1.

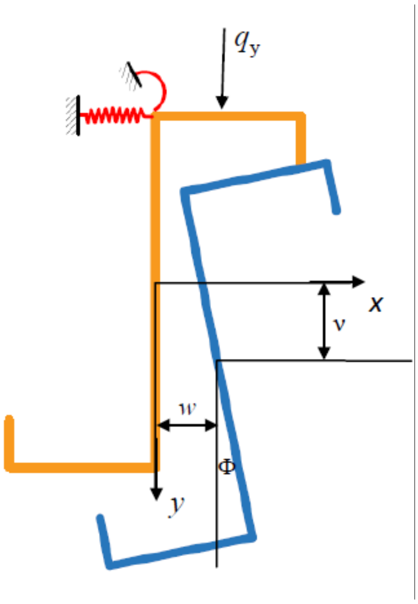

Figure 2.5 Lateral-torsional buckling model proposed by Li (2004)

Later, Chu et al. (2004, 2005) applied Li's model to explore the influence of lateral restraint on the lateral-torsional buckling of CFS zed, channel-section beams. The effect of moment variation along the longitudinal axis and boundary conditions were also investigated. It was found that the lateral restraint could increase the critical stresses and the moment gradient had a considerable influence on the lateral-torsional buckling, pure bending was the worst case (less than half of the critical moment in the uniformly distributed uplift load). Furthermore, the warping stress might not affect the lateral-torsional buckling of CFS channel-section beams. Ren et al. (2012) utilized similar model for describing bending and twisting buckling behaviour of partially restrained channel-section purlins subject to up-lift load. Calculating formula deduced by the classical bending theory was used to predict the bending stresses of the roof purlins.

2.3 Design method of cold-formed steel members

2.3.1 Generalised beam theory

The generalised beam theory (GBT) was originally proposed by Schardt (1989). The thin-walled members were supposed as an assembly of thin plates constrained to buckle as a linear combination of particular deformation modes. To take the distortional effects into account, Schardt (1994) presented a calculation equation for determining the critical stress,

$$[E\cdot{}^{k}C(\frac{\pi}{l})^{4}+G\cdot{}^{k}D(\frac{\pi}{l})^{2}+{}^{k}B]\cdot{}^{k}V_{m}-\lambda\cdot{}^{1}W_{0}\sum_{j=2}^{n}{}^{j}V_{m}\cdot{}^{1jk}\kappa\cdot(\frac{\pi}{l})^{2}=0 \tag{2-10}$$

where E is the Young's modulus, ${}^{k}C$ is the generalisation of warping constant, G is the shear modulus, ${}^{k}D$ is the generalisation of torsional constant, ${}^{k}B$ is the generalisation of transverse bending stiffness, ${}^{k}V_{m}$ is the generalisation of deformation resultant, λ is the half-wave length, ${}^{k}W_{m}$ is the generalisation of stress resultant, ${}^{ijk}\kappa$ is the second-order section property and l is the length.

After that, Davis and his colleagues (Davis et al., 1994a; Davis et al., 1994b) extended the GBT to the first-order and second-order GBT. The first order showed how this theory was used to analyze the buckling behaviour of CFS sections, whereas the second order added the geometric non-linearity into the basic equation of the GBT. Later, Davis et al. (1997) modified the GBT for calculating the critical stress of PCFS members, the concept of effective thickness was used.

More recently, Camotim and Silvestre made much contribution to the improvement of the GBT. In 2002, Silvestre and Camotim (2002a; 2002b) developed first-order and second-order GBT to describe the structural behaviour of composite thin-walled members. Subsequently, Silvestre and Camotim (2004a; 2004b; 2004c) derived analytical formula which was fully based on GBT for the distortional buckling of CFS C-, Z- and rack-section members. Later, Silvestre (2007; 2008) used the GBT to analyze the buckling behaviour of circular and elliptical hollow cross-sections.

Compared to other design method, the GBT can calculate the ultimate strength of CFS members more accurately. However, the procedure of GBT is complicated, plenty of differential equations need to be solved. It may not be promoted widely in the design guide for structural engineers.

2.3.2 Finite element method

It is known that solving stability of CFS members by using classical hand solutions is cumbersome. For this reason, nowadays the structural designers tend to utilize numerical method to analyze the buckling modes of CFS members, such as finite element method (FEM) and finite strip method (FSM).

The FEM divides large problems into smaller element, and then the simple equations of the finite elements can be assembled into a larger system of equations to solve the problem. Normally the FEM is performed with commercial program such as ANSYS and ABAQUS, the loading and boundary conditions need to be set correctly. There are two types of FEM to analyze the buckling behaviour of CFS members. One is eigenvalue analysis in which the critical stress and buckling modes can be obtained, the other one is nonlinear analysis in which the load-displacement curve can be obtained. It should be noting that stress-strain relationship of the materials, contact elements and large deflection theory are incorporated into the nonlinear analysis.

Compared to FSM, the FEM is available for all required situations. However, FEM cannot give a signature curve for a specific cross section because the beam length used in the analysis is the actual beam length, but not the wavelength of the buckling model. To obtain the critical stress of a single cross-section requires thousands of candidate buckling modes which is very time-consuming (Ádány and Shafer, 2006a).

2.3.3 Finite strip method

The basic idea of FSM is similar to those of FEM, the only difference is that one single strip is applied along the longitudinal direction. In the FSM, a special shape function is selected to describe the displacement of the whole length (Ádány, 2004).

The first paper about FSM for recognizing buckling behaviour of hot-rolled steel sections was written by Cheung (1968). Later, Hancock and his colleagues extended the spline FSM to evaluate the stabilities of thin flat-walled structures (Lau and Hancock, 1986). To estimate the effect of non-linear material stress-strain properties, strain hardening and residual stresses, Lau and Hancock (1989) presented an analytical method for inelastic buckling analysis of thin-walled sections which was based on spline FSM. Afterwards, the similar computing method was developed by Kwon and Hancock (1991), the local, distortional, overall buckling and the interaction between them in the post-buckling range can be solved.

More recently, Ádány and Shafer (2006a; 2006b; 2008) proposed constrained finite strip method (cFSM) to predict the critical load of unbranched CFS members. In the cFSM, the constrained matrices separated the degree of freedom (DOF) into those consistent with local, distortional and global modes. Thus, the number of DOF can be reduced. Later, Li and Schafer (2013) extended FSM to general end boundary conditions.

Compared to FEM, FSM is more efficient. The FSM program such as CUFSM (Shafer and Ádány, 2006) and THIN-WALL (Papangelis and Hancock, 1995) can determine the critical stress of CFS members automatically. However, the stress distribution is assumed constant along the longitude direction, the FSM cannot simulate the case that the beam subject to uniformly distributed uplift load. Furthermore, the FSM is not available for investigating the buckling behaviour of PCFS beams since the perforations cannot be easily modelled.

2.3.4 Effective width method

The local buckled plate can take considerable loads before it collapses. However, it is complicated to evaluate the structural behaviour of the post-buckled plate (Li and Chu, 2008). The effective width method (EWM) was originally introduced by von Karman et al. (1932) to determine the failure strength, the real width was replaced by effective width to simplify the calculation progress.

Winter (1968) modified the EWM for the CFS members. This method supposed that when the ultimate load reached, the effective sections would bear the total force. In other words, an actual plate with a nonlinear stress distribution due to the buckling was replaced by an effective plate with a simplified stress distribution (Schafer, 2008). The concept of effective width has been adopted by the primary design specifications (AS/NZS, 2005; EN 1993-1-5, 2006; AISI, 2016). Currently, some researchers presented a new design method based on EWM to predict the distortional buckling stress of CFS sections (Yu and Yan, 2011; Yao et al., 2016). This method was calibrated by the DSM in North America specification.

The effective width can be determined by an empirical formula which was based on a large number of experimental work. In EN 1993-1-5 (2006), the effective width of a compression element can be obtained from Table 2.1 and Table 2.2. It should be mentioned that the isolated plates of the CFS section are supposed to be simply supported. The effective cross-section of a CFS channel column or beam could be found in Figure 2.6.

The reduction factor ρ can be taken as follows,

For the internal compression elements:

$\rho = 1.0$ for $\lambda \leq 0.673$

$$\rho = \frac{\lambda - 0.055(3+\psi)}{\lambda^2} \leq 1.0 \qquad \text{for } \lambda > 0.673, \text{ where } (3+\psi) \geq 0 \qquad (2\text{-}11)$$

For the outstand compression elements:

$$\rho = 1.0 \qquad \text{for } \lambda \leq 0.748$$

$$\rho = \frac{\lambda - 0.188}{\lambda^2} \leq 1.0 \qquad \text{for } \lambda > 0.748 \qquad (2\text{-}12)$$

where $\lambda = \sqrt{\frac{f_y}{\sigma_{cr}}}$ and $\psi = \sigma_2/\sigma_1$.

Table 2.1 Internal compression elements (copy from EN 1993-1-5 (2006))

Stress distribution (compression positive)	Effective width b_{eff}
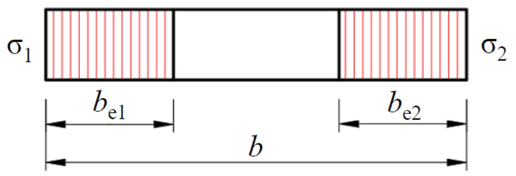	$\psi = 1$: $b_{eff} = \rho\, b$ $b_{e1} = 0.5\, b_{eff}$ $b_{e2} = 0.5\, b_{eff}$
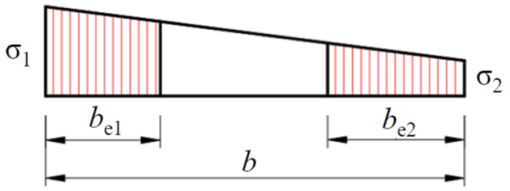	$1 > \psi \geq 0$: $b_{eff} = \rho\, b$ $b_{e1} = 2/(5-\psi)\, b_{eff}$ $b_{e2} = b_{eff} - b_{e1}$
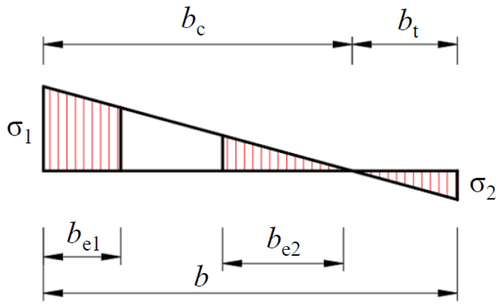	$\psi < 0$: $b_{eff} = \rho\, b_c = \rho\, b/(1-\psi)$ $b_{e1} = 0.4\, b_{eff}$ $b_{e1} = 0.6\, b_{eff}$

Table 2.2 Outstand compression elements (copy from EN 1993-1-5 (2006))

Stress distribution (compression positive)	Effective width b_{eff}
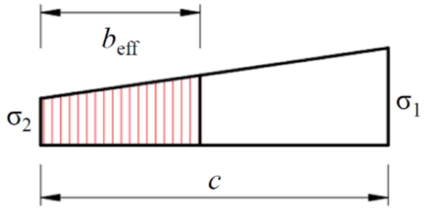	$1 > \psi \geq 0$: $b_{eff} = \rho\, c$
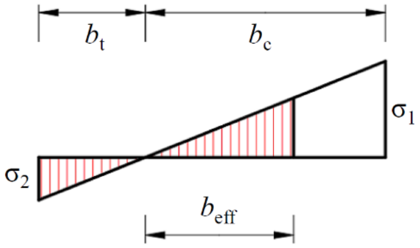	$\psi < 0$: $b_{eff} = \rho\, b_c = \rho\, b / (1-\psi)$
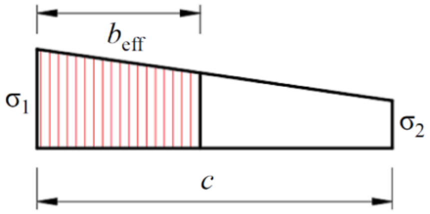	$1 > \psi \geq 0$: $b_{eff} = \rho\, c$
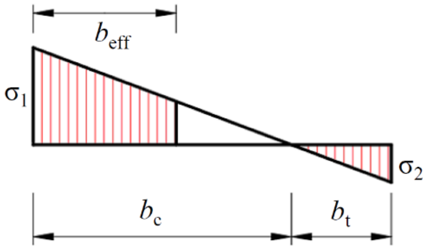	$\psi < 0$: $b_{eff} = \rho\, b_c = \rho\, b / (1-\psi)$

The EWM is a useful design approach. However, the elements of the CFS section are considered independently, the interaction between flange and web is ignored. Each element may fail at different stresses, hence the EWM is more conservative compared to other approaches. Furthermore, when it comes to more complex cross-section shapes (those with folded-in stiffeners or lips), determining the effective section can be cumbersome by using EWM.

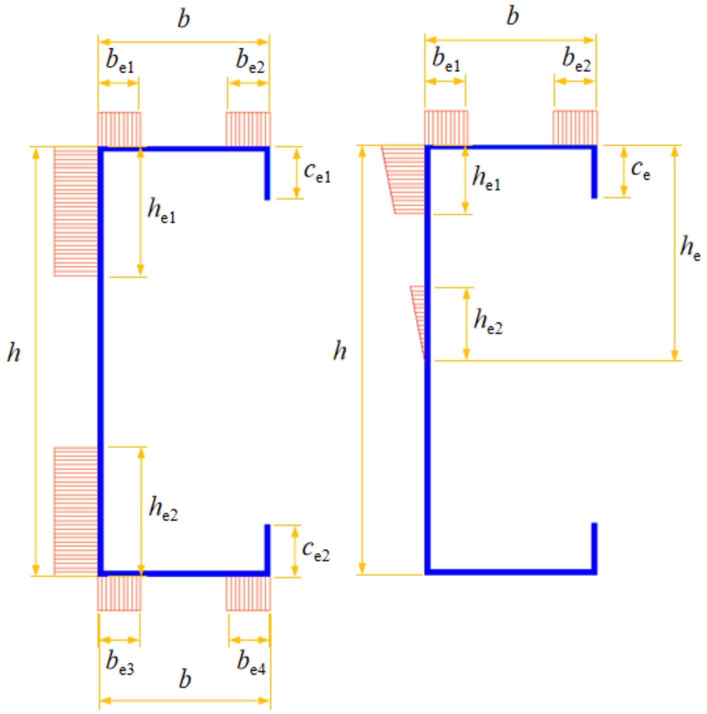

Figure 2.6 Effective cross-section of CFS channel members (a) column (b) beam (Copy from EN 1993-1-5 (2006))

2.3.5 Direct strength method

The root of the direct strength method (DSM) was the design method proposed by the researchers at the University of Sydney (Know and Hancock, 1992; Hancock et al., 1994). Schafer and Peköz (1998) first designated it as DSM, this method can be regarded as an extension of the use of column curves for global buckling with the application of local and distortional buckling. The post-buckling and the interaction between these buckling modes were also taken into account (Schafer, 2008).

In order to develop the DSM, Schafer (2002) conducted a series of tests for CFS columns failed by local, distortional and global buckling modes, the analytical and numerical solutions for the elastic buckling were also presented. Later, Yu and Schafer (2003, 2006) performed some flexural tests for C- and Z-section beams controlled by local buckling and distortional buckling, additional paired fasteners were used to isolate the two buckling modes. After that, numerical simulations of CFS beams in local and distortional buckling were conducted by Yu and Schafer (2007), all the experimental and numerical data were applied to the proposed design curves of the DSM.

The DSM was adopted in North American and Australia/New Zealand design specification (AISI, 2016; AS/NZS, 2005), the relative equations (Schafer, 2008) can be expressed as follows,

For columns:

Flexural, torsional, or torsional-flexural buckling

$$P_{ne} = (0.658^{\lambda_c^2})P_y \qquad \text{if } \lambda_c \leq 1.5$$

$$P_{ne} = \left(\frac{0.877}{\lambda_c^2}\right)P_y \qquad \text{if } \lambda_c > 1.5 \qquad (2\text{-}13)$$

where $\lambda_c = \sqrt{P_y / P_{cre}}$; P_y is the squash load; P_{cre} is minimum of the critical elastic column buckling load in flexural, torsional, or torsional-flexural buckling.

Local buckling

$$P_{n\lambda} = P_{ne} \qquad \text{if } \lambda_l \leq 0.776$$

$$P_{n\lambda} = \left[1 - 0.15\left(\frac{P_{crl}}{P_{ne}}\right)^{0.4}\right]\left(\frac{P_{crl}}{P_{ne}}\right)^{0.4} P_{ne} \qquad \text{if } \lambda_l > 0.776 \qquad (2\text{-}14)$$

where $\lambda_l = \sqrt{P_{ne} / P_{crl}}$; P_{crl} is the critical elastic local column buckling load.

Distortional buckling

$$P_{nd} = P_y \qquad \text{if } \lambda_d \leq 0.561$$

$$P_{nd} = \left[1 - 0.25\left(\frac{P_{crd}}{P_y}\right)^{0.6}\right]\left(\frac{P_{crd}}{P_y}\right)^{0.6} P_y \qquad \text{if } \lambda_d > 0.561 \qquad (2\text{-}15)$$

where $\lambda_d = \sqrt{P_y / P_{crd}}$; P_{crd} is the critical elastic distortional column buckling load.

For beams:

Lateral-torsional buckling

$$M_{ne} = M_{cre} \qquad \text{if } M_{cre} \le 0.56M_y$$

$$M_{ne} = \frac{10}{9}M_y(1-\frac{10M_y}{36M_{cre}}) \qquad \text{if } 0.56M_y \le M_{cre} \le 2.78M_y \tag{2-16}$$

$$M_{ne} = M_y \qquad \text{if } M_{cre} > 2.78M_y$$

where M_y is the cross-section first yield moment; M_{cre} is the critical elastic lateral-torsional buckling moment.

Local buckling

$$M_{n\lambda} = M_{ne} \qquad \text{if } \lambda_l \le 0.776$$

$$M_{n\lambda} = \left[1-0.15\left(\frac{M_{crl}}{M_{ne}}\right)^{0.4}\right]\left(\frac{M_{crl}}{M_{ne}}\right)^{0.4} M_{ne} \qquad \text{if } \lambda_l > 0.776 \tag{2-17}$$

where $\lambda_l = \sqrt{M_{ne} / M_{crl}}$; M_{crl} is the critical elastic local buckling moment.

Distortional buckling

$$M_{nd} = M_y \qquad \text{if } \lambda_d \le 0.673$$

$$M_{nd} = \left[1-0.22\left(\frac{M_{crd}}{M_y}\right)^{0.5}\right]\left(\frac{M_{crd}}{M_y}\right)^{0.5} M_y \qquad \text{if } \lambda_d > 0.673 \tag{2-18}$$

where $\lambda_d = \sqrt{M_y / M_{crd}}$; M_{crd} is the critical elastic distortional buckling moment.

It should be noted that the DSM presented by Schafer and Peköz (1998) is limited to pure compression and bending. Pham and Hancock (2009a) extended the DSM to purlin systems for combined shear and bending, eight different test series on purlin sheeting systems performed at the University of Sydney were used to calibrate the DSM design proposals. Later, the extended DSM were proposed by Pham and Hancock (2012a) for the design of CFS sections in shear and for combined bending and shear with or without tension field action. The shear tests of CFS sections were performed by Pham and Hancock (2012b), the result showed that the post buckling strength was caused by tension field action, relative design equations were proposed.

The spline FSM was employed by Pham and Hancock (2009b) to determine the elastic buckling stresses of CFS channel sections subject to shear force, the influence of the flange on the shear buckling was examined. Pham and Hancock (2012c) performed buckling analyses of CFS members subject to shear stresses. It was found that the long CFS member with narrow flange would buckle in a twisting mode, the CFS member with wide flange would fail by distortional buckling. When the flange is not wide enough to provide torsional resistance for the web, the CFS member would be controlled by local buckling. After that, Pham et al. (2014) summarized the extended DSM for shear buckling of plain C-sections, C-sections with rectangular and triangular web stiffeners. The shear buckling loads were computed by both semi-analytical and spline finite strip method.

Compared to the EWM, the calculation of effective width is not required in the DSM. The DSM provides new idea for engineers to obtain the ultimate load of CFS members based on determining the critical stress of elastic buckling behaviour and the yield stress (Schafer, 2008). Currently, researchers tend to extend the DSM to CFS sections in shear, combined bending and shear or web crippling.

2.4 The buckling behaviour of perforated cold-formed steel sections

As mentioned in Section 2.2, a great deal of work on the buckling behaviour of CFS members and the relevant design rules has been reported. Like CFS members, the perforated cold-formed steel (PCFS) sections may also experience three buckling modes: local, distortional and global buckling. The perforations may cause the stress concentration and decrease the cross-sectional properties (Moen, 2008). However, it is hard to determine the critical buckling loads of PCFS members, plenty of factors like the shape, size and location of holes need to be considered. The existing research on the buckling behaviour of PCFS sections including the experimental work, numerical investigation and theoretical study are scrutinized below.

2.4.1 Experimental work

Kesti and Mäkeläinen (1998) conducted a series of full-scale compression and bending tests to investigate the local and distortional buckling behaviour of the perforated steel wall studs, the influence of gypsum wallboard on the bending stiffness of the whole component was evaluated. Subsequently, the compression experiment of non-perforated and perforated equal-angle CFS stub columns were carried out by Dhanalakshimi and Shanmugam (2001). It was found that the existence of perforations could reduce the ultimate strength of the columns, the influence of multiple holes was more obvious for the member with low slenderness ratio. Furthermore, the ultimate strength of the column would decrease rapidly when the eccentric load was applied away from the corner, however the effect of eccentricity reduced for the member with large slenderness ratio.

Moen and Schafer (2008) conducted 24 compression tests of short and intermediate length CFS columns with and without slotted web holes to study the relationship between elastic buckling and column deformation. The influence of slotted holes on the buckling behaviour and ultimate strength was examined. The setup and instrumentation of column tests were shown in Figure 2.7, the steel platens were rigidly fixed to the crosshead and actuator. The friction-bearing boundary conditions were used in this test which means the columns were placed directly on the steel platens as the compression load was applied. After that, bending experiments on CFS joints with rectangular un-stiffened web holes were carried out by Moen et al. (2013). The experimental results were used to validate the extended DSM equations for CFS joints with holes.

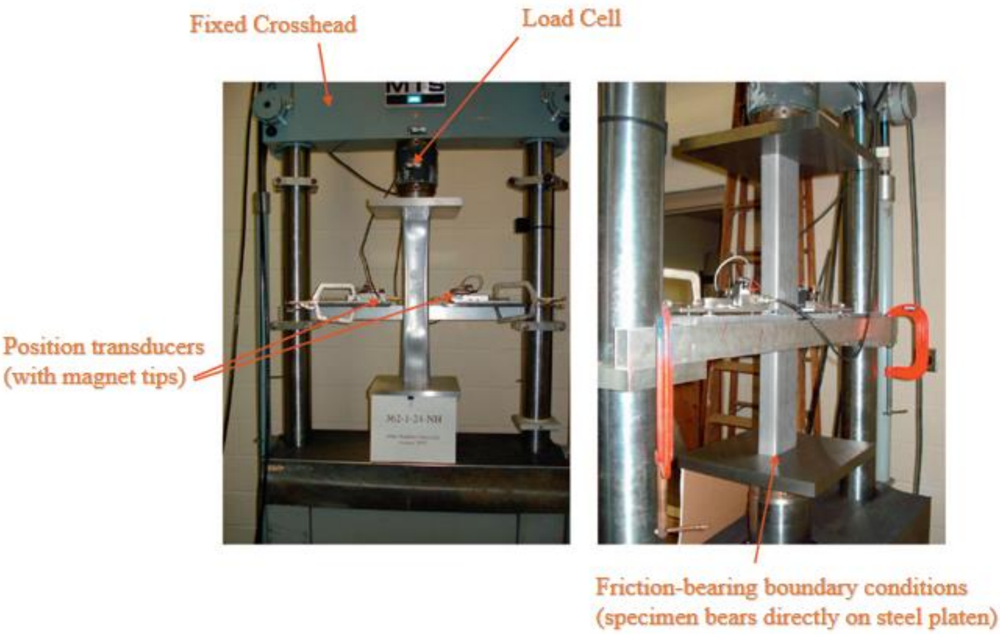

Figure 2.7 Setup and instrumentation of the column test (Moen and Schafer, 2008)

Kulatunga and his colleagues (Kulatunga and Macdonald, 2013; Kulatunga et al., 2014) performed compression experiments to evaluate the influence of cross-section dimension, perforation position, shape and size on the load capacity of PCFS columns. It was shown that the ultimate failure load of PCFS columns under compression varied with the web openings, and the load capacity of PCFS columns had a remarkable decrease with the increase of length and opening area of the perforations. Meanwhile, the design equations in AISI Specification, British Standard and EU Standard were employed to determine the relevant buckling load.

Chen et al. (2019) carried out 26 axial compression tests of CFS columns with edge-stiffened, un-stiffened web openings and plain web to evaluate the influence of edge-stiffened circular holes on the load capacity. Their test results showed that the compression resistance of CFS sections with edge-stiffened web openings was higher than that of CFS sections with plain web. The design equations based on the parametric study were proposed to predict the axial load capacity of CFS column with edge-stiffened web openings (Chen et al., 2020a). Later, Chen et al. (2020b) conducted 16 four-point bending tests to investigate the effects of hole size, stiffener length, specimen length and fillet radius on the moment capacity of CFS beams with edge-stiffened web openings. It was found that the AISI and AS/NZ design equation can well predict the moment capacity of CFS channel beams without web holes, but is over-conservative by around 11% and 28% respectively for CFS channel beams with un-stiffened and edge stiffened web openings.

Zhao et al. (2019) carried out 10 groups of pure bending test to estimate the flexural behaviour of PCFS beams. In the test, two experimental specimens were bolted to the load transfer blocks and the end support points, meanwhile the steel plates were installed at the non-research span of the compression flanges (see Figure 2.8). It was shown that for the beams with web openings tested the failure modes of the beams changed from the single distortional buckling model or single local buckling model to the interactive buckling between local and distortional models. The moment capacity of the beam reduced slightly when the hole height-to-web depth increase from 0 to 0.4, and reduced dramatically when the hole height-to-web depth further increase to 0.8. Furthermore, the current DSM equations were found to be unconservative for most PCFS beams, and hence the modified DSM formulas were proposed.

Figure 2.8 Four-point bending test rig (Zhao et al., 2019)

Recently, many researchers focused on the performance of PCFS members for steel storage rack systems since the web perforations could help to adjust the height of the shelf. For example, the compression steel pallet rack members of different cross-section dimensions, with and without perforations were tested by Crisan et al. (2012a). The calibrated finite element model and erosion of critical bifurcation load approach were applied to determine the buckling curves (Crisan et al., 2012b). Bernuzzi and Maxenti (2015) studied the performance of isolated rack columns subject to axial load and gradient moment and three European alternatives were proposed to design PCFS beam-columns for steel storage systems.

2.4.2 Numerical investigation

Shanmugam and Dhanalakshmi (2001) developed finite element models of channel sections with various hole sizes, shapes and web plate slenderness ratios using the commercial software ABAQUS to determine the ultimate load capacity of PCFS channel stub columns. The material and geometric non-linearity, residual stresses were taken into account in the numerical investigation. The quadratic equation was proposed to determine the load-carrying capacity based on the parametric studies. Subsequently, a total of 960 non-linear finite element models of steel beams covering different section sizes and perforation configurations were performed by Liu and Chung (2003).

As mentioned in Section 2.3.3, the web perforations lead to the variation of sectional property along the beam length direction and thus it is difficult to use FSM to do the analysis of the perforated beams. Nevertheless, some simplified models such as equivalent-thickness model and perforated model were employed in the FSM to represent the effect of web perforations, then the elastic buckling stresses obtained from the FSM were applied in the DSM for analysing the PCFS studs subject to axial load (Sputo and Tovar, 2005; Tovar and Sputo, 2005).

After that, Smith and Moen (2014) improved the calculation model in the FSM for thin-walled metal columns with perforation patterns. The weighted average of the net and gross cross-sectional moment of inertia along the length was used in the finite strip model to determine the critical stress of flexural buckling, and the weighted average of the warping constant and torsion constant was used for flexural-torsional buckling. For local buckling, the reduced thickness stiffened element equation based on Rayleigh-Ritz energy method was developed to simulate the influence of the perforation patterns. For distortional buckling, the reduced thickness equation was derived to simulate the decreased bending stiffness caused by the perforation patterns.

Casafont et al. (2012) carried out the numerical investigation on the elastic buckling of perforated steel storage rack columns, the reduced thickness based on regression analysis was used in the FSM to calculate the critical buckling load. The accuracy was verified by eigenvalue buckling FEM analysis and real test. It was found that the concept of reduced thickness can be applied to distortional and global buckling, but it is not able to cover all varieties of perforations for local buckling.

Moen and Schafer (2011) conducted the non-linear finite element simulation of 213 PCFS columns using ABAQUS to evaluate the proposed design formula. Specific column lengths and cross sections were selected for isolating the case collapsed by distortional buckling and local-global buckling, the buckling modes of PCFS columns obtained from eigenvalue buckling FEM analysis could be found in Figure 2.9. The boundary condition for the simulated columns were pinned-pinned free-to-warp, the node centered in flange was restrained in longitudinal direction to avoid the rigid body movement (see Figure 2.10). The non-linear finite element models were validated with the experiments on PCFS columns (Moen and Schafer, 2008), the recommended DSM equations for PCFS columns across a wide range of hole sizes, spacings, shapes and cross-section dimensions could be expressed as follows,

Local buckling

$$P_{nl} \leq P_{ynet} = A_{net} f_y \tag{2-19}$$

where P_{ynet} is the strength of the column net cross-section at the location of the hole and A_{net} is the area of the net cross-section.

Global buckling

$$P_{ne} = (0.658^{\lambda_c^2}) P_{ynet} \left(\frac{P_y}{P_{ynet}}\right)^{(\lambda_c/1.5)^2} \leq P_{ynet} \qquad \text{if } \lambda_c \leq 1.5$$

$$P_{ne} = \left(\frac{0.877}{\lambda_c^2}\right) P_y \leq P_{ynet} \qquad \text{if } \lambda_c > 1.5 \tag{2-20}$$

Distortional buckling

$$P_{nd} = P_{ynet} \qquad \text{if } \lambda_d \le \lambda_{d1}$$

$$P_{nd} = P_{ynet} - \left(\frac{P_{ynet} - P_{d2}}{\lambda_{d2} - \lambda_{d1}}\right)(\lambda_d - \lambda_{d1}) \qquad \text{if } \lambda_{d1} < \lambda_d \le \lambda_{d2} \tag{2-21}$$

$$P_{nd} = \left(1 - 0.25\left(\frac{P_{crd}}{P_y}\right)^{0.6}\right)\left(\frac{P_{crd}}{P_y}\right)^{0.6} P_y \qquad \text{if } \lambda_d > \lambda_{d2}$$

where $\lambda_{d1}=0.561(P_{ynet}/P_y)$, $\lambda_{d2}=0.56[(14(P_{ynet}/P_y)^{0.4}-13]$ and

$$P_{d2} = \left(1 - 0.25\left(\frac{1}{\lambda_{d2}}\right)^{1.2}\right)\left(\frac{1}{\lambda_{d2}}\right)^{1.2} P_y \tag{2-22}$$

The extended DSM approaches for PCFS beams were reported in Moen and Schafer (2010), relevant equations can be expressed as follows,

Global buckling

$$M_{ne} = M_{cre} \qquad \text{if } M_{cre} \le 0.56M_y$$

$$M_{ne} = \frac{10}{9} M_y \left(1 - \frac{10M_y}{36M_{cre}}\right) \qquad \text{if } 0.56M_y \le M_{cre} \le 2.78M_y \tag{2-23}$$

$$M_{ne} = M_y \qquad \text{if } M_{cre} > 2.78M_y$$

where M_{cre} includes the effect of holes.

Local buckling interaction

$$M_{nl} = M_{ne} \le M_{ynet} \qquad \text{if } \lambda_l \le 0.776$$

$$M_{nl} = \left[1 - 0.15\left(\frac{M_{crl}}{M_{ne}}\right)^{0.4}\right]\left(\frac{M_{crl}}{M_{ne}}\right)^{0.4} M_{ne} \qquad \text{if } \lambda_l > 0.776 \tag{2-24}$$

where M_{crl} includes the effect of holes.

Distortional buckling

$$M_{nd} = M_{ynet} \qquad \text{if } \lambda_d \le \lambda_{d1}$$

$$M_{nd} = M_{ynet} - \left(\frac{M_{ynet} - M_{d2}}{\lambda_{d2} - \lambda_{d1}}\right)(\lambda_d - \lambda_{d1}) \qquad \text{if } \lambda_{d1} < \lambda_d \le \lambda_{d2} \tag{2-25}$$

$$M_{nd} = \left(1 - 0.22\left(\frac{M_{crd}}{M_y}\right)^{0.6}\right)\left(\frac{M_{crd}}{M_y}\right)^{0.6} M_y \qquad \text{if } \lambda_d > \lambda_{d2}$$

where $\lambda_d=(M_y/M_{crd})^{0.5}$, $\lambda_{d1}=0.673(M_{ynet}/M_y)$, $\lambda_{d2}=0.673[(1.7(M_y/M_{ynet})^{1.7}-0.7]$, M_{crd} includes the effect of holes and

$$M_{d2} = \left(1 - 0.22\left(\frac{1}{\lambda_{d2}}\right)^{0.5}\right)\left(\frac{1}{\lambda_{d2}}\right)^{0.5} M_y \tag{2-26}$$

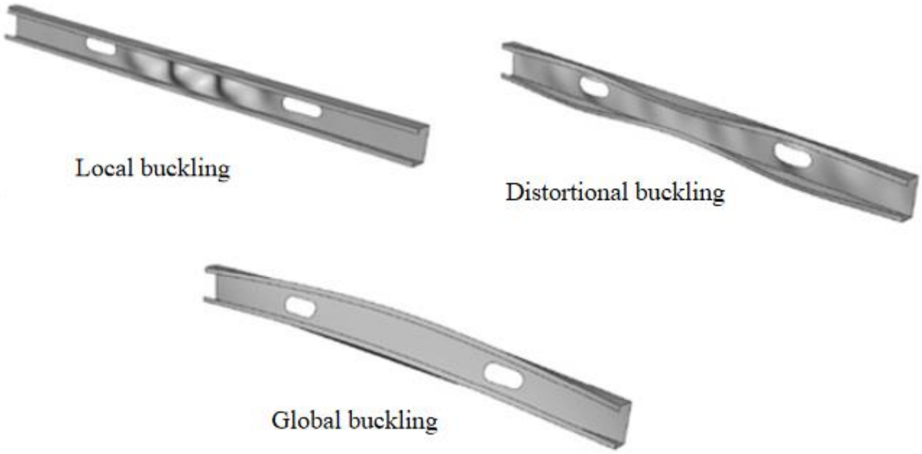

Figure 2.9 Buckling modes of PCFS columns obtained from eigenvalue buckling FEM analysis (Moen and Schafer, 2011)

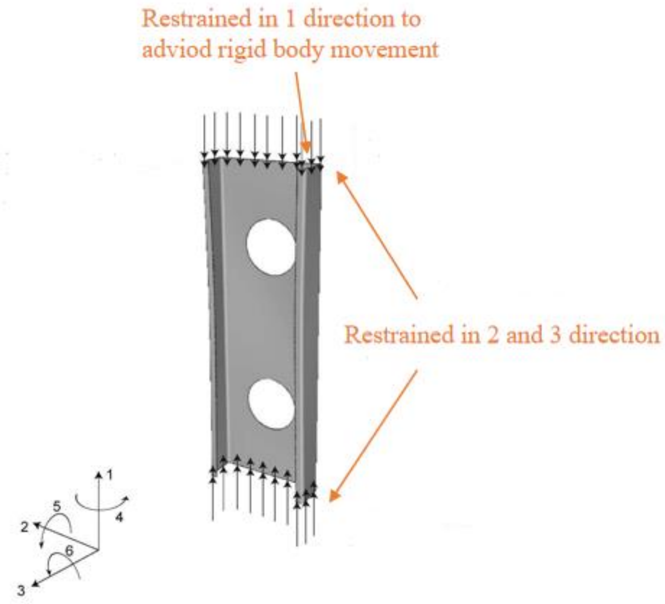

Figure 2.10 Boundary and loading conditions of finite-element model (Moen and Schafer, 2011)

2.4.3 Theoretical study

Early work tends to explore the influence of perforations on the buckling behaviour of rectangular plates. For example, Brown et al. (1987) utilised the conjugate load method to analyse the stability of plates with centrally located, rectangular perforation. Shanmugam et al. (1999) investigated the post-buckling behaviour of perforated plates subject to uniaxial or biaxial compression with different boundary conditions by using FEM, a design formula was proposed to determine the ultimate load based on their parametric studies. It was found that the ultimate strength of perforated plates would decrease with the increase of hole size and slenderness ratio, furthermore the ultimate loads of plates with circular holes were higher than the plates with square holes. Maiorana et al. (2009) developed the FEA studies of plates with circular and rectangular holes at different positions subject to axial compression and bending moment to evaluate the influence of position and dimension of perforation on the linear buckling behaviour.

Later, Moen and Schafer (2009b) put forward the forms of expressions based on the classical plate stability theory for stiffened and unstiffened elements to approximate the critical stress of thin plates in compression or bending. The finite element eigenvalue buckling studies were developed to validate the proposed expression. It was observed that the holes would change the half-wave length of the buckling modes (see Figure 2.11), thus the critical buckling stress of thin plates might decrease or increase depending on the geometry and spacing of perforations.

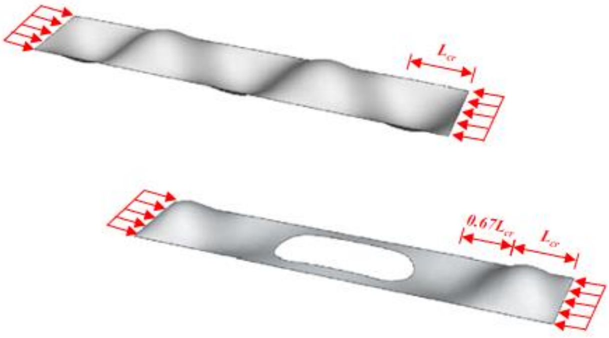

Figure 2.11 Local buckling shape of simply-supported plate with or without holes subject uniform compression (Moen and Schafer, 2009b)

Miller and Peköz (1994) presented the unstiffened strip approach for predicting post-buckling strengths of perforated wall studs. The web of the wall stud was assumed as two unstiffened elements which located on both sides of the perforation. The modified effective width approach was applied in the proposed analytical model. Davies et al. (1997) modified the GBT for analyzing PCFS sections subject to axial load and bending, in which the perforated plate was treated as unperforated plate with effective thickness. Szabo and Dubina (2004) calibrated effective width formula for the PCFS sections, the erosion of critical bifurcation load approach was used to evaluate an equivalent imperfection factor for EN buckling curves.

Moen and Schafer (2009a) introduced the simplified methods for calculating the critical stress of local, distortional and global buckling of PCFS sections. The formula for predicting the critical load of global buckling was deduced based on classical energy solutions, “weighted average” cross-section properties were employed to represent the influence of perforations. The critical loads of distortional and local buckling were obtained by semi-analytical FSM. The element thickness and buckling half-wavelength were modified in the finite strip models to consider the effect of holes.

Yao and Rasmussen (2011a) applied the isoparametric spline FSM to the material and geometric non-linear analysis of PCFS structures. The related formulas including kinematics assumptions, strain-displacement relations, constitutive relations and equilibrium equations were proposed. It was shown that the implicit backward Euler return method was superior to the explicit integration scheme due to the numerical efficiency and reliability. The proposed theoretical approach was validated against their numerical investigation. The results indicated that it was efficient and accurate for predicting the inelastic post-buckling behaviour of PCFS structures (Yao and Rasmussen, 2011b).

Lawson and Basta (2019) derived simplified formula to determine the deflection of simply supported C-section beams with isolated and closely spaced circular web openings subject to uniform loading. The additional deflection of a PCFS beam was expressed as a function of the pure bending deflection of the unperforated beam. Comparing to the results of tests and finite element models, it was shown that the proposed formula were reasonably accurate for the beams: L (beam span) $\geq 15h$ (section depth) and h_0 (opening diameter) $\leq 0.8h$ (section depth).

More recently, this research group proposed some analytical models to predict the distortional buckling stress of PCFS beams subject to pure moment and uniformly distributed load (Yuan et al., 2017; Yu et al., 2019; Yu et al., 2020; Yu et al., 2021). The variable moment distributed on the longitude direction could alter the half-wave length of distortional buckling and hence change the critical buckling stress. For beam subject to pure bending, the concept of equivalent width was applied to determine the reduction of web bending rigidity. It was shown that the analytical solution based on EN1993-1-3 model and Hancock's model can calculate the distortional buckling stress. A new analytical approach based on the stiffened plate buckling model was carried out for approximating the critical stress of flange/web distortional buckling, the relative eigenvalue equation was solved by using Rayleigh-Ritz method.

2.5 The structural behaviour of cold-formed steel built-up sections

The built-up members can be assembled by individual CFS studs using welds, self-drilling screws or bolts. Comparing to single open sections, the built-up members have larger torsional rigidity. Nowadays, they are widely used in the industry due to their excellent torsional resistance. The design method can be found in North American Specification standard (AISI, 2016). This section reviews the existing literature on the CFS built-up sections, CFS built-up sections with intermediate stiffeners as well as CFS built-up sections with perforations.

2.5.1 CFS built-up sections

Gjelsvik (1990) presented an analytical method for built-up columns. The method extended the classical Engesser method for columns and the Timoshenko shear-beam theory for beams. It was found that the stay plates could affect the buckling load and the chords' bending stiffness should be taken into account. Afterwards, the Engesser type approach was used to predict the buckling loads of shear columns, the influence of shear stiffness on the buckling load for usual standard boundary conditions was presented by Gjelsvik (1991).

Piyawat et al. (2013) developed an axial load capacity equation for doubly symmetric CFS built-up sections. The design equation was proposed based on a regression analysis of three-dimensional surface fitting and calibrated by the experimental data. It exhibited a good agreement with numerical and experimental results. Abbasi et al. (2018) applied the compound strip method to investigate the elastic buckling behaviour of CFS built-up sections with discrete fasteners. A beam element with adjustable stiffness properties was used to represent the fastener. The results demonstrated that the buckling capacity of the CFS built-up section increased when the fastener spacing ratio reduced.

A total of 32 compression tests were conducted by Stone and LaBoube (2005) to investigate the structural behaviour of CFS built-up I-sections. It was shown that the equations in current design specification were conservative to determine the ultimate load. Later, Georgieva et al.

(2012) performed 12 bending tests and 8 compression tests to study the behaviour of double-Z built-up members, the actual failure modes and overall buckling capacity of these sections were determined.

Xu et al. (2009) established finite element models using ANSYS to investigate the flexural strength of CFS built-up box section subject to eccentric loads. To consider the effect of screws, the translational and rotational degrees of freedom where the screws located were coupled in the x, y and z directions. In their parametric study, the influence of steel yield strength, web height-to-thickness ratio, screw spacing and location of applied load were investigated. After that, the flexural strength of CFS built-up lip-reinforced I-beams was evaluated by numerical and experimental study. The strength-reduction method and effective width method to predict the ultimate load were proposed by Zhou and Shi (2011).

Laím et al. (2013) carried out experimental and numerical studies on the structural behaviour of CFS built-up beams with C-, I-, R- and 2R- shaped cross sections. In the finite element analysis, the contact between the two profile surfaces was assumed as hard contact and the tangential friction coefficient was assumed as 0.2. The geometric imperfections for local, distortional and global buckling were chosen as $h/300$, $0.40t$ and $L/750$, respectively. The influence of the thickness, height and length on the structural behaviour were evaluated by parametric studies.

Li et al. (2014) studied the ultimate load-carrying capacity of CFS built-up box and I section through experimental and numerical investigations. The commercial software ANSYS was adopted for the finite element analysis, the nodes where the screws located were coupled to simulate the connection between the overlapping webs (see Figure 2.12), while the effect of friction was neglected. A total of 21 compression tests were carried out to validate against the numerical results. The strength estimation method was proposed for the CFS built-up members under axial compression.

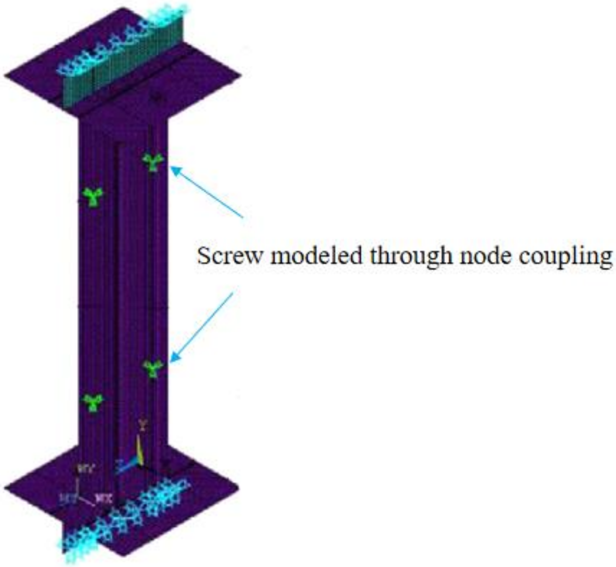

Figure 2.12 ANSYS model for CFS built-up members (Li et al., 2014)

Fratamico et al. (2018) investigated buckling and collapse behaviour of CFS built-up columns, a total of 17 concentric compression specimens were tested to explore the composite action in sheathed and bare columns. It can be observed that connecting the webs in CFS built-up members with fasteners could emerge the composite action and increase the load capacity in unsheathed columns. However, all sheathed columns failed in web local buckling, the composite action from the fasteners was not obvious.

Wang and Young (2018) explored the influence of screw arrangements on the behaviour and design of CFS built-up open or closed section beams. A total of 35 beams with different screw arrangements were tested under four-point bending. The results of experiment were used to verify the finite element models. According to the parametric study, the current DSM equations were shown to predict the ultimate strength of CFS built-up open section beams well. For the CFS built-up closed section beams, the current DSM equations were modified to predict the ultimate strength and the maximum screw spacing was recommended for the design rules.

Roy and his colleagues conducted both several experimental and numerical work to explore the structural behaviour of CFS built-up sections. For example, compression tests and non-linear finite element analysis were conducted to assess the effect of screw spacing and cross-sectional thickness on the structural behaviour of axially loaded back-to-back CFS built-up channel sections (Ting et al., 2017; Roy et al., 2018a). It could be found that the number of screws had limited influence on the slender columns, but the strength would decrease when the spacing of screws doubled for the short and intermediate columns. When the thickness was above 1.15 mm, the AISI specification would overestimate for the short and intermediate columns. Later, Roy et al. (2018b) presented an experimental study on the axial strength of back-to-back gapped CFS built-up channel columns to investigate the effect of the gap and link-channel spacing.

Iman’s research group carried out experimental and numerical studies on the strength and deflection behaviour of CFS built-up sections. For instance, Ye et al. (2018b) developed the numerical models to investigate the flexural strength and failure modes of CFS back-to-back channel-section beams. The verified FE models were used to assess the design capacity in EC3 and DSM, and it was showed that both the design rules can provide accurate predictions. Using compression tests they also investigated the effects of connector spacing on the behaviour and capacity of CFS built-up columns. It was found that the connector spacing has obvious effect on the buckling modes but has minimal influence on the ultimate capacity of CFS built-up columns (Meza et al., 2020a; Meza et al., 2020b). More recently, Mojitabaei et al. (2021) developed the optimization process for both single and built-up CFS beam-column members with various lengths and thicknesses subject to different loading conditions by using a generic algorithm.

In addition, the experimental investigations on the axial strength of CFS built-up box sections and face-to-face CFS built-up channel sections were presented (Roy et al., 2019a; Roy et al., 2019b). The specimens of the compression tests were selected from short to slender columns, non-linear finite element models verified against the experimental data were performed for their parametric study. The effect of fastener spacing on the axial strength was evaluated. It was shown that the current design equations were conservative for both CFS built-up box sections and face-to-face CFS built-up channel sections.

Chen et al. (2020c) presented new results on the axial strength of back-to-back CFS built-up sections with edge-stiffened holes, un-stiffened holes and plain webs through axial compression tests and finite element analysis. Tensile coupon tests were conducted to obtain the material properties of the channels. The test results showed that the axial strength of the column with edge-stiffened holes was 6.6% on average higher than the column with plain web, whereas the axial strength of the same section with un-stiffened holes had a 12.4% on average compared to the plain channel.

Other researchers also focused on the structural behaviour of CFS built-up sections connected by welds. For example, Landolfo et al. (2008) carried out the experimental investigations of laser welded built-up CFS beams to assess the load bearing capacity. The influences of connection strength and weld configuration on the load bearing capacity were also evaluated. Whittle and Ramseyer (2009) conducted hundreds of compression tests on closed-section, built-up C-channels to check the accuracy of the approach proposed in North America Specification. The results showed that the modified slenderness ratio was exceedingly conservative, the unmodified slenderness ratio and fastener spacing provisions were consistently conservative.

Reyes and Guzmán (2011) reported the experimental investigation to explore the comparative behaviour of CFS built-up box section subject to compression. The samples were connected by seam welds with different spacings and tested under the rigid and flexible end support conditions. The results obtained from the tests showed that the modified slenderness ratio was not always required for the member with 2.0 mm and 1.5 mm thick, the actual slenderness ratio could be applied to determine the ultimate strength. Substantially, Guzmán et al. (2021) evaluated the influence of seam welding space on CFS built-up box flexural members through an experimental study. The results concluded that the seam space should be less than the distortional buckling half-wave length of the single C section and box section and a mean value between these parameters was recommended for calculating the maximum separation between seam welds.

2.5.2 CFS built-up sections with intermediate stiffeners

Young's research group reported several experimental studies on the design of CFS built-up sections with edge or intermediate stiffeners during the past decades. The web stiffeners can reduce the slenderness of the plate element and improve the buckling strength. Current DSM equations were modified based on the experimental and numerical results to design the CFS built-up sections with intermediate stiffeners. For example, a range of column tests on CFS built-up closed sections with intermediate stiffeners were conducted by Young and Chen (2008). Three different method (single section, single restrained section and double section) were employed in the finite strip buckling analysis to obtain the local and distortional buckling stress. It was shown that the DSM where the critical stresses obtained from single section were conservative and reliable.

Zhang and Young (2012) performed several compression tests of CFS built-up I-shaped open sections with edge and web stiffeners to evaluate the suitability of the DSM. It was shown that the DSM was available for predicting the ultimate strength of CFS built-up I-shaped open sections with edge and web stiffeners. The critical stresses obtained using 1.2 times thickness of the web in the contact area were reliable. Later, the modified DSM based on the extensive numerical investigation was proposed for the design of CFS built-up open section columns with longitudinal stiffeners. More recently, Zhang and Young (2018) presented an experimental study on the structural behaviour of CFS built-up closed section columns with web stiffeners. According to their reliability analysis, the DSM using nominal plate thickness in the contact area to obtain the critical stress was considered more reliable and conservative compared to other methods.

Wang and Young (2015a, 2015b) carried out an experimental investigation on the structural behaviour of CFS built-up open and closed sections with intermediate stiffeners subject to bending. It was observed from their four-point and three-point bending tests that the local and distortional buckling behaviour of built-up beams were different from the single specimens. The modified DSM equations for CFS doubly symmetric built-up open and closed section with intermediate stiffeners were calibrated with the numerical parametric study.

Roy et al. (2020) presented experimental and numerical investigations on the flexural capacity of gapped CFS built-up channel sections. The results showed that the influence of link-channel spacing on the moment capacity was limited, however the influence of gap between the back-to-back channels on the moment capacity was more significant. Furthermore, the current design guidelines (AISI, 2016; AS/NZS, 2005) could be conservative as much as 27% for predicting the flexural capacity of gapped CFS built-up channel sections.

2.5.3 CFS built-up sections with perforations

For the CFS built-up section with perforations, the appearance of web openings can decrease cross-sectional properties and the sections could be controlled by local or distortional buckling more easily. Hence, the modified slenderness ratio method for CFS built-up sections addressed in North America Specification standard (AISI, 2016) is not available in this case. Sivakumaran et al. (2006) conducted the bending tests to investigate the flexural strength of CFS joists with unreinforced and reinforced web openings. The results showed that it was possible to set up reinforcement schemes for CFS sections with large web openings.

Wang and Young (2015c) tested a total of 43 CFS built-up beams with web perforations under four-point bending to observe the reduction of moment capacity and localized failure modes caused by the holes in the web. The specimens contained ten cross-section sizes with the hole diameter-to-web depth ranged from 0.25 to 0.7. Typical ultimate failure stage of CFS built-up beams with web perforation in the four-point bending tests was shown in Figure 2.13. It was evident from the results that the influence of hole on the moment capacity was small when the hole diameter-to-web depth was 0.5, whereas the influence increased when the hole diameter-to-web depth was up to 0.7.

After that, Wang and Young (2017) performed a wide range of nonlinear finite element analysis to develop extensive parametric studies on the CFS built-up beams with various hole sizes and beam slenderness. The finite element models were developed by commercial software ABAQUS, simply supported conditions were simulated by restraining U1, U2 and

UR3 at the end of the beam and using symmetric boundary condition (U3=0, UR1=0 and UR3=0) at the mid span of the beam (see Figure 2.14). To facilitate convergence, the displacement-controlled numerical analysis was employed during the non-linear solution. It was shown that the influence of hole on the moment capacity was more significant for CFS built-up closed beams than CFS built-up open beams. Furthermore, it proved that the DSM formulae were capable to calculate the ultimate strength of CFS built-up closed and open sections with web perforations.

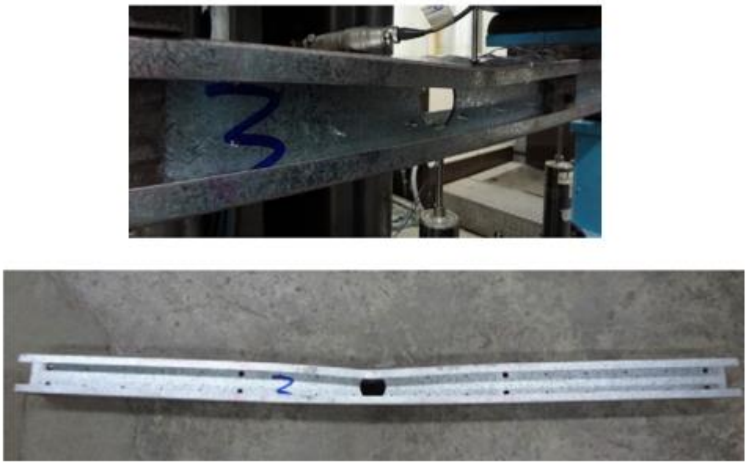

Figure 2.13 Ultimate stage of distortional and flexural buckling of CFS built-up beams with web perforation in the four-point bending tests. (Wang and Young, 2015c)

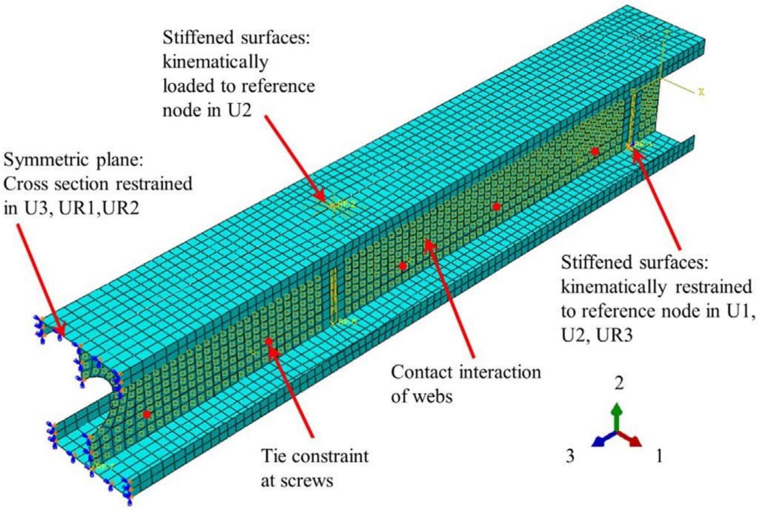

Figure 2.14 ABAQUS model for CFS built-up beams with web perforation (Wang and Young, 2017)

More recently, Chen et al. (2021) carried out an experiment to examine the moment capacity of 14 back-to-back CFS built-up beams with edge-stiffened holes, un-stiffened holes and plain webs. Non-linear finite element models were established by software ABAQUS, eigenvalue analysis was first performed to obtain the buckling modes and the load-displacement analysis was then performed to determine the moment capacity. The finite element simulation had a good agreement with the test results as shown in Figure 2.15. It was found that the moment capacity of built-up beam with five edge-stiffened holes was 15.4% higher than the specimen with plain web, whereas the same section with un-stiffened holes had a 15.1% reduction compared to the specimen with plain web. Furthermore, the moment capacity of back-to-back section was more than twice as much as the single section due to the effect of the contact due to the composite action.

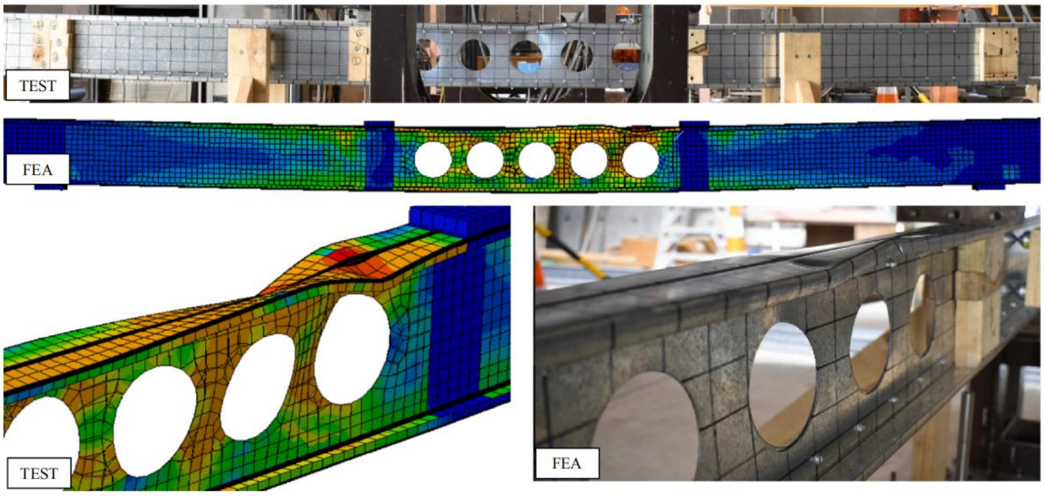

Figure 2.15 Distorsional buckling of CFS built-up beams with web perforations in test and finite element simulation (Chen et al., 2021)

2.6 Summary

This chapter has presented a literature review on the development of analytical approaches to determine the buckling load of CFS members and design rules for CFS sections to calculate the ultimate failure load. Special attentions have been paid to the buckling behaviour of PCFS members and the structural behaviour of CFS built-up sections with web perforations, including theoretical, numerical and experimental investigations. Some important findings and conclusions summarized from the literature review are listed as follows,

- Most existing analytical models to predict the critical stress of distortional buckling or lateral-torsional buckling were employed for the CFS sections with plain web, i.e. without holes on the web. Little work has been done to develop theoretical approaches for calculating the elastic buckling load of PCFS sections. The specific expressions for predicting the distortional or lateral-torsional buckling stress of PCFS beams are urgently required.

- In the current specifications, the design equations were established for the cases that the specimens subject to compression or pure bending. However, the design formula for determining the critical stress of PCFS sections subject to the uniformly distributed load has not been discussed in the literature. Hence, further research is needed.

- A great number of investigations on exploring the structural behaviour of CFS built-up sections and CFS built-up sections with intermediate stiffeners has been reviewed in the Section 2.5. However, the research related to CFS built-up sections with perforations was really limited, which implies the requirement of this project.

- The finite strip analysis software CUFSM (Shafer and Ádány, 2006) has been widely used to calculate the critical buckling loads of CFS members. However, the CUFSM dose not have the function to model the web perforations. The eigenvalue analysis by finite element software, ANSYS should be conducted to determine the critical buckling stress of PCFS sections.

- The load-controlled method conducted by ANSYS for the nonlinear analysis of CSF built-up sections might meet the convergence problems. Therefore, most researchers tried to use the displacement-controlled approach for the nonlinear finite element analysis to obtain the ultimate failure load of CSF built-up sections.

- The modified slenderness ratio method addressed in North America Specification standard (AISI, 2016) was not available to calculate the ultimate strength of CFS built-up sections. Recently, researchers tend to use the DSM to determine the ultimate failure loads which require the accurate critical stresses of local, distortional and global buckling. However, the DSM is limited to the CFS built-up sections without holes. Further modifications on the DSM equations are needed for the CFS built-up sections with web perforations.

Chapter 3 — Distortional buckling performance of perforated cold-formed steel channel beams

3.1 Introduction

This chapter describes the analytical and numerical investigations on the distortional buckling performance of perforated cold-formed steel channel channel beams subject to pure bending and uniformly distributed load.

The eigenvalue buckling analysis conducted by ANSYS is used to examine the distortional buckling behaviour of PCFS beams. The influence of hole sizes, cross-section dimensions and stress gradient is discussed. Finite strip models of CFS beams with plain web performed by CUFSM is used to check the boundary and loading conditions of the eigenvalue buckling analysis.

An analytical approximate solution for predicting the critical moment of distortional buckling of PCFS beams subject to pure bending is derived according to Hancock's model proposed in 1987. The reduction of rotational spring stiffness deduced by energy method is used to represent the effect of web perforations on the critical moment of distortional buckling.

A theoretical approach for calculating the critical stress of distortional buckling of PCFS beams subject to uniformly distributed load is proposed based on Li and Chen's model proposed in 2008. The influence of web perforations is reckoned by reducing the vertical spring stiffness. To obtain the critical stress of distortional buckling, the Rayleigh-Ritz method is employed to solve the eeigenvalue problems.

3.2 Numerical investigation

The commercial software ANSYS was employed to perform the finite element eigenvalue buckling analysis of PCFS beams subject to pure bending and uniformly distributed load. The linear buckling analysis was used to assess the influence of hole sizes, cross-section dimensions and stress gradient on the distortional buckling behaviour of PCFS beams. The finite strip method conducted by CUFSM was used to check the boundary and loading conditions of the finite element model with plain web.

3.2.1 Finite strip method

The finite strip software CUFSM is widely used to determine the elastic buckling stress of CFS sections due to its efficiency. It can provide a signature elastic buckling curve according to the cross-section dimension, while the elastic buckling loads obtained from finite element eigenvalue buckling analysis need to be identified from hundreds of buckling modes manually. However, the strip elements in CUFSM do not have the functions to model the web perforations, and thus it cannot be applied in this study to calculate the critical buckling moment of PCFS beams.

Nevertheless, the finite strip model produced by CUFSM can be used to validate the finite element model with plain web. It should be noted that the parameters (i.e. boundary conditions, loading conditions, material properties and mesh sizes) in the finite element model with plain web were the same as those in the finite element model with web perforations.

In order to ensure the CFS beam failed by distortional buckling and gain the lowest eigenvalue which represents the critical stress of distortional buckling, the cross-section dimensions of CFS beams need to be carefully selected. Three sections A, B and C which represent the small, medium and large section were chosen in the numerical and analytical investigations. The dimensions of cross sections can be found in Table 3.1.

Table 3.1 Cross-section dimensions of the selected CFS beams for numerical investigations in pure bending (unit: mm)

Sections	Web depth, *h*	Flange width, *b*	Lip height, *c*	Thickness, *t*
Section A	150	50	15	2
Section B	200	70	20	2.5
Section C	250	80	25	3

It is assumed that the simply supported CFS beam was subject to pure bending and the equivalent forces of pure bending were applied at the finite strip model. The cross section of a typical CFS channel beam (Section B) in CUFSM can be found in Figure 3.1, and the relevant material properties including Young’s modulus and Poisson’s ratio were set as 205 GPa and 0.3 respectively.

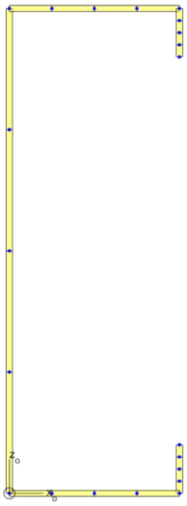

h=200 mm, b=70 mm, c=20 mm, t=2.5 mm

Figure 3.1 Cross section in CUFSM to obtain the distortional buckling stress of CFS beams subject to pure bending (Section B)

The typical distortional buckling modes of CFS beams in CUFSM are shown in Figure 3.2. It can be observed from Figure 3.2 that the distortional buckling modes were characterised by the rotation of the compressed flange and lip about the flange-web junction. The critical distortional buckling half-wave lengths of the three sections were 400 mm, 570 mm and 680 mm respectively.

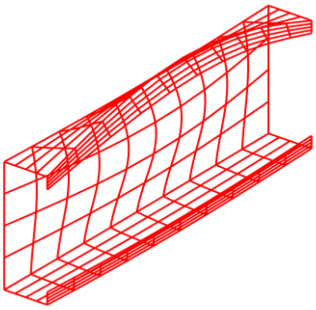

(a) Section A: h=150 mm, b=50 mm, c=15 mm, t=2 mm, half-wave length=400 mm

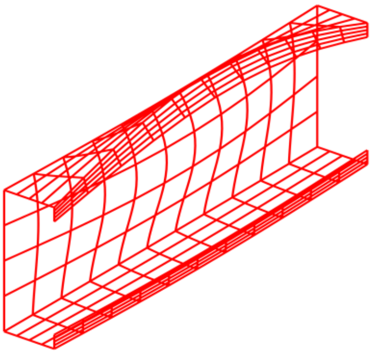

(b) Section B: h=200 mm, b=70 mm, c=20 mm, t=2.5 mm, half-wave length=570 mm

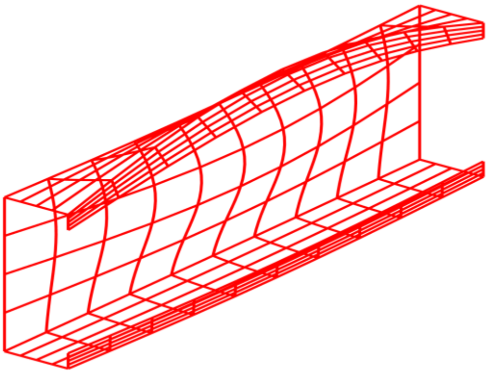

(c) Section C: h=250 mm, b=80 mm, c=25 mm, t=3 mm, half-wave length=680 mm

Figure 3.2 Typical distortional buckling modes of CFS beams in CUFSM

Figure 3.3 shows a log-based plot of distortional buckling curves of the three selected CFS beams produced by CUFSM, where M_{cr} is the critical moment of distortional buckling of CFS beam subject to pure bending and M_y is the yield moment. It can be found that when the slenderness ratio of the beam ranges from 10.5 to 71 (Section A), from 11.3 to 69.6 (Section B) and from 13.1 to 60.8 (Section C), the lowest value is the critical distortional buckling stress. Furthermore, the critical moments of local buckling of the three selected sections are higher than the critical moment of distortional buckling which indicates that the selected CFS beams were controlled by the distortional buckling.

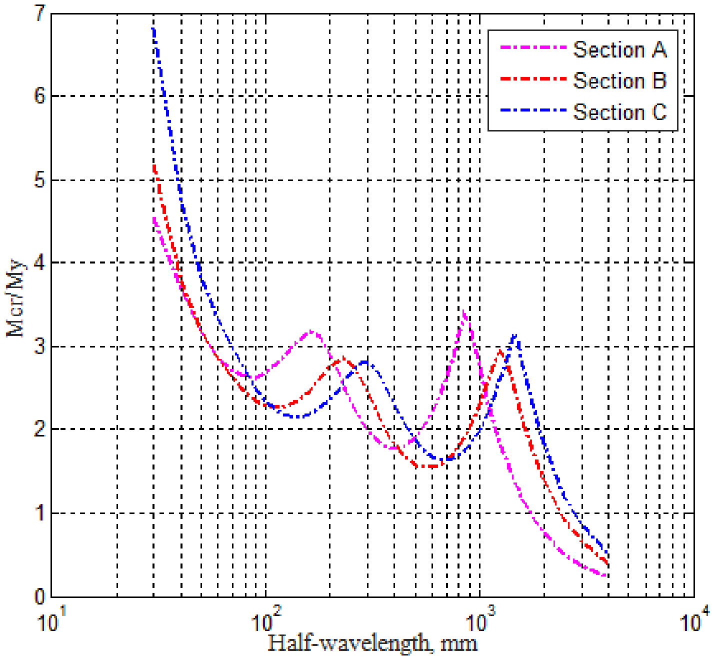

Figure 3.3 Distortional curves of selected CFS beams with plain web produced by CUFSM (σ_y=390 MPa, M_y is the yield moment)

3.2.2 Elastic finite element analysis

The finite element package ANSYS has been employed in Section 3.2.2 to generate the finite element model and perform the eigenvalue buckling analysis of PCFS and CFS beams. The data obtained from CUFSM has been used to validate the finite element models.

3.2.2.1 Geometry

The geometry of a PCFS beam with circular perforations in the web can be found in Figure 3.2. The web depth, flange width, lip height and thickness of the cross section were denoted as h, b, c and t, respectively. The circular perforations were supposed to displace along the neutral axis of the web equally and the diameter of the circular hole was symbolized by d. The beam length was regarded to be $l=n_h\pi d/2$, where n_h represented the total number of the holes in the web. In this study, Section A, Section B and Section C were selected for the simulation of PCFS beams subject to pure bending. Section D (*h*=200 mm, *b*=65 mm, *c*= 20 mm and *t*=2.5 mm) in Albion sections was selected for the case subject to uniformly distributed load.

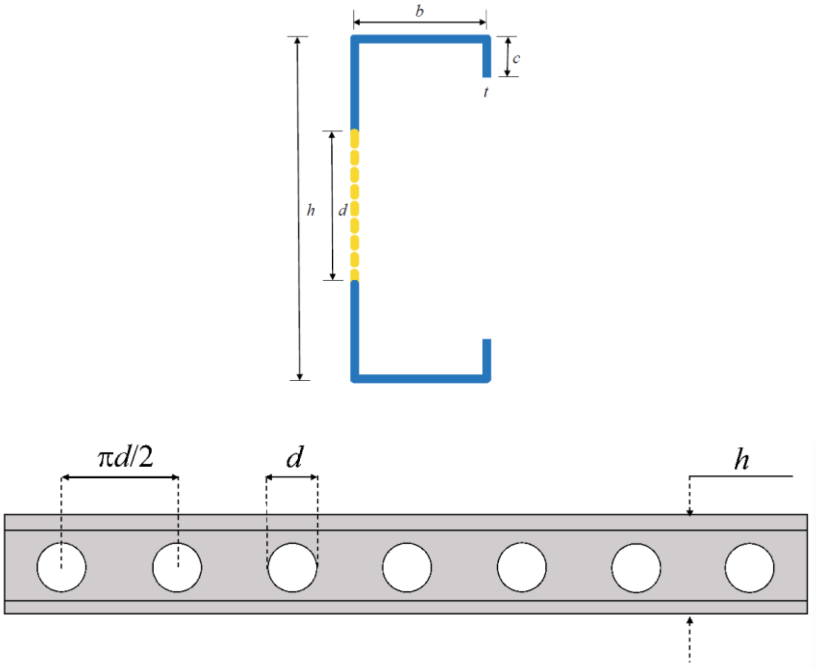

Figure 3.4 Geometry of a PCFS beam with circular perforations in the web

3.2.2.2 Element type and mesh

The PCFS beams were modelled by Shell 181 elements which are isoparametric four-node elements with six degrees of freedom at each node. The Young's modulus of the cold-formed steel was taken as E=205 GPa, Poisson's ratio was taken as μ=0.3 and the yield strength was taken as σ_y=390 MPa.

It is well known that the mesh sizes will affect the accuracy of critical stresses obtained from finite element analysis. The mesh sensitivity analysis was conducted by using trails with different sizes, the results showed that the critical loads obtained from different mesh sizes were almost same when the maximum element sizes were below 10 mm (see Appendix A.1). In the present study, the maximum mesh size was controlled not exceeding 5 mm for different beam lengths. Typical finite element mesh of a PCFS beam is shown in Figure 3.5.

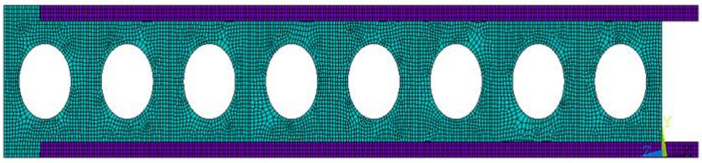

Figure 3.5 Typical finite element mesh of a PCFS beam (Section B, h=200 mm, b=70 mm, c=20 mm, t=2.5 mm, d=100 mm, l=1256 mm)

3.2.2.3 Boundary and loading conditions of PCFS beams subject to pure bending

Simply supported boundaries were applied at the PCFS beams, which means two ends were restricted to move in the lateral and transverse directions and free to move in the longitudinal direction. Hence, the boundary conditions had zero lateral and transverse displacement (UX=UY=0) and zero rotational deformation about z axis (ROTZ=0) for all nodes at two ends in present finite element analysis. Furthermore, the longitudinal movement of point A was prohibited to avoid the rigid displacement (See Figure 3.6).

During the eigenvalue buckling analysis, the pure bending moment was applied at the two ends in which the forces was assumed uniformly distributed on the flanges ($\sigma_y t$ for the top flange and $-\sigma_y t$ for the bottom flange) and linearly distributed on the web (from $\sigma_y t$ to $-\sigma_y t$) and lips (from $\sigma_y t$ to $\sigma_y t(1-2c/h)$ for the upper lip and from $-\sigma_y t(1-2c/h)$ to $-\sigma_y t$ for the lower lip), the boundary and loading conditions of PCFS beams subject to pure bending can be found in Figure 3.6.

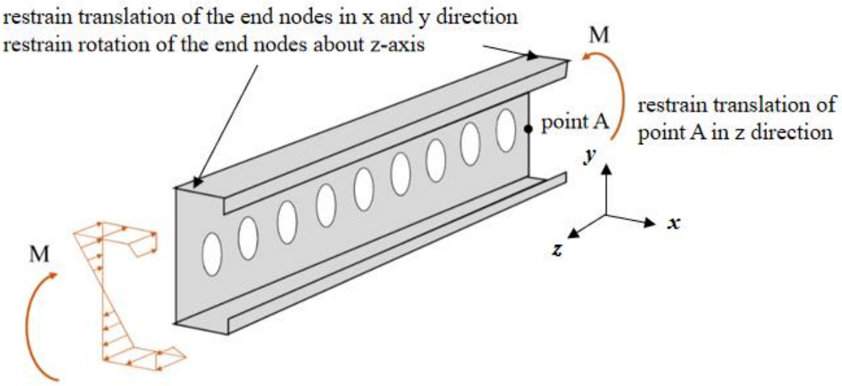

Figure 3.6 Boundary and loading conditions of PCFS beams subject to pure bending

3.2.2.4 Boundary and loading conditions of PCFS beams subject to uniformly distributed load

The setting of boundary conditions for PCFS beams subject to uniformly distributed load are the same with that in Section 3.2.1.3 (simply supported boundaries). The only difference is that the flange-web corner line was restrained in x direction to avoid lateral-torsional buckling, as shown in Figure 3.7. This is because the distortional buckling mode will couple with the lateral-torsional buckling mode when the length of PCFS beams increase and hence the relevant critical stress decrease.

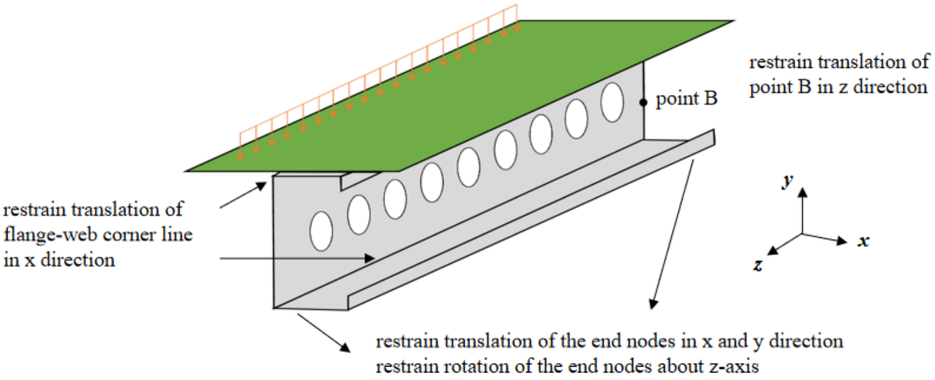

Figure 3.7 Boundary conditions of PCFS beams subject to uniformly distributed load

During the eigenvalue buckling analysis, the uniformly distributed load were applied at the shear center so that the PCFS beam can only suffer bending but without twist. To realize this force condition, the uniformly distributed load can be applied on the plate with infinite rigidity (plate length is equal to beam length and plate width is equal to the distance from shear center to web line), as shown in Figure 3.8(a). The other approach is applying the uniformly distributed load combined with equivalent distributed twist moment (the value of twist moment is equal to the value of transverse load times the distance from shear center to web line) at the web line (see Figure 3.8(b)). For convenience, the latter approach (Figure 3.8(b)) was adopted in present finite element eigenvalue buckling analysis.

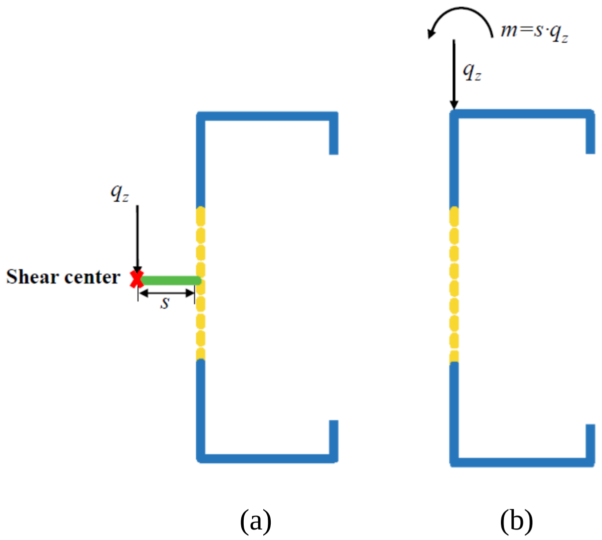

Figure 3.8 Loading conditions of PCFS beams subject to uniformly distributed load

3.2.3 Results and discussion

3.2.3.1 Influence of hole size

The distortional buckling curves of PCFS beams with three typical sections subject to pure bending were shown in Figure 3.9, the web perforations varied from d/h=2/7 to d/h=1/2 where M_{cr} is the critical moment and M_y is the yield moment. It can be found that all the curves had the similar tendency, the local minimum point represents the critical moment of distortional buckling of PCFS beams subject to pure bending.

It is evident from the figure that the PCFS beam with larger circular holes has smaller critical moment. This is because the web with larger perforations has weaker resistance to the compressed flange and lip. Furthermore, the half-wave lengths of PCFS beams increase with the increase of hole sizes (the half-wavelength changes from 400 mm to 430 mm when the d/h increases from 2/7 to 1/2 for Section A) but this effect is minimal. The details of the critical moment of distortional buckling of PCFS beams with different hole sizes subject to pure bending obtained from eigenvalue buckling analysis can be found in Appendix B.1.

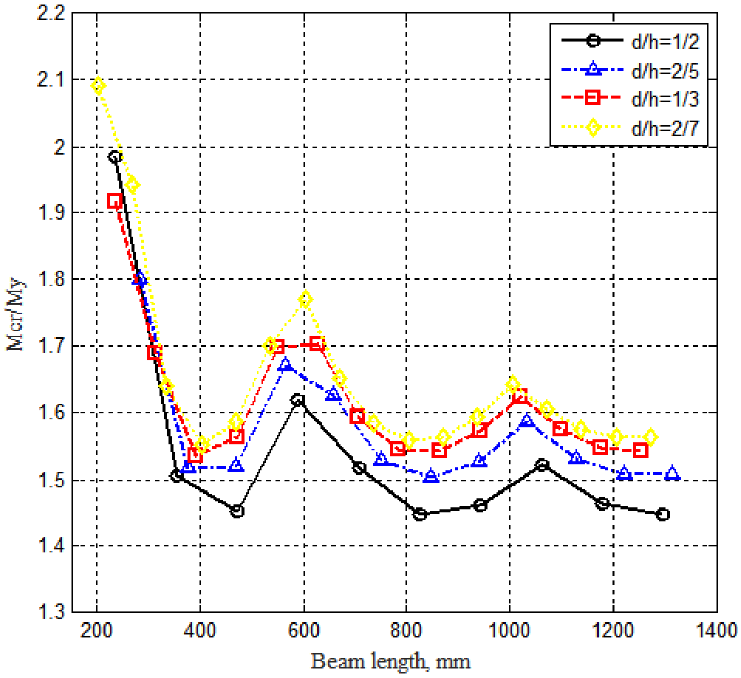

(a) h=150 mm, b=50 mm, c=15 mm, t=2 mm

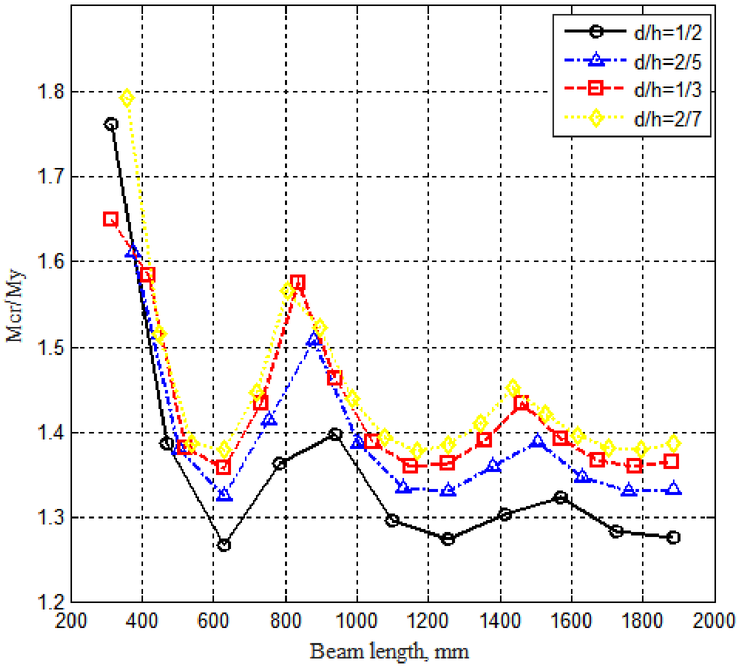

(b) h=200 mm, b=70 mm, c=20 mm, t=2.5 mm

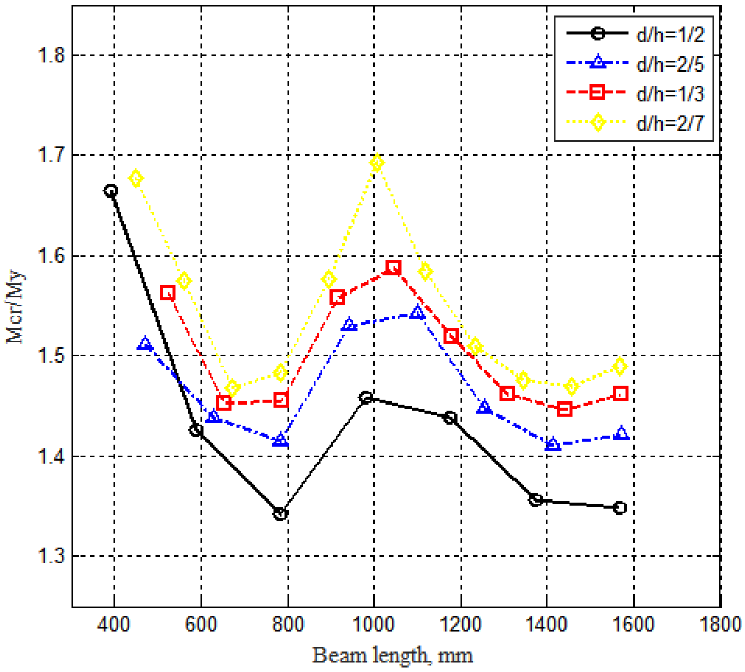

(c) h=250 mm, b=80 mm, c=25 mm, t=3 mm

Figure 3.9 Distortional buckling curves of PCFS beams with different hole sizes subject to pure bending (a) Section A (b) Section B (c) Section C (σ_y=390 MPa, M_y is the yield moment)

3.2.3.2 Influence of cross-section dimensions

The typical distortional buckling modes of PCFS beams subject to pure bending for the three selected sections (*d*/*h*=0.5) obtained from finite element analysis are shown in Figure 3.10, Figure 3.11 and Figure 3.12, respectively. It can be observed from the figures that Section A and Section B have three distortional buckling modes with one, two and three buckling waves, Section C has two buckling modes with one and two buckling waves, all the buckling modes of PCFS beams in different length are all characterised by the rotation of the compressed flange and lip about the flange-web junction which is same as that of the CFS beam with plain web. Furthermore, it is shown that the cross-section dimensions had a significant influence on the buckling behaviour of PCFS beams. For example, for the two same channels with different flange widths, the channel section with wider flange can buckle easily by the distortional buckling. Similarly, for the two same channels with different thicknesses, the channel section with thinner thickness can buckle easily by the local buckling.

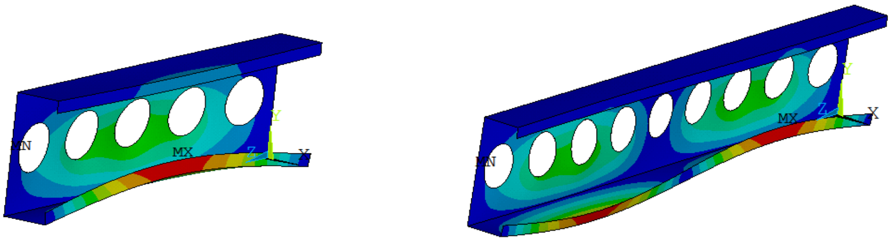

(a) One half-wave

(b) Two half-waves

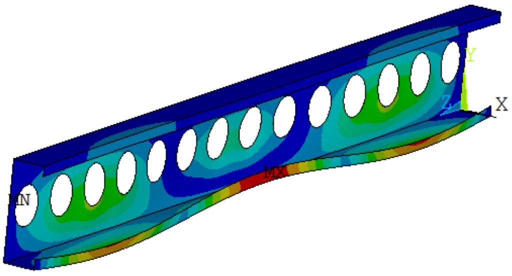

(c) Three half-waves

Figure 3.10 Distortional buckling modes of PCFS beams (Section A, d=h/2) subject to pure bending (a) 470 mm (b) 846 mm (c) 1316 mm

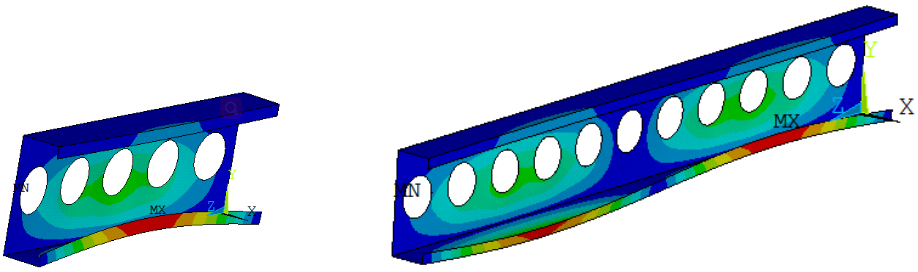

(a) One half-wave

(b) Two half-waves

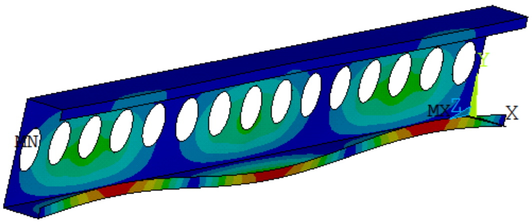

(b) Three half-waves

Figure 3.11 Distortional buckling modes of PCFS beams (Section B, d=h/2) subject to pure bending (a) 628 mm (b) 1256 mm (c) 1884 mm

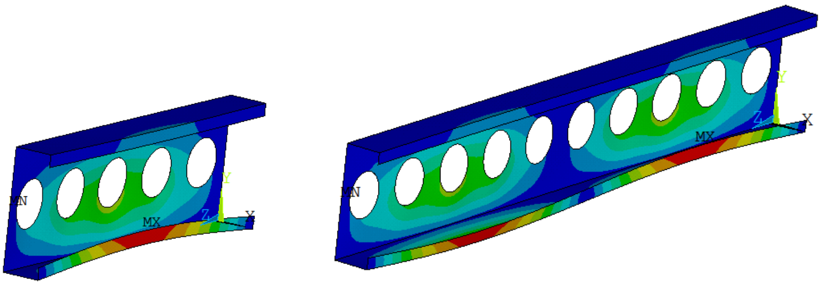

(a) One half-wave (b) Two half-waves

Figure 3.12 Distortional buckling modes of PCFS beams (Section C, d=h/2) subject to pure bending (a) 785 mm (b) 1570 mm

3.2.3.3 Influence of stress gradient

Figure 3.13 shows the typical distortional buckling modes of PCFS beams with different hole sizes (*d*/*h*=0 for Figure 3.13(a), *d*/*h*=0.25 for Figure 3.13(b) and *d*/*h*=0.5 for Figure 3.13(c)) subject to uniformly distributed load obtained from finite element analysis. It is evident that the distortional buckling modes are also identified by the rotation of the compressed flange and lip about the flange-web junction which is analogous to the case subject to pure bending. The only difference is that the half-wave lengths are different in the longitudinal direction when the PCFS beam subject to uniformly distributed load.

It can be observed from the figures that the shortest half-wave length occurs in the central region and the longest half-wave length appears at two ends of the beam. This is because the axial stresses vary parabolically along the longitudinal direction when the PCFS beam subject to uniformly distributed load. It is clear that the largest axial stress occurs in the central region of the beam and the smallest axial stress appears at the beam ends. The stress gradient along the beam length leads to the distortional buckling modes of PCFS beams appear with several buckling waves (each wave has different half-wave lengths) and hence changes the value of critical stress of distortional buckling.

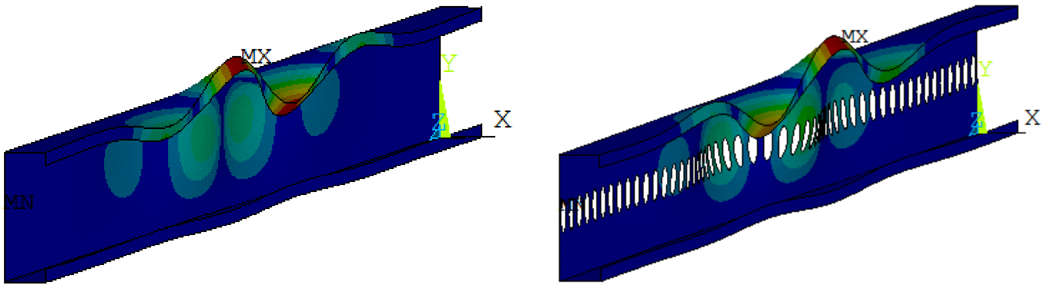

(a) d/h=0 (b) d/h=0.25

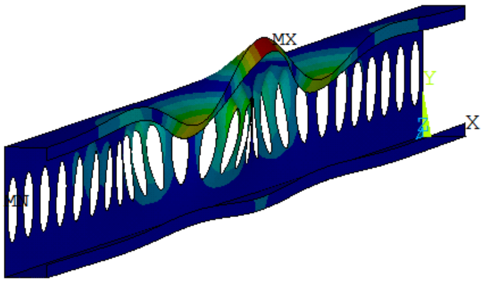

(c) d/h=0.5

Figure 3.13 Typical distortional buckling modes of PCFS beam subject to uniformly distributed load (h=200 mm, b=65 mm, c=20 mm and t=2.5 mm)

3.2.4 ANSYS-CUFSM results comparison

The finite element eigenvalue buckling analysis of CFS beams (without holes) subject to pure bending was conducted to compare with the result obtained from CUFSM. It should be pointed out that the parameters including material properties, mesh sizes, loading conditions and boundary conditions in finite element models of CFS beams with plain web were the same with that in finite element models of PCFS beams. The distortional buckling modes of CFS beams with plain web obtained from FSM and FEA can be observed in Figure 3.14.

The comparison of critical moment of distortional buckling of CFS beams with plain web calculated by CUFSM and ANSYS can be found in Table 3.2. The maximum gap between the results obtained from FSM and FEA was lower than 2% which indicated that the present element finite models were reliable to investigate the distortional behaviour of PCFS beams.

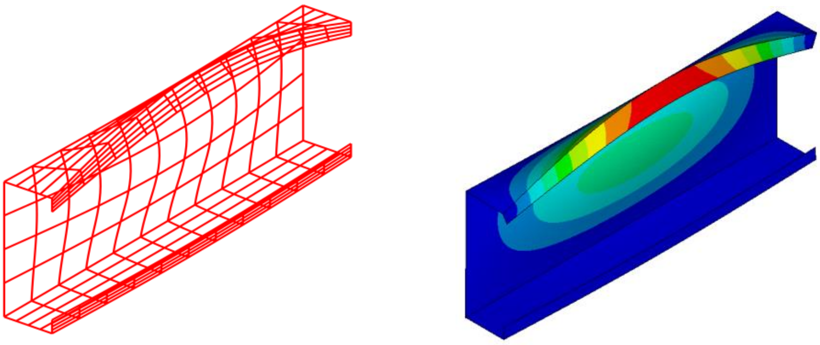

(a) FSM (b) FEA

Figure 3.14 Distortional buckling modes of CFS beams with plain web subject to pure bending obtained from FSM and FEA (Section B, h=200 mm, b=70 mm, c=20 mm, t=2.5 mm, l=570 mm)

Table 3.2 Comparison of critical moment of distortional buckling of the CFS beam with plain web obtained from FSM and FEA (Section selected from Albion Section)

Section	$M_{\mathrm{crd,FSM}}$ (N·mm)	$M_{\mathrm{crd,FEA}}$ (N·mm)	$M_{\mathrm{crd,FEA}}$ /$M_{\mathrm{crd,FSM}}$
C12515	7786362	7651869	0.98
C12516	8929630	8771681	0.98
C14614	8487595	8396131	0.99
C14515	9800079	9695672	0.99
C14616	11215004	11096347	0.99
C14618	14360457	14206215	0.99
C14620	17932463	17738878	0.99
C17616	12845107	12704062	0.99
C17618	16470259	16288020	0.99
C17620	20598457	20369134	0.99
C17623	27766412	27448880	0.99
C17625	33220420	32835011	0.99
C20618	17591022	17393131	0.99
C20620	22021628	21775813	0.99
C20623	29728661	29391278	0.99
C20625	35601006	35177264	0.99
C22620	23640708	23332396	0.99
C22623	31977273	31595035	0.99
C22625	38341653	37862774	0.99
C24623	33094628	32675985	0.99
C24625	39713371	39207085	0.99
C24630	59402398	58578888	0.99

C26625	41489193	40917602	0.99
C26630	62267075	61352789	0.99
C30725	41534248	40976363	0.99
C30730	62385749	61516305	0.99

3.3 Analytical model for PCFS beams subject to pure bending

3.3.1 The analytical model by Hancock

The analytical expressions were first proposed by Lau and Hancock (1987) to calculate the distortional buckling load of CFS columns. It should be noted that the distortional buckling mainly includes the rotation and translation of the compressed flange and lip. In the Hancock's theoretical model, the rotational and lateral spring at the flange-web junction were used to represent the influence of web on the compressed flange and lip (see Figure 3.15). Considering the equilibrium of forces in the horizontal and vertical directions, the equilibrium of moments about the shear center axis, the buckling load could be obtained by solving the following three simultaneous differential equations, Eq.(3-1) to Eq.(3-3)

$$EI_y \frac{d^4u}{dz^4} + EI_{xy}\frac{d^4v}{dz^4} + P\left(\frac{d^2u}{dz^2} + y_0\frac{d^2\phi}{dz^2}\right) + k_x u = 0 \tag{3-1}$$

$$EI_x \frac{d^4v}{dz^4} + EI_{xy}\frac{d^4u}{dz^4} + P\left(\frac{d^2v}{dz^2} - (b - x_0)\frac{d^2\phi}{dz^2}\right) + Q_y = 0 \tag{3-2}$$

$$EI_w \frac{d^4\phi}{dz^4} - \left(GJ - \frac{I_0}{A}P\right)\frac{d^2\phi}{dz^2} - P\left((b - x_0)\frac{d^2v}{dz^2} - y_0\frac{d^2u}{dz^2}\right) - Q_y\left((b - x_0) - x_0\right) + k_\phi \cdot \phi = 0 \tag{3-3}$$

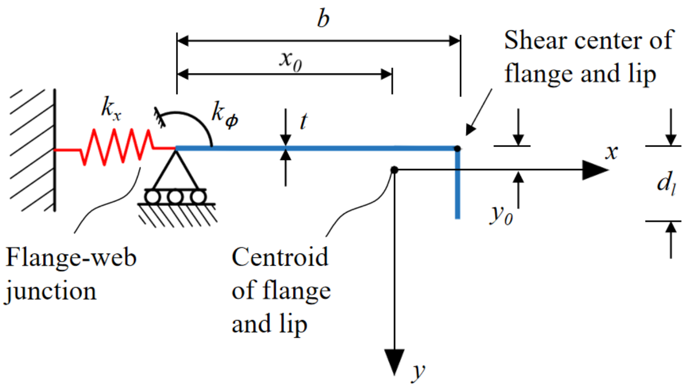

Figure 3.15 Analytical model proposed by Lau and Hancock (1987)

where b is the width of the flange, t is the thickness of the flange and lip, x_0 is the distance between the flange-web junction and centroid, y_0 is the distance between the shear center and centroid, A is the cross-section area of the compressed flange and lip. E is the Young's modulus, G is the shear modulus and J is the torsion constant. I_0 is the polar second moment of the cross-section area about the shear center, I_{xy} is the product of inertia about the shear center, I_w is the warping constant, I_x and I_y are the moment of inertia to the shear center about the x-axis and the y-axis, respectively. P is the buckling load, Q_y is the intensity of the reaction force distributed continuously along the support. k_x and k_ϕ are the lateral spring stiffness and the rotational spring stiffness, respectively. u is the displacement of the shear center in the x-direction, v is the displacement of the shear center in the y-direction and ϕ is the rotation of the compressed flange and lip about the shear center which can be expressed as,

$$\phi = A_1 \sin\frac{\pi z}{\lambda_d} \tag{3-4}$$

$$u = A_2 \sin\frac{\pi z}{\lambda_d} \tag{3-5}$$

$$v = (b - 2x_0)\phi = (b - 2x_0)A_1 \sin\frac{\pi z}{\lambda_d} \tag{3-6}$$

where A_1 and A_2 are arbitrary constants, λ_d is the distortional buckling half-wave length. Substituting Eq.(3-4) to Eq.(3-6) into Eq.(3-1) to Eq.(3-3), one obtains,

$$\begin{aligned}&\left[\frac{\pi^2}{{\lambda_d}^2} EI_{xy}(b - 2x_0) - Py_0\right]^2 - \left(\frac{\pi^2}{{\lambda_d}^2} EI_y + \frac{\lambda^2}{\pi^2} k_x - P\right)\\ &\left\{\frac{\pi^2}{{\lambda_d}^2}\left[EI_w + EI_x(b - 2x_0)^2\right] + GJ - \left(\frac{I_0}{A} - (b - x_0)^2 + {x_0}^2\right)P + \frac{\lambda_d^2}{\pi^2} k_\phi\right\} = 0\end{aligned} \tag{3-7}$$

To calculate the minimum value of the buckling load P, the critical half-wave length λ_d should be determined. It was assumed that the half-wave length λ_d approached the critical value as the lateral spring stiffness k_x was infinite. Hence, the buckling load P can be given by,

$$P_{cr}=\frac{\frac{\pi^2}{\lambda_d^2}EI_{wc}+GJ+\frac{\lambda_d^2}{\pi^2}k_\phi}{\frac{I_x+I_y}{A}+x_0^2+y_0^2} \tag{3-8}$$

in which,

$$I_{wc}=I_w+I_x(b-2x_0)^2 \tag{3-9}$$

Let

$$k_\phi=\frac{2D}{h} \tag{3-10}$$

where D is the flexural rigidity of the web, h is the height of the web. The critical value of the half-wave length can then be expressed as follows,

$$\lambda_d=\pi\left(\frac{EI_{wc}}{k_\phi}\right)^{0.25}=\pi\left(\frac{EI_{wc}h}{2D}\right)^{0.25} \tag{3-11}$$

It should be pointed out that the rotational spring stiffness in Eq.(3-10) ignored the influence of compression on the web. The reduction factor given by the ratio of the local buckling stress of web to the buckling stress of flange was proposed to represent the compressive force on the web and the rotational spring stiffness can be rewritten as,

$$k_\phi=\frac{2D}{h}\left(1-\frac{\frac{P'}{A}}{\sigma_w}\right) \tag{3-12}$$

where P'/A is the buckling stress of flange, σ_w is the local buckling stress of web which can be described as,

$$\sigma_w=\frac{\pi^2D}{th^2}\left(\frac{h}{\lambda_d}+\frac{\lambda_d}{h}\right)^2 \tag{3-13}$$

In order to adapt to the results obtained from finite strip analysis, the rotational spring stiffness was modified as,

$$k_{\phi,d} = \frac{2D}{\left(h+0.06\lambda_d\right)}\left[1-\frac{\left(\frac{P'}{A}\right)}{\sigma_w}\right] \tag{3-14}$$

In Hancock's model, the lateral restraint has been ignored (k_x=0). Substituting Eq.(3-11) and Eq.(3-14) into Eq.(3-7), the distortional buckling load becomes,

$$P_{crd} = \frac{E}{2}\left\{(\alpha_1+\alpha_2)\pm\sqrt{[(\alpha_1+\alpha_2)^2-4\alpha_3]}\right\} \tag{3-15}$$

in which,

$$\alpha_1 = \frac{\eta}{\beta_1}(I_x b^2 + 0.039J\lambda_d^2) + \frac{k_\phi}{\beta_1\eta E} \tag{3-16}$$

$$\alpha_2 = \eta\left(I_y + \frac{2}{\beta_1}y_0 b I_{xy}\right) \tag{3-17}$$

$$\alpha_3 = \eta\left(\alpha_1 I_y - \frac{\eta}{\beta_1}I_{xy}{}^2 b^2\right) \tag{3-18}$$

$$\beta_1 = x_0^2 + \left(\frac{I_x+I_y}{A}\right) \tag{3-19}$$

$$\eta = \left(\frac{\pi}{\lambda_d}\right)^2 \tag{3-20}$$

The initial distortional buckling load in Eq.(3-15) was obtained with rotational spring stiffness k_ϕ=0 in Eq.(3-16). After a couple of iterations, the distortional buckling load of CFS columns can be determined.

Later, Hancock (1997) applied this analytical model to predict the critical stress of distortional buckling of CFS beams. Similar to the compression members, the distortional buckling of the flexural members also contained the rotation of compressed flange and lip about the flange-web junction. In Hancock's model, the web of the channel section subject to compression was assumed as a simply supported beam in flexure (see Figure 3.16(a)) and hence the rotational stiffness at the end was $2EI/h$. However, the web of the channel section subject to pure bending can be treated as a beam simply supported at one end and fixed supported at the other end (see Figure 3.16(b)), then the rotational stiffness at the end was $4EI/h$. The critical value of the half-wave length and rotational spring stiffness can be further modified as,

$$\lambda_d = 4.80\left(\frac{I_x b^2 h}{2t^3}\right)^{0.25} \tag{3-21}$$

$$k_{\phi,d} = \frac{2Et^3}{5.46(h+0.06\lambda_d)}\left[1-\frac{1.11\sigma'_{crd}}{Et^2}\left(\frac{h^4\lambda_d^2}{12.56\lambda_d^4+2.192h^4+13.39\lambda_d^2h^2}\right)\right] \tag{3-22}$$

where σ'_{cr} is the distortional buckling stress which can be obtained as follows,

$$\sigma_{crd} = \frac{E}{2A}\left\{(\alpha_1+\alpha_2)-\sqrt{[(\alpha_1+\alpha_2)^2-4\alpha_3]}\right\} \tag{3-23}$$

The distortional buckling stress can be determined by assuming the rotational spring stiffness in Eq.(3-22) to be zero. After the iterations, the critical stress of distortional buckling of CFS beams can be obtained. The calculation processes to determine the distortional buckling stress of CFS beams were the same with that of CFS columns.

3.3.2 Proposed analytical model

To obtain the critical stress of distortional buckling of PCFS beams subject to pure bending, the influence of web openings should be clarified during the calculation processes. In the present study, the rotational spring stiffness in the model proposed by Hancock (1997) has been modified to represent the effect of web openings. As shown in Figure 3.17, the circular perforations were displayed identically in the centreline of the web and the shaded portion represented the solid area in perforated strip.

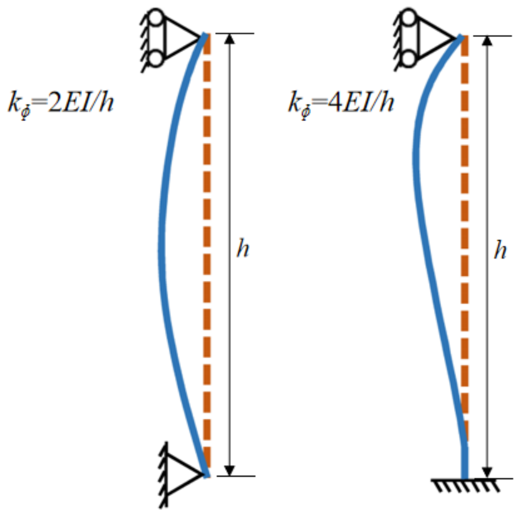

(a) (b)

Figure 3.16 Web deformation of the CFS sections due to the distortional buckling (a) pure compression (b) pure bending

For simplicity, the area of holes was supposed to be the same as the solid area in the perforated strip. Hence, the length of the PCFS beam was $n_h \pi d/2$, n_h was the total number of the perforations.

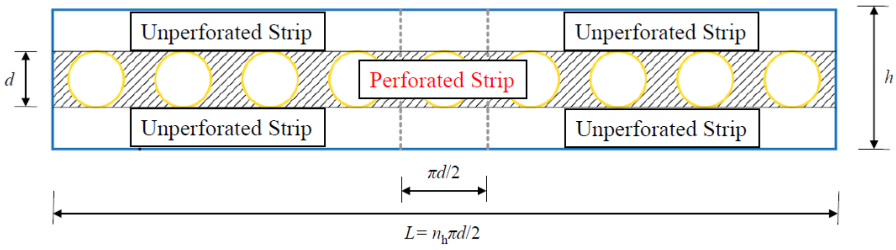

Figure 3.17 Notation and geometry of the PCFS beam in the longitudinal direction

In the proposed analytical model, the flexural rigidity of the perforated strip was assumed to be half of the unperforated strip in the web according to the concept of equivalent width. In order to determine the modified rotational spring stiffness, a unit bending moment was applied at the flange-web junction and then the rotation angle of the loading point can be evaluated (see Figure 3.18). The strain energy of the web is expressed as follows,

$$U = \frac{1}{2D}\int_0^h \left(\frac{M}{h}x\right)^2 dx + \left(\frac{1}{2D_h} - \frac{1}{2D}\right)\int_{\frac{h-d}{2}}^{\frac{h+d}{2}} \left(\frac{M}{h}x\right)^2 dx \qquad 0 \le x \le h \tag{3-24}$$

where D is the flexural rigidity of the unperforated strip and D_h is the flexural rigidity of the perforated strip.

$$D = \frac{Et^3}{12(1-\mu^2)} \tag{3-25}$$

$$D_h = \frac{\alpha Et^3}{24(1-\mu^2)} \tag{3-26}$$

The rotation angle of the loading point is

$$\phi = \frac{\partial U}{\partial M} \tag{3-27}$$

By solving Eq.(3-24) and Eq.(3-27), the rotational spring stiffness of the PCFS beam can be obtained as follows,

$$k_\phi^* = \frac{3D}{h}\frac{1}{1+\left(\frac{D}{D_h}-1\right)\left(\frac{d}{h}\right)\left[\frac{3}{4}+\frac{1}{4}\left(\frac{d}{h}\right)^2\right]} \tag{3-28}$$

It could be observed from Eq.(3-28) that if d=0 then k_ϕ^*=3D/h, which represents the rotational spring stiffness of the CFS beam with the plain web. The reduction factor of the rotational spring stiffness of the PCFS beam is given by,

$$\alpha = \frac{1}{1+\left(\frac{D}{D_h}-1\right)\left(\frac{d}{h}\right)\left[\frac{3}{4}+\frac{1}{4}\left(\frac{d}{h}\right)^2\right]} \tag{3-29}$$

Moen and Schafer (2009b) illustrated that the perforated web might buckle because of the buckling of plate which ignored the influence of holes or the buckling of unstiffened plate adjacent to the perforations or the combination of both two. The computing formula was proposed to predict the buckling stress of unstiffened plate. However, the perforations were not allowed to be too large nor too small, the spacing of holes cannot be too close in the design expressions proposed by Moen and Schafer (2009b). This was because the small perforations would change the half-wave length of the web and the large perforations would narrow the unstiffened strip to increase the stiffness of the web. Furthermore, if the holes were too close, the buckling behaviour would be restrained at the holes. It is hard to develop general expressions to calculate the local buckling stress of the perforated plate.

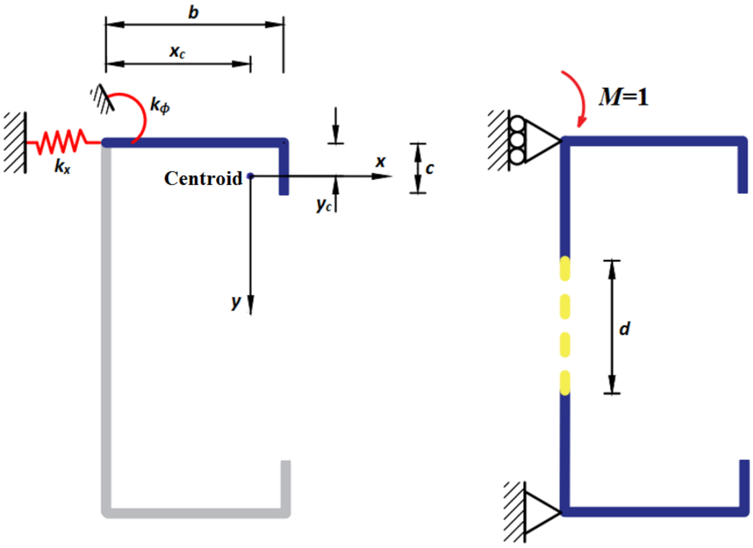

Figure 3.18 Distortional buckling model proposed by Hancock (1997) (left) and proposed analytical model used to determine rotational spring stiffness (right)

Note that, the different local buckling stress of the perforated web had minimal impact on the reduction factor in Eq.(3-14) which considered the effects of compressive force on the web. Moreover, it was found that if the PCFS beam controlled by the distortional buckling in pure bending, the main impact of the perforations was to reduce the rotational stiffness, the influence on the half-wave length was negligible (Moen and Schafer, 2009a). Therefore, the rotational spring stiffness of the PCFS beam can be further modified as follows,

$$k^{*}_{\phi,d} = \frac{2\alpha E t^{3}}{5.46(h+0.06\lambda_d)}\left(1-\frac{1.11\sigma_{crPB0}}{Et^{2}}\frac{h^{4}\lambda_d^{2}}{12.56\lambda_d^{4}+2.192h^{4}+13.39\lambda_d^{2}h^{2}}\right) \tag{3-30}$$

Substituting Eq.(3-30) and Eq.(3-21) into Eq.(3-23), and undergoing the iterative process, the critical stress of distortional buckling of PCFS beams subject to pure bending can be determined. The relevant critical moment of distortional buckling can be calculated as follows,

$$M_{crdPB} = \frac{2\sigma_{crdPB} I_{red}}{h} \tag{3-31}$$

where I_{red} is the second moment of the reduced area, that is

$$I_{red} = I_{full} - \frac{td^3}{12} = 2(\frac{bt^3}{12} + \frac{bth^2}{4}) + \frac{th^3}{12} - \frac{td^3}{12} \tag{3-32}$$

where I_{full} is the second moment of the area of the channel section with plain web.

3.2.3 Comparison between the proposed model and FEA

The comparisons of critical moments of distortional buckling of PCFS beams subject to pure bending among the proposed model (solid line), the analytical model proposed by Yuan et al. (2017) (dot dash line) and the results obtained from eigenvalue buckling analysis (point) were shown in Figure 3.19. Where M_{cr} and M_{cr0} is the critical moment of CFS beams with and without web perforations, four different values of d/h were selected in the eigenvalue buckling analysis to evaluate the accuracy of the proposed analytical model.

It is evident that the proposed analytical approach based on the Hancock’s model proposed in 1987 had a good agreement with the result obtained from eigenvalue buckling analysis (Figure 3.19(a) for Section A, Figure 3.19(b) for Section B and Figure 3.19(c) for Section C) which reveals that it can be utilized into the design codes of PCFS sections. Furthermore, the critical moments of distortional buckling calculated from the analytical model proposed by Yuan et al. (2017) were slightly lower than those from the eigenvalue buckling analysis. This is because Yuan’s model was proposed based on the stiffened element buckled on the elastic foundation, the expressions were simpler and more conservative. It indicates that the proposed analytical model can capture the distortional buckling behaviour of PCFS beams subject to pure bending well.

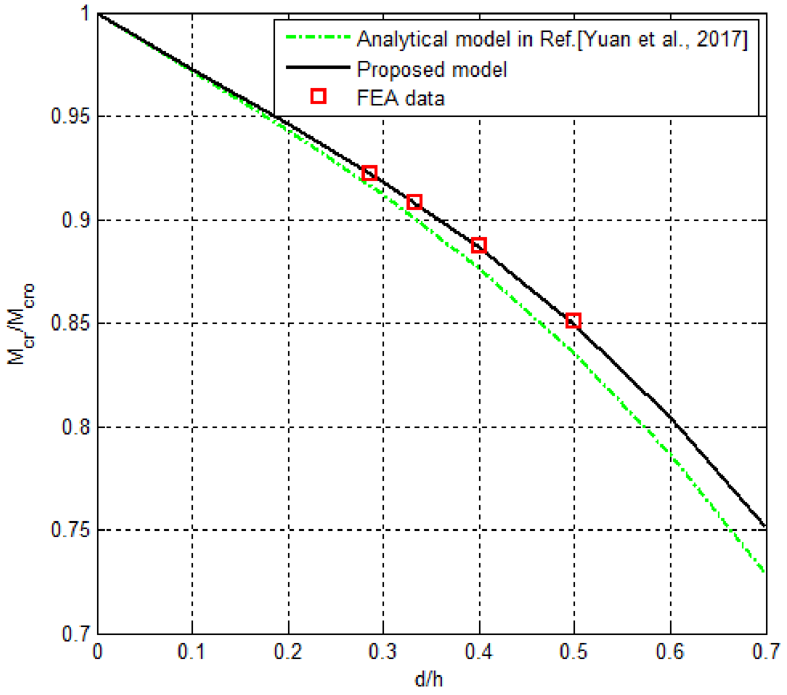

(a) h=150 mm, b=50 mm, c=15 mm, t=2 mm

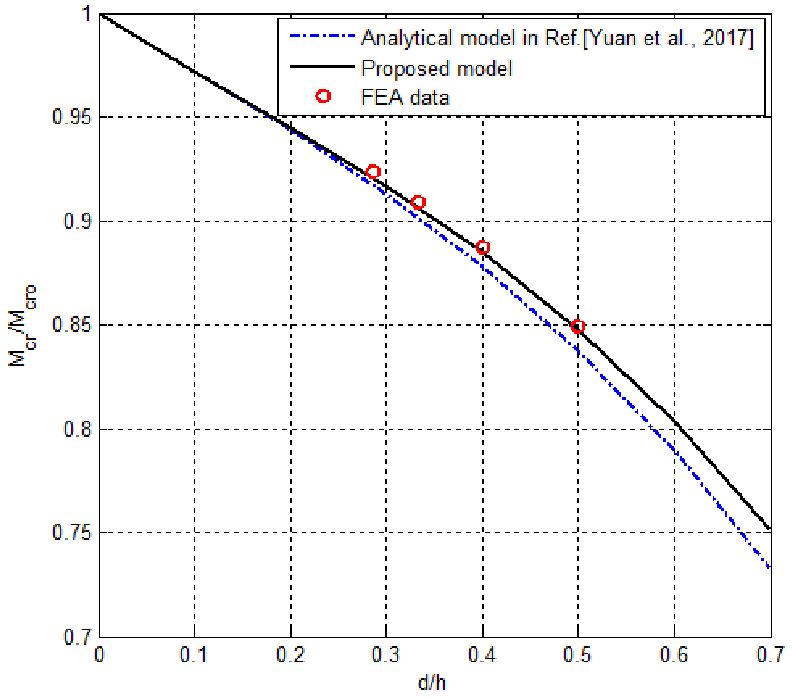

(b) h=200 mm, b=70 mm, c=20 mm, t=2.5 mm

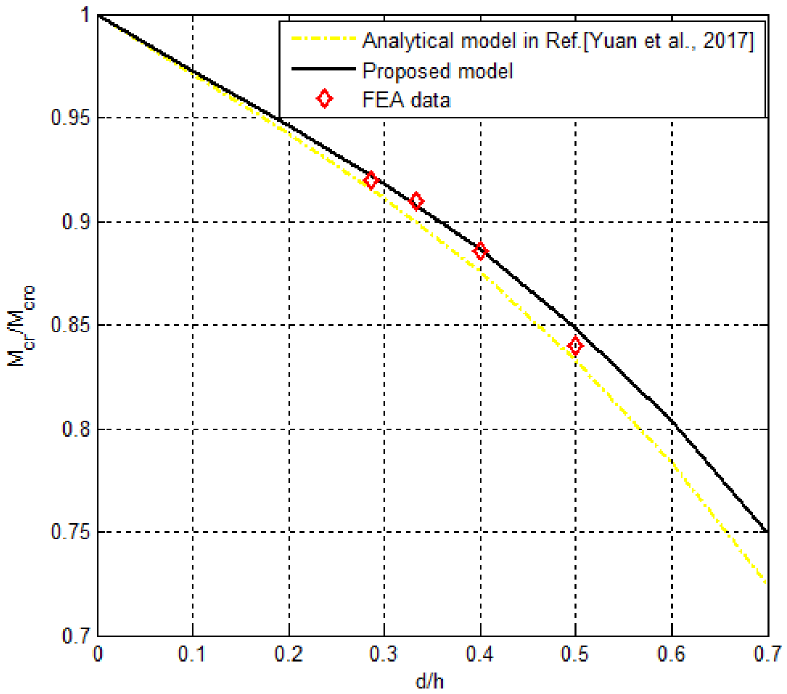

(c) h=250 mm, b=80 mm, c=25 mm, t=3 mm

Figure 3.19 Comparisons of critical moments of distortional buckling of PCFS beams subject to pure bending among the proposed analytical model, analytical model in Ref.[Yuan et al., 2017] and eigenvalue buckling analysis (a) Section A (b) Section B (c) Section C (σ_y=390 MPa, M_y is the yield moment)

3.4 Analytical model for PCFS beams subject to uniformly distributed load

3.4.1 The analytical model by Li and Chen

The analytical model by Li and Chen was very similar to the Hancock's model shown in Figure 3.15. The only difference was that Li and Chen (2008) added a vertical spring at the centroid to take place of the rotational spring at flange-lip junction, as shown in Figure 3.20. This idea was illuminated by the analytical model in Eurocode 3 (EN1993-1-3, 2006), the vertical spring represented the effect of the web on the compressed flange and lip as well as the flexure behaviour of the compressed flange and lip itself. Considering the equilibrium of forces in the y- and z-directions and the equilibrium of moments about the shear center axis, the buckling load can be obtained from the following three simultaneous differential equations, Eq.(3-33) to Eq.(3-35).

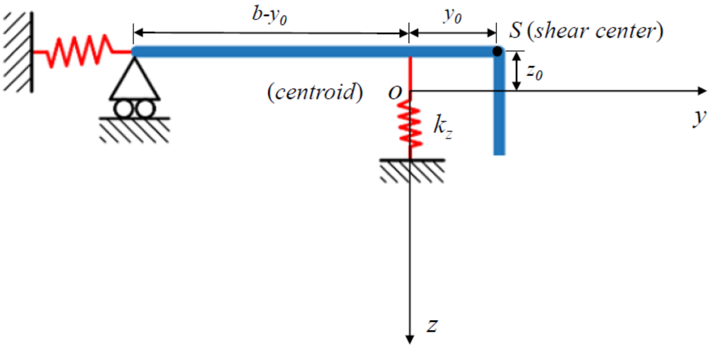

Figure 3.20 Analytical model proposed by Li and Chen (2008)

$$EI_z \frac{d^4u}{dx^4} + EI_{yz} \frac{d^4v}{dx^4} + P\left(\frac{d^2u}{dx^2} + z_0 \frac{d^2\phi}{dx^2}\right) + k_y u = 0 \tag{3-33}$$

$$EI_y \frac{d^4v}{dx^4} + EI_{yz} \frac{d^4u}{dx^4} + P\left(\frac{d^2v}{dx^2} - y_0 \frac{d^2\phi}{dx^2}\right) + k_z(v - y_0\phi) + Q_z = 0 \tag{3-34}$$

$$EI_w \frac{d^4\phi}{dx^4} - \left(GJ - \frac{I_0}{A}\right)\frac{d^2\phi}{dx^2} - P\left(y_0 \frac{d^2v}{dx^2} - z_0 \frac{d^2u}{dx^2}\right) - Q_z\left(y_0 - (b - y_0)\right) - k_z y_0 (v - y_0\phi) = 0 \tag{3-35}$$

where b is the width of the flange, t is the thickness of the flange and lip, y_0 is the lateral distance between the shear center and centroid, z_0 is the vertical distance between the shear center and centroid, A is the cross-section area of the compressed flange and lip. E is the Young's modulus, G is the shear modulus, J is the torsion constant and I_w is the warping constant. I_0 is the polar second moment of the cross-section area about the shear center, I_{yz} is the product of inertia, I_y and I_z are the moment of inertia about the y-axis and the z-axis, respectively. P is the buckling load, Q_y is the intensity of the reaction force distributed continuously along the support. k_y and k_z are the lateral spring stiffness and the vertical spring stiffness, respectively. u is the deflection of the shear center in the y-direction, v is the deflection of the shear center in the z-direction and ϕ is the rotation of the compressed flange and lip about the shear center, can be expressed as,

$$\phi(x) = C_1 \sin \frac{\pi x}{\lambda_d} \tag{3-36}$$

$$u(x) = C_2 \sin \frac{\pi x}{\lambda_d} \tag{3-37}$$

$$v(x) = [y_0 - (b - y_0)]C_1 \sin\frac{\pi x}{\lambda_d} \tag{3-38}$$

where C_1 and C_2 are the arbitrary constants, λ_d is the distortional buckling half-wave length. Substituting Eq.(3-33) to Eq.(3-35) into Eq.(3-36) to Eq.(3-38), it yields,

$$\begin{aligned}&\left[\frac{\pi^2}{\lambda_d^2}EI_{yz}\left(y_0 - (b - y_0)\right) - z_0 P\right]^2 \\ &-\left(\frac{\pi^2}{\lambda_d^2}EI_z + \frac{\lambda^2}{\pi^2}k_y - P\right)\left\{\frac{\pi^2}{\lambda_d^2}\left[EI_w + EI_y\left(y_0 - (b - y_0)\right)^2\right] + GJ\right. \\ &\left. -\left(\frac{I_0}{A} - {y_0}^2 + (b - y_0)^2\right)P + \frac{\lambda_d^2}{\pi^2}k_z(b - y_0)^2\right\} = 0\end{aligned} \tag{3-39}$$

It could be found that Eq.(3-39) was similar to Eq.(3-7), the only difference was the last term, which in the Hancock's model the it was k_ϕ but in the model by Li and Chen it was $k_z(b-y_0)^2$. The flexibility of the vertical spring k_z in the model by Li and Chen could be split into two parts. One was the rotation at the flange-web junction and the other was the flexure of the flange itself, which leads to,

$$\frac{1}{k_z} = \frac{(b - y_0)^2}{k_\phi} - \frac{(b - y_0)^3}{3D_f} = \frac{(b - y_0)^2}{k_\phi}\frac{3D_f - k_\phi(b - y_0)}{3D_f} \tag{3-40}$$

where k_ϕ is the rotational spring stiffness in the Hancock's model, D_f is the flexural rigidity of the flange plate. Obviously, when the flexural rigidity D_f is infinite, $k_z(b-y_0)^2$ will be equal to k_ϕ. For simplicity, Eq.(3-40) can be rewritten as,

$$k_\phi^{'} \equiv k_z(b - y_0)^2 = \frac{k_\phi}{1 - (b - y_0)k_\phi/\left(3D_f\right)} \tag{3-41}$$

If the vertical spring stiffness and half-wave length of a channel section were known, the distortional buckling load can be solved by Eq.(3-39). In the Hancock's model, the rotational spring stiffness k_ϕ was found to be $2D/h$ for the column and $4D/h$ for the beam. Let $dP/d\lambda_d=0$, for the case the lateral spring stiffness k_y was infinite. The critical half-wave length can then be determined as follows,

$$\lambda_d = \pi \left(\frac{EI_{wc}}{k_\phi^{'}} \right)^{0.25} \tag{3-42}$$

in which,

$$I_{wc} = I_w + I_y (2y_0 - b)^2 \tag{3-43}$$

The critical stress of distortional buckling of CFS sections can be calculated from Eq.(3-39) as follows,

$$\sigma_{crd} = \frac{\left(2\alpha_1 - \alpha_3 - \alpha_2\alpha_4\right) \pm \sqrt{\left(2\alpha_1 - \alpha_3 - \alpha_2\alpha_4\right)^2 - 4\left(1-\alpha_4\right)\left(\alpha_1^2 - \alpha_2\alpha_3\right)}}{2A\left(1-\alpha_4\right)} \tag{3-44}$$

in which,

$$\alpha_1 = \frac{\pi^2 EI_{yz}}{\lambda_d^2} \left(\frac{y_0 - (b - y_0)}{z_0} \right) \tag{3-45}$$

$$\alpha_2 = \frac{\pi^2 EI_z}{\lambda_d^2} + \frac{\lambda_d^2 k_y}{\pi^2} \tag{3-46}$$

$$\alpha_3 = \frac{\pi^2 EI_y}{\lambda_d^2} \left[\frac{EI_w}{z_0^2 EI_y} + \frac{\left(y_0 - (b - y_0)\right)^2}{z_0^2} \right] + \frac{GJ}{z_0^2} + \frac{\lambda^2}{\pi^2} \frac{k_\phi^{'}}{z_0^2} \tag{3-47}$$

$$\alpha_4 = \frac{I_0}{Az_0^2} + \frac{(b - y_0)^2 - y_0^2}{z_0^2} \tag{3-48}$$

Similar to the Hancock's model, the reduction factor was multiplied by the rotational spring stiffness to represent the effect of the compressive force on the web. For the CFS columns subject to compression,

$$k_\phi = \frac{2D}{h} \left(1 - \frac{\sigma_{cr}\big|_{k_\varphi^{'}=0}}{\sigma_w\big|_{\lambda=\lambda_d}} \right) \tag{3-49}$$

For the CFS beams subject to pure bending,

$$k_{\phi}=\frac{4D}{h}\left(1-\frac{\sigma_{cr}\big|_{k_{\varphi}^{'}=0}}{\sigma_{w}\big|_{\lambda=\lambda_{d}}}\frac{h}{h+2z_{0}}\right) \tag{3-50}$$

It should be pointed out that the two buckling stresses were not in the same position, the project factor $h/(h+2z_0)$ was adopted in Eq.(3-50) to reduce the errors. Where $\sigma_{cr}|_{k_\phi{}'=0}$ is the distortional buckling stress determined by Eq.(3-44) with $k_\phi{}'=0$ and $\sigma_{cr}|_{\lambda=\lambda d}$ is the local buckling stress of web which can be expressed as,

For the CFS columns subject to compression,

$$\sigma_{w}\big|_{\lambda=\lambda_{cr}}=\frac{\pi^{2}D}{h^{2}t}\left(\frac{h}{\lambda_{d}}+\frac{\lambda_{d}}{h}\right)^{2} \tag{3-51}$$

For the CFS beams subject to pure bending,

$$\sigma_{w}\big|_{\lambda=\lambda_{cr}}=\frac{Et^{2}}{\lambda_{cr}^{2}h^{4}}\left(11.32\lambda_{d}^{4}+1.97h^{4}+12.06\lambda_{cr}^{2}h^{2}\right) \tag{3-52}$$

Substituting Eq.(3-49) and Eq.(3-50) into Eq.(3-41), the expression of $k_\phi{}'$ for compression and pure bending can be obtained. After the iterative processes, the critical stress of distortional buckling of CFS channel sections can be determined.

3.4.2 Proposed analytical model

It is known that when the beam is subject to uniformly distributed load, the moment curve is parabolic. While the beam is subject to pure bending, the relevant moment curve is straight, as shown in Figure 3.21. The distortional half-wave length is equal for the beam subject to pure bending. However, it becomes unequal for the beam subject to uniformly distributed load due to variant moment distribution along the longitudinal direction. The design expressions presented in Section 3.3.2 are not available for calculating the distortional buckling stress of PCFS subject to uniformly distributed load. In the present study, the analytical model based on the model by Li and Chen was proposed to predict the distortional buckling stress of PCFS beams subject to uniformly distributed load. Furthermore, the effects of perforations and stress gradient on the distortional buckling behaviour of PCFS beams were examined.

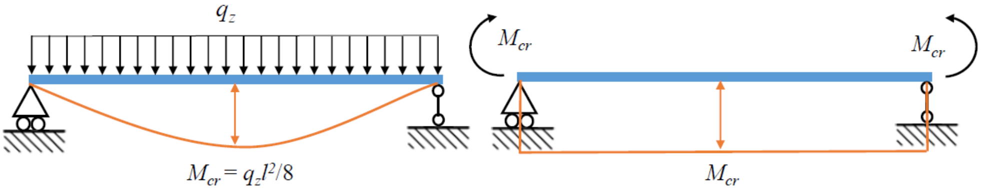

Figure 3.21 Bending moment diagram for uniformly distributed load (left) and pure bending (right)

In the proposed analytical model, the vertical spring stiffness in the model by Li and Chen needs to be reduced to consider the influence of web openings. Hence, a unit load, F was applied at the centroid of the compressed flange and lip to determine the modified vertical spring stiffness (see Figure 3.22). The strain energy of the web and compressed flange can be expressed as follows,

$$\begin{aligned} U &= \frac{1}{2EI_1}\int_0^{b-y_0}(Fy)^2 dy + \frac{1}{2EI_1}\int_0^h [F(b-y_0) - \frac{F(b-y_0)}{h}z]^2 dz \\ &+ (\frac{1}{2EI_2} - \frac{1}{2EI_1})\int_{\frac{h-d}{2}}^{\frac{h+d}{2}} [F(b-y_0) - \frac{F(b-y_0)}{h}z]^2 dz \end{aligned} \tag{3-53}$$

where EI_1 and EI_2 are the bending stiffnesses of the plain and perforated webs respectively.

The deflection of the vertical spring has been found to be

$$\begin{aligned} \delta &= \frac{\partial U}{\partial F} \\ &= \frac{F(b-y_0)^3}{3EI_1} + \frac{F(b-y_0)^2 h}{3EI_1} + (\frac{1}{EI_2} - \frac{1}{EI_1})F(b-y_0)^2 \frac{h}{3}[(\frac{h+d}{2h})^3 - (\frac{h-d}{2h})^3] \end{aligned} \tag{3-54}$$

The modified vertical spring stiffness can be determined as follows,

$$k_z^{'} = \frac{F}{\delta} = \frac{3D}{(b-y_0)^2(b-y_0+h)} \times \frac{1}{1+\frac{1}{4}(\frac{d}{h})\left[\frac{3+(d/h)^2}{1+(b-y_0)/h}\right](\frac{D}{D_h}-1)} \qquad (3\text{-}55)$$

where D is the flexural rigidity of the unperforated strip and D_h=0.5D is the flexural rigidity of the perforated strip.

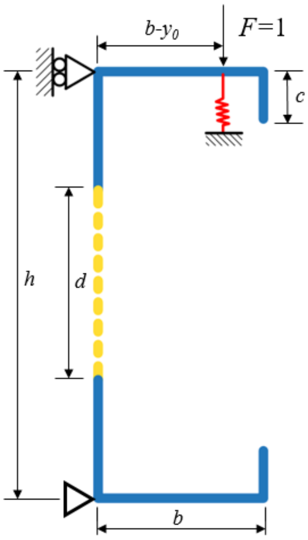

Figure 3.22 Model used to determine the stiffness of the vertical spring

For the CFS beam with plain web (d = 0), the vertical spring stiffness in Eq.(3-55) becomes

$$k_z = \frac{1}{\frac{(b-y_0)^3}{3D} + \frac{(b-y_0)^2}{\frac{3D}{h}}} \qquad (3\text{-}56)$$

The factor 3D/h in Eq.(3-56) represents the rotational spring stiffness of CFS beams at the flange-web junction, by multiplying the reduction factor, it yields,

$$k_\phi = \frac{2Et^3}{5.46[h+\frac{4}{3}(b-y_0)]}(1-1.11\frac{\sigma_{crPB0}}{Et^2}\frac{h^4\lambda_d^2}{12.56\lambda_d^4+2.192h^4+13.39\lambda_d^2h^2}\frac{h}{h-2z_0}) \qquad (3\text{-}57)$$

The reduction factor of the vertical spring stiffness of the PCFS beam can be defined as,

$$\beta = \frac{1}{1 + \frac{1}{4}(\frac{d}{h})\left[\frac{3 + (d/h)^2}{1 + (b - y_0)/h}\right](\frac{D}{D_h} - 1)} \tag{3-58}$$

Let Eq.(3-57) replace the factor 3*D*/*h* in Eq.(3-56), the modified vertical spring stiffness can be expressed as,

$$k_z^{'} = \beta \cdot \frac{1}{\frac{(b - y_0)^3}{3D} + \frac{(b - y_0)^2}{k_\phi}} \tag{3-59}$$

In order to avoid twisting, the uniformly distributed load is applied at the shear center of the PCFS beam as illustrated in Section 3.2.2.3. If the PCFS beam is simply supported, the internal moment along the longitudinal axis can be given by

$$M(x) = \frac{q_z l}{2} x - \frac{1}{2} q_z x^2 \tag{3-60}$$

where q_z is the density of uniformly distributed load and l is the length of the PCFS beam.

Then the external force in the compressed flange and lip can be expressed as follows,

$$P = \sigma_x A = \frac{M(x)}{M_{crdUDL}} \sigma_{crdUDL} A = \frac{4x(l - x)}{l^2} \sigma_{crdUDL} A \tag{3-61}$$

where $M_{crdUDL} = q_z l^2/8$ is the largest internal moment, σ_{crdUDL} is the distortional buckling stress of the PCFS beam subject to uniformly distributed load, $A=(b+c)t$ is the area of the compressed flange and lip.

For the simply supported PCFS beam subject to pure bending, the relevant external force in the compressed flange and lip is

$$P = \sigma_{crdPB} A \tag{3-62}$$

If the PCFS beam subject to uniformly distributed load is controlled by distortional buckling, the strain energy stored in the compressed flange and lip can be described as follows,

$$U_0 = \frac{1}{2}\int_0^l [(EI_w + EI_y b^2)(\frac{d^2\phi}{dx^2})^2 + GJ(\frac{d\phi}{dx})^2 + k_z^{'}(b-y_0)^2\phi^2]dx \tag{3-63}$$

A loss of the potential energy gives

$$W_p = \frac{z_0^2 + (b-y_0)^2 + r_c^2}{2}\int_0^l P(\frac{d\phi}{dx})^2 dx \tag{3-64}$$

where r_c is the polar radius of gyration of the compressed flange and lip about the centroid and some parameters in Eq.(3-63) and Eq.(3-64) are given by,

$$y_0 = b - \frac{b^2/2 + bc}{b+c} \tag{3-65}$$

$$z_0 = \frac{c^2/2}{b+c} \tag{3-66}$$

$$I_y = \frac{1}{12}bt^3 + btz_0{}^2 + \frac{1}{12}c^3t + ct(\frac{c}{2} - z_0)^2 \tag{3-67}$$

$$I_z = \frac{1}{12}tb^3 + bt(y_0 - \frac{b}{2})^2 + \frac{1}{12}ct^3 + cty_0{}^2 \tag{3-68}$$

$$G = \frac{E}{2(1+\mu)} \tag{3-69}$$

$$J = \frac{(b+c)t^3}{3} \tag{3-70}$$

$$r_c{}^2 = \frac{1}{A}(I_y + I_z) \tag{3-71}$$

The rotation of the compressed flange and lip about the shear center is defined as follows,

$$\phi(x) = a_1 \sin\frac{\pi x}{l} + a_2 \sin\frac{2\pi x}{l} + a_3 \sin\frac{3\pi x}{l} + \cdots + a_n \sin\frac{n\pi x}{l} \tag{3-72}$$

where a_1, a_2, … , a_n are arbitrary constants and hence various shapes of the rotation curves can be obtained. According to the energy method, the critical buckling stress of the compressed flange and lip with continuous vertical spring support can be determined by

$$\partial^2\Pi = \partial^2(U_0 - W_p) = 0 \tag{3-73}$$

Substituting Eq.(3-61), Eq.(3-63) and Eq.(3-64) into Eq.(3-73), one obtains,

$$\begin{gathered}\frac{z_0^2+(b-y_0)^2+r_c^2}{l^2}\Big[\sum_{n=1}^{\infty}\Big(\frac{n^2\pi^2}{3}-1\Big)a_n^2-4\sum_{n}\sum_{m}\Big(\frac{mn}{\left(m+n\right)^2}+\frac{mn}{(n-m)^2}\Big)a_m a_n\Big]2\sigma_{crdUDL}-\\ \sum_{n=1}^{\infty}\Big[\frac{EI_w+EI_y b^2}{A}\frac{n^4\pi^4}{l^4}+\frac{GJ}{A}\frac{n^2\pi^2}{l^2}+\frac{k_z^{'}(b-y_0)^2}{A}\Big]a_n^2=0\end{gathered} \tag{3-74}$$

It should be pointed out that *n* is not equal to *m* and the sum of *n* and *m* is even in Eq.(3-74). Substituting Eq.(3-59) into Eq.(3-74), the critical distortional stress of PCFS beams subject to uniformly distributed load can be determined. Eq.(3-74) can be evaluated by using the Rayleigh-Ritz method, the derivation of Eq.(3-74) with respect to a_1, a_2, … , a_n vanish, it yields,

$$\left\|\begin{bmatrix} a_{11} & \cdots & a_{1n} \\ \vdots & \ddots & \vdots \\ a_{n1} & \cdots & a_{nn}\end{bmatrix} - \sigma_{crdUDL}\begin{bmatrix} b_{11} & \cdots & b_{1n} \\ \vdots & \ddots & \vdots \\ b_{n1} & \cdots & b_{nn}\end{bmatrix}\right\| = 0 \tag{3-75}$$

in which,

$$a_{ij} = 0 \qquad (i \neq j) \tag{3-76}$$

$$a_{nn} = \frac{(EI_w + EI_y b^2)(\frac{n\pi}{l})^4 + GJ(\frac{n\pi}{l})^2 + k_z^{'}(b-y_0)^2}{A} \tag{3-77}$$

$$b_{pn} = 0 \qquad \left(p \neq n; p+n = odd\right) \tag{3-78}$$

$$b_{mn} = \frac{{z_0}^2 + \left(b-y_0\right)^2 + r_c^2}{l^2}\Big[-16\times\frac{nm(n^2+m^2)}{(n^2-m^2)^2}\Big] \tag{3-79}$$

$$b_{nn} = \frac{{z_0}^2 + \left(b-y_0\right)^2 + r_c^2}{l^2}\Big[2\times\Big(\frac{n^2\pi^2}{3}-1\Big)\Big] \tag{3-80}$$

Eq.(3-75) is the linear equations in a_1, a_2, … , a_n with infinite dimensions which represents the eigenvalue problem. The eigenvalues can be calculated by using MATLAB and the minimum value is the critical distortional buckling stress. It should be noted that the distortional buckling half-wave length of the CFS beam is mainly dependent on the cross-section dimension. However, it is found that most half-wavelengths of CFS sections selected from Albion Section are around 500 mm, and the relevant results obtained by using software CUFSM are summarized in Appendix C. Hence the largest value of *n* can be determined by the beam length, e.g., for the beam with 3000 mm length, the relevant *n* should be taken at least 6.

For the same PCFS beam subject to pure bending, substituting Eq.(3-62), Eq.(3-63) and Eq.(3-64) into Eq.(3-73), the relevant critical distortional buckling stress can be calculated as follows,

$$\sigma_{crdPB} = \frac{(EI_w + EI_y b^2)(\frac{n\pi}{l})^2 + GJ + k_z(b-y_0)^2(\frac{l}{n\pi})^2}{A(z_0{}^2 + \left(b-y_0\right)^2 + r_c^2)} \tag{3-81}$$

The comparison of critical distortional buckling stress of PCFS beams (Section D, *h*=200 mm, *b*=65 mm, *c*=20 mm and *t*=2 mm) subject to pure bending and uniformly distributed load is shown in Figure 3.23. It can be found that when the PCFS beam was subject to uniformly distributed load, the critical stress of distortional buckling was highly dependent on the beam length. For the PCFS beams less than 3000 mm, the distortional buckling stress decreased sharply with the increase of beam length. Whereas this decrease weakened for the PCFS beams more than 4500 mm. Furthermore, the distortional buckling stress of the PCFS beam subject to uniformly distributed load was continually higher than that of the same beam subject to pure bending. However, this gap tended to be close for the long beam. Hence, for the beam lengths ranging from 2 meters to 4 meters, the effect of variant moment distribution along the longitudinal direction of PCFS beams should be taken into account in the design of the beams.

3.4.3 Comparison between the proposed model and FEA

The comparison of the critical distortional buckling stress of PCFS beams with different hole sizes subject to uniformly distributed load between the proposed model and FEA was shown in Figure 3.24, where σ_{crdUDL} is the critical stress and σ_y is the yield stress (σ_y=390MPa). It can be identified from the figure that the critical stress curves of PCFS beams with different hole sizes have the similar variation pattern. Furthermore, the relevant critical stresses of PCFS beams decreased with the increase of hole size. The details of the critical moment of distortional buckling of PCFS beams with different hole sizes subject to uniformly distributed load obtained from eigenvalue buckling analysis can be found in Appendix B.2.

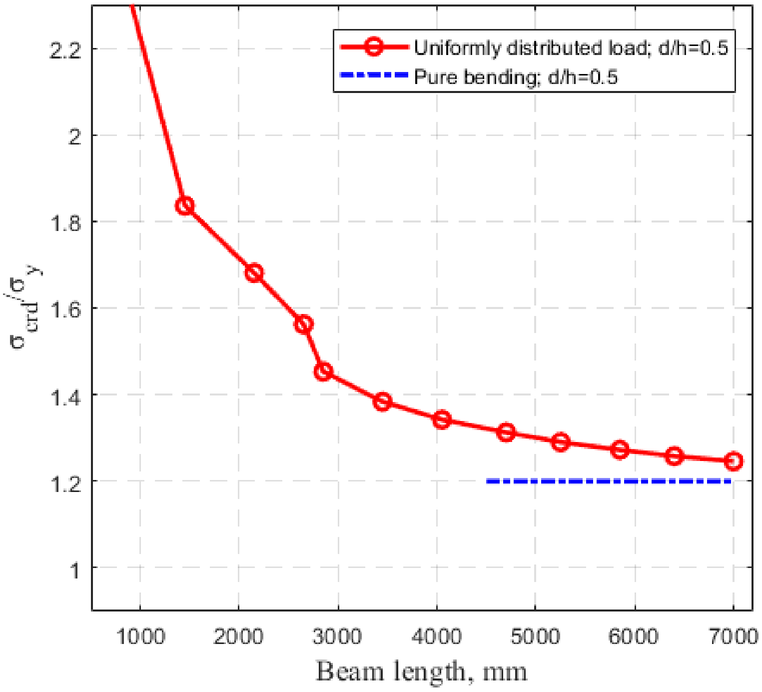

Figure 3.23 Comparisons of critical distortional buckling stress of PCFS beams subject to uniformly distributed load and pure bending (σ_y=390 MPa, h=200 mm, b=65 mm, c= 20 mm and t=2 mm)

The critical stresses calculated by the proposed analytical model can match the results obtained from eigenvalue buckling analysis well when the lengths of PCFS beams were longer than 3500 mm, but the critical stresses obtained from the proposed analytical model were much higher than that obtained from finite element analysis for the short beams as detailed in Figure 3.24. This is because the shear stresses are more serious than the bending stresses near the support ends of short beams when the PCFS beam is subject to uniformly distributed load. As a result, the failure modes of PCFS beams with short length would be controlled by shear buckling rather than distortional buckling. Furthermore, the stress concentration near the web openings might lead to the local buckling.

It should be mentioned that the proposed analytical model only focuses on the distortional buckling, but the local buckling modes, shear buckling modes and combination of these two modes are all included in the eigenvalue buckling analysis. For the short beam subject to uniformly distributed load, the distortional buckling is not the dominate mode. This is the reason why the proposed analytical approach cannot predict the critical stress of the PCFS beam (beam length is less than 3500 mm) accurately. It should, however, be noted that the proposed analytical model can predict the critical stresses of distortional buckling of PCFS beams subject to uniformly distributed load well as the beam lengths increase.

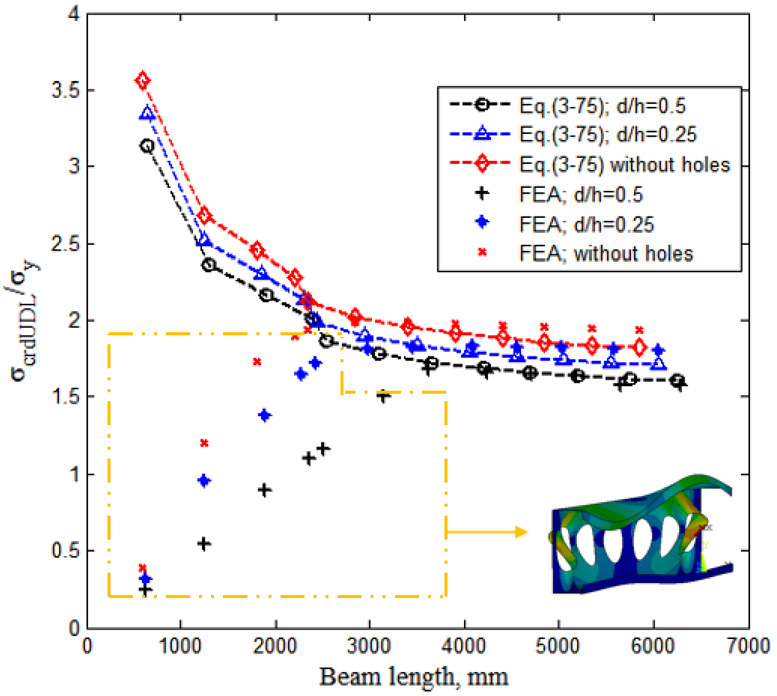

Figure 3.24 Comparison between the proposed model and eigenvalue buckling analysis of PCFS beams with different hole sizes subject to uniformly distributed load (σ_y=390 MPa, h=200 mm, b=65 mm, c= 20 mm and t=2.5 mm)

`

3.5 Summary

The analytical studies on the distortional buckling of PCFS beams subject to pure bending and uniformly distributed load have been presented in this Chapter in which models by Hancock (1987) and Li and Chen (2008) have been modified to predict the critical stress of distortional buckling. The results from numerical analysis have been used to validate against the proposed analytical solutions. From the results obtained from both analytical and numerical studies, the following major conclusions can be drawn.

- The circular perforations in the web can reduce the flexural rigidity of the web and thus decrease the rotational resistance of the compressed flange and lip. Consequently, the critical stresses of distortional buckling of PCFS beams decrease.

- The Hancock model (1987) can be applied to predict the critical moment of distortional buckling of PCFS beams subject to pure bending if the rotational spring stiffness is adequately reduced.

- The model by Li and Chen (2008) can be modified to determine the critical stress of distortional buckling of PCFS beams subject to uniformly distributed load. The influence of web perforations can be estimated by reducing the vertical spring stiffness of the compressed flange and lip system.

- The concept of the equivalent width can be applied for determining the reduction of bending rigidity of the perforated web and hence the modified rotational spring stiffness or the modified vertical spring stiffness can be obtained by means of the classical energy solution.

- When the PCFS beams are subject to uniformly distributed load, the half-wave lengths of the distortional buckling modes are different along the longitudinal direction due to the effects of stress gradient and the largest deflection appears at the mid-span.

- The effects of stress gradient on the distortional buckling behaviour of PCFS beams are highly dependent on the beam length. The critical stress of distortional buckling of a PCFS beam subject to uniformly distributed load is higher than that of the same beam subject to pure bending, this gap becomes closer with the increase of the beam length.

- The critical stresses of distortional buckling of PCFS beams subject to pure bending and uniformly distributed load decrease with the increase of circular hole sizes.

- For the short PCFS beams (beam length is less than 3500 mm) subject to uniformly distributed load, the section might experience shear failure in which case the distortional buckling is not the dominant mode. This explains why there is poor agreement between the adopted FEA results and the proposed analytical model.

- There is a good agreement between the results calculated by the proposed analytical models and the data obtained from eigenvalue buckling analysis for the beam longer than 3500 mm, indicating that the proposed theoretical approaches are reliable and can be applied into the design guideline for PCFS sections controlled by distortional buckling.

Chapter 4 — Lateral-torsional buckling performance of perforated cold-formed steel channel beams

4.1 Introduction

This chapter presents the theoretical approach and finite element analysis on the lateral-torsional buckling performance of perforated cold-formed steel channel beams subject to pure bending and uniformly distributed uplift load.

The finite element eigenvalue buckling analysis performed by ANSYS is used to investigate the influence of web openings, gradient moment and lateral restraint on the lateral-torsional buckling of PCFS beams. The finite strip solution by CUFSM is employed to verify the loading and boundary conditions of the finite element model.

The theoretical solution for determining the critical moments of lateral-torsional buckling of PCFS beams subject to pure bending and uniformly distributed uplift load is deduced based on the energy method. The horizontal and rotational springs are used to represent the restraint provided by the sheeting, the influence of horizontal and rotational spring stiffness on the lateral-torsional buckling behaviour of the PCFS beams is examined.

4.2 Numerical investigation

Eigenvalue buckling analysis of unrestrained and restrained PCFS beams subject to pure bending and uniformly distributed uplift load was conducted using finite element software ANSYS. The influences of hole sizes, variant moment along the longitudinal axis and restraint by the sheeting on the lateral-torsional buckling behaviour were explored. The finite strip method performed by CUFSM was used to demonstrate the adequacy of the boundary and loading conditions used in the finite element models.

4.2.1 Finite strip method

As described in Section 3.2.1, the finite strip method performed by CUFSM is an accurate predictor to calculate the critical buckling stress of simply supported CFS members (without holes) subject to pure bending. It was used to verify the reliability of the finite element models presented in this chapter. Section E (*h*=200 mm, *b*=70 mm, *c*=20 mm, *t*=2 mm) was selected as a typical cross section for the buckling analysis in CUFSM (see Figure 3.1). The simulation process of the finite strip model was the same as that in Section 3.2.1, the material properties such as Young’s modulus and Poisson’s ratio were also set as 205 GPa and 0.3, respectively.

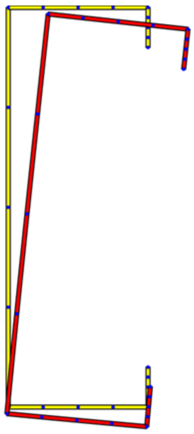

Section E (h=200 mm, b=70 mm, c=20 mm, t=2 mm)

Figure 4.1 Cross section in CUFSM to obtain the critical moments of lateral-torsional buckling of CFS beams (without holes) subject to pure bending

The typical lateral-torsional buckling mode of a 3-meter-long CFS beam (without holes) subject to pure bending is provided in Figure 4.2. It can be seen that the compression flange of the cross section bend laterally with respect to the major axis, and other parts move with the compression flange when the lateral-torsional buckling occurs. The whole CFS beam moves like a rigid body and the shape of the cross section remains unchanged.

Figure 4.2 Lateral-torsional buckling mode of a 3-meter-long CFS beam (without holes) in CUFSM. (h=200 mm, b=70 mm, c=20 mm, t=2 mm)

4.2.2 Elastic finite element analysis

4.2.2.1 Geometry

The geometry and notations used in the PCFS beam with circular holes in the web were defined in Figure 4.3, the web depth, flange width, lip length, thickness of the beam and circular hole diameter were labeled as h, b, c, t and d, respectively. The circular perforations were assumed to be punched in the web evenly, the beam length was considered as $l=n_h\pi d/2$ in which n_h was the total number of perforations. All the symbols used for the lateral-torsional buckling analysis were the same as those for distortional buckling analysis in Section 3.2.2.1. In this chapter, Section E (h=200 mm, b=70 mm, c=20 mm, t=2 mm) was selected for the eigenvalue buckling analysis of PCFS beams subject to pure bending and uniformly distributed uplift load.

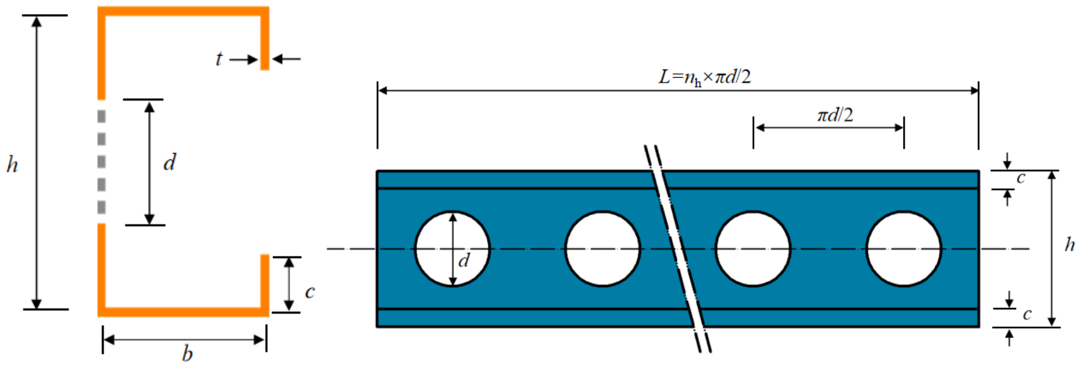

Figure 4.3 Geometry and notations used in the PCFS beam with circular holes in the web

4.2.2.2 Element type and mesh

The isoparametric four-node elements Shell 181 with six degrees of freedom at each node were used to model the PCFS beams for lateral-torsional buckling analysis. The material properties of the cold-formed steel including Young's modulus, Poisson's ratio and the yield strength were taken as E=205 GPa, μ=0.3 and σ_y=390 MPa respectively. The mesh size of a PCFS beam was roughly 5×5 mm (corresponding mesh sensitivity analysis can be found in Appendix A.2), smooth transition meshes were arranged around the circular perforations as shown in Figure 4.4.

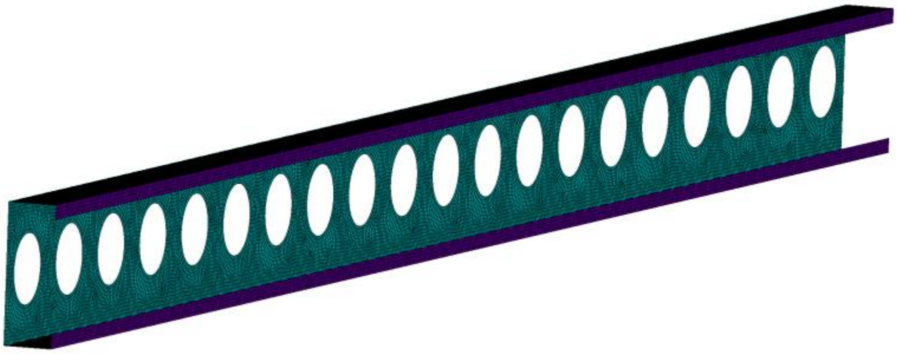

Figure 4.4 Typical finite element meshes of a PCFS beam in ANSYS (Section E, h=200 mm, b=70 mm, c=20 mm, t=2 mm, d=100 mm, l=3140 mm)

4.2.2.3 Boundary conditions of PCFS beams

In this section, the simply supported boundary conditions were assumed to be applied at two ends of the PCFS beam which is same to the description in Section 3.2.2.3. Two general cases were considered in this section, one was that there were no lateral restraint on the PCFS beam (k_z=0, k_ϕ=0). The other was that the tension flange of the PCFS beam was laterally restrained by sheeting (k_z=∞, k_ϕ=0).

Case 1: Laterally unrestrained PCFS beams (k_z=0, k_ϕ=0)

Figure 4.5 provides simply supported boundary conditions of a PCFS beam without lateral restraint. It can be found in the figure that the translations of end nodes were restrained in the y and z direction (that is UY=UZ=0), the rotation of end nodes was restrained about the x-axis (that is ROTX=0). To avoid the rigid displacement, the translation of Point C located in the middle of the web at one end was restrained in the x direction.

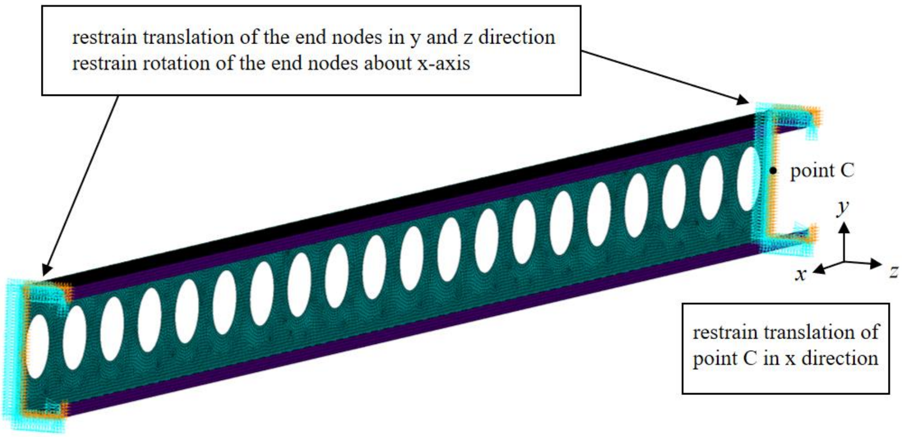

Figure 4.5 Boundary conditions of an unrestrained PCFS beam in ANSYS

Case 2: Laterally restrained PCFS beams (k_z=∞, k_ϕ=0)

When the PCFS beams were restrained by sheeting, the translation of tension flange-web corner line should be restrained in the z direction (that is UZ=0) as shown in Figure 4.6. Other setting of simply-supported boundary conditions were the same as that in Case 1. It should be pointed out two flange-web corner lines were both restrained laterally to ensure the PCFS beam controlled by distortional buckling in Section 3.2.2.4, however, only the tension flange-web corner line was restrained laterally in this Section.

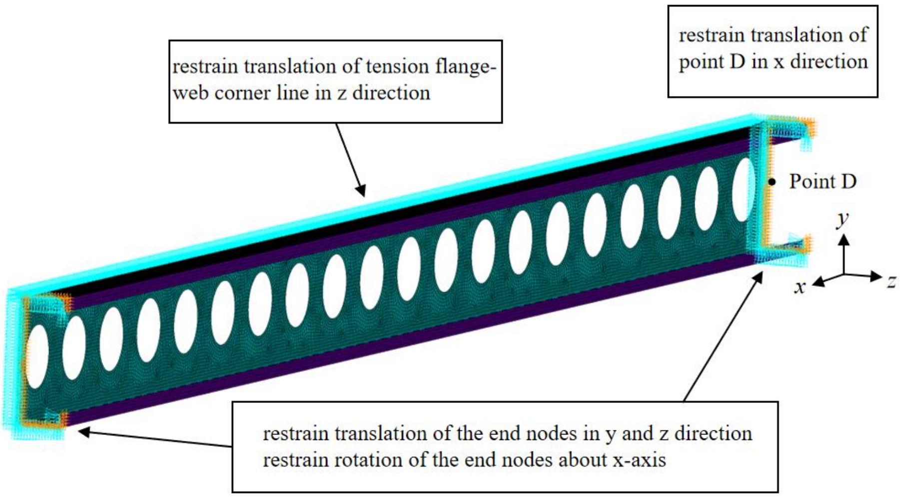

Figure 4.6 Boundary conditions of a laterally restrained PCFS beam in ANSYS

4.2.2.4 Loading conditions of PCFS beams

In this section, two general loading conditions (pure bending and uniformly distributed uplift load) were applied in the eigenvalue buckling analysis. The equivalence of forces were employed to simulate the above two loading cases.

Case 1: Pure bending

The equivalent forces of pure bending were applied at both ends of the PCFS beam in which the forces were uniformly distributed on the flanges but linearly distributed on the web and lips as shown in Figure 4.7.

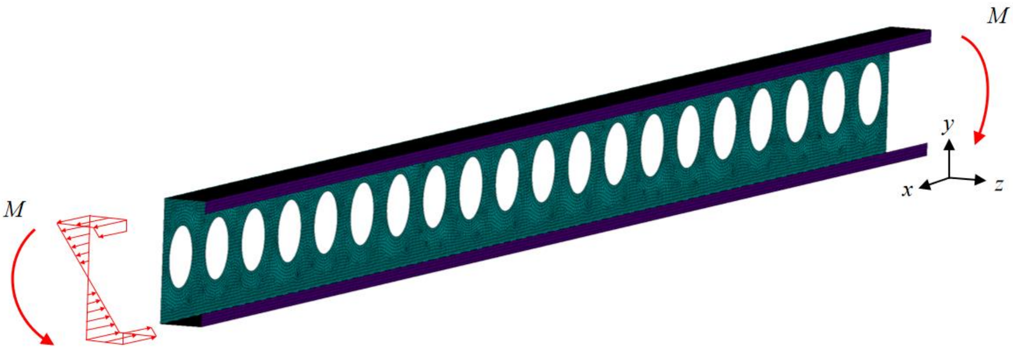

Figure 4.7 Loading conditions of a PCFS beam subject to pure bending

Case 2: Uniformly distributed uplift load

To avoid additional torsional moment, the uniformly distributed uplift load was applied at the intersection of shear center line and upper flange line of the cross section. To simulate this loading condition, the uniformly distributed uplift load coupled with equivalent moment was applied at the web line which is very similar to that described in Section 3.2.2.4 (see Figure 4.8).

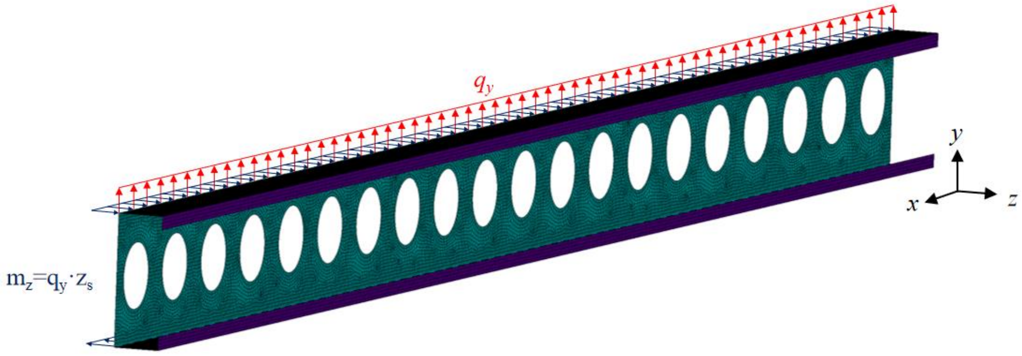

Figure 4.8 Loading conditions of a PCFS beam subject to uniformly distributed uplift load

4.2.2.5 Results and discussion

The critical moments of lateral-torsional buckling of laterally unrestrained and restrained PCFS beams with different hole sizes subject to pure bending and uniformly distributed uplift load obtained from eigenvalue buckling analysis are summarized in Appendix D, the beam length ranges from 3 meters to 14.5 meters.

Typical lateral-torsional buckling modes of a 3-meter-long PCFS beam with or without lateral restraint subject to pure bending are shown in Figure 4.9. Similar to the CFS beam (without holes), the cross section of the PCFS beam rotated about the major axis and moved laterally during lateral-torsional buckling, but the shape of the cross section did not change. It can also be found that the half-wave length of lateral-torsional buckling was equal to full length of the PCFS beam.

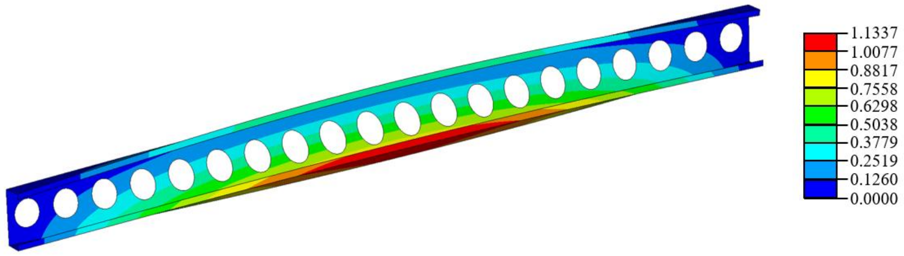

(a) k_z=0, k_ϕ=0

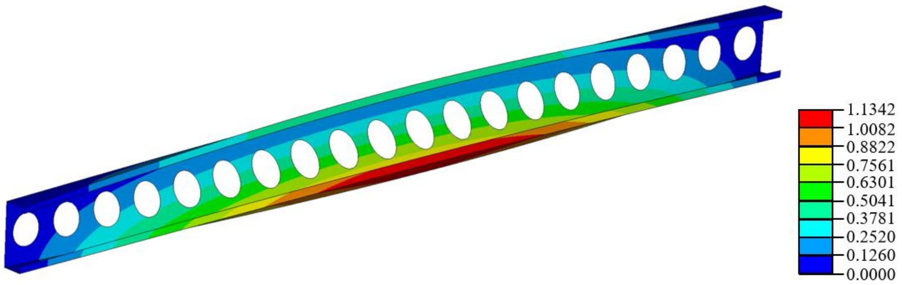

(b) k_z=∞, k_ϕ=0

Figure 4.9 Typical lateral-torsional buckling modes of a PCFS beam subject to pure bending in ANSYS (h=200 mm, b=70 mm, c=20 mm, t=2 mm, d=100 mm, l=3140 mm) (a) with no lateral restraint (b) with lateral restraint at the tension flange

Furthermore, it is interesting to notice that the lateral-torsional modes in Figure 4.9(a) and Figure 4.9(b) were almost the same which indicated that the influence of lateral restraint at the tension flange on the lateral-torsional buckling of PCFS beams subject to pure bending was negligible. This is mainly because the beam only deflects in the xy plane before buckling for the pure bending and the effect of lateral restraint on the pre-buckling moment distribution could be ignored.

The lateral-torsional buckling modes of a 3-meter-long PCFS beam with or without lateral restraint subject to uniformly distributed uplift load were analogous to the same beam subject to pure bending as shown in Figure 4.10. However, the cross-section rotation in Figure 4.10(a) was severer than that in Figure 4.10(b) which revealed that the lateral restraint at the tension flange can increase the critical moment of lateral-torsional buckling of PCFS beams subject to uniformly distributed uplift load. The reason is that the beam not only deflects in the xy plane but also in the xz plane before buckling for the uniformly distributed uplift load and the lateral restraint could affect the relevant pre-buckling moment distribution.

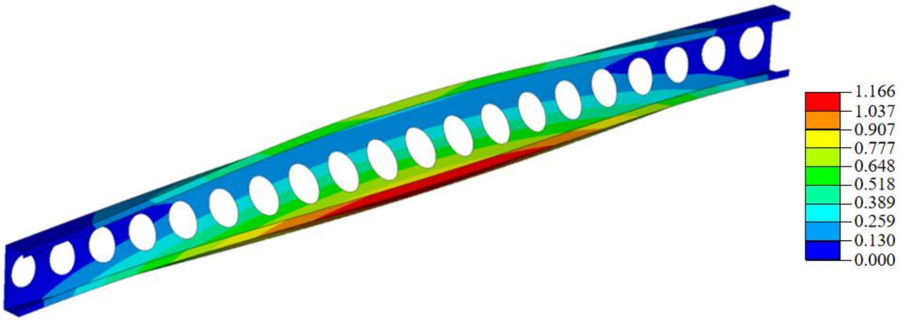

(a) k_z=0, k_ϕ=0

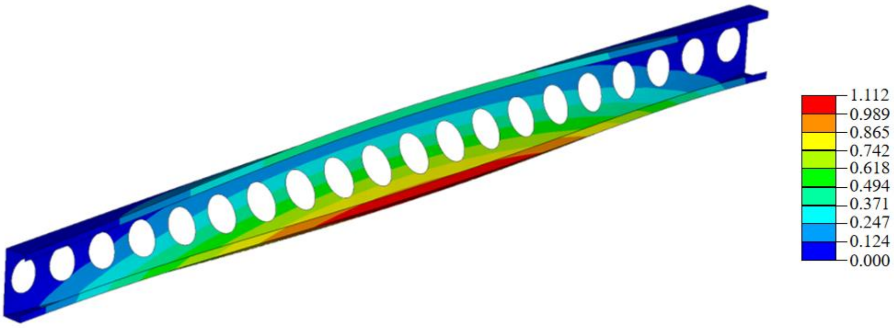

(b) k_z=∞, k_ϕ=0

Figure 4.10 Typical lateral-torsional buckling modes of a PCFS beam subject to uniformly distributed uplift load in ANSYS (h=200 mm, b=70 mm, c=20 mm, t=2 mm, d=100 mm, l=3140 mm) (a) with no lateral restraint (b) with lateral restraint at the tension flange

4.2.3 ANSYS-CUFSM results comparison

The comparison of lateral-torsional buckling modes of a 3-meter-long CFS beam (without holes) subject to pure bending obtained from FSM and FEA is provided in Figure 4.11. The finite element model had the same geometry, material properties, boundary and loading conditions used in CUFSM. It can be observed from the figures that the buckling modes generated by CUFSM and ANSYS had similar deformation patterns. Furthermore, it should be mentioned that the finite element parameters including material properties, mesh sizes, loading conditions and boundary conditions in this section were the same as that in Case 1 Section 4.2.2.4, the only difference was that there was no holes punched in the web.

(a) FSM

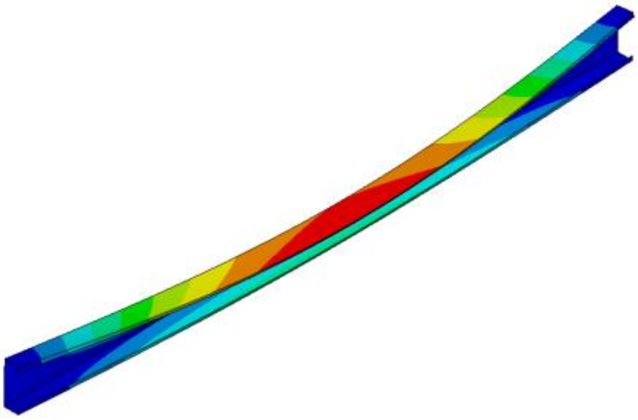

(b) FEA

Figure 4.11 Comparison of lateral-torsional buckling modes of CFS beams (without holes) subject to pure bending obtained from FSM and FEA (h=200 mm, b=70 mm, c=20 mm, t=2 mm, l=3000 mm)

Table 4.1 summarizes the numerical results of lateral-torsional buckling of CFS beams (without holes) ranging from 3000 mm to 14000 mm. It should be mentioned that in the practical cases the beam length might not be longer than 6000 mm. However, to make a straightforward comparison between the critical moments of lateral-torsional buckling obtained from CUFSM and eigenvalue buckling analysis by ANSYS, the longest length of the beams was selected to 14000 mm in the present study. It can be seen that the FEA-to-FSM moment ratios ($M_{\mathrm{cr}\lambda,\mathrm{FEA}}$ /$M_{\mathrm{cr}\lambda,\mathrm{FSM}}$) for CFS beams were all higher than 99.5% which revealed that the loading and boundary conditions of the finite element models built in this chapter were suitable and hence the models can be used to calculate the critical moments of lateral-torsional buckling of PCFS beams subject to pure bending and uniformly distributed uplift load.

Table 4.1 Comparison of the critical moments of lateral-torsional buckling of CFS beams (without holes) obtained from FSM and FEA (Section E, h=200 mm, b=70 mm, c=20 mm, t=2 mm)

Length (mm)	Slenderness ratio	$M_{\mathrm{cr\lambda,FSM}}$ (N·mm)	$M_{\mathrm{cr\lambda,FEA}}$ (N·mm)	$M_{\mathrm{cr\lambda,FEA}}$ /$M_{\mathrm{cr\lambda,FSM}}$
3000	113	11247734	11209025	0.997
3500	132	8417563	8386739	0.996
4000	150	6560385	6535480	0.996
4500	169	5278048	5258164	0.996
5000	188	4356176	4339836	0.996
5500	207	3671256	3656855	0.996
6000	226	3148283	3136392	0.996
6500	244	2739682	2728775	0.996
7000	263	2413920	2404452	0.996
37500	282	2150102	2141490	0.996
8000	301	1924718	1925299	1
8500	320	1752210	1745289	0.996
9000	338	1599740	1593446	0.996
9500	357	1469864	1464248	0.996
10000	376	1358217	1352734	0.996
10500	395	1261422	1256636	0.996
11000	414	1176847	1172408	0.996
11500	433	1102459	1098003	0.996
12000	451	1036579	1032392	0.996
12500	470	977901	974521	0.997
13000	489	925380	921655	0.996
13500	508	878101	874568	0.996
14000	527	835357	832002	0.996

4.3 Analytical model for lateral-torsional buckling analysis of PCFS beams

4.3.1 Li's model

An analytical solution for calculating the critical stress of lateral-torsional buckling of cold-formed zed-purlins was proposed by Li (2004). This model was built for the case that the CFS members partially restrained by sheeting or interval anti-sag bars and subject to transverse loads, in which the horizontal and rotational spring on the upper flange were used to represent the restraint of the sheeting, see Figure 4.12.

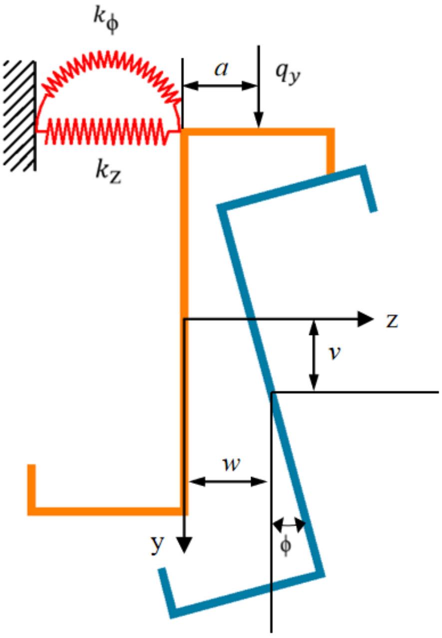

Figure 4.12 Analytical model proposed by Li (2004)

According to the coordinate system shown in Figure 4.12, the bending moment can be expressed as follows,

$$\begin{Bmatrix} M_y \\ M_z \end{Bmatrix} = E\begin{bmatrix} I_y & I_{yz} \\ I_{yz} & I_z \end{bmatrix}\begin{Bmatrix} 1/R_z \\ 1/R_y \end{Bmatrix} \tag{4-1}$$

where E is the Young's modulus, M_y and M_z are the bending moments about the y and z axes, I_y and I_z are the moment of inertia about the y and z axes, I_{yz} is the product of inertia. R_y and R_z are the radii of curvature of neutral axis in the xz and xy planes which can be expressed as follows,

$$\frac{1}{R_y} = -\frac{d^2v}{dx^2} \tag{4-2}$$

$$\frac{1}{R_z} = -\frac{d^2w}{dx^2} \tag{4-3}$$

where w and v are the horizontal and vertical displacements of the zed-purlin at the centroid.

The strain energy stored in the zed-purlin due to bending about the y and z axes, twisting and warping torsion can be expressed as,

$$U_{beam} = \frac{1}{2}\int_0^l \left(\frac{M_y}{R_z} + \frac{M_z}{R_y}\right)dx + \frac{1}{2}\int_0^l GJ\left(\frac{d\phi}{dx}\right)^2 dx + \frac{1}{2}\int_0^l EI_w\left(\frac{d^2\phi}{dx^2}\right)^2 dx \tag{4-4}$$

where ϕ is the twist of angle about x-axis, l is the length of the zed-purlin. G is the shear modulus, J is the torsion constant and I_w is the warping constant.

The strain energy stored in the horizontal and rotational springs on the upper flange due to the deformation of the zed-purlin can be expressed as,

$$U_{\text{spring}} = \frac{k_z}{2}\int_0^l \left(w - \frac{h\phi}{2}\right)^2 dx + \frac{k_\phi}{2}\int_0^l \phi^2 dx \tag{4-5}$$

where k_z and k_ϕ are the per-unit-length stiffness of the horizontal and rotational spring, h is the height of the zed-purlin.

If the zed-purlin is subject to uniformly distributed uplift load within the span and bending moment at two ends, the potential energy produced by the external loads is given by,

$$W_0 = \int_0^l q_y (v - a\phi)dx + \left(M_{yo}\left.\frac{dw}{dx}\right|_{x=0} - M_{yl}\left.\frac{dw}{dx}\right|_{x=l}\right) + \left(M_{zo}\left.\frac{dv}{dx}\right|_{x=0} - M_{zl}\left.\frac{dv}{dx}\right|_{x=l}\right) \tag{4-6}$$

where q_y is the density of uniformly distributed uplift load in the vertical direction, a is the distance of loading point to the web. M_{yo}, M_{yl}, M_{zo} and M_{zl} are the bending moment about the y and z axes at the ends of the zed-purlin.

According to the principle of the minimum potential energy, the deflections of the zed-purlin i.e. horizontal displacement, vertical displacement and rotational displacement due to the external loads can be determined.

$$\delta\Pi = \delta(U - W_0) = \delta(U_{\text{beam}} + U_{\text{spring}} - W_0) = 0 \tag{4-7}$$

It is assumed that the pre-buckling moment is distributed as M_{yo} and M_{zo}, then the pre-buckling longitudinal stress is

$$\sigma_x(x,y,z)=\frac{M_{zo}I_y-M_{yo}I_{yz}}{I_yI_z-I_{yz}^2}y+\frac{M_{yo}I_z-M_{zo}I_{yz}}{I_yI_z-I_{yz}^2}z \tag{4-8}$$

The horizontal and vertical deflections of the zed-purlin $\overline{w}(x,y,z)$ and $\overline{v}(x,y,z)$ at point (x,y,z) during buckling can be expressed as follows,

$$\overline{w}(x,y,z)=w+z(\cos\phi-1)+y\sin\phi\approx w+y\phi-\frac{1}{2}z\phi^2 \tag{4-9}$$

$$\overline{v}(x,y,z)=v-z\sin\phi+y(\cos\phi-1)\approx v-z\phi-\frac{1}{2}y\phi^2 \tag{4-10}$$

The longitudinal deflection of the zed-purlin $\overline{u}(x,y,z)$ at point (x,y,z) during buckling can be expressed as follows,

$$\begin{aligned}\overline{u}(x,y,z)&=u-(y\cos\phi-z\sin\phi)\frac{dv}{dx}-(z\cos\phi+y\sin\phi)\frac{dw}{dx}+\beta(y,z)\frac{d\phi}{dx}\\&\approx u-y\frac{dv}{dx}-z\frac{dw}{dx}+\beta\frac{d\phi}{dx}+z\phi\frac{dv}{dx}-y\phi\frac{dw}{dx}\end{aligned} \tag{4-11}$$

where $\beta(y,z)$ is the warping function of St. Venant torsion, $u(x)$ is the longitudinal deflection of the zed-purlin at point $(x,0,0)$. Then the longitudinal strain and shear strains produced by the buckling deflections can be obtained as follows,

$$\varepsilon_x(x,y,z)=\frac{\partial\overline{u}}{\partial x}+\frac{1}{2}[(\frac{\partial\overline{v}}{\partial x})^2+(\frac{\partial\overline{w}}{\partial x})^2] \tag{4-12}$$

$$\gamma_{xy}(x,y,z)=\frac{\partial\overline{u}}{\partial y}+\frac{\partial\overline{v}}{\partial x}+\frac{\partial\overline{w}}{\partial x}\frac{\partial\overline{w}}{\partial y} \tag{4-13}$$

$$\gamma_{xz}(x,y,z)=\frac{\partial\overline{u}}{\partial z}+\frac{\partial\overline{w}}{\partial x}+\frac{\partial\overline{v}}{\partial x}\frac{\partial\overline{v}}{\partial z} \tag{4-14}$$

Substituting Eq.(4-9) and Eq.(4-10) into Eq.(4-11) to Eq.(4-13) and splitting them into linear and nonlinear parts. Then, the second-order nonlinear strains can be obtained as follows,

$$\varepsilon_{x2}(x,y,z)=\frac{1}{2}[(\frac{dv}{dx})^2+(\frac{dw}{dx})^2+(y^2+z^2)(\frac{d\phi}{dx})^2]+\phi(z\frac{d^2v}{dx^2}-y\frac{d^2w}{dx^2}) \tag{4-15}$$

$$\gamma_{xy2}(x,y,z)=0 \tag{4-16}$$

$$\gamma_{xz2}(x,y,z)=0 \tag{4-17}$$

Hence, the potential energy produced by pre-buckling longitudinal stress due to the second-order nonlinear strains can be given by,

$$W_1=-\int_0^l\int_A\sigma_x(x,y,z)\varepsilon_{x2}(x,y,z)dAdx \tag{4-18}$$

The negative sign in Eq.(4-18) is because the pre-buckling longitudinal stress and the second-order nonlinear strains are in opposite direction. Substituting Eq.(4-15) into Eq.(4-18), it yields,

$$W_1=\int_0^l\int_A\sigma_x(x,y,z)(y\frac{d^2w}{dx^2}-z\frac{d^2v}{dx^2})\phi dAdx=\int_0^l\phi(M_{zo}\frac{d^2w}{dx^2}-M_{yo}\frac{d^2v}{dx^2})dx \tag{4-19}$$

When the uniformly distributed uplift load is not acting at the shear center, the work due to the lowering of the loads during the rotation should be taken into account. That is,

$$W=W_1+W_2=\int_0^l\phi(M_{zo}\frac{d^2w}{dx^2}-M_{yo}\frac{d^2v}{dx^2})dx+\frac{h}{4}\int_0^l q_y\phi^2dx \tag{4-20}$$

The cubic spline interpolations were used to represent the horizontal and vertical deflections of the zed-purlin in Li’s analytical model. Comparing to the traditional trigonometric series, the selected spline function can fit various boundary conditions and stimulate the restraint of interval anti-sag bars. Thus,

$$w(x) = \sum_{i=1}^{n} w_i f_i(x, x_i) \tag{4-21}$$

$$v(x) = \sum_{i=1}^{n} v_i f_i(x, x_i) \tag{4-22}$$

where w_i and v_i are the horizontal and vertical deflections at interpolation point x_i which need to be determined. $f_i(x, x_i)$ is the spine interpolation functions at n interpolation points (x_1, x_2, x_3,..., x_n) and can be defined as follows,

$$f_i(x, x_i) = 1 \quad \text{for} \quad x = x_i \tag{4-23}$$

$$f_i(x, x_i) = 0 \quad \text{for} \quad x = x_j \neq x_i \quad j = 0,1,..., n+1 \tag{4-24}$$

It should be pointed out that the derivation values of the spline functions at end points mainly depend on the actual boundary conditions. For a fixed boundary at the end point x_j ,

$$\frac{df_j(x, x_j)}{dx} \equiv 0 \tag{4-25}$$

For a simply supported boundary at end point x_j ,

$$\frac{d^2 f_j(x, x_j)}{dx^2} \equiv 0 \tag{4-26}$$

The rotational displacement of the zed-purlin can be expressed in terms of the horizontal deflection as,

$$\phi(x) = \frac{2}{h} w(x) \tag{4-27}$$

Noting that the buckling occurs when the strain energy produced by the buckling deflections is less than the potential energy generated by the pre-buckling stresses. The critical buckling stress can be calculated by following buckling equation.

$$\delta(U_{\text{beam}} + U_{\text{spring}} - \lambda W) = 0 \tag{4-28}$$

where λ is the critical load factor, the smallest eigenvalue calculated by Eq.(4-28) represents the buckling load factor. Substituting Eq.(4-21), Eq.(4-22) and Eq.(4-27) into Eq.(4-4), Eq.(4-5) and Eq.(4-20) and then into Eq.(4-28), the critical load of lateral-torsional buckling of partially restrained cold-formed zed-purlin can be determined.

4.3.2 Proposed analytical model

4.3.2.1 PCFS beams subject to pure bending

In this section, an analytical model was derived by using the energy method to predict the critical stress of lateral-torsional buckling of PCFS beams subject to pure bending. The cross-sectional properties were reduced in the energy-based stability equations to account for the influence of web openings. Unlike the case in Section 4.3.1, the present study mainly focused on the simple boundary condition and ignored the interval restraints by anti-sag bars. Hence, for convenience, the traditional trigonometric series were used to express the deflections rather than the cubic spline functions.

Let the x-axis be along the longitudinal direction of the beam, the y and z axes be the two principle axes of the cross section which are parallel to the web line and flange line respectively. Furthermore, the origin of the coordinate was located at the centroid of the cross section, as shown in Figure 4.13(a).

It should be pointed out that the web perforations have minimal effect on the position of the centroid and shear center. Hence, the distance from the centroid to the web line z_c and the distance from the shear center to the web line z_s of the PCFS beam are the same as that of the CFS beam (see Figure 4.13 (a)) and can be calculated as follows,

$$z_c = \frac{b^2 + 2bc}{2b + 2c + h} \tag{4-29}$$

$$z_s = \frac{tb(3bh^2 + 6ch^2 - 8c^3)}{12I_{z1}} \tag{4-30}$$

where I_{z1} the moment of inertia about the z-axis of CFS beams (without holes) and can be calculated as follows,

$$I_{z1} = \frac{t}{12}(h^3 + 6bh^2 + 6ch^2 - 12c^2h + 8c^3) \tag{4-31}$$

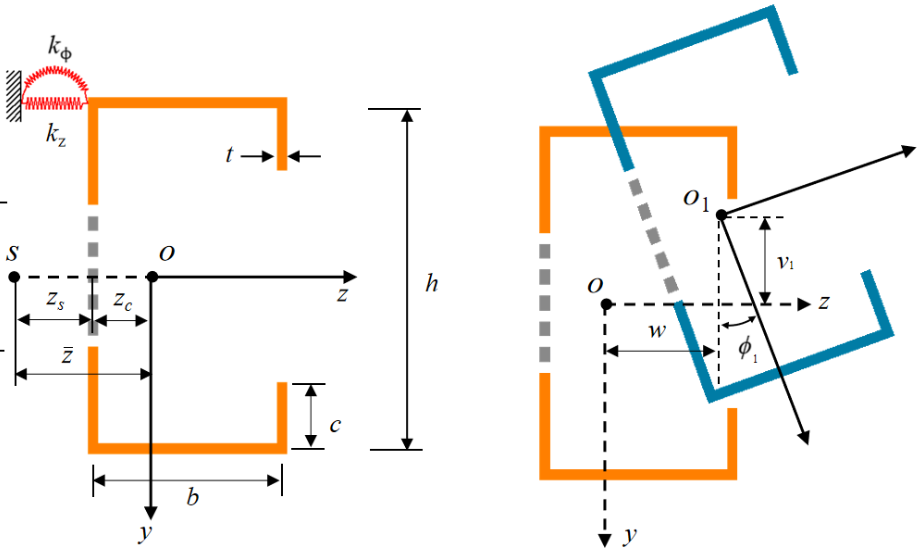

(a) (b)

Figure 4.13 Model used for lateral-torsional buckling analysis of PCFS beams subject to pure bending (a) Notation and geometry (b) Analytical model

The strain energy stored in the PCFS beam due to the buckled displacements i.e. horizontal deflection, vertical deflection and rotation can be expressed by,

$$U_{PCFS} = \frac{1}{2}\int_0^l [EI_y^*(\frac{d^2w}{dx^2})^2 + EI_z^*(\frac{d^2v_1}{dx^2})^2 + GJ^*(\frac{d\phi_1}{dx})^2 + EI_w(\frac{d^2\phi_1}{dx^2})^2]dx \tag{4-32}$$

where I_y^* and I_z^* are the moment of inertia about the y and z axes, J^* is the torsion constant, I_w is the warping constant about the shear center.

The cross-section properties of a PCFS beam can be divided into three different regions i.e. upper part of beam (unperforated strip), mid part of beam (perforated strip) and bottom part of beam (unperforated strip) as shown in Figure 4.14. For the thin-walled section with uniformly distributed perforations punched in the web, the contribution of solid part in the mid part of beam to the cross-section properties is negligible due to the discontinuities. Therefore, the relevant parameters can be calculated as follows,

$$I_y{}^* = 2ct(b - z_c)^2 + (h - d)tz_c{}^2 + \frac{2}{3}b^3t - 2b^2tz_c + 2btz_c{}^2 \tag{4-33}$$

$$I_z{}^* = \frac{t}{12}(h^3 + 6bh^2 + 6ch^2 - 12c^2h + 8c^3 - d^3) \tag{4-34}$$

$$J^* = \frac{t^3}{3}(h + 2b + 2c - d) \tag{4-35}$$

According to the work by Moen and Schafer (2009), the discontinuities generated by the perforations do not allow warping resistance at the end of the beam and hence the warping strain energy can be taken as zero in the unperforated strip. Hence, the warping constant of a PCFS beam can be calculated as follows,

$$I_w = \frac{tb^2}{6}(bh^2 + 3ch^2 + 6c^2h + 4c^3) - I_{z1}z_s^2 \tag{4-36}$$

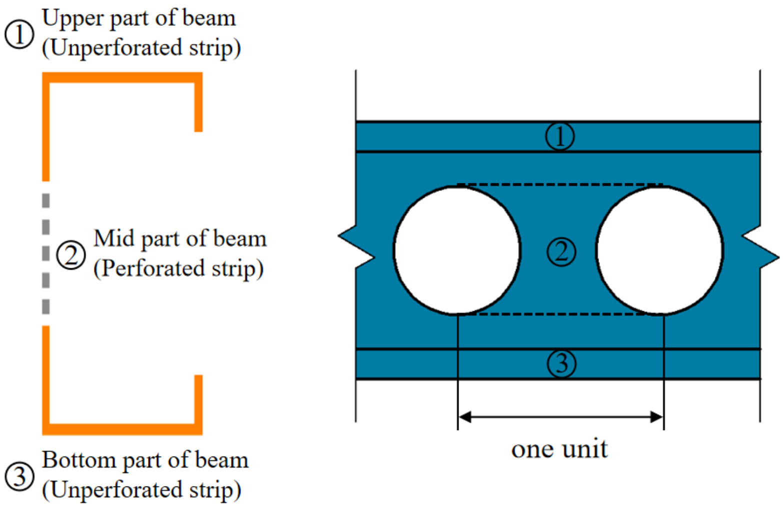

Figure 4.14 Cross-section properties of the PCFS beam in different regions

Similar to Li’s model, rotational and horizontal springs continuously distributed in the x-axis are used to represent the restraint by the sheeting. The strain energy stored in the horizontal and rotational springs (see Figure 4.13 (a)) due to the deformation of the PCFS beam is

$$U_{spring} = \frac{1}{2} k_z \int_0^l [(w - \frac{h\phi_1}{2})^2]dx + \frac{1}{2} k_\phi \int_0^l \phi_1{}^2 dx \tag{4-37}$$

The horizontal, vertical and rotational displacements of the PCFS beam at the centroid (see Figure 4.13 (b)) for the lateral-torsional buckling mode is given by,

$$w(x) = B_1 \sin \frac{\pi x}{l} \tag{4-38}$$

$$v_1(x) = B_2 \sin \frac{\pi x}{l} \tag{4-39}$$

$$\phi_1(x) = B_3 \sin \frac{\pi x}{l} \tag{4-40}$$

where l is the beam length, B_1, B_2 and B_3 are constants need to be determined.

For a simply supported PCFS channel beam subject to pure bending in which two equal bending moments in the opposite direction at both ends, the internal bending moment along the longitudinal axis is

$$M_z(x) = M_0 \tag{4-41}$$

where M_0 is the internal bending moment about the z-axis.

The potential energy generated by the pure bending is equal to the product of the bending moment and corresponding angle due to the lateral-torsional buckling, thus

$$W_{PB} = \int_0^l M_0 \frac{d^2 v_1}{dx^2} dx \tag{4-42}$$

After the rotation and deflections, the pre-buckling longitudinal stress generated by the internal bending moment about the z-axis can be calculated as,

$$\sigma_x(x,y,z)=\frac{M_0}{I_z}y \tag{4-43}$$

The work done by the longitudinal stress via the second-order nonlinear strains can be expressed as,

$$W_{\sigma x}=-\int_0^l\int_A\sigma_x(x,y,z)\varepsilon_{x2}(x,y,z)dAdx \tag{4-44}$$

where ε_{x2} is the second nonlinear strains and is expressed as Eq.(4-15) in the Section 4.3.1.

It should be pointed out that the channel section is symmetric about the z-axis, thus

$$\int_A\sigma_x dA=0 \tag{4-45}$$

$$\int_A(y^2+z^2)\sigma_x dA=0 \tag{4-46}$$

Substituting Eq.(4-43) and Eq.(4-15) into Eq.(4-44), it yields,

$$W_{\sigma xPB}=\int_0^l\phi_1 M_0\frac{d^2w}{dx^2}dx \tag{4-47}$$

Hence, the total work done by the pure bending during the lateral-torsional buckling can be expressed as follows,

$$W_1=W_{\sigma xPB}+W_{PB} \tag{4-48}$$

The total potential energy of the proposed analytical model subject to pure bending becomes

$$
\begin{aligned}
\Pi &= U_{PCFS} + U_{spring} - W_1 \\
&= \int_0^l [EI_y{}^*(\frac{d^2w}{dx^2})^2 + EI_z{}^*(\frac{d^2v_1}{dx^2})^2 + GJ^*(\frac{d\phi_1}{dx})^2 + EI_w(\frac{d^2\phi_1}{dx^2})^2]dx \\
&\quad + \frac{1}{2}k_z\int_0^l[(w-\frac{h\phi_1}{2})^2]dx + \frac{1}{2}k_\phi\int_0^l \phi_1{}^2dx - \int_0^l M_0\frac{d^2v_1}{dx^2}dxW_{\sigma x} - \int_0^l \phi_1 M_0\frac{d^2w}{dx^2}dx
\end{aligned}
\tag{4-49}
$$

Substituting Eq.(4-38) to Eq.(4-40) into Eq.(4-49), it yields,

$$
\begin{aligned}
\Pi &= \frac{l}{4}(\frac{\pi}{l})^4 EI_y{}^*B_1{}^2 + \frac{l}{4}(\frac{\pi}{l})^4 EI_z{}^*B_2{}^2 + \frac{l}{4}(\frac{\pi}{l})^2 GJ^*B_3{}^2 + \frac{l}{4}(\frac{\pi}{l})^4 EI_wB_3{}^2 \\
&\quad + k_z\frac{l}{4}(B_1{}^2 - hB_1B_3 + \frac{h^2}{4}B_3{}^2) + k_\phi\frac{l}{4}B_3{}^2 - M_0\frac{2l}{\pi}(\frac{\pi}{l})^2B_2 - M_0\frac{l}{2}(\frac{\pi}{l})^2B_1B_3
\end{aligned}
\tag{4-50}
$$

According to the principle of minimum potential energy, the total potential energy of the proposed analytical model will reach the state of equilibrium with respect to the constants B_1, B_2 and B_3 when the lateral-torsional buckling occurs. That is

$$\frac{\partial\Pi}{\partial B_1} = \frac{\partial}{\partial B_1}(U_{PCFS} + U_{spring} - W_1) = 0 \tag{4-51}$$

$$\frac{\partial\Pi}{\partial B_2} = \frac{\partial}{\partial B_2}(U_{PCFS} + U_{spring} - W_1) = 0 \tag{4-52}$$

$$\frac{\partial\Pi}{\partial B_3} = \frac{\partial}{\partial B_3}(U_{PCFS} + U_{spring} - W_1) = 0 \tag{4-53}$$

By using Raleigh-Ritz derivation the eigenvalue equations can be re-written as follows,

$$\left\{\begin{bmatrix} A_{11} & 0 & A_{13} \\ 0 & A_{22} & 0 \\ A_{31} & 0 & A_{33} \end{bmatrix} - M_0\begin{bmatrix} 0 & 0 & 1 \\ 0 & 0 & 0 \\ 1 & 0 & 0 \end{bmatrix}\right\}\begin{Bmatrix} B_1 \\ B_2 \\ B_3 \end{Bmatrix} = \begin{Bmatrix} 0 \\ 0 \\ 0 \end{Bmatrix} \tag{4-54}$$

in which A_{11}, A_{13}, A_{22}, A_{31}, A_{33} are the coefficients of Eq.(4-54) and can be expressed as follows,

$$A_{11} = (\frac{\pi}{l})^2 EI_y{}^* + k_z(\frac{l}{\pi})^2 \tag{4-55}$$

$$A_{13} = -\frac{k_z}{2}(\frac{l}{\pi})^2 h \tag{4-56}$$

$$A_{22} = \frac{\pi^3}{4l^2} EI_z^* \tag{4-57}$$

$$A_{31} = -\frac{k_z}{2}(\frac{l}{\pi})^2 h \tag{4-58}$$

$$A_{33} = GJ^* + (\frac{\pi}{l})^2 EI_w + k_z(\frac{l}{\pi})^2 \frac{h^2}{4} + k_\phi(\frac{l}{\pi})^2 \tag{4-59}$$

Eq.(4-54) is an eigenvalue equation with three dimensions and can be solved by the calculation software MATLAB. The smallest eigenvalue is treated as the critical moment of lateral-torsional buckling of a PCFS beam with typical length subject to pure bending.

4.3.2.2 PCFS beams subject to uniformly distributed uplift load

In some practical cases, the sheeting fixed in the upper flange of a PCFS beam is used to enclose the building. To some extent, it helps to reduce the possibility of lateral-torsional buckling. However, when the PCFS beams are subject to uplift wind loads, the lateral-torsional buckling is still the dominant mode for the PCFS beam with long length (see Figure 4.15(a)). In this section, the restraint by the sheeting is simplified to the rotational and lateral spring (see Figure 4.15(b)), the analytical model proposed in Section 4.3.2.1 is used to calculate the critical load of lateral-torsional buckling of PCFS channel beams subject to uniformly uplift distributed load.

For a simply supported PCFS channel beam, the uniformly uplift distributed load is assumed to apply at the intersection of shear center line and upper flange line to avoid additional torsional moment as shown in Figure 4.15(b) and the internal moment along the x-axis can be calculated as follows,

$$M_z(x) = \frac{q_y l}{2} x - \frac{1}{2} q_y x^2 \tag{4-60}$$

where q_y is uniformly distributed uplift load.

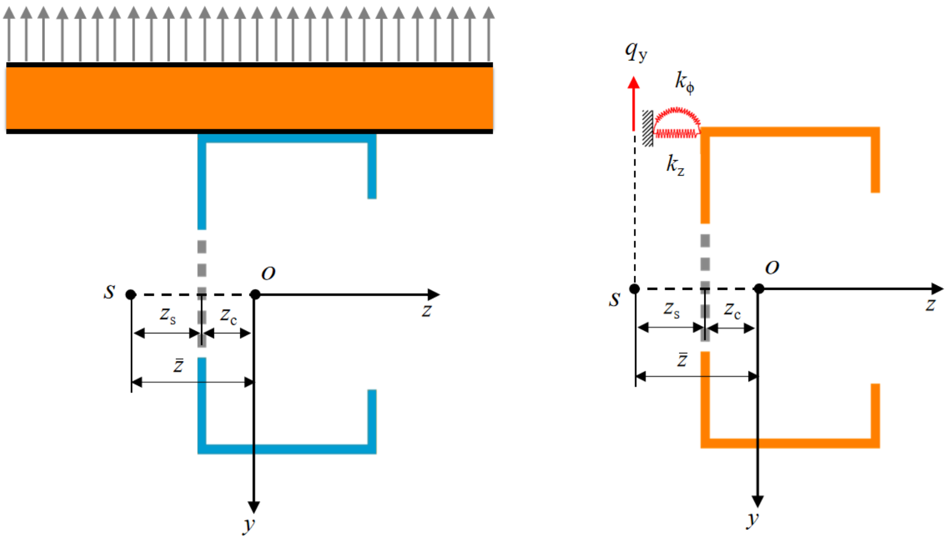

(a) (b)

Figure 4.15 Model used for lateral-torsional buckling analysis of PCFS beams subject to uniformly distributed uplift load (a) Practical case (b) Simplified model

Hence, after the lateral-torsional buckling, the pre-buckling longitudinal stress produced by the internal moment can be expressed as follows,

$$\sigma_{xUDL}(x,y,z)=\frac{q_y x(l-x)}{2I_z}y \tag{4-61}$$

Substituting Eq.(4-61) and Eq.(4-15) into Eq.(4-44), the potential energy generated by the pre-buckling longitudinal stress leads to,

$$W_{\sigma xUDL}=\int_0^l \phi_1 \frac{q_y x(l-x)}{2}\frac{d^2 w}{dx^2}dx \tag{4-62}$$

The work done by the uniformly distributed uplift load can be divided into two parts, one is the product of the bending moment generated by uniformly distributed uplift load and corresponding angle, the other is the product of uniformly distributed uplift load and the lowering distance during rotation, that is

$$W_{UDL} = \int_0^l M_z(x)\frac{d^2 v_1}{dx^2}dx + \int_0^l q_y \frac{h}{4}\phi_1^{\,2} dx \tag{4-63}$$

Hence, the total work done by the uniformly distributed uplift load during the lateral-torsional buckling can be expressed as follows,

$$W_2 = W_{\sigma xUDL} + W_{UDL} \tag{4-64}$$

The total potential energy of the proposed analytical model subject to uniformly distributed uplift load is

$$\begin{aligned}\Pi &= U_{PCFS} + U_{spring} - W_2 \\ &= \int_0^l [EI_y^{\,*}(\frac{d^2 w}{dx^2})^2 + EI_z^{\,*}(\frac{d^2 v_1}{dx^2})^2 + GJ^*(\frac{d\phi_1}{dx})^2 + EI_w(\frac{d^2\phi_1}{dx^2})^2]dx \\ &+ \frac{1}{2}k_z\int_0^l [(w - \frac{h\phi_1}{2})^2]dx + \frac{1}{2}k_\phi\int_0^l \phi_1^{\,2}dx - \int_0^l \phi_1 \frac{q_y x(l-x)}{2}\frac{d^2 w}{dx^2}dx \\ &- \int_0^l M_z(x)\frac{d^2 v_1}{dx^2}dx - \int_0^l q_y \frac{h}{4}\phi_1^{\,2}dx\end{aligned} \tag{4-65}$$

Substituting Eq.(4-38) to Eq.(4-40) into Eq.(4-65), it yields,

$$\begin{aligned}\Pi &= \frac{l}{4}(\frac{\pi}{l})^4 EI_y^{\,*}B_1^{\,2} + \frac{l}{4}(\frac{\pi}{l})^4 EI_z^{\,*}B_2^{\,2} + \frac{l}{4}(\frac{\pi}{l})^2 GJ^* B_3^{\,2} + \frac{l}{4}(\frac{\pi}{l})^4 EI_w B_3^{\,2} \\ &+ k_z\frac{l}{4}(B_1^{\,2} - hB_1B_3 + \frac{h^2}{4}B_3^{\,2}) + k_\phi\frac{l}{4}B_3^{\,2} - q_y\frac{l(\pi^2+3)}{24}B_1B_3 \\ &- q_y\frac{2l}{\pi}B_2 - q_y\frac{hl}{8}B_3^{\,2}\end{aligned} \tag{4-66}$$

The calculation procedure to determine the critical load of a PCFS beam subject to uniformly distributed uplift load is the same as that in Section 4.2.2.1. The total potential energy will have a stationary with respect to the constants B_1, B_2 and B_3 when the lateral-torsional buckling happens, that is

$$\frac{\partial \Pi}{\partial B_1} = \frac{\partial}{\partial B_1}(U_{PCFS} + U_{spring} - W_2) = 0 \tag{4-67}$$

$$\frac{\partial \Pi}{\partial B_2} = \frac{\partial}{\partial B_2}(U_{PCFS} + U_{spring} - W_2) = 0 \tag{4-68}$$

$$\frac{\partial \Pi}{\partial B_3} = \frac{\partial}{\partial B_3}(U_{PCFS} + U_{spring} - W_2) = 0 \tag{4-69}$$

Based on the Raleigh-Ritz method, the simultaneous equations (4-67) to (4-69) can be re-written as follows,

$$\left\{ \begin{bmatrix} C_{11} & 0 & C_{13} \\ 0 & C_{22} & 0 \\ C_{31} & 0 & C_{33} \end{bmatrix} - q_y \begin{bmatrix} 0 & 0 & D_{13} \\ 0 & 0 & 0 \\ D_{31} & 0 & D_{33} \end{bmatrix} \right\} \begin{Bmatrix} B_1 \\ B_2 \\ B_3 \end{Bmatrix} = \begin{Bmatrix} 0 \\ 0 \\ 0 \end{Bmatrix} \tag{4-70}$$

in which C_{ij} and D_{ij} are the coefficients of Eq.(4-54) and can be expressed as follows,

$$C_{11} = (\frac{\pi}{l})^4 \frac{l}{2} EI_y{}^* + k_z \frac{l}{2} \tag{4-71}$$

$$C_{13} = -k_z \frac{lh}{4} \tag{4-72}$$

$$C_{22} = (\frac{\pi}{l})^4 (\frac{l}{2}) EI_z{}^* \tag{4-73}$$

$$C_{31} = -k_z \frac{lh}{4} \tag{4-74}$$

$$C_{33} = (\frac{\pi}{l})^2 \frac{l}{2} GJ^* + (\frac{\pi}{l})^4 \frac{l}{2} EI_w + k_z l \frac{h^2}{8} + k_\phi \frac{l}{2} \tag{4-75}$$

$$D_{13} = \frac{(\pi^2 + 3)l}{24} \tag{4-76}$$

$$D_{31} = \frac{(\pi^2 + 3)l}{24} \tag{4-77}$$

$$D_{33} = \frac{lh}{4} \tag{4-78}$$

The eigenvalue equation (4-70) can be solved by the calculation software MATLAB. For the failure mode dominated by the lateral-torsional buckling, the smallest eigenvalue is the critical load of a PCFS beam subject to uniformly distributed uplift load.

4.3.3 Comparison between the proposed analytical model and FEA

4.3.3.1 PCFS beams subject to pure bending

The critical moments of lateral-torsional buckling of a PCFS beam with different hole sizes subject to pure bending calculated from the proposed analytical model were plotted for varying beam length and compared to the eigenvalue buckling analysis data in Figure 4.16, where $M_{cr\lambda PB}$ is the critical moment of lateral-torsional buckling of a PCFS beam subject to pure bending and M_y is the yield moment (σ_y=390MPa).

Section E (h=200 mm, b=70 mm, c= 20 mm and t=2 mm) was selected as a typical cross section in the analytical and numerical analysis. The diameters of circular holes in the web were chosen as 100 mm, 80 mm, 66.7 mm and 50 mm. Hence, the ratios of d/h were 0.5, 0.4, 0.33 and 0.25 respectively.

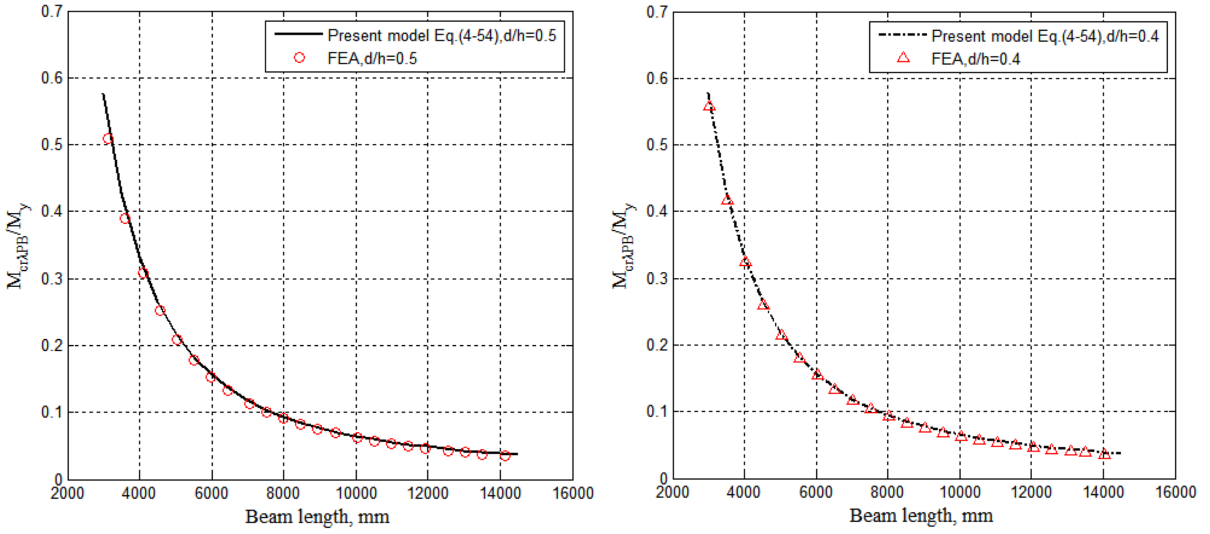

(a) (b)

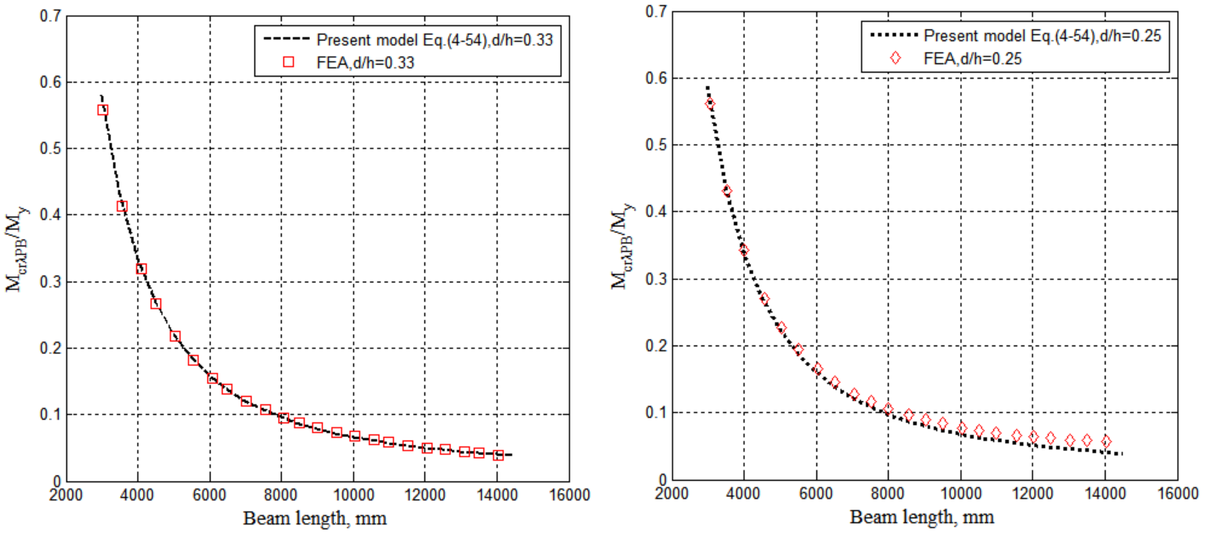

(c) (d)

Figure 4.16 Comparison between critical moments of lateral-torsional buckling obtained from present model and FEA for PCFS beams with different hole sizes subject to pure bending. (a) d=100 mm (b) d=80 mm (c) d=66.7 mm (d) d=50mm (σ_y=390 MPa, h=200 mm, b=70 mm, c= 20 mm and t=2 mm)

As expected, the proposed analytical solution gives an excellent agreement with FEA. For the PCFS beams with small perforations (d=50 mm), the FEA data was slightly higher than the results calculated from the present solution as the beam length increased longer than 8000 mm. This is probably because the solid part of perforated strip still had a minimal contribution to the cross-sectional properties of the PCFS beam which made the present solution a little conservative in this case. Furthermore, the critical moment of lateral-torsional buckling decreased with the increase of beam length. It is interesting to find that the critical moments of PCFS beams with different hole sizes had the same decreasing trend, this decreasing tendency slowed down as the beam length increased.

The critical moments of lateral-torsional buckling of PCFS beams (d=100 mm) subject to pure bending were compared to that of CFS beams (without holes) as shown in Figure 4.17. It should be mentioned that these two kinds of beams have the same cross-section, the only difference is that the PCFS beams have the circular holes (d=100 mm) in the web. It is evident that the critical moments of lateral-torsional buckling of PCFS beams were lower than that of CFS beams which indicated that the PCFS beam was more susceptible to lateral-torsional buckling. In addition, the gap of critical lateral-torsional buckling moments between

PCFS and CFS beams widened with the increase of beam length. The critical moment of lateral-torsional buckling of the PCFS beam (h=200 mm, b=70 mm, c= 20 mm, t=2 mm) was found to reduce by 11% at the length of 3140 mm, but to 20% at the length of 11932 mm.

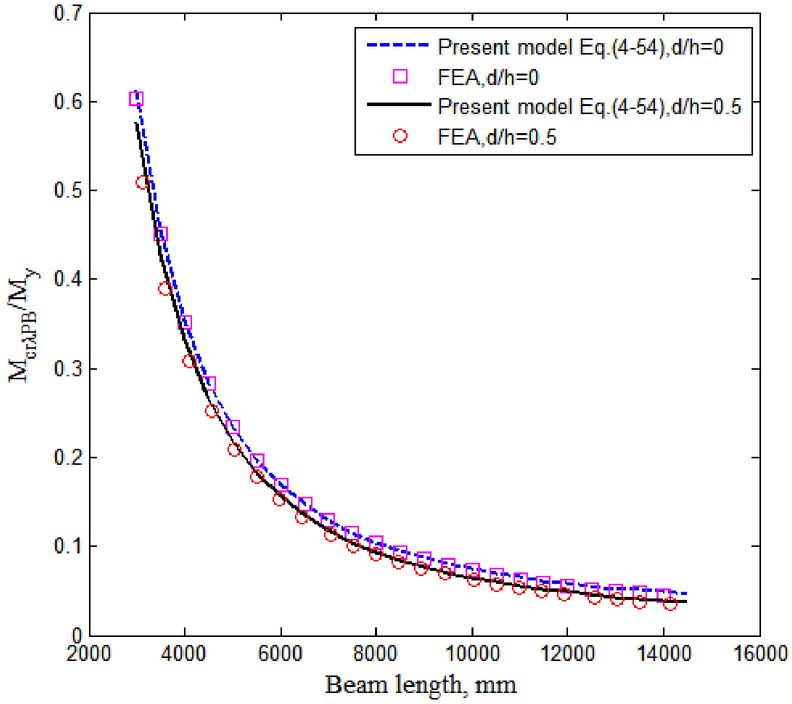

Figure 4.17 Comparisons of critical moments of lateral-torsional buckling of CFS beams (without holes) with PCFS beams (d=100 mm) subject to pure bending (σ_y=390 MPa, h=200 mm, b=70 mm, c= 20 mm, t=2 mm)

4.3.3.2 PCFS beams subject to uniformly distributed uplift load

The comparisons between the proposed analytical model and eigenvalue buckling analysis demonstrated that the present solution was practical for calculating the critical moments of lateral-torsional buckling of PCFS beams subject to uniformly distributed uplift load as shown in Figure 4.18. Similar to the case that subject to pure bending, the critical moment of lateral-torsional buckling $M_{cr\lambda UDL}$ decreased with the increase of beam length, but this downward trend lessened with the growth of span length. It should be mentioned here that, the first points obtained from FEA shown in Figure 4.18(a)-Figure 4.18(d) are all lower than those predicted by the present model. The reason is that for the short beam (less than 3000 mm) subject to uniformly distributed uplift loading, the shear stress has a great effect on the buckling modes, which is considered in the FEA but not in the present analytical model.

To evaluate the influence of stress gradient distributed along the longitudinal axis, the critical moments of lateral torsional buckling of PCFS beams (d=100 mm) subject to uniformly distributed uplift load were compared to that subject to pure bending in Figure 4.19. As explained before, the uniformly distributed load was applied at the shear center rather than at the intersection of shear center line and upper flange line. It can be seen from the figure that the critical moments of lateral-torsional buckling for the pure bending were lower than those for the uniformly distributed uplift load (e.g., the critical moment for the pure bending is 16% lower than that for the uniformly distributed uplift load at the length of 3000 mm). However, the difference between these two cases narrowed as the beam length increased and the difference between them could be ignored when the beam length is longer than 7000 mm). Most CFS beam lengths used in practice are about 6000 mm. Hence, the design load obtained according to the pure bending may be conservative.

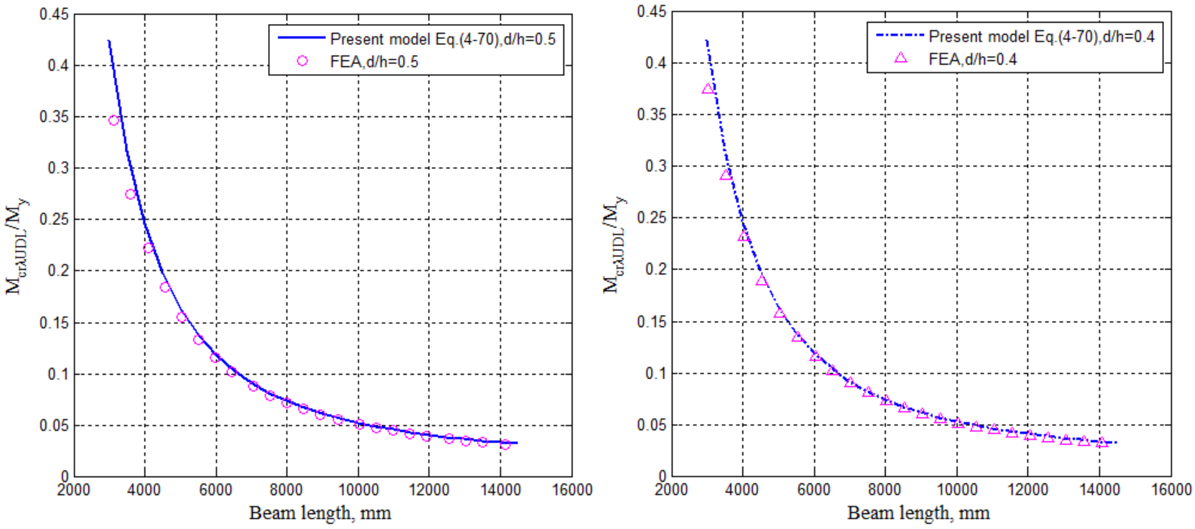

(a)

(b)

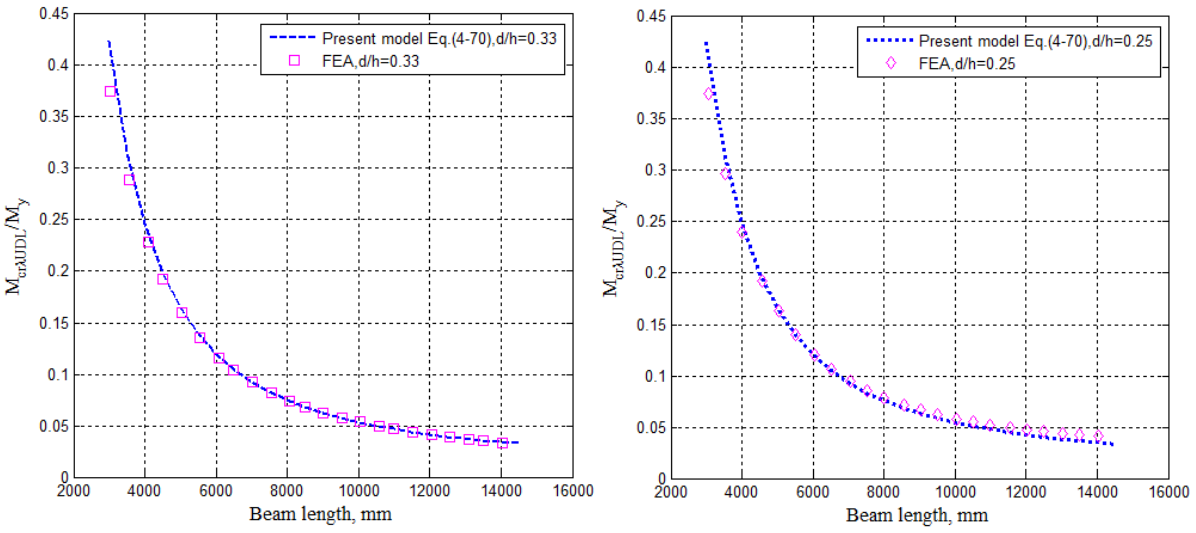

(c) (d)

Figure 4.18 Comparison between critical moments of lateral-torsional buckling obtained from present model and FEA for PCFS beams with different hole sizes subject to uniformly distributed uplift load. (a) d=100 mm (b) d=80 mm (c) d=66.7 mm (d) d=50mm (σ_y=390 MPa, h=200 mm, b=70 mm, c=20 mm and t=2 mm)

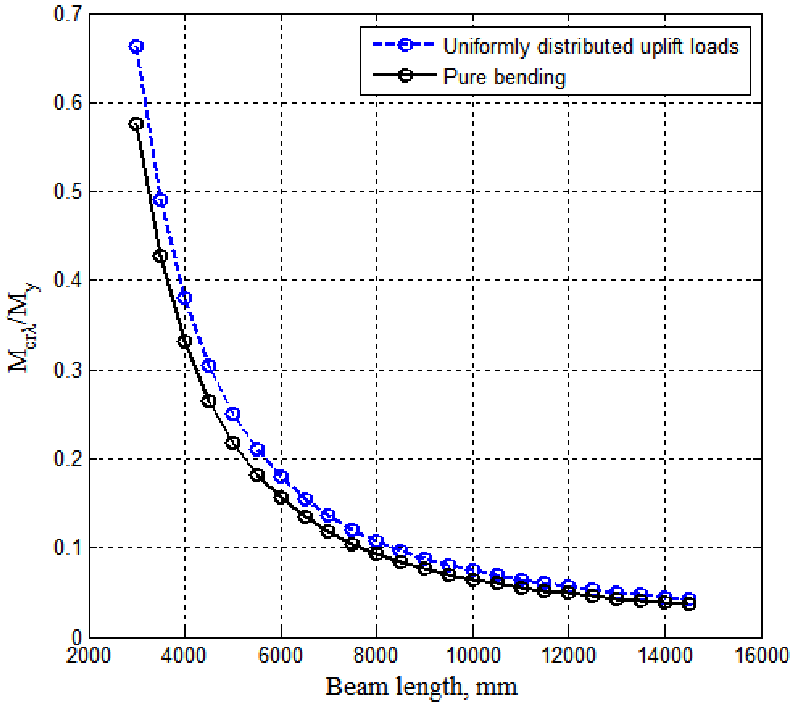

Figure 4.19 Comparisons of critical moments of lateral-torsional buckling of PCFS beams subject to uniformly distributed uplift load and pure bending (h=200 mm, b=70 mm, c= 20 mm, t=2 mm, d=100 mm)

4.3.3.3 Influence of the horizontal and rotational springs

Figure 4.20 compares the influence of lateral restraint on the critical moments of lateral-torsional buckling of PCFS beams subject to pure bending. It is interesting to notice that the effect of lateral displacement restraint at the tension end of web on the lateral-torsional buckling is limited for the pure bending. This is mainly because when the PCFS beam is subject to pure bending, it only deflects in the longitudinal direction before the lateral-torsional buckling occurs and hence the lateral restraint does not change the pre-buckling moment distribution. It is known that the lateral restraint affects the pre-buckling moment distributions and then provides influence on the lateral-torsional buckling rather than the buckling modes.

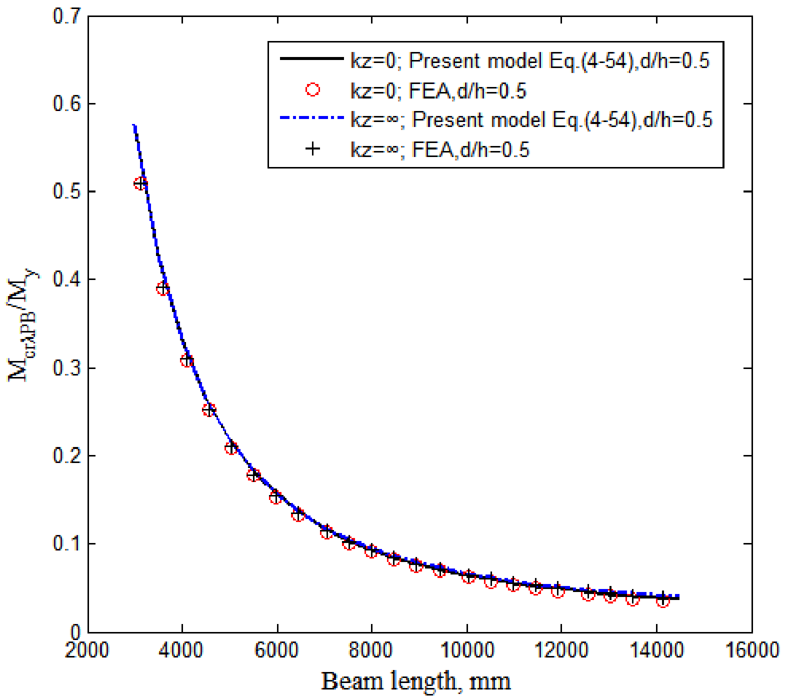

Figure 4.20 Comparisons of critical moments of lateral-torsional buckling for the laterally restrained and unrestrained PCFS beams subject to pure bending (k_ϕ=0, σ_y=390 MPa, h=200 mm, b=70 mm, c=20 mm, t=2 mm and d=100 mm)

The influence of spring stiffness on the critical moments of lateral-torsional buckling of a 6-meter-long PCFS beam subject to uniformly distributed uplift load was shown in Figure 4.21. It can be observed from Figure 4.21(a) that when the rotational spring stiffness was equal to zero (k_ϕ=0), the critical moment of lateral-torsional buckling slightly increased with the increase of horizontal spring stiffness in the range of $10^{-4} \leq k_z \leq 10$. Different from the beam subject to pure bending, the lateral restraint can help to increase the critical moment of lateral-torsional buckling when the PCFS beam subject to uniformly distributed uplift load.

In addition, when the horizontal spring stiffness was equal to zero ($k_z=0$), the critical moment of lateral-torsional buckling remarkably increased with the increase of rotational spring stiffness in the region that was larger than 0.1 ($k_\phi \geq 0.1$), as shown in Figure 4.21(b). It can be found that the rotational spring stiffness has more influence than the horizontal spring stiffness on the lateral-torsional buckling of PCFS beams.

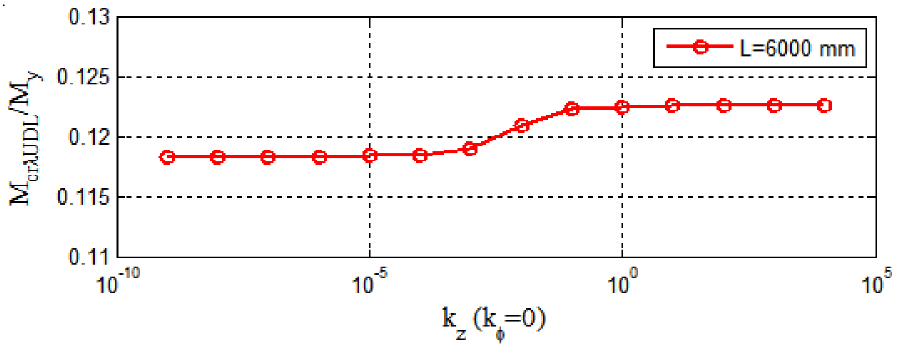

(a)

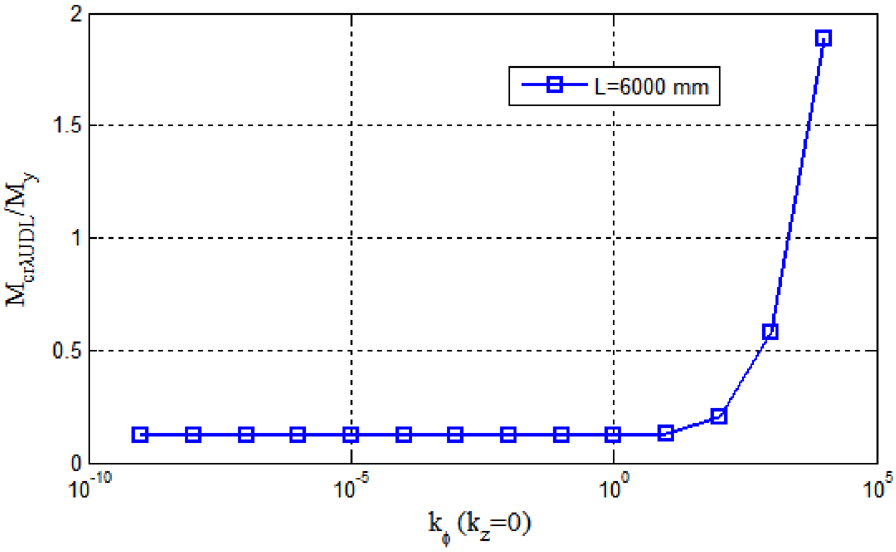

(b)

Figure 4.21 Influence of spring stiffness on the critical moments of lateral-torsional buckling of a 6-meter-long PCFS beam subject to uniformly distributed uplift load (σ_y=390 MPa, h=200 mm, b=70 mm, c= 20 mm, t=2 mm and d=100 mm)

4.4 Summary

In this chapter, theoretical expressions based on the energy method are developed and presented to predict the critical moments of lateral-torsional buckling of PCFS beams subject to pure bending and uniformly distributed uplift load. Eigenvalue buckling analysis performed by ANSYS is used to verify the proposed analytical model. According to the results from theoretical and numerical analyses, the following conclusions have been drawn.

- The critical moments of lateral-torsional buckling decrease as the diameter of circular holes increases for PCFS beams subject to the pure bending. The same happened when subject to the uniformly distributed uplift load.

- The restraint of sheeting on the PCFS beam can be simplified by a horizontal spring and a rotational spring which is very similar to the model proposed by Li (2004). The influence of web perforations on the lateral-torsional buckling can be evaluated by reducing the cross-sectional properties.

- For the beam length within 6000 mm, the critical moments of lateral-torsional buckling of PCFS beams subject to uniformly distributed uplift load are higher than those of the same beams subject to pure bending due to the moment gradient along the beam longitudinal direction.

- The lateral restraint at the tension end of the web can help to increase the critical moment of lateral-torsional buckling if the PCFS beam is subject to uniformly distributed uplift load. However, the influence of lateral restraint on the lateral-torsional buckling is negligible when the PCFS beam is subject to pure bending.

- The rotational spring stiffness has more influence than the horizontal spring stiffness on the critical moments of lateral-torsional buckling of the PCFS beams.

- The critical moments of lateral-torsional buckling determined by the present analytical solution can match well with the results obtained the ANSYS eigenvalue buckling analysis, demonstrating that the proposed analytical method is valuable for predicting the buckling loads of PCFS beams.

Chapter 5 — Numerical investigation on cold-formed steel built-up channel beams with web perforations

5.1 Introduction

The numerical investigation was performed by ANSYS to investigate the structural behaviour of CFS built-up beams with and without web perforations subject to four-point bending loads. Details of developing non-linear finite element models including geometry, element type, mesh density, boundary conditions, loading conditions, material non-linearity, contact non-linearity, initial geometric imperfections and solution algorithm are presented in this chapter.

Four-point bending tests of CFS built-up beams with or without web perforations conducted by Wang and Young (2015 and 2018) are used to validate against the proposed non-linear finite element models. The non-linear finite element modelling protocol reached from this chapter are used for the parametric study in Chapter 6.

5.2 Evaluation of existing experimental data

As mentioned in Section 1.3, the back-to-back CFS built-up beam with web perforations has higher capacity and stability comparing to the single PCFS beam, the self-tapping screws in the web can avoid the individual section failing by distortional or lateral-torsional buckling independently. However, the relevant research on the structural behaviour of CFS built-up beam with web perforations is limited in the literature.

Wang and Young (2015) carried out a total of 43 four-points bending tests to investigate the structural behaviour of CFS built-up open and closed section beams with circular web holes. The steel stiffening plates were bolted on the upper flanges and two sides of the web to transfer the load. To simulate the simply supported condition, half round and round bar were placed at the two ends, as shown in Figure 5.1.

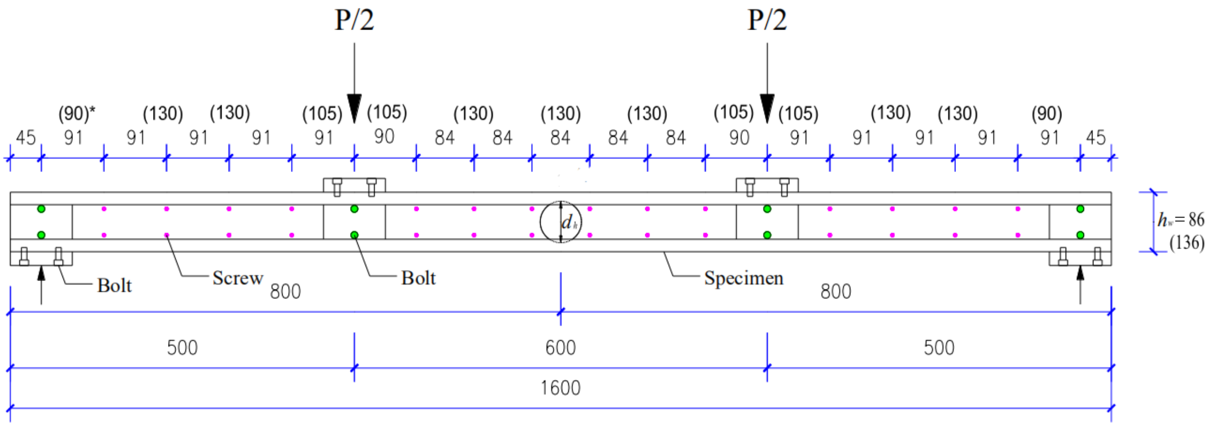

Figure 5.1 Loading rig for CFS built-up open section beams by Wang and Young (2015)

During the four-point bending tests, the servo-controlled hydraulic testing machine was employed to exert loads on the spread beam. Displacement control was adopted in the test by driving the hydraulic actuator at a constant rate of 0.5 mm/min, then the data acquisition system would record the applied loads and displacements at 1.5 second intervals. To obtain the moment-curvature curves, the hydraulic actuator stopped applying force for 90 seconds near the ultimate load.

Among all the specimens in the tests by Wang and Young (2015), the single circular hole was located in the mid-span and the ratio of hole diameter to web depth was ranging from 0.25 to 0.7. The screw spacing was about equal to the web depth of the cross section. Table 5.1 summarized the results of built-up open sections obtained from the four-point bending tests and finite element analysis by Wang and Young (2015).

The specimens were labeled based on the cross section of a CFS built-up beam with web perforations. For example, “OH0.25T0.42-86” represented that the CFS built-up open section (O) had a single hole (H) in the web, the ratio of hole diameter to web depth was 0.25, the thickness (T) of the cross section was 0.42 and the web depth of the cross section was 86 mm.

The buckling modes including i) flexural buckling (F) , ii) distortional buckling (D), iii) local buckling (L), iv) the interaction of distortional and flexural buckling (D+F) and v) the interaction of local, distortional and flexural buckling (D+L+F) observed in the tests and finite element analysis were also added in Table 5.1. The local buckling mainly occurred in the web or compressed flange, which has short half-wavelength buckling modes. The distortional buckling was identified as the rotation and translation of the compressed flange and lip. For some specimens, the interaction of different buckling modes were also observed in the post-buckling models, which have significant influence on the ultimate strength and failure mechanism.

Table 5.1 Summary of four-points bending tests for cold-formed steel built-up channel beam with web perforations by Wang and Young (2015)

Specimens	Tests		FEA		Comparison
	M_{EXP} (kN·mm)	Failure modes	M_{FEA} (kN·mm)	Failure modes	M_{EXP}/M_{FEA}
OH0.25T0.42-86	1108	D+L+F	1133	D+L+F	0.98
OH0.5T0.42-86	1062	D+L+F	1141	D+L+F	0.93
OH0.7T0.42-86	1017	D+L+F	1100	D+L+F	0.92
OH0.25T1.2-86	6993	D+L+F	6978	D+L+F	1.00
OH0.5T1.2-86	6820	D+L+F	6795	D+L+F	1.00
OH0.7T1.2-86	6295	D+L+F	6430	D+L+F	0.98
OH0.25T1.2-136	11603	D+L+F	12725	D+L+F	0.91
OH0.5T1.2-136	11807	D+L+F	12747	D+L+F	0.93

OH0.7T1.2-136	11031	D+L+F	11227	D+L+F	0.98
OH0.25T1.9-86	12217	D+F	12091	D+F	1.01
OH0.25T1.9-86R	12310	D+F	12091	D+F	1.02
OH0.5T1.9-86	12146	D+F	11895	D+F	1.02
OH0.7T1.9-86	11136	D+L+F	10809	D+F	1.03
OH0.25T1.9-136	22334	D+F	22471	D+F	0.99
OH0.5T1.9-136	21205	D+F	22038	D+F	0.96
OH0.7T1.9-136	19062	D+L+F	19866	D+F	0.96

Recently, Chen et al. (2021) conducted six four-point bending tests to explore the influence of hole spacing on the moment capacity of back-to-back CFS built-up channel with web perforations. The experimental data obtained from the bending test was summarized in Table 5.2, the label of the specimen involved the web depth, beam length and the hole types. For example, “B240-L4000-S100-UH1” means a CFS built-up (B) beam had one un-stiffened hole (UH1) in the web, the depth of web was 240 mm, the length of beam (L) was 4000 mm and the spacing of screws (S) was 100 mm.

Table 5.2 Summary of four-points bending test for built-up cold-formed steel channel beam with web perforations by Chen et al. (2021)

Specimens	Web depth d (mm)	Flange width b_f (mm)	Lip height b_l (mm)	Beam length L (mm)	Screw spacing s (mm)	Hole spacing a (mm)	Test $M_{EXP\cdot B}$ (kN·m)
B240-L4000-S100-UH1	240.9	45.0	14.6	4002	100	-	23.3
B240-L4000-S100-UH3	240.2	44.5	15.0	4001	100	100	22.3
B240-L4000-S100-UH5	239.6	45.0	15.6	4001	100	50	21.3
B240-L4000-S50-UH1	240.5	45.8	15.3	4000	50	-	23.9
B240-L4000-S50-UH3	238.9	46.1	14.5	4000	50	100	22.9
B240-L4000-S50-UH5	240.0	45.6	15.0	4001	50	50	22.0

Wang and Young (2018) undertook the experimental and numerical study on the structural behaviour of CFS built-up open and closed section beams with different screw arrangements. A total of 35 beams were tested under four-point loading to investigate the influence of screw spacing. It should be mentioned that the procedure of these experiment was the same as the previous test conducted by Wang and Young (2015).

The experimental and numerical results of CFS built-up open section beams were shown in Table 5.3, the label of the specimen was very similar to that in the previous test (Wang and Young, 2015). For example, "OT1.2-86-S75R1-R" represented that the CFS built-up open section beam (O) had a thickness of 1.2 mm (T) and web depth of 86 mm, the one row (R1) screw spacing (S) of 75 mm and the beam test was the repeated one (R). If the specimen had two rows of screws, none other symbols would be added in the label. Furthermore, the buckling modes including distortional buckling (D), local buckling (L) and the interaction of local and distortional buckling (D+L) occurred in the test and finite element analysis were also summarized in Table 5.3.

Table 5.3 Summary of four-points bending tests for cold-formed steel built-up channel beam (without web perforations) by Wang and Young (2018)

Specimens	Tests		FEA		Comparison
	M_{EXP} (kN·mm)	Failure modes	M_{FEA} (kN·mm)	Failure modes	M_{EXP}/M_{FEA}
OT0.42-86-S75	1206	D+L	1149	D+L	1.05
OT0.42-86-S75R1	1229	D+L	1150	D+L	1.07
OT0.42-86-S300	1222	D+L	1149	D+L	1.06
OT0.42-86-S300R	1160	D+L	1149	D+L	1.01
OT1.2-86-S75	7417	D+L	7159	D+L	1.04
OT1.2-86-S75R1	7303	D+L	7132	D+L	1.02
OT1.2-86-S75R1-R	7341	D+L	7132	D+L	1.03
OT1.2-86-S300	7030	D+L	7128	D+L	0.99
OT1.9-86-S75	12535	D	12129	D+L	1.03
OT1.9-86-S75R1	12528	D	12206	D+L	1.03
OT1.9-86-S300	12513	D	12224	D+L	1.02
OT1.2-136-S150	12240	D+L	12107	D+L	1.01
OT1.2-136-S150-R	12126	D+L	12107	D+L	1.00
OT1.2-136-S300	12240	D+L	12033	D+L	1.02
OT1.2-136-S600	12126	D+L	12248	D+L	0.99
OT1.9-136-S150	22796	D	22572	D+L	1.01
OT1.9-136-S300	22159	D	22643	D+L	0.98
OT1.9-136-S600	22750	D	22451	D	1.01

It can be observed from Table 5.3 that the influence of screw arrangements on the moment capacities of CFS built-up open section beams was not significant. When the screw spacing was larger than the distortional buckling half-wave length of a single CFS beam, the effect of screw arrangements on the ultimate load of CFS built-up open section beams could be ignored.

5.3 Nonlinear finite element modelling in ANSYS

It is known that non-linear finite element solution is effective for investigating the load-displacement response of CFS sections. In this section, the commercial software ANSYS was used to establish finite element models and carry out non-linear analysis for CFS built-up beams with web perforations. The non-linear finite element models including material non-linearity, geometric non-linearity and contact non-linearity were developed based on the four-point bending tests conducted by Wang and Young (2015 and 2018).

5.3.1 Geometry

The CFS built-up open section beam with web perforations was assembled by individual PCFS beams, the geometry and notations of the specimens in Wang and Young's test (Wang and Young, 2015) were shown in Figure 5.2. The web depth, flange width, lip length and thickness were defined as h_w, b_f, b_l and t, respectively. The screw spacing along the longitudinal axis was close to web depth and the vertical distance between the screw and flange was marked as e. The single circular hole was punched in the middle of the moment span and the ratio of hole diameter (d) to web depth (h_w) ranged from 0.25 to 0.7.

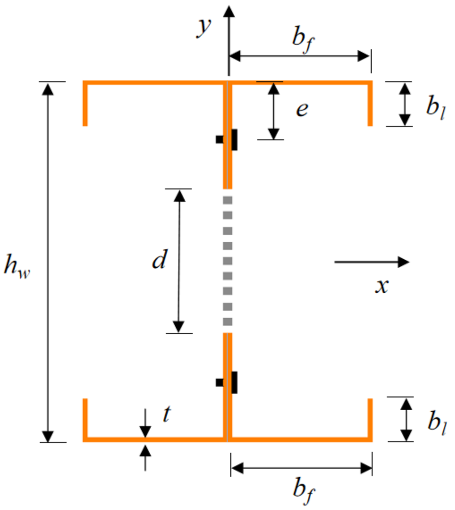

Figure 5.2 Geometry and notations in the CFS built-up beam with web perforations according to the four-point bending tests (Wang and Young, 2015)

5.3.2 Element type and mesh

The CFS built-up beam with web perforations were modeled with shell elements Shell 181, material non-linearity was embodied in the finite element models by using the bilinear isotropic hardening material model with the assumption of von Mises yield criterion. The material properties of cold-formed steel involving Young's modulus and yield stress were obtained from the tensile coupon tests (Wang and Young, 2015), Poisson's ratio was taken as 0.3. Table 5.4 summarized Young's modulus and yield stress of coupon specimens (plate thicknesses of 0.42, 1.2 and 1.9) in Wang and Young's tensile coupon tests.

Table 5.4 Material properties obtained from the tensile coupon tests (Wang and Young, 2015)

Coupon specimens	Young's modulus (GPa)	Yield stress (MPa)
OT0.42-86	220	662
OT1.2-86	213	577
OT1.2-136	213	578
OT1.9-86	201	486
OT1.9-136	199	484

Based on the mesh sensitivity analysis, two types of meshes were employed in the finite element models (i.e. coarse mesh with element size of 10×10 mm was used in the region away from the perforation and fine mesh with element size of 2×2 mm was used around the perforation). A typical finite element mesh of the CFS built-up beam with web perforations was shown in Figure 5.3.

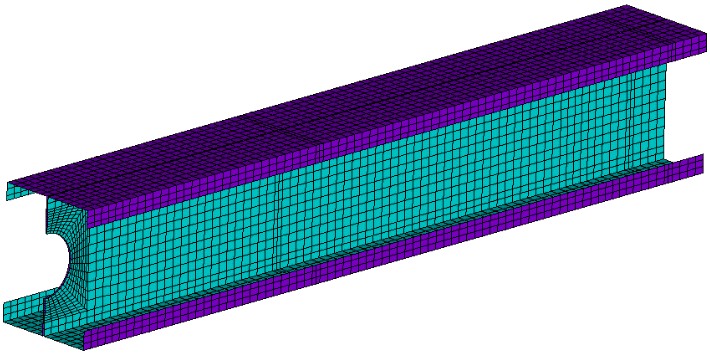

Figure 5.3 Typical finite element meshes of the CFS built-up beam with web perforations (Specimen OH0.5T1.9-136)

5.3.3 Boundary and loading conditions

Similar to the numerical models in Wang and Young's research (Wang and Young, 2015), only half-span of the CFS built-up beam with web perforations was created using the symmetric property in the present non-linear finite element analysis so that the computational time could be saved.

The simply support boundary conditions were attributed to the reference point 1 at the position of round bar, the translation in the x and y directions and the rotation about the z-axis were constrained (UX=UY=ROTZ=0), the symmetric boundary conditions were applied at the end nodes of mid-span of the beam (ZSYM=0, UZ=ROTX=ROTY=0), as shown in Figure 5.4.

In Wang and Young's tests (Wang and Young, 2015), the load was applied through the load bearing plates. Hence, the contact area between the load bearing plates and top flange/web of the beam was modeled as coupling constraints, these reinforced regions were coupled with the reference point 2 in all degrees of freedoms (see Figure 5.5). In this way, the motion of multiple points can be simplified to the motion of a single point, then the load was applied to the reference point 2 in the numerical analysis.

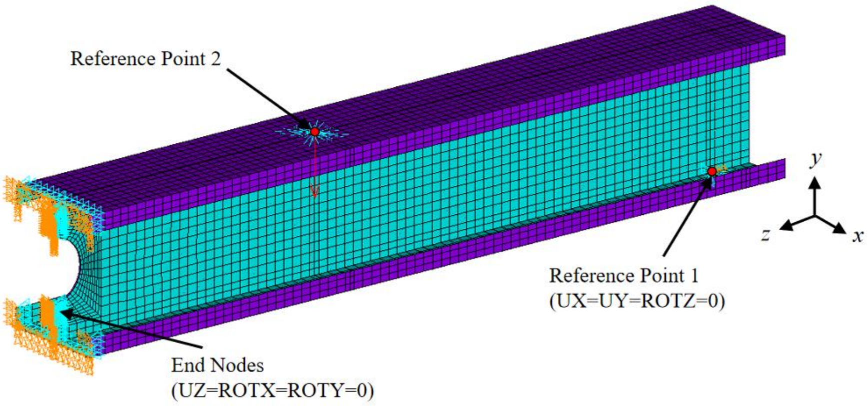

Figure 5.4 Boundary and loading conditions of a CFS built-up beam with web perforations under four-point bending (Specimen OH0.5T1.9-136)

5.3.4 Contact of webs and constraint of screws

The interaction between the contacted webs of the CFS built-up beam with web perforations were defined as surface-to-surface contact pairs. The web of a PCFS beam was considered as the master surface, whereas the web of other PCFS beam was considered as the slave surface. Enhanced Lagrange algorithm was used to establish the relationship of the contact pairs in the normal direction. Hence, the separation of the contact pairs was allowed when the tension force occurred but the penetration of the contact pairs was prohibited in the finite element models. Furthermore, the contact property was defined as friction-less in the tangential direction.

Several studies have reported the relevant approaches on modelling the screws. For example, Lim and Nethercot (2003) used the simplified bolt model which consisted of two perpendicular nonlinear springs to simulate the behaviour of self-tapping screws. Liu et al. (2015) used the solid brick element and surface-to-surface contact interaction to model the bolt behaviour. It should be pointed out that in present study the strength of self-tapping screws was plenty of times higher than the cold-formed steel and the CFS built-up beam with web perforations usually failed before the destruction of screws during the tests. In the present finite element models, multi-point constraint beam connector elements MPC 184 were used to stimulate the self-tapping screws, which was similar to the method presented by Ye et al. (2018b). The nodes at the position of screws on the contact pairs were connected by MPC 184 so that the node pairs would have the same degrees of freedom.

5.3.5 Initial geometric imperfections

The initial geometric imperfections of the specimens were always formed in the process of manufacturing and transportation. The value of initial geometric imperfections might affect the accuracy of the non-linear finite element analysis. To incorporate the initial geometric imperfections into the finite element model, eigenvalue buckling analysis of the CFS built-up beam with web perforations was performed to determine the elastic buckling modes. The lowest buckling mode was used as the shape of imperfect geometries and then multiplied by the values obtained from experimental measurement. In Wang and Young's tests (Wang and Young, 2015), the maximum measured geometric imperfections were 0.294, 0.424 and 0.542 mm for the specimens with thicknesses of 0.42, 1.2, 1.9 mm which were employed in the non-linear finite element analysis in this chapter.

It is known that the presence of geometric imperfections has a significant influence on the post-buckling behaviour of CFS sections, especially when the interaction of different buckling modes is taken into account (Ye et al., 2018a). Schafer and Peköz (1998) proposed the cumulative function value to determine the magnitudes of the local and distortional buckling imperfections with the value of 0.34t and 0.94t, respectively. The global buckling imperfection magnitude was chosen as L/1500. In Euro code, the local buckling imperfection magnitude was recommended as 0.4t for the CFS sections, whereas the global buckling imperfection magnitude was given as L/400 for the hot rolled steel beams.

For the parametric study presented in Chapter 6, the local buckling imperfection magnitude was taken as 0.5t, which has been verified to be reasonable by Wang and Young (2015). The global buckling imperfection magnitude was chosen as L/1000, which has been used as the maximum value for CFS flexural members (Kankanamge and Mahendran, 2012).

5.3.6 Non-linear solution

It is well known that the arc-length method (or the modified RIKS method) is a powerful tool for solving nonlinear equation of the systems and can predict the post-buckling behaviour of CFS built-up beams with web perforations. Two general static steps were performed for the nonlinear solution, eigenvalue buckling analysis was first conducted to obtain the geometric imperfections, nonlinear modified RIKS method was then employed to determine the ultimate load.

The post-peak equilibrium paths in modified RIKS method are sensitive to the loading method in which the load-controlled method was loaded with a concentrated load at the reference point 2 and the displacement-controlled method was loaded with imposed displacement at the reference point 2.

Figure 5.5 compares the moment-curvature curves obtained from load-controlled method, displacement-controlled method and experimental data. It can be found in the figure that the tendency of the three curves is identical before the peak load occurs. The load-controlled method can find the peak load but terminates quickly due to the convergence problem. The displacement-controlled method can predict the peak load and find the post-peak equilibrium path before terminating which is similar the experimental curve. Therefore, the displacement-controlled method was selected for the non-linear analysis of the following parametric study.

In the present study, a small displacement was first applied at the reference point 2 to generate the contact relationship between the master surface and slave surface. Then the full displacement was applied until the CFS built-up beam failed. The automatic stabilization algorithm was employed in the non-linear solution to help to overcome the convergence issues.

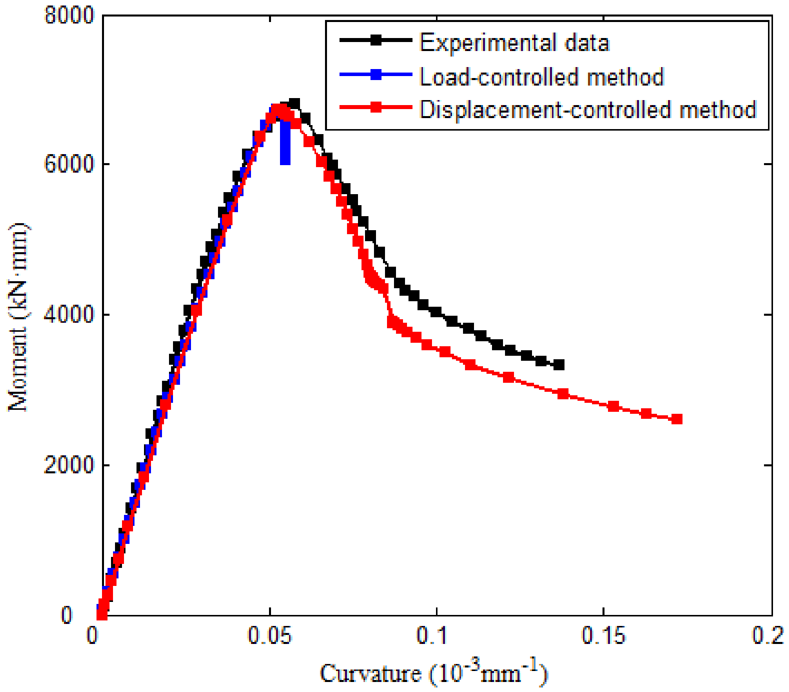

Figure 5.5 Comparisons of moment-curvature curves obtained from load-controlled method, displacement-controlled method and experimental data (Specimen OH0.5T1.2-86)

5.4 Verification of the finite element models

As mentioned in Section 5.2, Chen's tests (Chen et al., 2021) mainly focused on the influence of edge-stiffened and un-stiffened holes on the moment capacity of CFS built-up beams with web perforations. In addition, the specimens in Chen's tests failed due to the distortional buckling and the relevant experimental data cannot cover all cases. Hence, in this section, Wang and Young's tests (Wang and Young, 2015; Wang and Young, 2018) were used to validate against the nonlinear finite element models built in Section 5.3.

5.4.1 CFS built-up beams with web perforations

The comparisons of FEA results and experimental data obtained from four-point bending tests (Wang and Young, 2015) for CFS built-up beams with web perforations were shown in Table 5.5. The mean value of the experiment-to-FEA moment ratio ($M_{\mathrm{EXP}}/M_{\mathrm{FEA}}$) is 0.99 with corresponding coefficient of variation (COV) of 0.032 which proved that the proposed finite element models can predict the ultimate moment capacity of CFS built-up beams with web perforations well.

Table 5.5 Comparisons of FEA results against experimental data (Wang and Young, 2015) for CFS built-up beams with web perforations

Specimens	Tests		FEA		Comparison
	M_{EXP} (kN·mm)	Failure modes	M_{FEA} (kN·mm)	Failure modes	$M_{\mathrm{EXP}}/M_{\mathrm{FEA}}$
OH0.25T0.42-86	1108	D+L+F	1098	D+L+F	1.01
OH0.5T0.42-86	1062	D+L+F	1086	D+L+F	0.98
OH0.7T0.42-86	1017	D+L+F	1073	D+L+F	0.95
OH0.25T1.2-86	6993	D+L+F	6927	D+L+F	1.01
OH0.5T1.2-86	6820	D+L+F	6730	D+L+F	1.01
OH0.7T1.2-86	6295	D+L+F	6257	D+L+F	1.01
OH0.25T1.2-136	11603	D+L+F	12633	D+L+F	0.92
OH0.5T1.2-136	11807	D+L+F	12328	D+L+F	0.96
OH0.7T1.2-136	11031	D+L+F	11376	D+L+F	0.97
OH0.25T1.9-86	12217	D+F	12173	D+F	1.00
OH0.5T1.9-86	12146	D+F	11917	D+F	1.02
OH0.7T1.9-86	11136	D+L+F	10795	D+F	1.03
OH0.25T1.9-136	22334	D+F	21406	D+F	1.04
OH0.5T1.9-136	21205	D+F	21278	D+F	1.00
OH0.7T1.9-136	19062	D+L+F	19522	D+F	0.98
Mean					0.99
COV					0.032

The comparisons of moment-curvature curves for CFS built-up beams with web perforations (Specimen OH0.7T1.9-86, Specimen OH0.25T1.9-86 and Specimen OH0.5T1.9-136) obtained from experimental data (Wang and Young, 2015), FEA performed by ANSYS and FEA performed by ABAQUS (Wang and Young, 2015) were plotted in Figure 5.6. It can be observed from the figure that, both FEA curves match the peak load and initial stiffness very well with the experimental results. There are some differences between the predictions and test results in terms of the post-buckling behaviour. The reason for this could be due to the differences in the initial geometric imperfections and/or in the material properties (e.g., the residual stress and variation in yielding strength in the tested specimens caused by cold forming process). Nevertheless, since our interest is to obtain the ultimate failure moment of CFS built-up beams with web perforations, the accuracy of the peak point in the FEA predicted curves is most important to us.

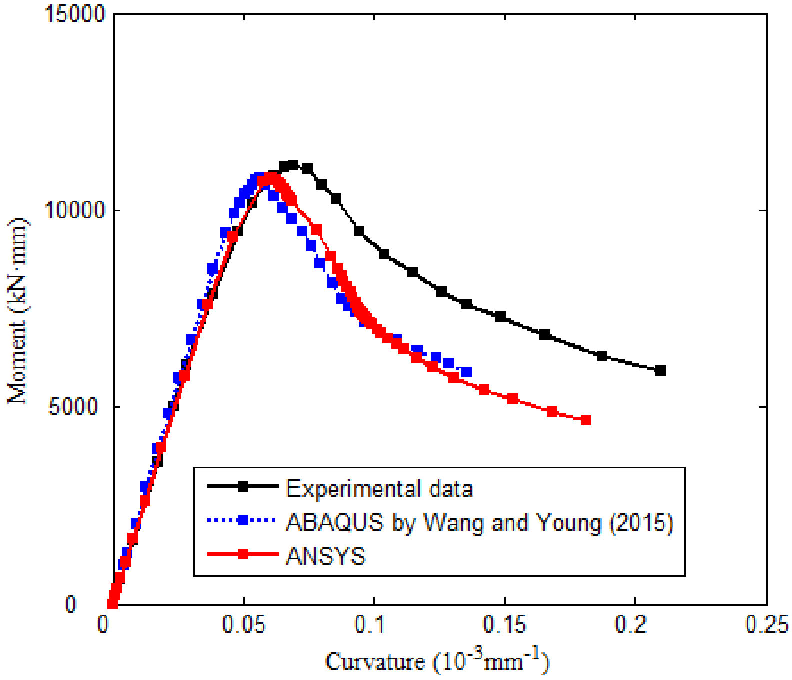

(a) Specimen OH0.7T1.9-86

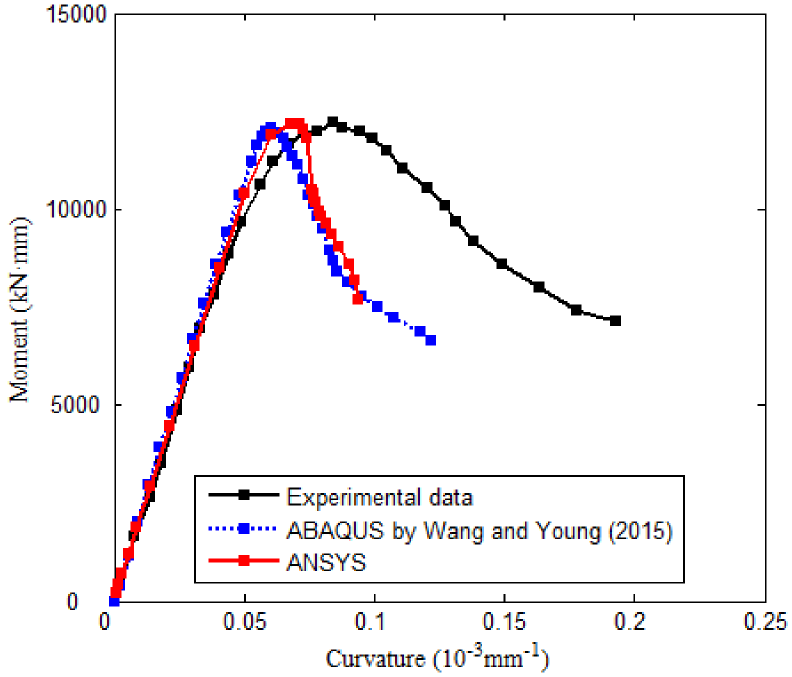

(b) Specimen OH0.25T1.9-86

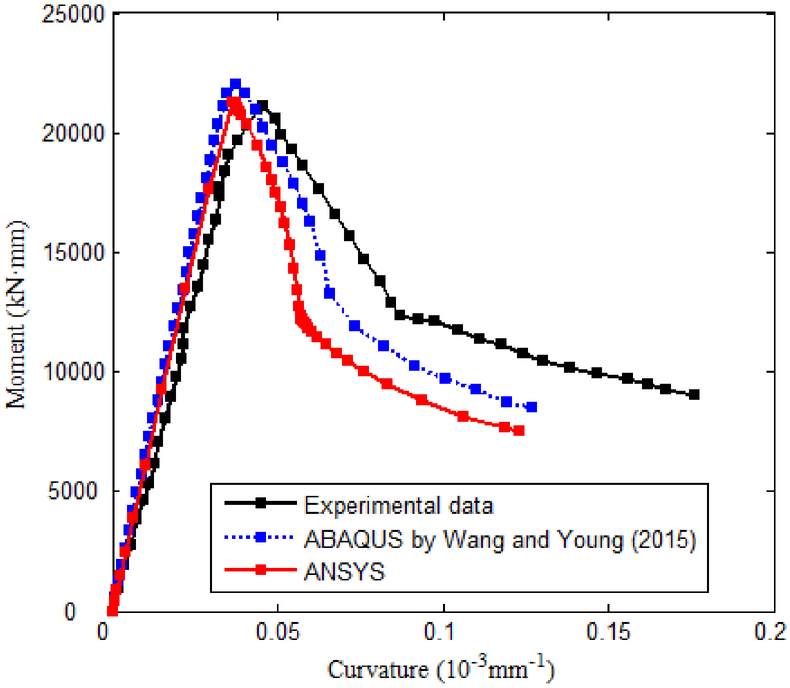

(c) Specimen OH0.5T1.9-136

Figure 5.6 Comparisons of moment-curvature curves of CFS built-up beams with web perforations obtained from test, ABAQUS and ANSYS (Wang and Young, 2015)

The typical deformed shapes of CFS built-up beams with web perforations obtained from the non-linear finite element analysis were compared to the deformed shapes occurred in the four-point bending tests (Wang and Young, 2015) as shown in Figure 5.7 for Specimen OH0.7T1.9-86, Specimen OH0.25T1.9-86 and Specimen OH0.5T1.9-136. As expected, in most cases, the deflected shapes obtained from numerical and experimental investigations were analogous after the collapse of the beams.

For Specimen OH0.7T1.9-86, the failure modes observed in the tests involved local buckling, distortional buckling, flexural buckling and the interaction of two buckling modes. However, this specimen failed by distortional buckling and the local buckling cannot be observed in the non-linear finite element analysis. Nevertheless, this influence was negligible to determine the moment capacity. Most deformed shapes obtained from numerical investigations matched well with the experimental results. Hence, the present finite element models were capable for demonstrating the structural behaviour of CFS built-up beams with web perforations under four-point bending loads.

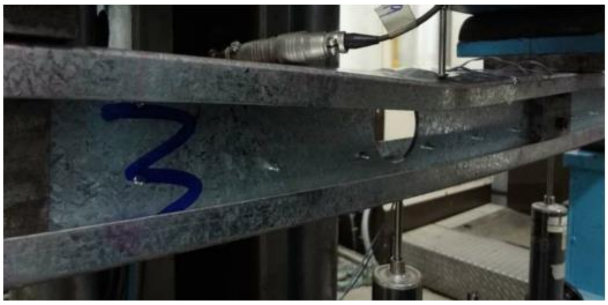

Test

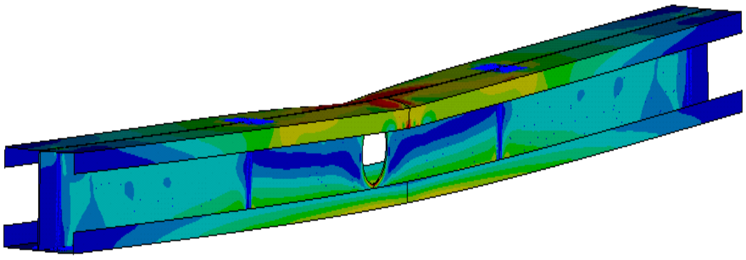

FEA

(a) Specimen OH0.7T1.9-86

Test

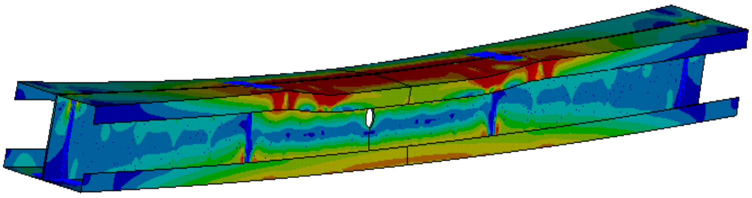

FEA

(b) Specimen OH0.25T1.9-86

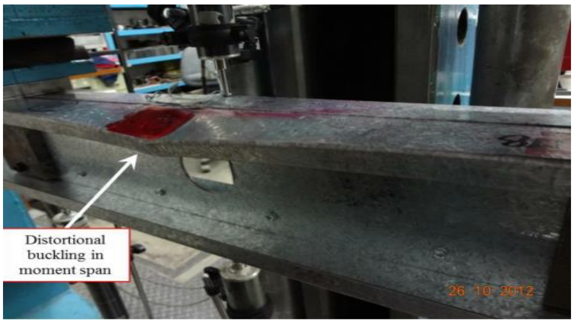

Test

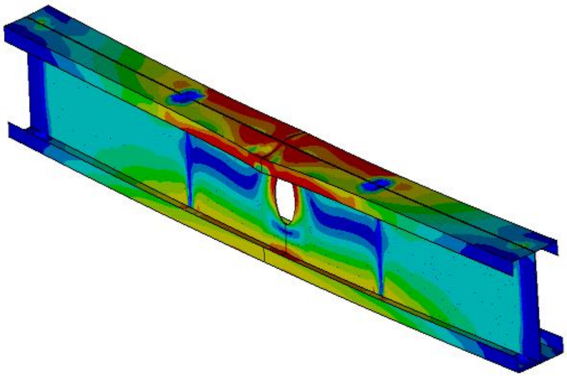

FEA

(c) Specimen OH0.5T1.9-136

Figure 5.7 Typical deformed shapes of CFS built-up beams with web perforations obtained from four-point bending tests (Wang and Young, 2015) and FEA

5.4.2 CFS built-up beams

As mentioned in Section 5.2, Wang and Young (2018) conducted the four-point bending tests to investigate the influence of screw arrangements on the structural behaviour of CFS built-up beams. The experimental processes were the same as those in Section 5.4.1, the only difference was that no perforations punched in the web for the specimens in the present tests. Therefore, the experimental results can be used to validate the proposed non-linear finite element modelling method.

It should be mentioned here that the methodology used in the finite element model (i.e. finite-element type, mesh density, initial geometric imperfection, solution algorithm, material and contact non-linearity) is similar to that described in Section 5.4.1, and thus is not explained further. The comparisons between FEA results and experimental data obtained from four-point bending tests (Wang and Young, 2018) for CFS built-up beams were reported in Table 5.6. It can be found that the mean value of the experiment-to-FEA moment ratio ($M_{\mathrm{EXP}}/M_{\mathrm{FEA}}$) was 1.02 and the corresponding coefficient of variation (COV) was 0.033.

Table 5.6 Comparisons of FEA results against experimental data (Wang and Young, 2018) for CFS built-up beams

Specimens	Tests		FEA		Comparison
	M_{EXP} (kN·mm)	Failure modes	M_{FEA} (kN·mm)	Failure modes	$M_{\mathrm{EXP}}/M_{\mathrm{FEA}}$
OT0.42-86-S75	1206	D+L	1167	D+L+F	1.03
OT0.42-86-S300	1222	D+L	1153	D+L+F	1.06
OT1.2-86-S75	7417	D+L	7069	D+L+F	1.00
OT1.2-86-S300	7030	D+L	7014	D+L+F	0.99
OT1.9-86-S75	12535	D	12166	D+F	1.03
OT1.9-86-S300	12513	D	12207	D+F	1.03
OT1.2-136-S150	12240	D+L	12236	D+L+F	1.00
OT1.2-136-S300	12240	D+L	12284	D+L+F	1.00
OT1.2-136-S600	12126	D+L	12584	D+L+F	0.96
OT1.9-136-S150	22796	D	21348	D+F	1.07
OT1.9-136-S300	22159	D	21361	D+F	1.04
OT1.9-136-S600	22750	D	21384	D+F	1.06
Mean					1.02
COV					0.033

The finite element analysis results for moment-curvature curves and deformed shapes of specimen OT1.9-136-S300 were shown in Figure 5.8 and Figure 5.9, respectively. It can be seen from the figures that the moment-curvature curves obtained from experimental data (Wang and Young, 2018), FEA performed by ANSYS and FEA performed by ABAQUS (Wang and Young, 2018) were in good agreement for the peak load, the deformed shapes observed from the experiment presented a good match with the FEA results which indicating that the proposed non-linear finite element modelling method was reliable for predicting the ultimate failure moment of CFS built-up sections.

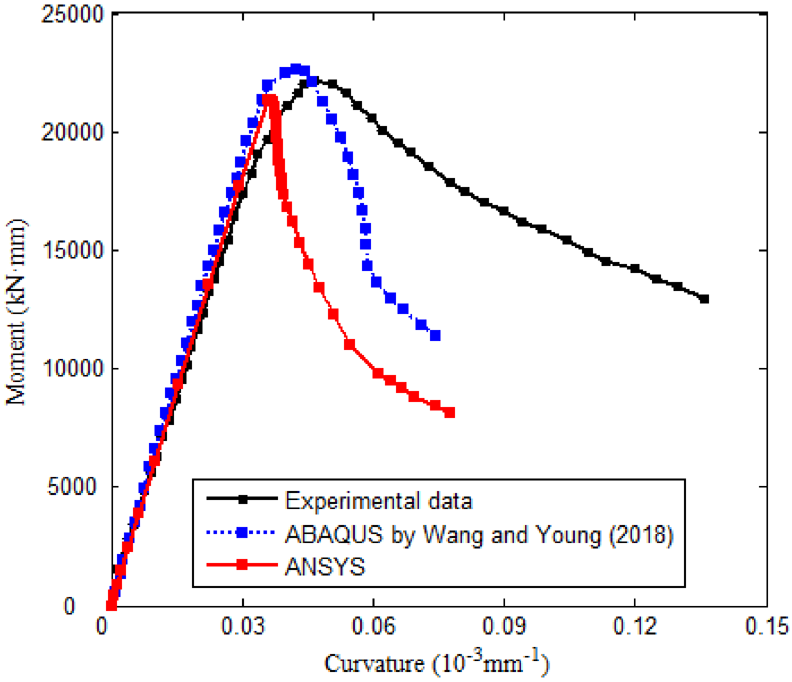

Figure 5.8 Comparisons of moment-curvature curves of CFS built-up beams obtained from test, ABAQUS and ANSYS (Specimen: OT1.9-136-S300) (Wang and Young, 2018)

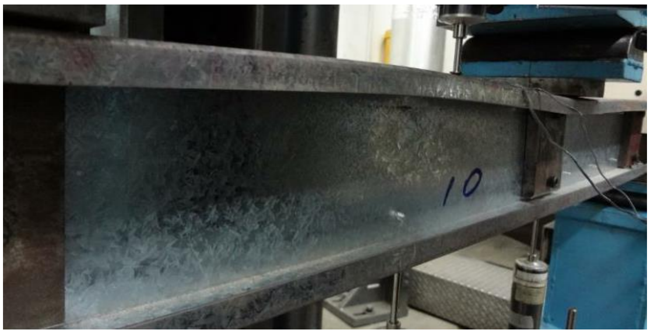

(a) Test

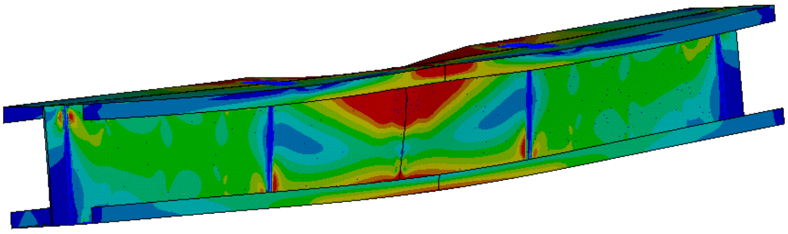

(b) FEA

Figure 5.9 Typical deformed shapes of CFS built-up beams obtained from four-point bending tests (Wang and Young, 2018) and FEA (Specimen OT1.9-136-S300)

5.5 Summary

Finite element analysis of simply supported CFS built-up beams with and without web perforations subject to four-point bending loads has been performed by commercial software ANSYS in this chapter. The influences of initial geometric imperfection, solution algorithm, material and contact non-linearity are investigated. It was found that the displacement-controlled method was more suitable for the non-linear solution due to the convergence issues. The comparison of FEA results and experimental data obtained from four-point bending tests (Wang and Young, 2015; Wang and Young, 2018) proved that the present finite element models were capable to predict the moment capacity of CFS built-up beams with or without web perforations and the proposed non-linear finite element modelling protocol was reliable for the extended parametric study.

Chapter 6 — Proposed design rule for cold-formed steel built-up channel beams with web perforations

6.1 Introduction

The structural behaviour including failure modes and moment capacities of CFS built-up beams with web perforations subject to pure bending have been investigated in this chapter. The non-linear finite element modelling protocol developed in Chapter 5 is employed for the numerical investigations.

The non-linear FEA models are parameterized by APDL language for the parametric study. The influences of screw spacing, hole sizes, hole spacing and slenderness ratio on the moment capacities of CFS built-up beams with web perforations are evaluated.

The verified FEA results obtained from parametric study are merged with analytical models for elastic buckling presented in Chapter 3 and Chapter 4 to modify the existing DSM prediction curves for the failure modes controlled by local buckling, distortional buckling and lateral-torsional buckling. The final modified DSM formulae is proposed for the design of CFS built-up beams with web perforations.

6.2 Numerical examples

The non-linear finite element models described in Chapter 5 can closely demonstrate the structural behaviour of CFS built-up beams with web perforations and predict the relevant moment capacities. However, the specimens selected from the four-point bending tests (Wang and Young, 2015; Wang and Young, 2018) only involved single circular hole in the mid-span of beams. In this section, multiple perforations with various hole sizes and spacing were punched in the webs of beams and the non-linear finite element modelling protocol proposed in Chapter 5 was used to build the numerical models for the parametric study.

6.2.1 Specimen labelling

To identify the cross-sectional properties of the CFS built-up beams with web perforations, the specimens in the parametric study were labelled based on the web height, beam length, cross-section thickness, screw spacing, distance between two adjacent holes and ratio of the diameter of the circular hole to web height as shown in Figure 6.1(a).

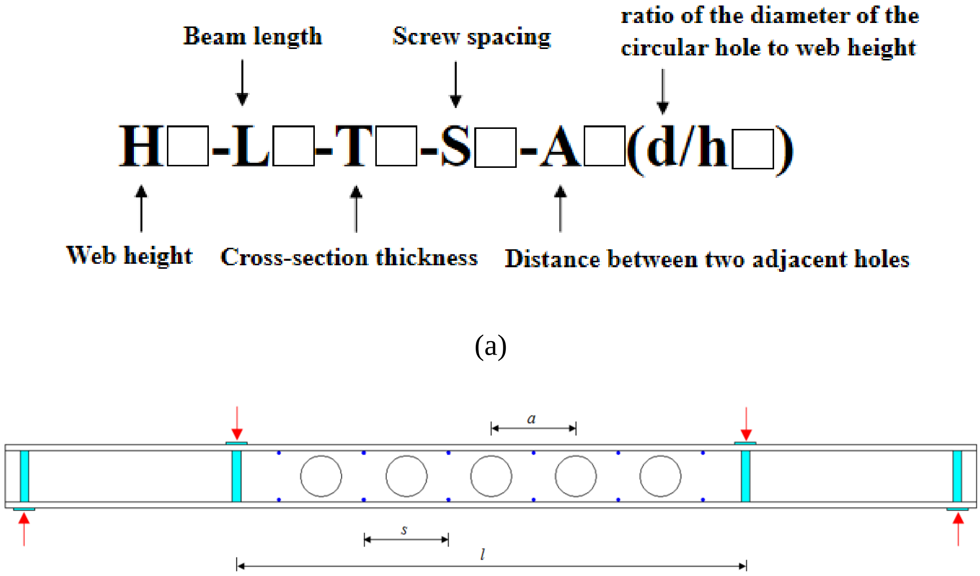

(a)

(b)

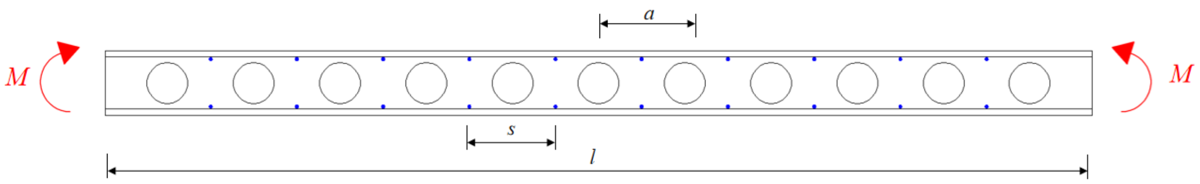

(c)

Figure 6.1 Specimens in the parametric study (a) Labelling rule (b) Four-point bending load for local and distortional buckling (c) Pure bending for lateral-torsional buckling

For example, the label “H150-L2000-T2-S300-A300(d/h0.5)” can be interpreted as the single piece of the specimen has web height (H) of 150 mm, beam length (L) of 2000 mm and cross-section thickness (T) of 2 mm. The screw spacing of the specimen (S) is 300 mm, the distance between two adjacent holes (A) is 300 and the ratio of the diameter of the circular hole to web height (d/h) is 0.5.

It is worth noting that if the beam failed by the local or distortional buckling (i.e., the mid-span length is longer than the half-wavelength of the buckling mode), the four-point bending load is able to simulate the pure bending, in which case the beam length is the length of the pure bending span of the four-point bending beam (see Figure 6.1(b)). However, if the beam failed by the lateral-torsional buckling (i.e., the half-wavelength is longer than mid-span length), the beam with four-point bending load will be different from the beam with pure bending. This is simply because they have different bending moment diagrams. Hence, in the following the uniform bending moment at two ends was used to represent the pure bending for the specimens controlled by the lateral-torsional buckling (see Figure 6.1(c)).

6.2.2 Results and discussion

The moment-curvature curves and deformed shapes of three typical specimens (H200-L1200-T1.4-S200-A300(d/h0.25), H300-L1200-T2.4-S300-A300(d/h0.5) and H150-L4000-T1.8-S150-A300(d/h0.65)) which controlled by local buckling, distortional buckling and lateral-torsional buckling were shown in Figure 6.2, Figure 6.3 and Figure 6.4, respectively. It should be mentioned that the finite element models adopted here are mainly purposed for the prediction of ultimate failure load not for the post-buckling behavior prediction as already explained in Section 5.4.1.

It can be found in the figures that the local buckling and distortional buckling controlled in cases of short and intermediate built-up beams. The single PCFS channels buckled separately and independently when the CFS built-up beams with web perforations controlled by local buckling or distortional buckling. However, in the longer and slender built-up beams, the lateral-torsional buckling became more obvious before the peak loads occurred. Unlike the cases that controlled by local buckling or distortional buckling, the built-up beam buckle as a whole and the single PCFS channels did not buckle alone when the CFS built-up beams with web perforations controlled by lateral-torsional buckling.

The details of prediction results of ultimate moments of CFS built-up beams with web perforations failed by local buckling, distortional buckling, lateral-torsional buckling or the combination of the above buckling modes obtained from the nonlinear finite element analysis were listed in Appendix E.

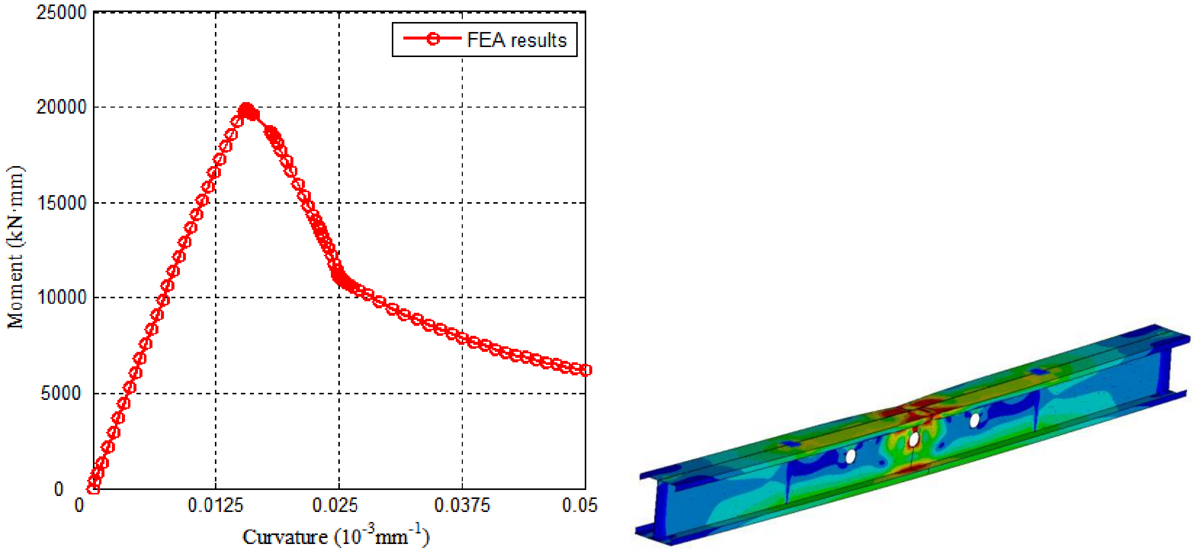

(a) (b)

Figure 6.2 Nonlinear FEA results of the CFS built-up beam with web perforations controlled by local buckling (H200-L1200-T1.4-S200-A300(d/h0.25)) (a) moment-curvature curve (b) deformed shape

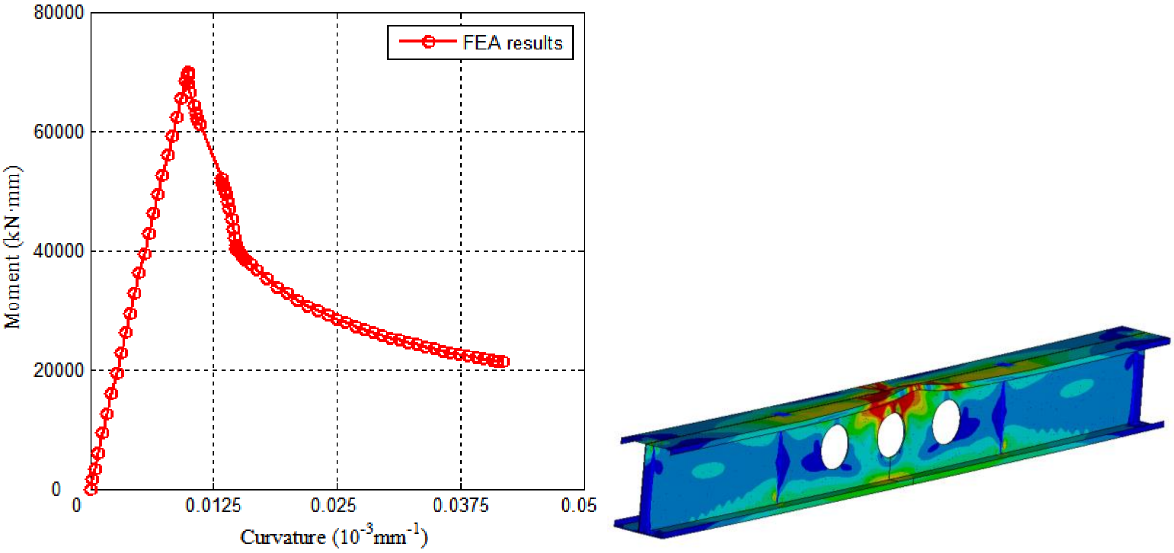

(a) (b)

Figure 6.3 Nonlinear FEA results of the CFS built-up beam with web perforations controlled by distortional buckling (H300-L1200-T2.4-S300-A300(d/h0.5)) (a) moment-curvature curve (b) deformed shape

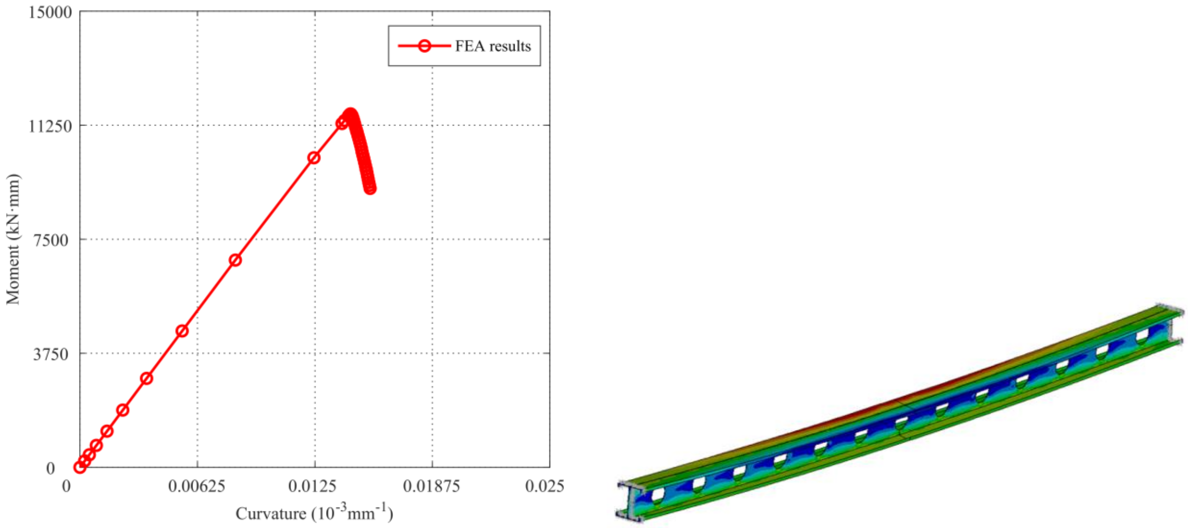

(a) (b)

Figure 6.4 Nonlinear FEA results of the CFS built-up beam with web perforations controlled by lateral-torsional buckling (H150-L4000-T1.8-S150-A300(d/h0.65)) (a) moment-curvature curve (b) deformed shape

6.3 Parametric study

The finite element parametric study comprising 398 CFS built-up beams with various beam length, cross-section profiles, screw arrangements, hole sizes and spacing was carried out to extend the current DSM design equations. The cross-section profiles include large (h=300 mm, b=100 mm and c=20 mm), medium (h=200 mm, b=75 mm and c=20 mm) and small (h=150 mm, b=65 mm and c=15 mm) sections, the beam length ranges from 1200 mm to 6000 mm, the screw arrangement ranges from 50 mm to 4000 mm, the ratio of diameter of the circular hole to web height ranges from 0.25 to 0.8 and the distance between two adjacent holes ranges from 150 mm to 450 mm. The material properties of the specimen including yield stress, Young's modulus and Poisson's ratio in the parametric study were selected as 390 MPa, 2.05 GPa and 0.3 respectively.

6.3.1 Influence of screw arrangement

The ultimate moment capacities of 1.2-meter-long CFS built-up beams with web perforations controlled by the distortional buckling obtained from FEA were compared for different screw arrangements and are plotted in Figure 6.5. It can be seen that when the screw spacing ranged from 50 mm to 1200 mm, the influence of screw spacing on the ultimate failure moment of the beam was negligible (see Figure 6.5(a) for the specimens H150-L1200-T1.4-A300(d/h0.5), Figure 6.5(b) for the specimens H200-L1200-T1.4-A300(d/h0.5), and Figure 6.5(c) for the specimens H300-L1200-T1.4-A300(d/h0.5)). This is because the screws on the webs of the CFS built-up beams with web perforations had little restraint on the compressed flange/lip system and hence the effects of the screws on the distortional buckling behaviour were limited.

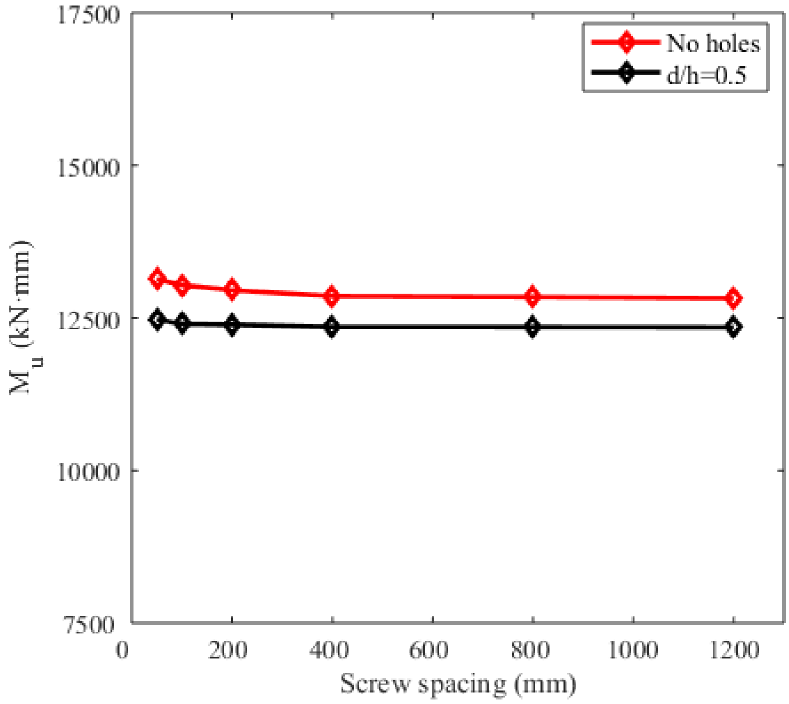

(a) h=150 mm, b=65 mm, c=15mm, t=1.4 mm and a=300 mm

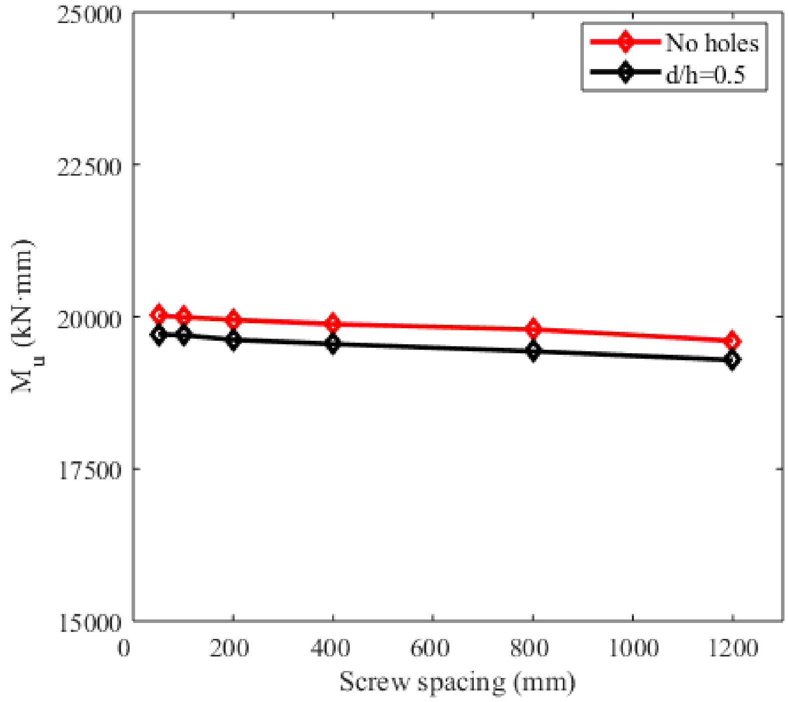

(b) h=200 mm, b=75 mm, c=20 mm, t=1.4 mm and a=300 mm

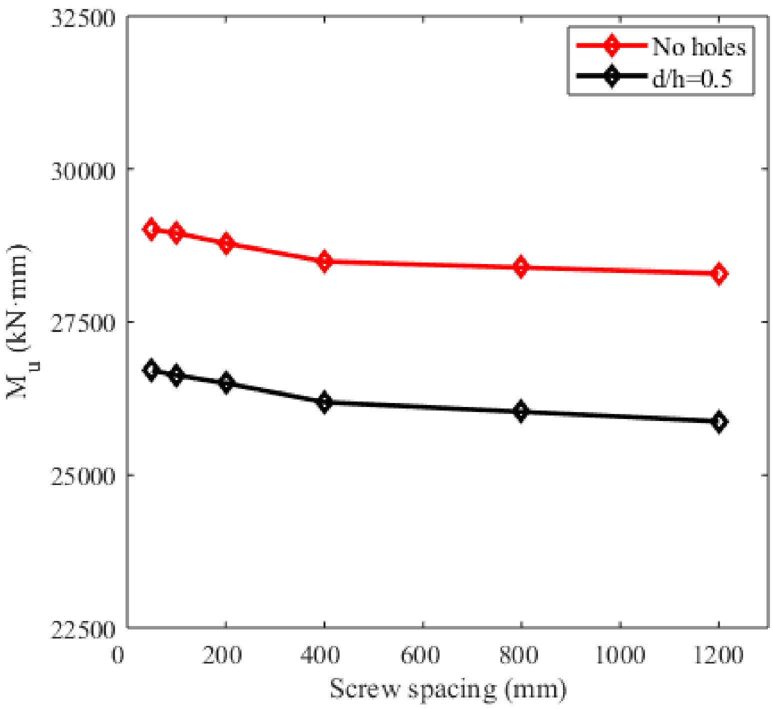

(c) h=300 mm, b=100 mm, c=20 mm, t=1.4 mm and a=300 mm

Figure 6.5 Ultimate moment curves of 1.2-meter-long CFS built-up beams with web perforations in different screw arrangements obtained from FEA

Figure 6.6 demonstrates the ultimate moment capacities of 4-meter-long CFS built-up beams with web perforations controlled by the lateral-torsional buckling in different screw arrangements, where Figure 6.6(a) is for the specimens H150-L4000-T1.6-A300(d/h0.5) and Figure 6.6(b) is for the specimens H200-L4000-T1.6-A300(d/h0.5). It can be observed from the figure that the ultimate failure moment decreased with the increase of screw spacing. When the screw spacing increased from 50 mm to 4000 mm, the ultimate failure moment of the specimen H150-L4000-T1.6-A300(d/h0.5) had 46% reduction. The reason is that for the longer beam failed by lateral-torsional buckling, the screw can enhance the composite action of two single beams and then increase the ultimate failure moment.

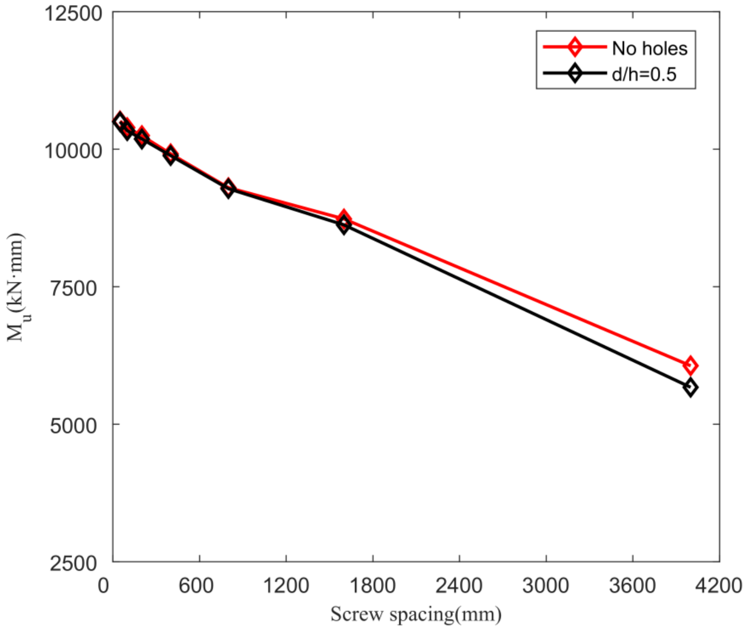

(a) h=150 mm, b=65 mm, c=15mm, t=1.6 mm and a=300 mm

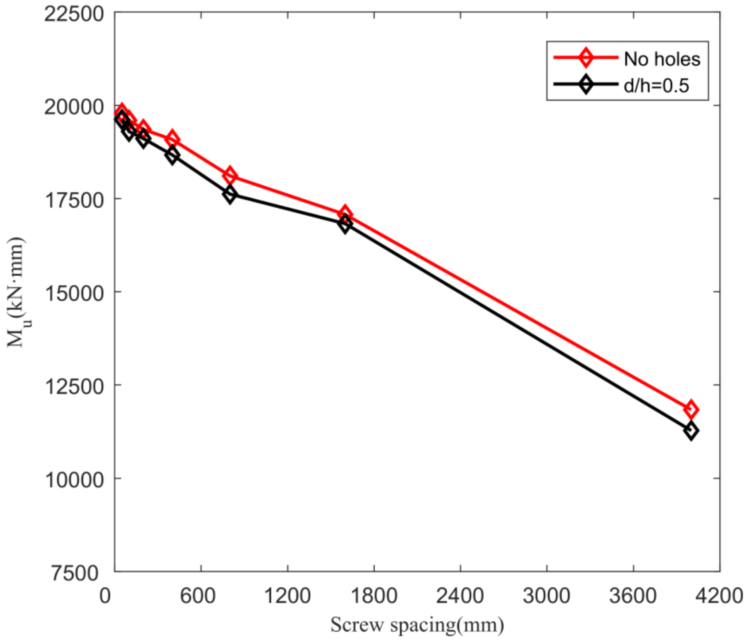

(b) h=200 mm, b=75 mm, c=20 mm, t=1.6 mm and a=300 mm

Figure 6.6 Ultimate moment curves of 4-meter-long CFS built-up beams with web perforations in different screw arrangements obtained from FEA

6.3.2 Influence of hole sizes

The ultimate moment capacities of 1.2-meter-long CFS built-up beams with web perforations controlled by the distortional buckling obtained from FEA were compared for different hole sizes and are shown in Figure 6.7. It can be observed from the figures that the ultimate failure moment decreased with the increase of hole sizes. For the specimen H150-L1200-T2.4-S150-A300, for example, when the ratio of diameter of the circular hole to web height (d/h) increased from 0.25 to 0.8, the reduction of ultimate moment reached by 12%. This is because for the beam failed by distortional buckling, the beam with larger web perforations had weaker restraint to the compressed flange and lip from the web.

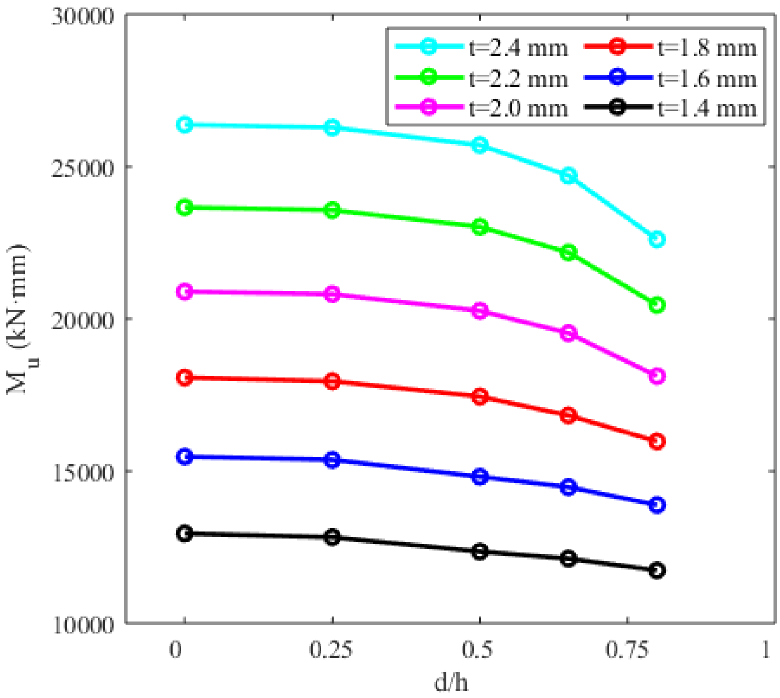

(a) h=150 mm, b=65 mm, c=15 mm, a=300 mm and s=150 mm

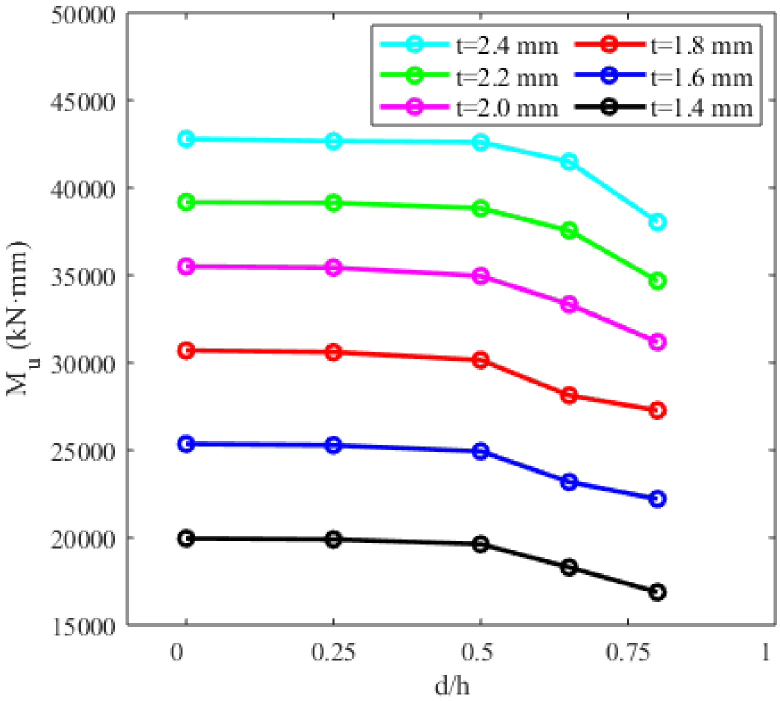

(b) h=200 mm, b=75 mm, c=20 mm, a=300 mm and s=200 mm

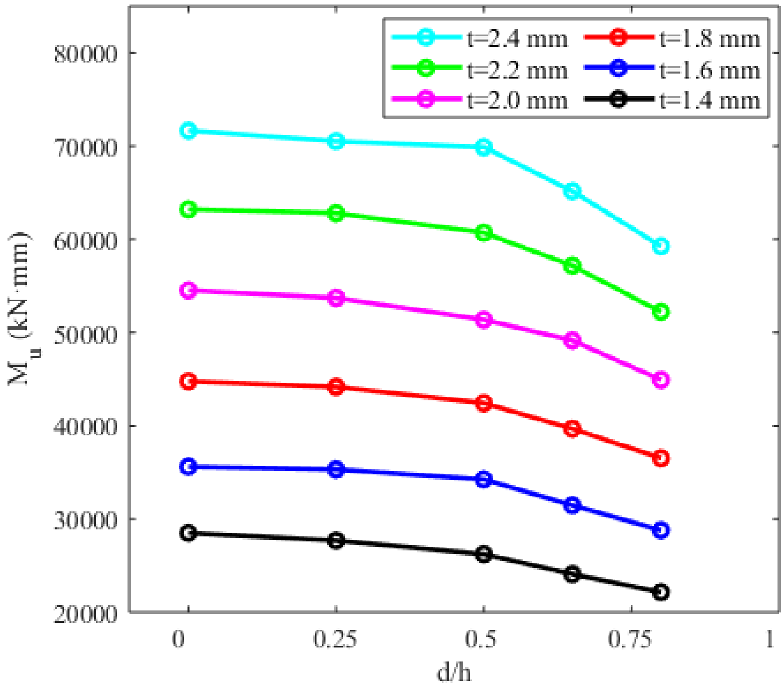

(c) h=300 mm, b=100 mm, c=20 mm, a=300 mm and s=300 mm

Figure 6.7 Ultimate moment curves of 1.2-meter-long CFS built-up beams with different hole sizes obtained from FEA

Figure 6.8 exhibits the ultimate moment curves of 4-meter-long CFS built-up beams controlled by the lateral-torsional buckling with web perforations in different hole sizes obtained from FEA. It can be found that the hole sizes had minimal influence on the ultimate failure moment of the specimens H150-L4000-S200-A300 (see Figure 6.8(a)) and the specimens H150-L4000-S200-A300 (see Figure 6.8(b)) when d/h increased from 0.25 to 0.8. The reason is that the reduction of the cross-section properties due to the web perforations was not significant. Furthermore, the effect of the composite action can also help to eliminate the effect of hole sizes on the ultimate failure moment.

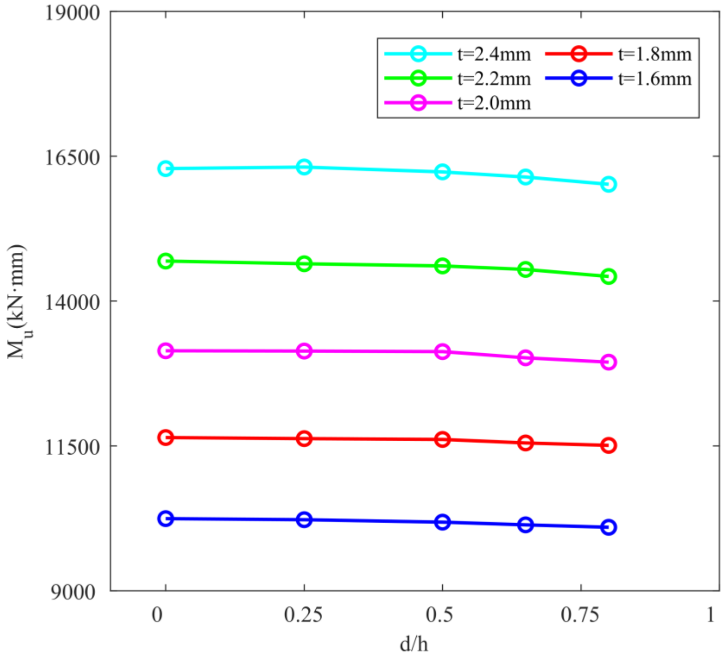

(a) h=150 mm, b=65 mm, c=15 mm, a=300 mm and s=200 mm

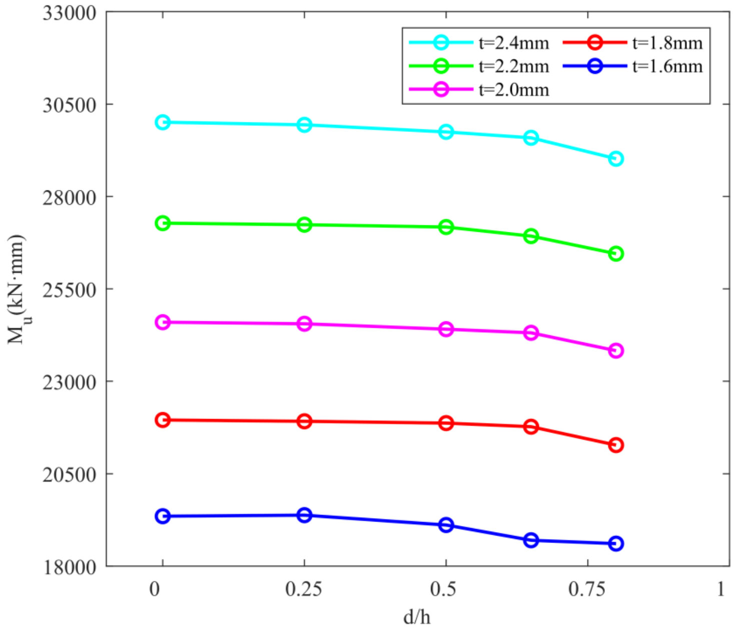

(b) h=200 mm, b=75 mm, c=20 mm, a=300 mm and s=200 mm

Figure 6.8 Ultimate moment curves of 4-meter-long CFS built-up beams with web perforations in different hole sizes obtained from FEA

6.3.3 Influence of hole spacing

The ultimate moment capacities of 1.8-meter-long CFS built-up beams with web perforations controlled by the distortional buckling obtained from FEA were compared for different hole spacing and are shown in Figure 6.9. It can be seen that the influences of hole spacing on the ultimate failure moment of the specimens H150-L1800-S150(d/h0.5) (see Figure 6.9(a)), the specimens H200-L1800-S200(d/h0.5) (see Figure 6.9(b)) and the specimens H300-L1800-S300(d/h0.5) (see Figure 6.9(c)) were not obvious when the distance between two adjacent holes (s) increased from 150 mm to 450 mm. This is because the values of hole spacing selected in the present study were limited and the perforated area in the web of the beam did not change a lot when the hole spacing changed.

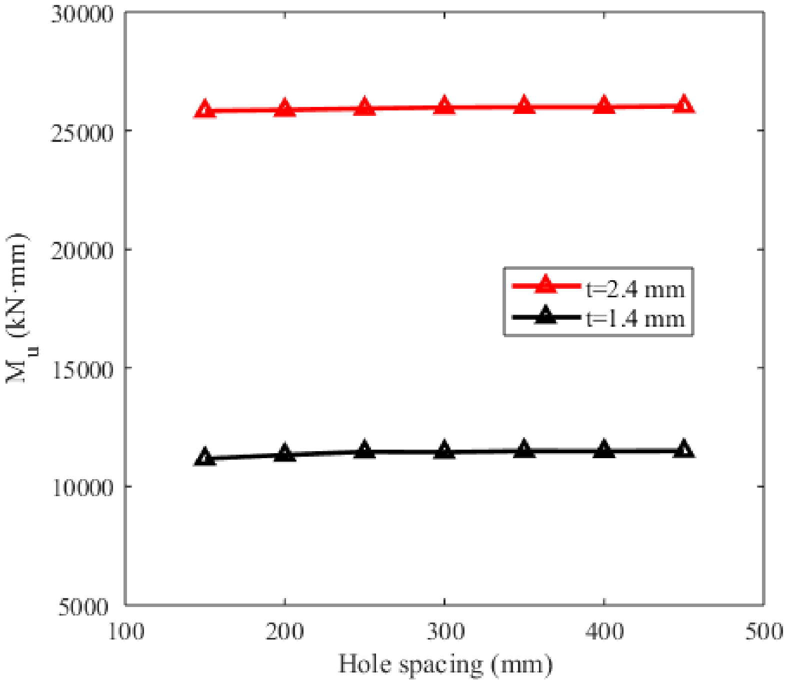

(a) h=150 mm, b=65 mm, c=15 mm, d=75 mm and s=150 mm

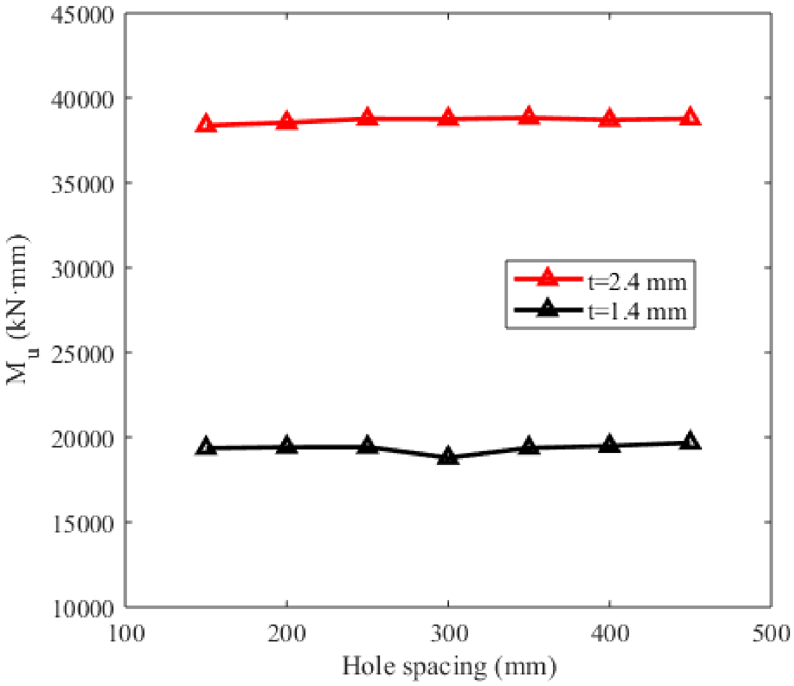

(b) h=200 mm, b=75 mm, c=20 mm, d=100 mm and s=200 mm

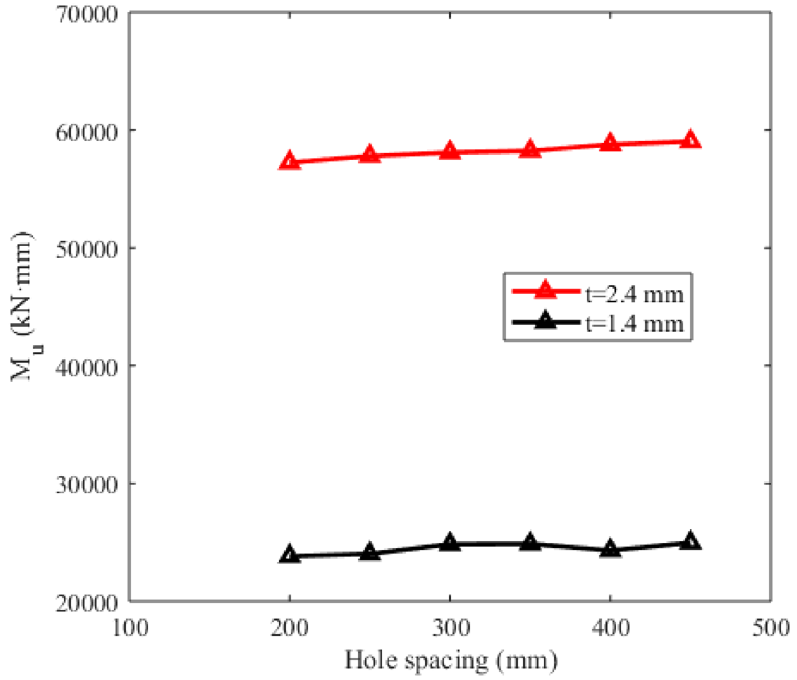

(c) h=300 mm, b=100 mm, c=20 mm, d=150 mm and s=300 mm

Figure 6.9 Ultimate moment curves of 1.8-meter-long CFS built-up beams with web perforations in different hole spacing obtained from FEA

Figure 6.10 summarizes the ultimate moment curves of 4-meter-long CFS built-up beams with web perforations controlled by the lateral-torsional buckling in different hole spacing obtained from FEA. Similar to the beam failed by distortional buckling, the ultimate failure moment of the specimens H150-L4000-S200(d/h0.5) (see Figure 6.10(a)) and the specimens H150-L4000-S200(d/h0.5) (see Figure 6.10(b)) did not change a lot when the spacing increased from 150 mm to 450 mm. As explained before, the hole spacing did not have significant effect on the ultimate failure moment due to the limitation of the hole spacing value selected in the present study.

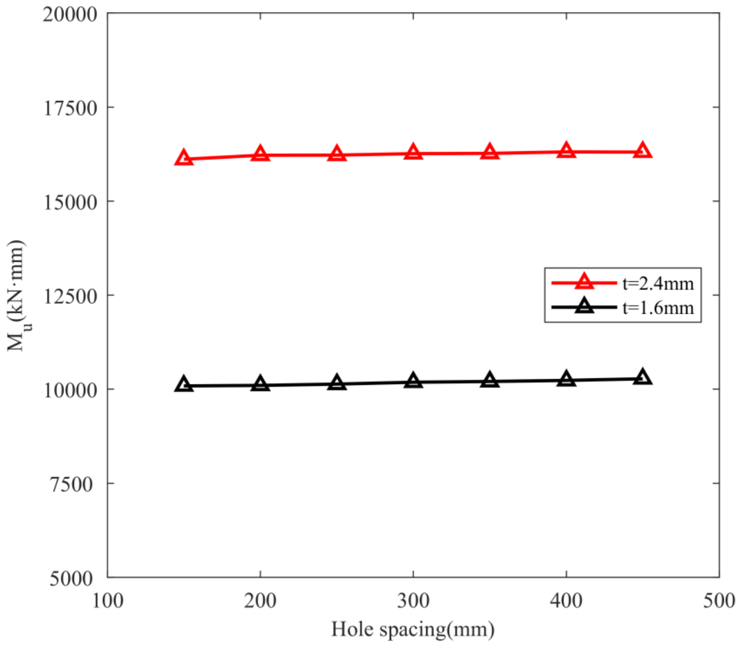

(a) h=150 mm, b=65 mm, c=15 mm, d=75 mm and s=200 mm

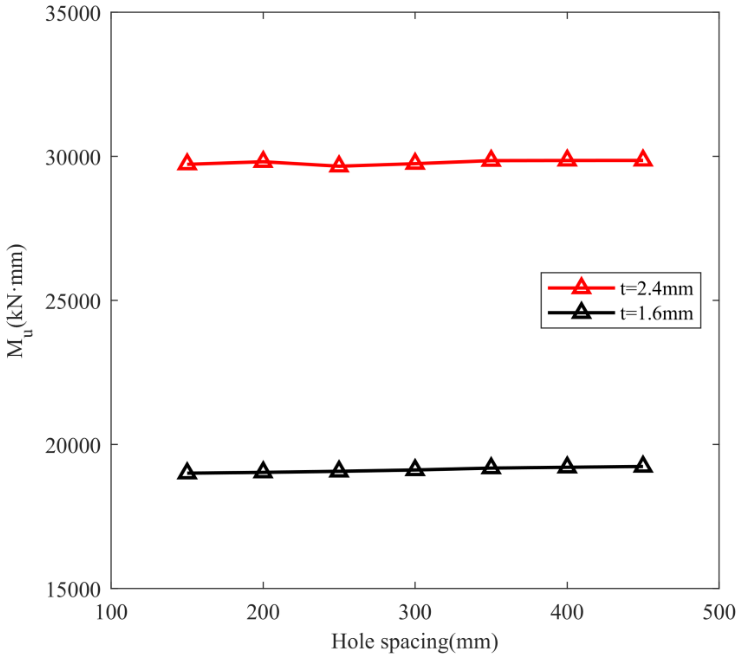

(b) h=200 mm, b=75 mm, c=20 mm, d=100 mm and s=200 mm

Figure 6.10 Ultimate moment curves of 4-meter-long CFS built-up beams with web perforations in different hole spacing obtained from FEA

6.3.4 Influence of slenderness ratio

The ultimate moment capacities of CFS built-up beams with web perforations obtained from FEA were compared in different slenderness ratios and hole sizes as shown in Figure 6.11. It can be seen from the figure that the ultimate failure moment of the specimens H150-T2-S200-A300 (see Figure 6.11(a)) and the specimens H200-T2-S200-A300 (see Figure 6.11(b)) decreased with the increase of slenderness ratio. It seemed that the ultimate failure moment was more sensitive to the slenderness ratio when the beam failed by the lateral-torsional bucking. As described before, it is interesting to find that the hole size had more influence on the ultimate failure moment of the beam controlled by the distortional buckling than that controlled by the lateral-torsional buckling.

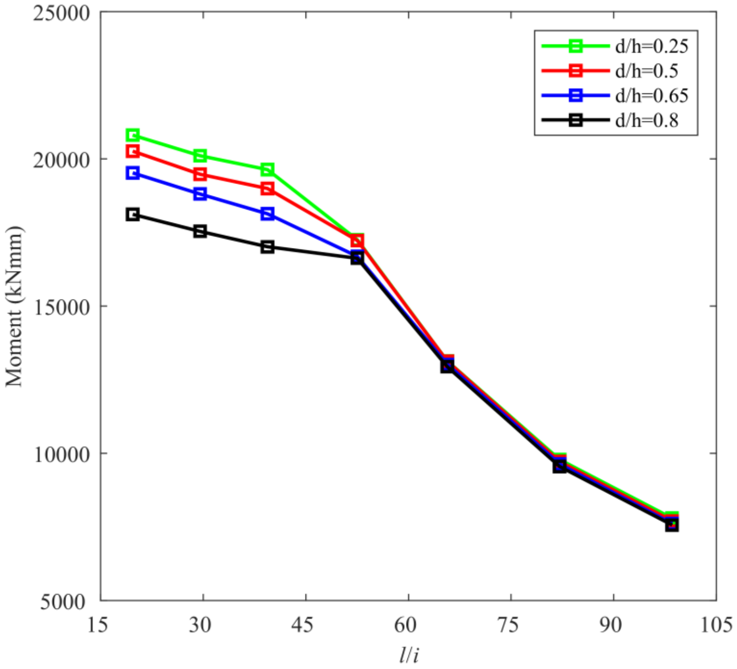

(a) h=150 mm, b=65 mm, c=15 mm, t=2 mm, a=300 mm and s=200 mm

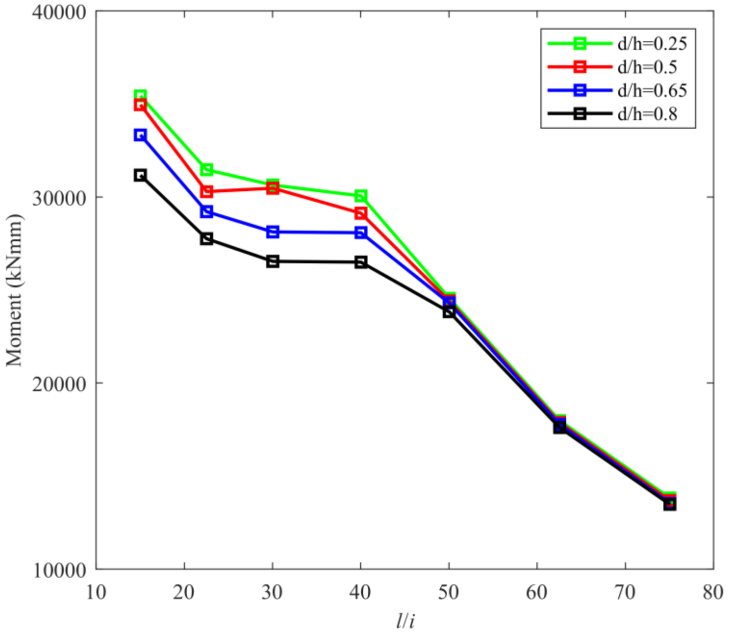

(b) h=200 mm, b=75 mm, c=20 mm, t=2 mm, a=300 mm and s=200 mm

Figure 6.11 Ultimate moment curves of CFS built-up beams with web perforations in different hole sizes and slenderness ratios obtained from FEA

6.4 Modified direct strength method for CFS built-up beam with web perforations

Moen and Schafer (2010) extended the classical DSM equations for predicting the ultimate moment of PCFS beams which has been prescribed in the North America Specification standard (AISI, 2016), the specific design formulae are illustrated in Section 2.4.2. In this section, new numerical results obtained from the parametric study were used to further extend the DSM equations of PCFS beams for determining the ultimate moment of CFS built-up beams with web perforations. The comparisons of FEA results with design strength obtained from original DSM equations for some selected specimens controlled by local buckling, distortional buckling and lateral-torsional buckling are listed in Table 6.1, Table 6.2 and Table 6.3, respectively. It can be seen that if the specimens were controlled by the local buckling or distortional buckling, the original DSM formulae were able to provide an accurate prediction of the ultimate failure moment. However, if the specimens were failed by the lateral-torsional buckling, the original DSM design rule would be conservative. The details of FEA results obtained from the present parametric study can be found in Appendix E.

Table 6.1 Comparison of ultimate moment obtained from FEA with original DSM prediction for selected specimens controlled by local buckling

Specimen	FEA	DSM	Comparison
	M_{FEA} (kN·mm)	$M_{\mathrm{DSM,o}}$ (kN·mm)	$M_{\mathrm{FEA}}/M_{\mathrm{DSM,o}}$
H200-L1200-T1.4-S200-A300(d/h0.25)	19895	18991	1.05
H200-L1200-T1.4-S200-A300(d/h0.5)	19622	15568	1.26
H200-L1200-T1.4-S200-A300(d/h0.65)	18292	15350	1.19
H200-L1800-T1.4-S200-A150(d/h0.5)	19357	15568	1.24
H200-L1800-T1.4-S200-A200(d/h0.5)	19423	15568	1.25
H200-L1800-T1.4-S200-A250(d/h0.5)	19427	15568	1.25
H200-L1800-T1.4-S200-A300(d/h0.5)	19379	15568	1.24
H200-L1800-T1.4-S200-A350(d/h0.5)	19374	15568	1.24
H200-L1800-T1.4-S200-A400(d/h0.5)	19492	15568	1.25
H200-L1800-T1.4-S200-A450(d/h0.5)	19681	15568	1.26
H300-L1200-T1.4-S100-D300(d0.5)	26629	23347	1.14
H300-L1200-T1.4-S200-D300(d0.5)	26500	23347	1.14
H300-L1200-T1.4-S300-D300(d0.5)	26225	23347	1.12
H300-L1200-T1.4-S400-D300(d0.5)	26189	23347	1.12
H300-L1200-T1.4-S800-D300(d0.5)	26032	23347	1.11
H300-L1200-T1.4-S1200-D300(d0.5)	25876	23347	1.11

Table 6.2 Comparison of ultimate moment obtained from FEA with original and modified DSM prediction for selected specimens controlled by distortional buckling

Specimen	FEA	DSM	Comparison
	M_{FEA} (kN·mm)	$M_{\mathrm{DSM,o}}$ (kN·mm)	$M_{\mathrm{FEA}}/M_{\mathrm{DSM,o}}$
H150-L1200-T1.8-S150-A300(d/h0.25)	17952	16737	1.07
H150-L1200-T1.8-S150-A300(d/h0.5)	17447	16392	1.06
H150-L1200-T1.8-S150-A300(d/h0.65)	16828	15975	1.05
H150-L1200-T1.8-S150-A300(d/h0.8)	15973	15155	1.05
H200-L1800-T2.4-S200-A150(d/h0.5)	38378	36538	1.05
H200-L1800-T2.4-S200-A200(d/h0.5)	38539	37161	1.04
H200-L1800-T2.4-S200-A250(d/h0.5)	38764	37463	1.03
H200-L1800-T2.4-S200-A300(d/h0.5)	38748	37644	1.03
H200-L1800-T2.4-S200-A350(d/h0.5)	38825	37762	1.03
H200-L1800-T2.4-S200-A400(d/h0.5)	38700	37846	1.02
H200-L1800-T2.4-S200-A450(d/h0.5)	38771	37910	1.02
H300-L1200-T2.4-S50-A300(d/h0.5)	70814	59619	1.19
H300-L1200-T2.4-S100-A300(d/h0.5)	70798	59619	1.19
H300-L1200-T2.4-S200-A300(d/h0.5)	70377	59619	1.18
H300-L1200-T2.4-S300-A300(d/h0.5)	69873	59619	1.17
H300-L1200-T2.4-S400-A300(d/h0.5)	69116	59619	1.16
H300-L1200-T2.4-S800-A300(d/h0.5)	68876	59619	1.16
H300-L1200-T2.4-S1200-A300(d/h0.5)	68637	59619	1.15

Table 6.3 Comparison of ultimate moment obtained from FEA with original and modified DSM prediction for selected specimens controlled by lateral-torsional buckling

Specimen	FEA	DSM	Comparison
	M_{FEA} (kN·mm)	$M_{\mathrm{DSM,o}}$ (kN·mm)	$M_{\mathrm{FEA}}/M_{\mathrm{DSM,o}}$
H150-L4000-T1.4-S200-A300(d/h0.25)	8842	4562	1.94
H150-L4000-T1.4-S200-A300(d/h0.5)	8810	4326	2.04
H150-L4000-T1.4-S200-A300(d/h0.65)	8760	4180	2.10
H150-L4000-T1.4-S200-A300(d/h0.8)	8673	4032	2.15
H200-L4000-T2.4-S200-A150(d/h0.5)	29724	16970	1.75
H200-L4000-T2.4-S200-A200(d/h0.5)	29813	16970	1.76
H200-L4000-T2.4-S200-A250(d/h0.5)	29658	16970	1.75
H200-L4000-T2.4-S200-A300(d/h0.5)	29746	16970	1.75
H200-L4000-T2.4-S200-A350(d/h0.5)	29852	16970	1.76
H200-L4000-T2.4-S200-A400(d/h0.5)	29857	16970	1.76
H200-L4000-T2.4-S200-A450(d/h0.5)	29859	16970	1.76
H200-L4000-T1.6-S50-A300(d/h0.5)	19619	10936	1.79
H200-L4000-T1.6-S100-A300(d/h0.5)	19297	10936	1.76
H200-L4000-T1.6-S200-A300(d/h0.5)	19111	10936	1.75
H200-L4000-T1.6-S400-A300(d/h0.5)	18670	10936	1.71
H200-L4000-T1.6-S800-A300(d/h0.5)	17617	10936	1.61
H200-L4000-T1.6-S1600-A300(d/h0.5)	16824	10936	1.54
H200-L4000-T1.6-S4000-A300(d/h0.5)	11278	10936	1.03

6.4.1 Local buckling investigation

As described in Section 6.2.2, if the CFS built-up beams with web perforations are controlled by local buckling, the single PCFS channels will buckle separately and independently. Therefore, the ultimate moment of built-up beams can be assumed as the sum of two single PCFS beams. According to the extended DSM formulae for the local buckling of PCFS beams proposed by Moen and Schafer (2010), the ultimate moment of CFS built-up beams with web perforations controlled by local buckling can be expressed as follows,

$$M_{ul} = \begin{cases} 2 \times M_{ynet} & \text{if } \lambda_l \le \lambda_{l1} \\ 2 \times \kappa_l \left[1 - 0.15 \left(\dfrac{M_{crlPB}}{M_y} \right)^{\gamma_l} \right] \left(\dfrac{M_{crlPB}}{M_y} \right)^{\gamma_l} M_y \le 2 \times M_{ynet} & \text{if } \lambda_l > \lambda_{l1} \end{cases} \tag{6-1}$$

where M_{crlPB} is the critical moment of local buckling of the single PCFS beam which can be obtained from the design equations proposed by Moen and Schafer (2009b), M_{ynet} is the yield moment of net cross-section and M_y is the yield moment of gross cross-section.

The factor η represents the influence of hole sizes which is defined as,

$$\eta = M_{ynet} / M_y \tag{6-2}$$

The modified factor κ_l and γ_l for local buckling are determined based on the factor η,

$$\kappa_l = \begin{cases} 1 & \text{if } 0.975 \le \eta \le 1 \\ 1.3 & \text{if } \eta < 0.975 \end{cases} \tag{6-3}$$

$$\gamma_l = \begin{cases} 0.4 & \text{if } 0.975 \le \eta \le 1 \\ 0.5 & \text{if } \eta < 0.975 \end{cases} \tag{6-4}$$

In which λ_l is the section slenderness for local buckling which is given by,

$$\lambda_l = \left(\frac{M_y}{M_{crlPB}} \right)^{0.5} \tag{6-5}$$

The limit of the local buckling slenderness transition λ_{l1} can be solved by,

$$\frac{\kappa_l\left(1-0.15/\lambda_{l1}^{2\gamma_l}\right)}{\lambda_{l1}^{2\gamma_l}}=\eta \qquad (6\text{-}6)$$

The modified DSM curves for CFS built-up beams with web perforations subject to local buckling were compared with FEA results as shown in Figure 6.12. For the built-up beams with small perforations ($0.975 \le \eta \le 1$), the original DSM curves were reliable to predict the ultimate moment (see Figure 6.12(a)). However, for the built-up beams with large perforations ($\eta < 0.975$), the prediction moments determined by the original DSM equations were conservative. The mean value of the ratio of FEA results to beam strength determined by original DSM formulae was 1.11 and the corresponding coefficient of variation (COV) was 0.088.

The modified factor κ_l and γ_l were carried out to extend the original DSM equations, the factor η was chosen as 0.95 for the built-up beam with large perforations (see Figure 6.12(b)). The mean value of the ratio of FEA results to beam strength determined by modified DSM formulae was 1.02 and the corresponding COV was 0.038. The comparisons of FEA results with design strength obtained from original and modified DSM equations for selected specimens controlled by the local buckling are listed in Table 6.4.

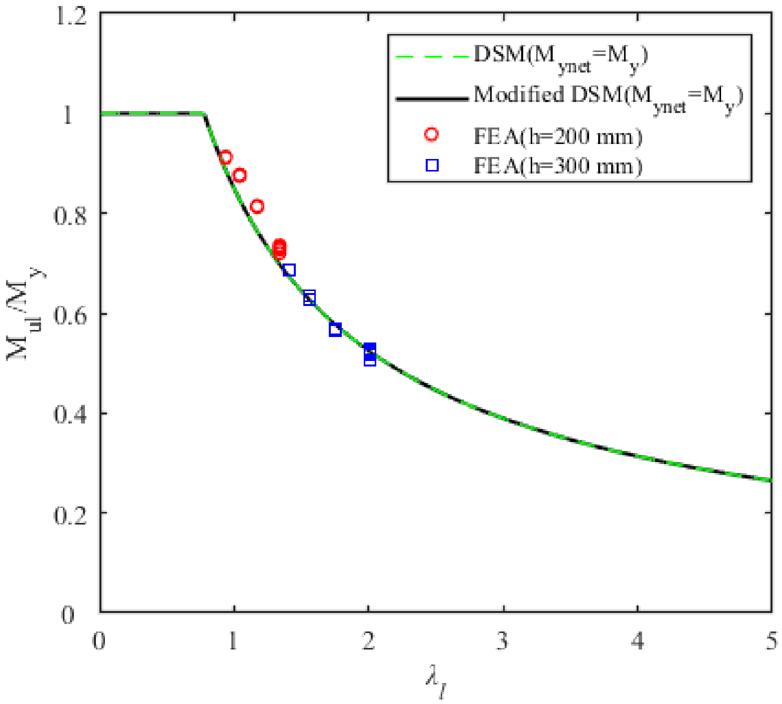

(a) η=1

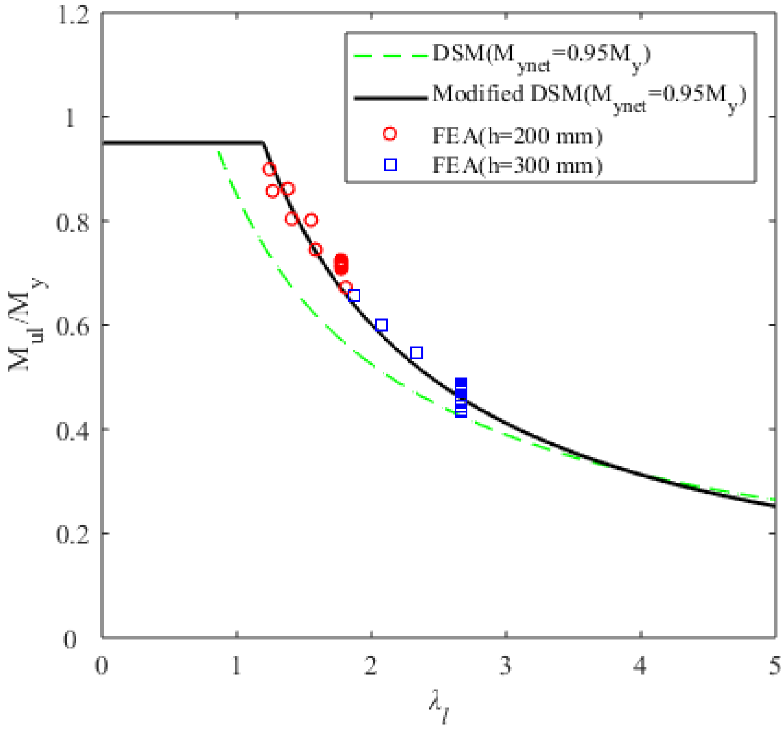

(b) η=0.95

Figure 6.12 Comparison of the modified DSM curves with FEA results for CFS built-up beams with web perforations controlled by local buckling

Table 6.4 Comparison of ultimate moment obtained from FEA with original and modified DSM prediction for selected specimens controlled by local buckling

Specimen	FEA	DSM		Comparison	
	M_{FEA} (kN·mm)	$M_{DSM,o}$ (kN·mm)	$M_{DSM,m}$ (kN·mm)	$M_{FEA}/M_{DSM,o}$	$M_{FEA}/M_{DSM,m}$
H200-L1200-T1.4-S200-A300(d/h0.25)	19895	18991	18991	1.05	1.05
H200-L1200-T1.4-S200-A300(d/h0.5)	19622	15568	18240	1.26	1.08
H200-L1200-T1.4-S200-A300(d/h0.65)	18292	15350	17917	1.19	1.02
H200-L1800-T1.4-S200-A150(d/h0.5)	19357	15568	18240	1.24	1.06
H200-L1800-T1.4-S200-A200(d/h0.5)	19423	15568	18240	1.25	1.06
H200-L1800-T1.4-S200-A250(d/h0.5)	19427	15568	18240	1.25	1.07
H200-L1800-T1.4-S200-A300(d/h0.5)	19379	15568	18240	1.24	1.06
H200-L1800-T1.4-S200-A350(d/h0.5)	19374	15568	18240	1.24	1.06
H200-L1800-T1.4-S200-A400(d/h0.5)	19492	15568	18240	1.25	1.07
H200-L1800-T1.4-S200-A450(d/h0.5)	19681	15568	18240	1.26	1.08
H300-L1200-T1.4-S100-D300(d0.5)	26629	23347	25267	1.14	1.05
H300-L1200-T1.4-S200-D300(d0.5)	26500	23347	25267	1.14	1.05
H300-L1200-T1.4-S300-D300(d0.5)	26225	23347	25267	1.12	1.04
H300-L1200-T1.4-S400-D300(d0.5)	26189	23347	25267	1.12	1.04
H300-L1200-T1.4-S800-D300(d0.5)	26032	23347	25267	1.11	1.03
H300-L1200-T1.4-S1200-D300(d0.5)	25876	23347	25267	1.11	1.02

The reliability analysis based on the frame work of North America Specification standard (AISI, 2016) was proposed to assess the suitability of the original and modified DSM equations. According to the Load and Resistance Factor Design (LRFD), the strength of the tested member should satisfy the following equation,

$$\sum \gamma_i Q_i \leq \phi_b R_n \tag{6-7}$$

where the left side is required strength based on the most critical load combination, γ_i are load factors and Q_i are load effects, respectively; The right side is the design strength, R_n is the average of all test results and Φ_b is the resistance factor which can be determined by,

$$\phi_b = C_{\phi_b} \cdot (M_{\mathrm{m}} P_{\mathrm{m}} F_{\mathrm{m}}) e^{-\beta_0 \sqrt{C_{\mathrm{P}} V_{\mathrm{P}}{}^2 + V_{\mathrm{M}}{}^2 + V_{\mathrm{F}}{}^2 + V_{\mathrm{Q}}{}^2}} \tag{6-8}$$

where $C_{\Phi b}$ is the calibration coefficient, M and F denote the ratio of the actual to the nominal material properties and the ratio of the actual to the nominal cross-sectional dimensions, P is the ratio of the buckling moment obtained from FEA to the design predictions, M_m F_m and P_m are the mean values of M, F and P, V_M, V_F and V_P represent the coefficient of variations (COVs) of M, F and P, respectively, V_Q is the COV of load effect, β_0 is the target reliability index and can be taken as 2.5 for structural members for LRFD.

The reliability index of the parametric study can be evaluated as follows,

$$\beta_1 = \frac{\ln\left[C_{\phi_b} \cdot \frac{M_{\mathrm{m}} P_{\mathrm{m}} F_{\mathrm{m}}}{\phi_b} \right]}{\sqrt{C_{\mathrm{P}} V_{\mathrm{P}}{}^2 + V_{\mathrm{M}}{}^2 + V_{\mathrm{F}}{}^2 + V_{\mathrm{Q}}{}^2}} \tag{6-9}$$

According to the LRFD, the resistance factor (Φ_b) of 0.9 was adopted in this study. $C_{\Phi b}$ is equal to 1.52, the mean value M_m and F_m can be taken as 1.10 and 1.00, the COV V_M, V_F and V_Q can be taken as 0.10, 0.05 and 0.21, respectively. The mean value P_m and COV V_P can be calculated from the present parametric study. Furthermore, to take account of the effect of limited number of data samples, a correction factor C_P of 5.7 was included.

The reliability index β_1 obtained from the original and modified DSM predictions for the specimens controlled by local buckling were 2.849 and 2.668 (see Appendix E.1) which were larger than the target reliability index β_0 (2.5)). This proves that both design rules were reliable and the proposed design modified DSM formulae can give a more accurate prediction.

6.4.2 Distortional buckling investigation

Similar to the case illustrated in Section 6.4.1, if the CFS built-up beams with web perforations were controlled by distortional buckling, the single PCFS channels would also buckle separately and independently. Hence the ultimate moment of built-up beams can be regarded as the sum of two single PCFS beams.

According to the extended DSM formulae for the distortional buckling of PCFS beams proposed by Moen and Schafer (2010), the modified DSM equations for calculating the ultimate moment of CFS built-up beams with web perforations subject to distortional buckling are listed as follows,

$$M_{ud} = \begin{cases} 2\times M_{ynet} & \text{if } \lambda_{d0} \le \lambda_{d1} \\ 2\times[M_{ynet} - \dfrac{M_{ynet} - M_{d2}}{\lambda_{d2} - \lambda_{d1}}(\lambda_{d0} - \lambda_{d1})] & \\ \le 2\times\kappa_d \left[1 - 0.22\left(\dfrac{M_{crdPB}}{M_y}\right)^{0.5\gamma_d}\right]\left(\dfrac{M_{crdPB}}{M_y}\right)^{0.5\gamma_d} M_y & \text{if } \lambda_{d1} < \lambda_{d0} \le \lambda_{d2} \\ 2\times\kappa_d \left[1 - 0.22\left(\dfrac{M_{crdPB}}{M_y}\right)^{0.5\gamma_d}\right]\left(\dfrac{M_{crdPB}}{M_y}\right)^{0.5\gamma_d} M_y & \text{if } \lambda_{d0} > \lambda_{d2} \end{cases} \tag{6-10}$$

where M_{crdPB} is the critical moment of distortional buckling of the single PCFS beam which can be calculated by the analytical model presented in Section 3.3.2, λ_{d0} is the section slenderness for distortional buckling which can be expressed as follows,

$$\lambda_{d0} = \left(\frac{M_y}{M_{crdPB}}\right)^{0.5} \tag{6-11}$$

The limit of the distortional buckling slenderness transition λ_{d1} and λ_{d2} can be determined by the following equations,

$$\lambda_{d1} = 0.78\eta^3 \tag{6-12}$$

$$\lambda_{d2} = 0.78\left(1.7\eta^{-1.44} - 0.7\right) \tag{6-13}$$

The modified factor κ_d and γ_d for distortional buckling are given by,

$$\kappa_d = 1.065 \tag{6-14}$$

$$\gamma_d = 1.19\eta^{0.58} \tag{6-15}$$

M_{d2} is determined by Eq.(6-13),

$$M_{d2} = \kappa_d (1 - \frac{0.22}{\lambda_{d2}^{\ \gamma_d}}) \frac{1}{\lambda_{d2}^{\ \gamma_d}} M_y \tag{6-16}$$

The comparison of ultimate moment calculated by the modified DSM equations with FEA results for CFS built-up beams with web perforations controlled by distortional buckling were plotted in Figure 6.13. According to the hole sizes, the factor η were selected as 1, 0.95, 0.9 and 0.85 (see Figure 6.13(a), Figure 6.13(b), Figure 6.13(c) and Figure 6.13(d)). It can be found that the original DSM curves were conservative compared to the FEA results in most cases, the mean value of the ratio of FEA results to beam strength calculated by original DSM formulae was 1.07 and the corresponding COV was 0.058.

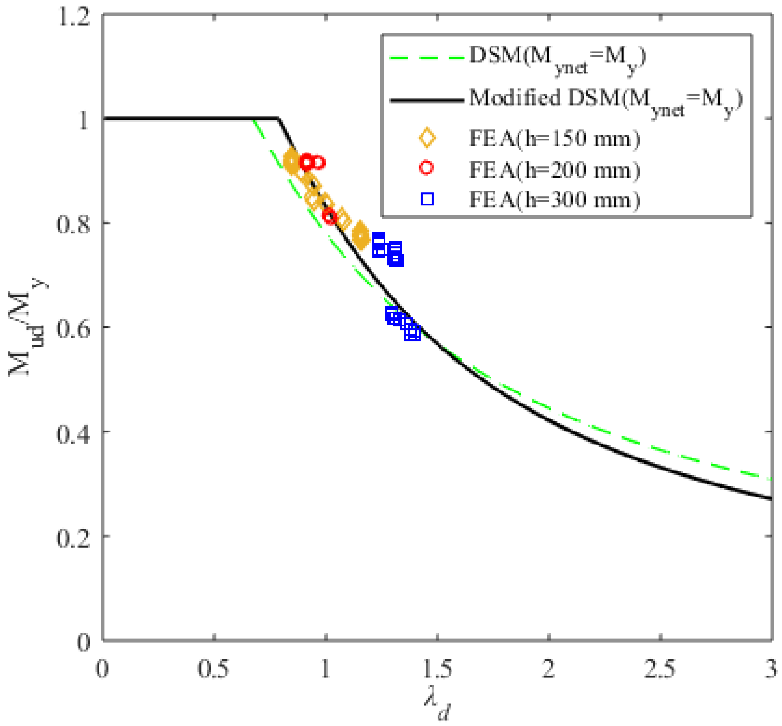

(a) η=1

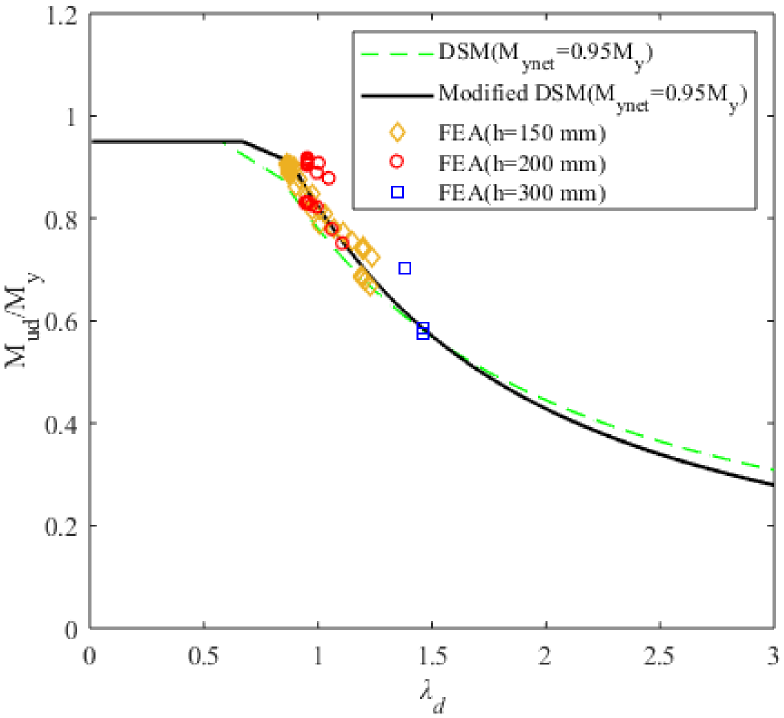
DSM(M_{ynet}=0.95M_y)
Modified DSM(M_{ynet}=0.95M_y)
FEA(h=150 mm)
FEA(h=200 mm)
FEA(h=300 mm)
M_{ud}/M_y
λ_d
0
0.2
0.4
0.6
0.8
1
1.2
0
0.5
1
1.5
2
2.5
3

(b) η=0.95

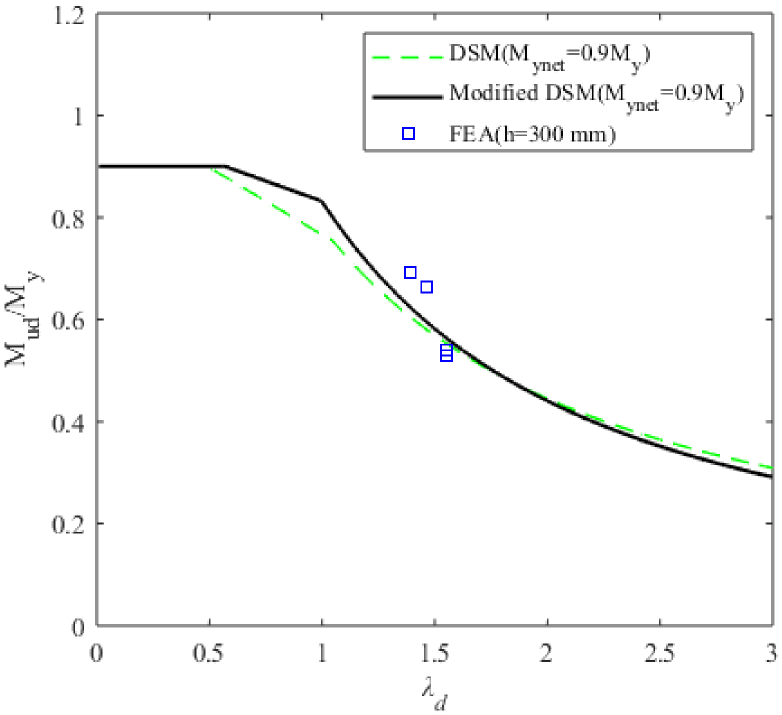
DSM(M_{ynet}=0.9M_y)
Modified DSM(M_{ynet}=0.9M_y)
FEA(h=300 mm)
M_{ud}/M_y
λ_d
0
0.2
0.4
0.6
0.8
1
1.2
0
0.5
1
1.5
2
2.5
3

(c) η=0.9

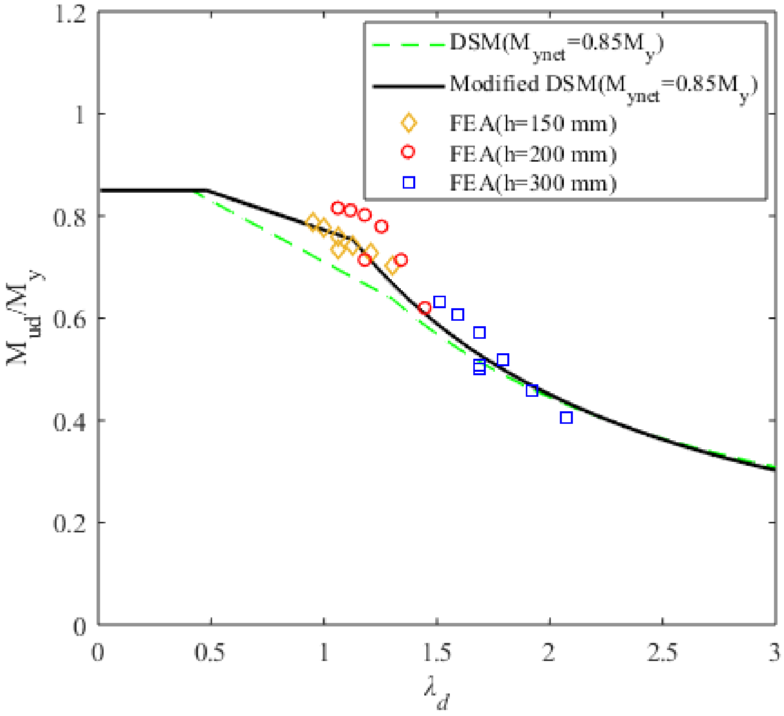

(d) η=0.85

Figure 6.13 Comparison of the modified DSM curves with FEA results for CFS built-up beams with web perforations controlled by distortional buckling

To improve the accuracy of design strength, the modified factors are applied into the original DSM equations. Then the mean value of the ratio of FEA results to beam strength calculated by modified DSM formulae turned into 1.02 and the corresponding COV turned into 0.059. The comparisons of FEA results with design strength obtained from original and modified DSM equations for selected specimens controlled by the distortional buckling can be found in Table 6.5.

Based on the results of the reliability analysis, the reliability index β_1 obtained from the original and modified DSM predictions for the specimens controlled by the distortional buckling were 2.823 and 2.627 (see Appendix E.2) which were larger than the target reliability index β_0 (2.5). It is shown that the original and proposed modified DSM formulae are both reliable for predicting the moment capacities of the CFS built-up beams with web perforations controlled by distortional buckling.

Table 6.5 Comparison of ultimate moment obtained from FEA with original and modified DSM prediction for selected specimens controlled by distortional buckling

Specimen	FEA	DSM		Comparison	
	M_{FEA} (kN·mm)	$M_{DSM,o}$ (kN·mm)	$M_{DSM,m}$ (kN·mm)	$M_{FEA}/M_{DSM,o}$	$M_{FEA}/M_{DSM,m}$
H150-L1200-T1.8-S150-A300(d/h0.25)	17952	16737	17695	1.07	1.01
H150-L1200-T1.8-S150-A300(d/h0.5)	17447	16392	17250	1.06	1.01
H150-L1200-T1.8-S150-A300(d/h0.65)	16828	15975	16728	1.05	1.01
H150-L1200-T1.8-S150-A300(d/h0.8)	15973	15155	15989	1.05	1.00
H200-L1800-T2.4-S200-A150(d/h0.5)	38378	36538	38621	1.05	0.99
H200-L1800-T2.4-S200-A200(d/h0.5)	38539	37161	39385	1.04	0.98
H200-L1800-T2.4-S200-A250(d/h0.5)	38764	37463	39757	1.03	0.98
H200-L1800-T2.4-S200-A300(d/h0.5)	38748	37644	39979	1.03	0.97
H200-L1800-T2.4-S200-A350(d/h0.5)	38825	37762	40124	1.03	0.97
H200-L1800-T2.4-S200-A400(d/h0.5)	38700	37846	40227	1.02	0.96
H200-L1800-T2.4-S200-A450(d/h0.5)	38771	37910	40304	1.02	0.96
H300-L1200-T2.4-S50-A300(d/h0.5)	70814	59619	60689	1.19	1.17
H300-L1200-T2.4-S100-A300(d/h0.5)	70798	59619	60689	1.19	1.17
H300-L1200-T2.4-S200-A300(d/h0.5)	70377	59619	60689	1.18	1.16
H300-L1200-T2.4-S300-A300(d/h0.5)	69873	59619	60689	1.17	1.15
H300-L1200-T2.4-S400-A300(d/h0.5)	69116	59619	60689	1.16	1.14
H300-L1200-T2.4-S800-A300(d/h0.5)	68876	59619	60689	1.16	1.13
H300-L1200-T2.4-S1200-A300(d/h0.5)	68637	59619	60689	1.15	1.13

6.4.3 Lateral-torsional buckling investigation

Unlike local buckling and distortional buckling, if the CFS built-up beams with web perforations were controlled by lateral-torsional buckling, the single PCFS channels would not buckle alone, rather the built-up beam would buckle as a whole. The ultimate moment of built-up beams subject to lateral-torsional buckling cannot be simply assumed as the sum of two single PCFS channels, the effect of the contact due to the composite action on the moment capacities should be taken into account.

Figure 6.14 shows the comparison of beam strength calculated by original DSM formulae with FEA results for CFS built-up beams with web perforations controlled by lateral-torsional buckling. It can be seen that the prediction moment obtained from the original DSM curve was over conservative compared to the FEA results and the disparity widened with the increase of beam length. In order to calculate the ultimate failure moment of CFS built-up beams with web perforations subject to lateral-torsional buckling accurately, the original DSM equations need to be modified.

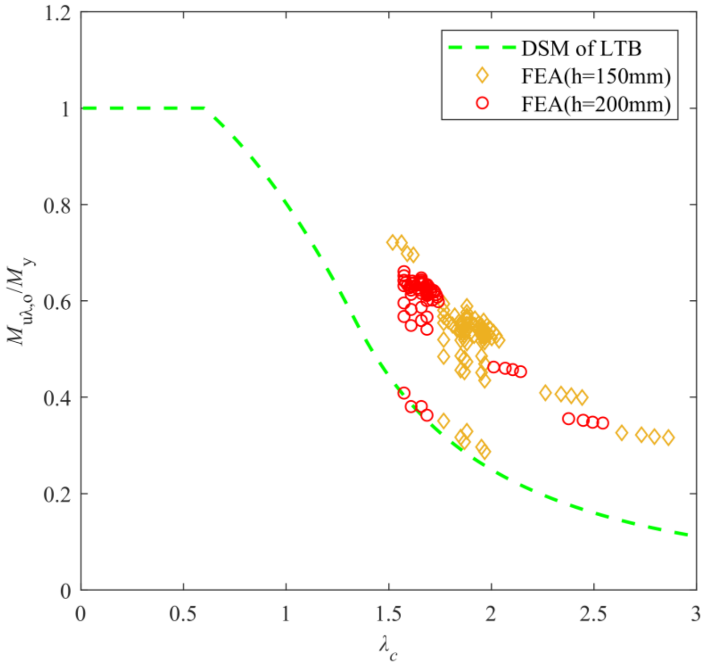

Figure 6.14 Comparison of the original DSM curves with FEA results for CFS built-up beams with web perforations controlled by lateral-torsional buckling

According to the extended DSM formulae for the lateral-torsional buckling of PCFS beams proposed by Moen and Schafer (2010), the modified DSM equations for calculating the ultimate moment of CFS built-up beams with web perforations failed by lateral-torsional buckling can be expressed as,

$$M_{u\lambda} = \kappa_{\lambda}\gamma_{\lambda}M_{u\lambda,\mathrm{o}} \tag{6-17}$$

The ultimate moment calculated by original DSM equations $M_{u\lambda,\mathrm{o}}$ is

$$M_{u\lambda,o} = \begin{cases} 2\times M_{cr\lambda PB} & \text{for } M_{cr\lambda PB} \le 0.56M_y \\ 2\times \dfrac{10}{9}M_y\left(1-\dfrac{10M_y}{36M_{cr\lambda PB}}\right) & \text{for } 0.56M_y < M_{cr\lambda PB} \le 2.78M_y \\ 2\times M_{cr\lambda PB} & \text{for } M_{cr\lambda PB} > 2.78M_y \end{cases} \tag{6-18}$$

where $M_{cr\lambda PB}$ is the critical moment of lateral-torsional buckling of the single PCFS beam which can be calculated by the analytical model presented in Section 4.3.2.1.

The section slenderness for lateral-torsional buckling λ_c is given by,

$$\lambda_c = \left(\frac{M_y}{M_{cr\lambda PB}}\right)^{0.5} \tag{6-19}$$

It can be seen from the parametric study (shown in Section 6.3) that the slenderness ratio (l/i) and screw spacing (s) had significant influence on the structural behaviour of CFS built-up beams with web perforations controlled by lateral-torsional buckling.

FEA results were compared with ultimate failure moment calculated by original DSM equations for CFS built-up beams with web perforations failed by lateral-torsional buckling in different slenderness ratio as shown in Figure 6.15. The screw spacing was equal to 200 mm, the slenderness ratio varied from 40 to 100, the factor η were chosen as 1, 0.95 and 0.85 which represent the size of the perforations from large to small (see Figure 6.15(a), Figure 6.15(b) and Figure 6.15(c)). It can be observed from the figures that the gap between the FEA results and the ultimate moment determined by the original DSM equations increased with the increase of slenderness ratio. The maximum deviation value of the ratio of FEA results to beam strength calculated by original DSM formulae was 259%, the mean value of the ratio of FEA results to beam strength calculated by original DSM formulae was 1.972 and the corresponding COV was 0.199.

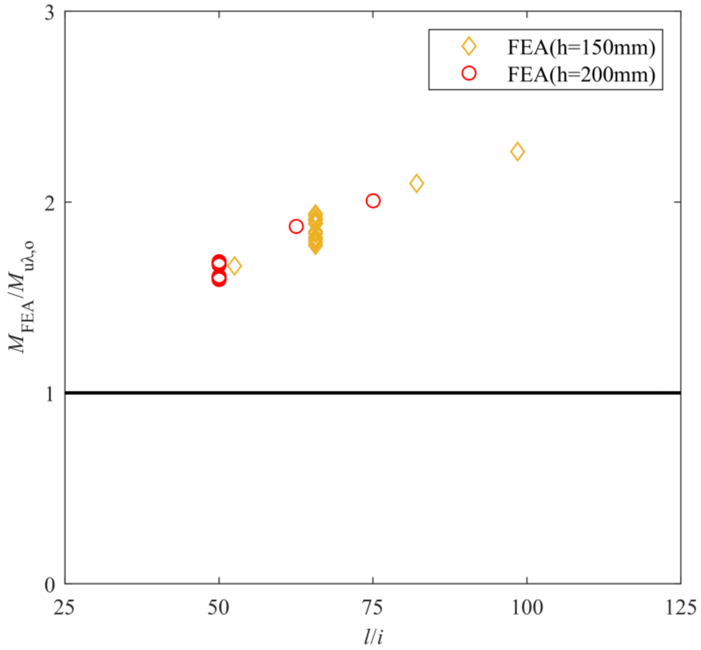

(a) η=1

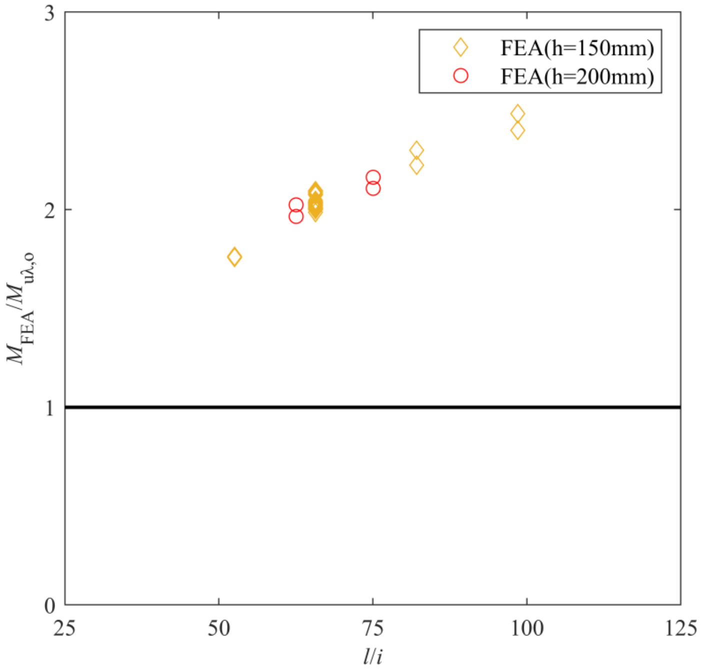

(b) η=0.95

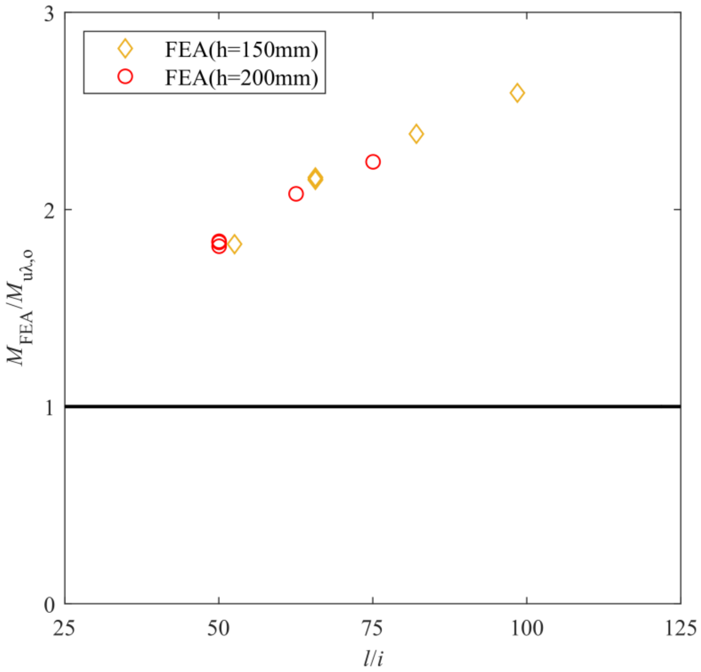

(c) η=0.85

Figure 6.15 Comparison of FEA results with design strength calculated by original DSM for CFS built-up beams with web perforations failed by lateral-torsional buckling in different slenderness ratio

To clarify the effects of slenderness ratio and hole sizes, the modified factor γ_λ was carried out by fitting the FEA results, the relevant fitting function was given by,

$$\gamma_\lambda = 0.03\frac{l}{i} - 0.0001\left(\frac{l}{i}\right)^2 + 40.65\eta - 22.74\eta^2 - 17.45 \tag{6-20}$$

According to the comparison of FEA results with different screw spacing for CFS built-up beams with web perforations failed by lateral-torsional buckling (see Figure 6.16), the modified factor κ_d was represented by the proposed fitting function which included the effect of screw spacing,

$$\kappa_\lambda = -1.04\left(\frac{s}{l}\right)^3 + 1.39\left(\frac{s}{l}\right)^2 - 0.8\left(\frac{s}{l}\right) + 1.02 \tag{6-21}$$

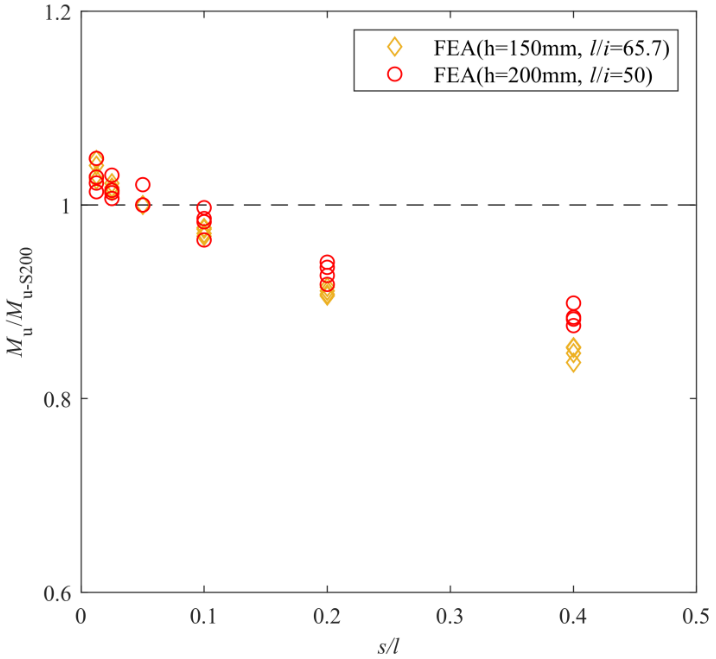

Figure 6.16 Comparison of FEA results with different screw spacing for CFS built-up beams with web perforations failed by lateral-torsional buckling

The comparisons of FEA results with design strength calculated by modified DSM for CFS built-up beams with web perforations failed by lateral-torsional buckling in different slenderness ratio were plotted in Figure 6.17. Compared to the original DSM formulae, the maximum deviation value of the ratio of FEA results to beam strength calculated by modified DSM formulae turned into 7%, the mean value of the ratio of FEA results to beam strength calculated by modified DSM formulae turned into 1.00 and the corresponding COV turned into 0.022. The comparisons of FEA results with design strength obtained from original and modified DSM equations for selected specimens controlled by the lateral-torsional buckling are shown in Table 6.6.

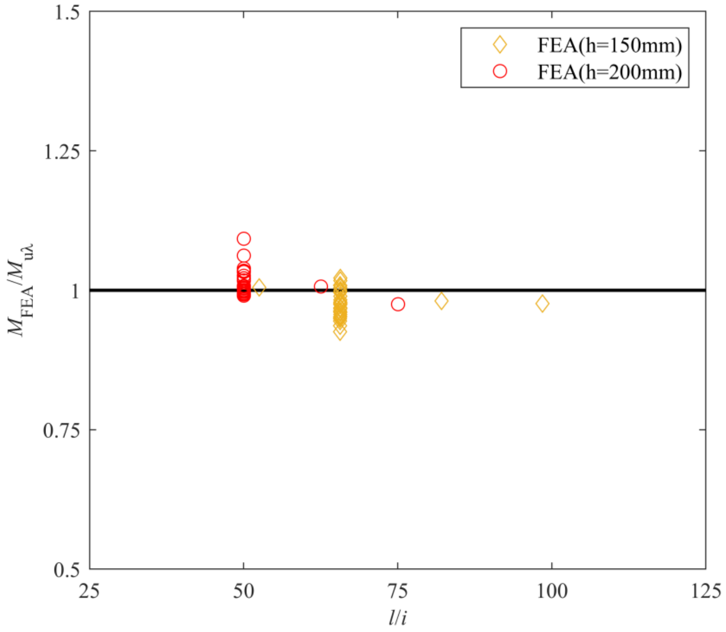
1.5
1.25
1
0.75
0.5
25
50
75
100
125
$M_{FEA}/M_{u\lambda}$
l/i
FEA(h=150mm)
FEA(h=200mm)

(a) η=1

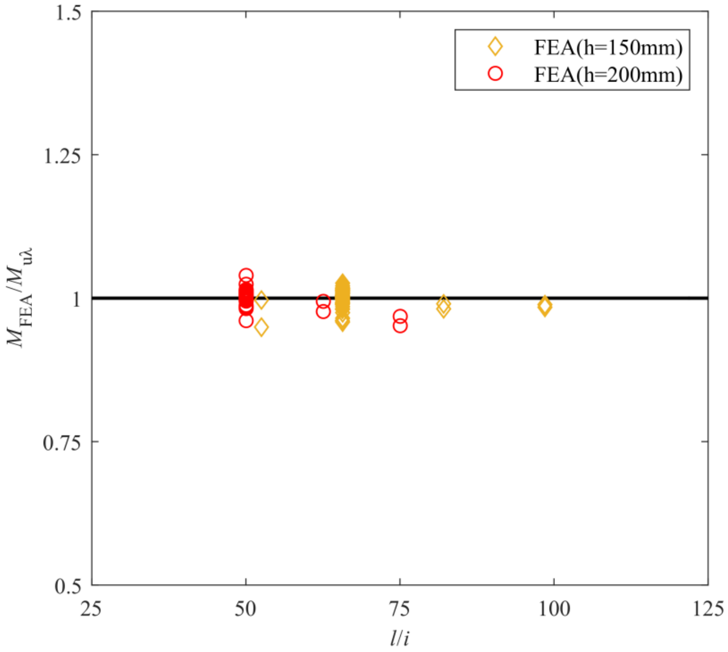
1.5
1.25
1
0.75
0.5
25
50
75
100
125
$M_{FEA}/M_{u\lambda}$
l/i
FEA(h=150mm)
FEA(h=200mm)

(b) η=0.9

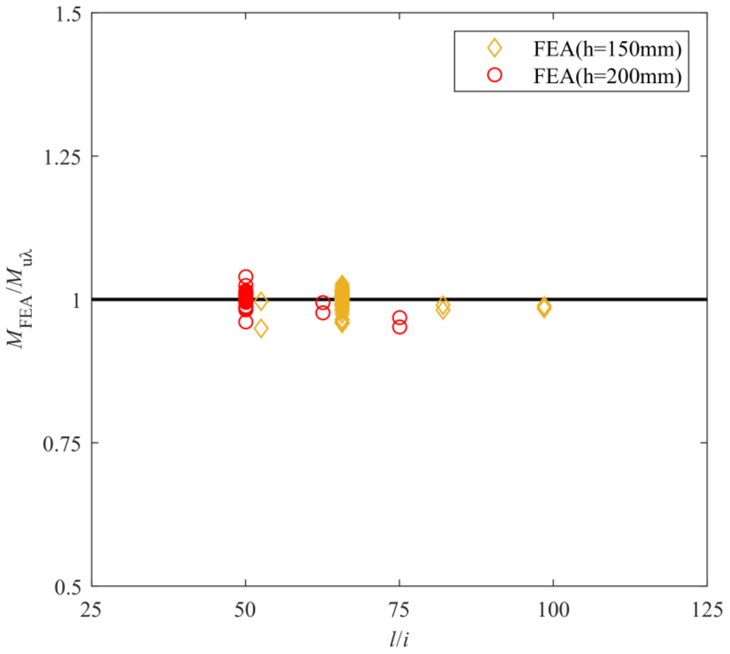

(c) η=0.85

Figure 6.17 Comparison of FEA results with design strength calculated by modified DSM for CFS built-up beams with web perforations failed by lateral-torsional buckling in different slenderness ratio

According to the reliability analysis, the calculated reliability index β_1 for the original and modified DSM predictions of the specimens controlled by the lateral-torsional buckling were taken as 4.32 and 2.592 (see Appendix E.3), respectively. It is shown that both the design rules were reliable. However, the original DSM predictions are too conservative, whereas the proposed modified DSM formulae provides more accurate and reasonable prediction which can be recommended for the design strength of CFS built-up beams with web perforations failed by the lateral-torsional buckling.

Table 6.6 Comparison of ultimate moment obtained from FEA with original and modified DSM prediction for selected specimens controlled by lateral-torsional buckling

Specimen	FEA	DSM		Comparison	
	M_{FEA} (kN·mm)	$M_{DSM,o}$ (kN·mm)	$M_{DSM,m}$ (kN·mm)	$M_{FEA}/M_{DSM,o}$	$M_{FEA}/M_{DSM,m}$
H150-L4000-T1.4-S200-A300(d/h0.25)	8842	4562	8652	1.94	1.02
H150-L4000-T1.4-S200-A300(d/h0.5)	8810	4326	8668	2.04	1.02
H150-L4000-T1.4-S200-A300(d/h0.65)	8760	4180	8774	2.10	1.00
H150-L4000-T1.4-S200-A300(d/h0.8)	8673	4032	8570	2.15	1.01
H200-L4000-T2.4-S200-A150(d/h0.5)	29724	16970	29591	1.75	1.00
H200-L4000-T2.4-S200-A200(d/h0.5)	29813	16970	29591	1.76	1.01
H200-L4000-T2.4-S200-A250(d/h0.5)	29658	16970	29591	1.75	1.00
H200-L4000-T2.4-S200-A300(d/h0.5)	29746	16970	29591	1.75	1.01
H200-L4000-T2.4-S200-A350(d/h0.5)	29852	16970	29591	1.76	1.01
H200-L4000-T2.4-S200-A400(d/h0.5)	29857	16970	29591	1.76	1.01
H200-L4000-T2.4-S200-A450(d/h0.5)	29859	16970	29591	1.76	1.01
H200-L4000-T1.6-S50-A300(d/h0.5)	19619	10936	19547	1.79	1.00
H200-L4000-T1.6-S100-A300(d/h0.5)	19297	10936	19368	1.76	1.00
H200-L4000-T1.6-S200-A300(d/h0.5)	19111	10936	19033	1.75	1.00
H200-L4000-T1.6-S400-A300(d/h0.5)	18670	10936	18449	1.71	1.01
H200-L4000-T1.6-S800-A300(d/h0.5)	17617	10936	17573	1.61	1.00
H200-L4000-T1.6-S1600-A300(d/h0.5)	16824	10936	16572	1.54	1.02
H200-L4000-T1.6-S4000-A300(d/h0.5)	11278	10936	11008	1.03	1.02

6.5 Summary

The numerical investigation on the structural behaviour of CFS built-up beams with web perforations subject to pure bending has been performed in this chapter. The influence of screw spacing, hole sizes, hole spacing and slenderness ratio on the moment capacities of built-up beams has been estimated in the parametric study. According to the FEA results, the modified DSM formulae were proposed to predict the ultimate moment. The results obtained from the present investigation in this chapter have shown that,

- For the specimens selected in this study controlled by local buckling or distortional buckling, the effects of screw spacing on the moment capacities are negligible. However, the moment capacities increase with the decrease of screw spacing if the specimens selected in this study are failed by the lateral-torsional buckling due to the composite action of the two single beams.

- For the specimens selected in this study controlled by distortional buckling, the ultimate failure moments decrease with the increase of hole size (e.g., for the specimen H150-L1200-T2.4-S150-A300, when the ratio of diameter of the circular hole to web height (d/h) increased from 0.25 to 0.8, the reduction of ultimate reached at 12%). However, the hole size has minor effect on the ultimate failure moments if the specimens selected in this study controlled by lateral-torsional buckling.

- The slenderness ratio has significant influence on the moment capacities of CFS built-up beams with web perforations controlled by lateral-torsional buckling, the ultimate moments decrease with the increase of slenderness ratio.

- The FEA results of CFS built-up beams with web perforations have been compared against the ultimate moment of corresponding single PCFS channels obtained from original DSM formulae, the mean value of the ratio of FEA results to two times the ultimate moment of single PCFS channel is 1.11, 1.07 and 1.826 for the built-up beams controlled by local buckling, distortional buckling and lateral-torsional buckling, respectively. It is shown that the effect of the contact due to the composite action of two single beams cannot be ignored when the built-up beam fail by lateral-torsional buckling.

- To check the accuracy of the modified DSM formulae, the FEA results of CFS built-up beams with web perforations have been compared against the modified DSM results. The mean value of the ratio of FEA results to modified DSM results is 1.02, 1.02 and 1 for the built-up beams controlled by local buckling, distortional buckling and lateral-torsional buckling, respectively. The results of the reliability analysis demonstrate that the proposed modified DSM can be recommended for the design of CFS built-up beams with web perforations subject to pure bending.

Chapter 7 — Conclusions and future work

7.1 Conclusions

This thesis has investigated the distortional and lateral-torsional buckling performance of PCFS beams when subjected to pure bending and uniformly distributed load. In addition, the structural behaviour of CFS built-up beams with web perforations when subjected to pure bending has been studied through the use of non-linear finite element analysis. Analytical and numerical approaches have been developed to predict the critical moments of distortional and lateral-torsional buckling of PCFS beams under pure bending and uniformly distributed load. Based on the results obtained from parametric study, the DSM design equations have been modified to determine the ultimate moment capacities of CFS built-up beams with web perforations under pure bending. The main conclusions are drawn as follows,

Distortional buckling analysis of PCFS beams

- The hole sizes have remarkable influence on the critical moment of distortional buckling of PCFS beam. The distortional buckling stress was found to decrease with the increased hole size.

- For PCFS beams under pure bending, the effect of web perforations on the critical moment of distortional buckling can be represented by their influence on the rotational resistance of the compressed flange and lip system. The reduction of the bending rigidity of the web due to the circular perforations can be evaluated by using the concept of equivalent width.

- The analytical model proposed by Lau and Hancock (1987) can be used to calculate the critical moment of distortional buckling of PCFS beams subject to pure bending by reducing the stiffness of the rotational spring. The modified rotational spring stiffness can be determined by applying a unit bending moment at the flange/web junction.

- For PCFS beams under uniformly distributed load, the stress gradient along the beam longitude direction has considerable influence on the distortional buckling. The half-wave length of the distortional buckling modes varies along the longitudinal axis and the longest half wave occurs at the mid-span of the beam.

- The analytical model proposed by Li and Chen (2008) can be used to predict the critical moment of distortional buckling of PCFS beams subject to uniformly distributed load by cutting down the stiffness of the vertical spring. The modified vertical spring stiffness can be estimated by applying a unit concentrated load at the centroid of the compressed flange and lip system.

- For the most cases, the critical stress of distortional buckling of the PCFS beam under uniformly distributed load is larger than that of the same beam under pure bending. However, this difference narrows with the increase of beam length.

- Comparisons of PCFS beams subject to pure bending and uniformly distributed load have been made between the proposed analytical methods and finite element analysis results. The results have shown that the two simplified theoretical models are capable to predict the critical moment of distortional buckling of PCFS beams and can be recommended for the design of PCFS sections.

Lateral-torsional buckling analysis of PCFS beams

- The web perforation was found to have a significant influence on the lateral-torsional buckling performance of PCFS beams. The critical moment of lateral-torsional buckling decreases with the increase of the diameter of circular holes.

- The analytical model based on the energy method can be used to determine the critical moments of lateral-torsional buckling of PCFS beams under pure bending and uniformly distributed uplift load by reducing the cross-sectional properties. The contribution of the solid parts where the web perforations are located to the cross-sectional properties is negligible due to the discontinuities caused by the uniformly distributed perforations.

- For the case that the PCFS beams restrained by the metal sheeting, the horizontal and rotational springs can be applied at the tension end of the web to estimate the restraints provided by the sheeting.

- For PCFS beams under pure bending, the influence of the horizontal spring stiffness on the critical moments of lateral-torsional buckling can be ignored.

- For PCFS beams under uniformly distributed uplift load, the horizontal and rotational springs have different influences on the critical moment of lateral-torsional buckling. The rotational spring stiffness has more effect on the lateral-torsional buckling behaviour than the horizontal spring stiffness. The critical moment of lateral-torsional buckling increases significantly with the increase of rotational spring stiffness when $k_\phi \geq 0.1$, whereas the critical moment increases slightly with the increase of horizontal spring stiffness when $10^{-4} \leq k_z \leq 10$.

- The critical moment of lateral-torsional buckling of a PCFS beam under uniformly distributed uplift load is larger than that of the same beam under pure bending due to the effect of stress gradient. However, this gap becomes closer with the increase of beam length.

- The proposed theoretical approaches have been compared with the eigenvalue analysis results, which have shown a good agreement. This proves that the proposed analytical models are reliable for calculating the critical moment of lateral-torsional buckling when subjected to pure bending and uniformly distributed uplift load.

Non-linear analysis of CFS built-up beams with web perforations

- The non-linear finite element models involving the geometric imperfection, geometrical, material and contact non-linearity have been developed for the numerical investigation of CFS built-up beams with web perforations. The FEA results have been validated against the existing experimental data in terms of the ultimate moment capacities and deformed shapes.

- The influence of hole sizes on the ultimate failure moment of CFS built-up beams with web perforations selected in this study controlled by the distortional buckling is more obvious than that controlled by the lateral-torsional buckling.

- The effect of screw spacing on the moment capacities of CFS built-up beams with web perforations selected in this study failed by lateral-torsional buckling is more obvious than that failed by local buckling or distortional buckling.

- The ultimate moment of CFS built-up beams with web perforations can be treated as the sum of two single PCFS beams, if the beams are subject to local buckling or distortional buckling. However, to calculate the ultimate moment of CFS built-up beams with web perforations subject to lateral-torsional buckling, the influence of the contact due to composite action of the two single beams on the beam strength should be taken into account.

- The ultimate moments of CFS built-up beams with web perforations calculated by using modified and original DSM formulae are compared with the verified FEA results. It is shown that the modified DSM equations provide a more accurate prediction for the design of CFS built-up beams with web perforations controlled by local buckling, distortional buckling or lateral-torsional buckling.

7.2 Future work

The research work including analytical and numerical analysis on PCFS beams and CFS built-up beams with web perforations have been conducted in this thesis. The main findings and conclusions described in Section 7.1 have implemented the primary objectives of the project. However, in order to fully understand the buckling behaviour and failure mechanism of PCFS beams in complex loading systems, further research is still needed in some area. This includes,

- The analytical models proposed in this thesis can only be applied to the PCFS beams failed by distortional buckling and lateral-torsional buckling. Further study can be investigated for the PCFS beams controlled by shear buckling.

- The shape of the specimens chosen in this thesis is limited to the channel cross section. Further research on the PCFS beam with various cross-section shapes is suggested to optimize new PCFS section types using in the industry.

- The experimental work has not been conducted in this thesis, only the numerical investigations are performed to study the structural behaviour of CFS built-up beams with web perforations under pure bending. It is recommended to carry out the uniformly distributed loading tests to evaluate the effect of stress gradient on the failure modes of CFS built-up beams with web perforations. A further modification of DSM equations may be needed for the design of CFS built-up beams with web perforations subject to uniformly distributed load.

- The residual stresses and plastic strains of cold-formed steel are not considered in the non-linear finite element analysis presented in this thesis. Future numerical studies are planned to recognize the effects of residual stresses and plastic strains on the moment capacities and failure modes of CFS built-up beams with web perforations.

- The boundary condition of the beams studied in this thesis is limited to simply supported boundary condition. In practice, other boundary conditions (i.e. fixed-fixed, pinned-fixed) are also used and thus should be studied in the further research.

REFERENCES

Abbasi, M., Khezri, M., Rasmussen, K. J. R. and Schafer, B. W. (2018): Elastic buckling analysis of cold-formed steel built-up sections with discrete fasteners using the compound strip method. Thin-walled Structures, 124, 58-71.

Ádány, S. (2004): Buckling mode classification of members with open thin-walled cross-sections by using the finite strip method. Johns Hopkins University Press, Baltimore.

Ádány, S. and Schafer, B. W. (2006a): Buckling mode decomposition of single-branched open cross-section members via finite strip method: Derivation. Thin-Walled Structures, 44(5), 563-584.

Ádány, S. and Schafer, B. W. (2006b): Buckling mode decomposition of single-branched open cross-section members via finite strip method: Application and examples. Thin-Walled Structures, 44(5), 585-600.

Ádány, S. and Schafer, B. W. (2008): A full modal decomposition of thin-walled, single branched open cross-section members via the constrained finite strip method. Journal of Constructional Steel Research, 64(1), 12-29.

AISI (1946): Specification for the Design of Light Gage Steel Structure Members. New York, USA.

AISI (2016): North American Specification for the Design of Cold-formed Steel Structural Members (NAS). Washington, D.C., USA.

AISC (2016): Castellated and Cellular Beam Design. Chicago, USA.

AS/NZS (2005): AS/NZS 4600 Cold-formed Steel Structures. Standards of Australian and Standards of New Zealand, Sydney-Wellington, Australian.

Bernuzzi, C. and Maxenti, F. (2015): European alternatives to design perforated thin-walled cold-formed beam–columns for steel storage systems. Journal of Constructional Steel Research, 110, 121-136.

Brown, C. J., Yettram, A. L. and Burnett, M. (1987): Stability of plates with rectangular holes. Journal of Structural Engineering, 113(5), 1111-1116.

Casafont, M., Pastor, M., Bonada, J., Roure, F. and Peköz T. (2012): Linear buckling analysis of perforated steel storage rack columns with the Finite Strip Method. Thin-Walled Structures, 61, 71-85.

Chen, B. S., Roy, K., Uzzaman, A., Raftery, G. M., Nash, D., Clifton, G. C., Pouladi, P. and Lim, J. B. P. (2019): Effects of edge-stiffened web openings on the behaviour of cold-formed steel channel sections under compression. Thin-walled Structures, 144, 106307.

Chen, B. S., Roy, K., Uzzaman, A., Raftery, G. M. and Lim, J. B. P. (2020a): Parametric study and simplified design equations for cold-formed steel channels with edge-stiffened holes under axial compression. Journal of Constructional Steel Research, 172, 106161.

Chen, B. S., Roy, K., Uzzaman, A. and Lim, J. B. P. (2020b): Moment capacity of cold-formed steel channels with edge-stiffened holes, un-stiffened holes and plain webs. Thin-walled Structures, 157, 107070.

Chen, B. S., Roy, K., Uzzaman, A., Raftery, G. M. and Lim, J. B. P. (2020c): Axial strength of back-to-back cold-formed steel channels with edge-stiffened holes, un-stiffened holes and plain webs. Journal of Constructional Steel Research, 174, 106313.

Chen, B. S., Roy, K., Fang, Z. Y., Uzzaman, A., Raftery, G. M. and Lim, J. B. P. (2021): Moment capacity of back-to-back cold-formed steel channels with edge-stiffened holes, un-stiffened holes, and plain webs. Engineering Structures, 235, 112042.

Chen, J. K. and Li, L. Y. (2010): Distortional buckling of cold-formed steel sections subjected to uniformly distributed transverse loading. International Journal of Structural Stability and Dynamics, 10(5), 1017-1030.

Cheng, S. S., Kim, B. and Li, L. Y. (2013): Lateral-torsional buckling of cold-formed channel sections subject to combined compression and bending. Journal of Constructional Steel Research, 80, 174-180.

Cheung, Y. K. (1968): The finite strip method in the analysis of elastic plates with two opposite simply supported ends. Proceedings of the Institution of Civil Engineers, 40(1), 1-7.

Crisan, A., Ungureanu, V. and Dubina, D. (2012a): Behaviour of cold-formed steel perforated sections in compression. Part 1—Experimental investigations. Thin-Walled Structures, 61, 86-96.

Crisan, A., Ungureanu, V. and Dubina, D. (2012b): Behaviour of cold-formed steel perforated sections in compression: Part 2—numerical investigations and design considerations. Thin-Walled Structures, 61, 97-105.

Chu, X. T., Rickard, J. and Li, L. Y. (2004): Lateral-tortion buckling analysis of partial-laterally restrained thin-walled channel-section beams. Journal of Constructional Steel Research, 60, 1159-1175.

Chu, X. T., Rickard, J. and Li, L. Y. (2005): Influence of lateral restraint on lateral-torsional buckling of cold-formed steel purlins. Thin-Walled Structures, 43(5), 800-810.

Davies, J. M. and Leach, P. (1994a): First-order generalised beam theory. Journal of Constructional Steel Research, 31(2-3), 187-220.

Davies, J. M. and Leach, P. (1994b): Second-order generalised beam theory. Journal of Constructional Steel Research, 31(2-3), 221-241.

Davies, J. M., Leach, P. and Taylor, A. (1997): The design of perforated cold-formed steel sections subject to axial load and bending. Thin-Walled Structures, 29(1-4), 141-157.

Dhanalakshmi, M. and Shanmugam, N. E. (2001): Design for openings in equal-angle cold-formed steel stub columns. Thin-Walled Structures, 39(2), 167-187.

EN1993-1-3 (2006): Design of Steel Structures. Part 1-3: General rules- Supplementary rules for cold-formed members and sheeting. BSI, Brussels.

EN1993-1-5 (2006): Design of Steel Structures. Part 1-5: Plated structural elements. BSI, Brussels.

Erdal, F. and Saka, M. P. (2013): Ultimate load carrying capacity of optimally designed steel cellular beams. Journal of Constructional Steel Research, 80, 355-368.

Fratamico, D. C., Torabian S., Zhao, X., Rasmussen, K. J. R. and Schafer, B. W. (2018): Experimental study on the composite action in sheathed and bare built-up cold-formed steel columns. Thin-Walled Structures, 127, 290-305.

Georgieva, I., Sehueremans, L., Pyl, L. and Vandewalle, L. (2012): Experimental investigation of built-up double-Z members in bending and compression. Thin-Walled Structures, 53, 48-57.

Gjelsvik, A. (1990): Buckling of built-up columns with or without stay plates. Journal of Engineering Mechanics, 116(5), 1142-1159.

Gjelsvik, A. (1991): Stability of built-up columns. Journal of Engineering Mechanics, 117(6), 1331-1345.

Guzmán, A., Guzmán, O., Arteta, C. and Carrillo, J. (2021): Experimental study of the influence of welding space in cold-formed built-up box flexural members. Engineering Structures, 228, 111541.

Hancock, G. J., Kwon, Y. B. and Bernard, E. S. (1994): Strength design curves for thin-walled sections undergoing distortional buckling. Journal of Construction Steel Research, 31(2-3), 169-186.

Hancock, G. J. (1997): Design for distortional buckling of flexural members. Thin-Walled Structures, 27(1), 3-12.

Harper, C. (1991): Design in Steel 4: Castellated and Cellular Beams. British Steel, Port Talbot, UK.

Huang, X. H. and Zhu, J. (2016): A stiffened-plate buckling model for calculating critical stress of distortional buckling of CFS columns. International Journal of Mechanical Science, 119, 237-242.

Huang, X. H., Yang, J., Liu, Q. F., Zhu, J., Bai, L., Wang, F. L. and Wang, J. H. (2018): A simplified flange-lip model for distortional buckling of cold-formed steel channel-sections with stiffened web. International Journal of Mechanical Science, 136, 451-459.

Huang, X. H., Bai, L., Yang, J., Wang, F. L., Zhu, J. and Liu, Q. F. (2019): Distortional-buckling analysis of channel sections with web stiffened by longitudinal ribs subjected to axial compression or bending. Thin-walled Structures, 144, 106322.

Kankanamge, N. D. and Mahendran, M. (2012): Behaviour and design of cold-formed steel beams subject to lateral-torsional buckling. Thin-Walled Structures, 51, 25-38.

Kesti, J. and Mäkeläinen, P. (1998): Design of gypsum-sheathed perforated steel wall studs. Journal of Constructional Steel Research, 46(1-3), 215-216.

Knowles, P. R. (1985): Design of Castellated Beams. Constrado, London, UK.

Kim, B., Li, L. Y. and Edmonds, A. (2016): Analytical solutions of lateral-torsional buckling of castellated beams. International Journal of Structural Stability and Dynamics, 16(8), 1550044.

Kulatunga, M. P. and Macdonald, M. (2013): Investigation of cold-formed steel structural members with perforations of different arrangements subjected to compression loading. Thin-Walled Structures, 67, 78-87.

Kulatunga, M. P., Macdonald, M., Rhodes, J. and Harrison, D. K. (2014): Load capacity of cold-formed column members of lipped channel cross-section with perforations subjected to compression loading – Part I: FE simulation and test results. Thin-Walled Structures, 80, 1-12.

Kwon, Y. B. and Hancock, G. J. (1991): A nonlinear elastic spline finite strip analysis of thin-walled sections. Thin-Walled Structures, 12(4), 295-319.

Kwon, Y. B. and Hancock, G. J. (1992): Tests of cold-formed channels with local and distortional buckling. Journal of Structural Engineering, 118(7), 1786-1803.

Laím, L., Rodrigues, J. P. C., and da Silva, L. S. (2013): Experimental and numerical analysis on the structural behaviour of cold-formed steel beams. Thin-Walled Structures, 72, 1-13.

Landolfo, R., Mammana, O., Portioli, F., Di Lorenzo, G., and Guerrieri, M. R. (2008): Laser welded built-up cold-formed steel beams: Experimental investigations. Thin-Walled Structures, 46(7-9), 781-791.

Lau, S. C. W. and Hancock, G. J. (1986): Buckling of thin flat-walled structures by a spline finite strip method. Thin-Walled Structures, 4(4), 269-294.

Lau, S. C. W. and Hancock, G. J. (1987): Distortional buckling formulas for channel columns. Journal of Structural Engineering, 113(5), 1063-1078.

Lau, S. C. W. and Hancock, G. J. (1989): Inelastic buckling analyses of beams, columns and plates using the spline finite strip method. Thin-Walled Structures, 7(3-4), 213-238.

Lawson, R. M. and Basta, A. (2019): Deflection of C section beam with circular web openings. Thin-walled Structures, 134, 277-290.

Li, L. Y. (2004): Lateral-torsional buckling of cold-formed zed-purlins partial-laterally restrained by metal sheeting. Thin-Walled Structures, 42(7), 995-1011.

Li, L. Y. and Chu, X. T. (2008): Cold-formed Steel Sections. in Martin, L. H. and Purkiss, J. A. (eds.) Structural Design of Steelwork. 3rd edn. Amsterdam, Elsevier, Chapter 11, 413-457.

Li, L. Y. and Chen, J. K. (2008): An analytical model for analysing distortional buckling of cold-formed steel sections. Thin-walled Structures, 46(12), 1430-1436.

Li, L. Y. (2009): Analyses of distortional buckling of cold-formed sigma purlins using EN1993-1-3. Journal of Constructional Steel Research, 62(12), 2099-2102.

Li, L. Y. (2011): Calculation of moment capacity of cold-formed steel members. International Journal of Structural Engineering, 2(2), 101-115.

Li, Z. and Schafer, B.W. (2013): Constrained finite strip method for thin-walled members with general end boundary conditions. Journal of Engineering Mechanics, 139(11), 1566-1576.

Li, Y. Q., Li, Y. L., Wang, S. K. and Shen, Z. Y. (2014): Ultimate load-carrying capacity of cold-formed thin-walled columns with built-up box and I section under axial compression. Thin-Walled Structures, 79, 202-217.

Lim, J. B. P. and Nethercot, D. A. (2003): Ultimate strength of bolted moment-connections between cold-formed steel members. Thin-Walled Structures, 41, 1019-1039.

Liu, T. C. H. and Chung, K. F. (2003): Steel beams with large web openings of various shapes and sizes: finite element investigation. Journal of Constructional Steel Research, 59, 1159-1176.

Liu, Q., Yang, J. and Wang, F. L. (2015): Numerical simulation of sleeve connections for cold-formed steel sigma sections. Engineering Structures, 177, 641-654.

Maiorana E., Carlo P. and Claudio M. (2009): Elastic stability of plates with circular and rectangular holes subjected to axial compression and bending moment. Thin-Walled Structures, 47(3), 241-255.

Meza, F. J., Becque, J. and Hajirasouliha, I. (2020a): Experimental study of cold-formed steel built-up columns. Thin-Walled Structures, 149, 106291.

Meza, F. J., Becque, J. and Hajirasouliha, I. (2020b): Experimental study of the cross-sectional capacity of cold-formed steel built-up columns. Thin-Walled Structures, 155, 106958.

Miller T. H. and Peköz, T. (1994): Unstiffened strip approach for perforated wall studs. Journal of Structural Engineering, 120(2), 410-421.

Moen, C. D. (2008): Direct strength design for cold-formed steel members with perforations. Ph.D. Thesis, Johns Hopkins University.

Moen C. D. and Schafer B. W. (2008): Experiments on cold-formed steel columns with holes. Thin-Walled Structures, 46(10), 1164-1182.

Moen, C. D. and Schafer, B. W. (2009a): Elastic buckling of cold-formed steel columns and beams with holes. Engineering Structures, 31(12), 2812-2824.

Moen, C. D. and Schafer, B. W. (2009b): Elastic buckling of thin plates with holes in compression or bending. Thin-Walled Structures, 47(12), 1597-1607.

Moen, C. D. and Schafer, B. W. (2010): Extending direct strength design to cold-formed steel beams with holes, Proceedings of the 20th international specialty conference on cold-formed steel structures. St. Louis, Missouri, USA: November 3&4.

Moen, C. D. and Schafer, B. W. (2011): Direct strength method for design of cold-formed steel columns with holes. Journal of Structural Engineering, 137(5), 559-570.

Moen, C. D., Schudlich, A., and von der Heyden, A. (2013): Experiments on Cold-Formed Steel C-Section Joists with Unstiffened Web Holes. Journal of Structural Engineering, 139(5), 695-704.

Mojtabaei, S. M., Becque, J. and Hajirasouliha, I. (2021): Structural size optimization of single and built-up cold-formed steel beam-column members. Journal of Structural Engineering, 147(4), 04021030.

Mousavi, H., Azhari, M., Saadatpour, M. M. and Sarrami-Foroushani1, S. (2020): Application of improved element-free Galerkin combining with fnite strip method for buckling analysis of channel-section beams with openings. Engineering with Computers, DOI:10.1007/s00366-020-01087-8.

Papangelis, J. P. and Hancock, G. J. (1995): Computer analysis of thin-walled structural members. Computers & Structures, 56(1), 157-176.

Pham, C. H. and Hancock G. J. (2009a): Direct strength design of cold-formed purlins. Journal of Structural Engineering, 135(3), 229-238.

Pham, C. H. and Hancock G. J. (2009b): Shear buckling of thin-walled channel sections. Journal of Constructional Steel Research, 65(3), 578-585.

Pham, C. H. and Hancock G. J. (2012a): Direct strength design of cold-formed C-sections for shear and combined actions. Journal of Structural Engineering, 138(6), 759-768.

Pham, C. H. and Hancock G. J. (2012b): Tension field action for cold-formed sections in shear. Journal of Constructional Steel Research, 72, 168-178.

Pham, C. H. and Hancock G. J. (2012c): Elastic buckling of cold-formed channel sections in shear. Thin-Walled Structures, 61, 22-26.

Pham, S. H., Pham, C. H. and Hancock G. J. (2014): Direct strength method of design for shear including sections with longitudinal web stiffeners. Thin-Walled Structures, 81, 19-28.

Piyawat, K., Ramseyer, C., and Kang, T. H. K. (2013): Development of an axial load capacity equation for doubly symmetric built-up cold-formed sections. Journal of Structural Engineering, 139(12), 04013008.

Reyes, W. and Guzmán, A. (2011): Evaluation of the slenderness ratio in built-up cold-formed box sections. Journal of Constructional Steel Research, 67(6), 929-935.

Ren, C., Li, L. Y. and Yang, J. (2012): Bending analysis of partially restrained channel-section purlins subjected to up-lift loadings. Journal of Constructional Steel Research, 72, 254-260.

Roy, K., Ting, T. C. H., Lau, H. H. and Lim, J. B. P. (2018a): Effect of thickness on the behaviour of axially loaded back-to-back cold-formed steel built-up channel sections - Experimental and numerical investigation. Structures, 16, 327-346.

Roy, K., Ting, T. C. H., Lau, H. H. and Lim, J. B. P. (2018b): Nolinear behaviour of back-to-back gapped built-up cold-formed steel channel sections under compression. Journal of Constructional Steel Research, 147, 257-276.

Roy, K., Mohammadjani, C. and Lim, J. B. P. (2019a): Experimental and numerical investigation into the behaviour of face-to-face built-up cold-formed steel channel sections under compression. Thin-walled Structures, 134, 291-309.

Roy, K., Ting, T. C. H., Lau, H. H. and Lim, J. B. P. (2019b): Experimental and numerical investigations on the axial capacity of cold-formed steel built-up box sections. Journal of Constructional Steel Research, 160, 411-427.

Roy, K., Lau, H. H., Ting, T. C. H., Chen, B. S. and Lim, J. B. P. (2020): Flexural capacity of gapped built-up cold-formed steel channel sections including web stiffeners. Journal of Constructional Steel Research, 172, 106154.

Schafer, B. W. and Peköz, T. (1998): Direct strength prediction of cold-formed steel members using numerical elastic buckling solutions. Proceedings of the 14th international specialty conference on cold-formed steel structures. St. Louis, Missouri, 69-76.

Schafer, B. W. and Peköz, T. (1998): Computational modeling of cold-formed steel: characterizing geometric imperfections and residual stresses. Journal of Constructional Steel Research, 47, 193-210.

Schafer, B. W. and Peköz, T. (1999): Laterally braced cold-formed steel flexural members with edge stiffened flanges. Journal of Structural Engineering, 125(2), 118-127.

Schafer, B. W. (2002): Local, distortional and Euler buckling in thin-walled columns. Journal of Structural Engineering, 128(3), 289-299.

Schafer, B. W. and Ádány, S. (2006): Buckling analysis of cold-formed steel members using CUFSM: conventional and constrained finite strip methods. 18th International Specialty Conference on Cold-Formed Steel Structures. Orlando, Florida, USA: October 26&27.

Shafer, B. W. (2008): Review: the direct strength method of cold-formed steel member design. Journal of Constructional Steel Research, 64(7-8), 766-778.

Schardt, R. (1989): Verallgemeinerte Technische Biegetheorie. Springer, Berlin, Heidelberg, New York.

Schardt, R. (1994): Lateral torsional and distortional buckling of channel- and hat-sections. Journal of Constructional Steel Research, 31(2-3), 243-265.

Seah, L. K. and Khong, P. W. (1990): Lateral-torsional buckling of channel beams. Journal of Constructional Steel Research, 17(4), 265-282.

Shanmugam N. E., Thevendran, V. and Tan, Y. H. (1999): Design formula for axially compressed perforated plates. Thin-Walled Structures, 34(1), 1-20.

Shanmugam, N. E. and Dhanalakshmi, M. (2001): Design for openings in cold-formed steel channel stub columns. Thin-Walled Structures, 39(12), 961-981.

Sivakumaran, K. S., Ng, M. Y. and Fox, S. R. (2006): Flexural strength of cold-formed steel joists with reinforced web openings. Canadian Journal of Civil Engineering, 33(9), 1195-1208.

Silvestre, N. and Camotim, D. (2002a): First-order generalised beam theory for arbitrary orthotropic materials. Thin-Walled Structures, 40(9), 755-789.

Silvestre, N. and Camotim, D. (2002b): Second-order generalised beam theory for arbitrary orthotropic materials. Thin-Walled Structures, 40(9), 791-820.

Silvestre, N. and Camotim, D. (2004a): Distortional buckling formulae for cold-formed steel C- and Z-section members: Part I—Derivation. Thin-Walled Structures, 42(11), 1567-1597.

Silvestre, N. and Camotim, D. (2004b): Distortional buckling formulae for cold-formed steel C- and Z-section members: Part II—Validation and application. Thin-Walled Structures, 42(11), 1599-1629.

Silvestre, N. and Camotim, D. (2004c): Distortional buckling formulae for cold-formed steel rack-section members. Steel and Composite Structures, 4(1), 49-75.

Silvestre, N. (2007): Generalised beam theory to analyse the buckling behaviour of circular cylinder shells and tubes. Thin-Walled Structures, 45(2), 185-198.

Silvestre, N. (2008): Buckling behaviour of elliptical cylindrical shells and tubes under compression. International Journal of Solids and Structures, 45(16), 4427-4447.

Smith, F. H. and Moen, C. D. (2014): Finite strip elastic buckling solutions for thin-walled metal columns with perforation patterns. Thin-Walled Structures, 79, 187-201.

Sputo, T. and Tovar, J. (2005): Application of direct strength method to axially loaded perforated cold-formed steel studs: Longwave buckling. Thin-Walled Structures, 43(12), 1852-1881.

Stone, T. A. and LaBoube, R. A. (2005): Behaviour of cold-formed steel built-up I-sections. Thin-Walled Structures, 43(12), 1805-1817.

Szabo, I. F. and Dubina, D. (2004): Recent research advances on the ECBL approach. Part II: interactive buckling of perforated sections. Thin-Walled Structures, 42(2), 195-210.

Teng, J. G., Yao, J. and Zhao, Y. (2003): Distortional buckling of channel beam-columns. Thin-Walled Structures, 41(7), 595-617.

Timoshenko, S. P. and Gere, J. M. (1961): Theory of elastic stability. New York: McGraw Hill, USA.

Ting, T. C. T., Roy, K., Lau, H. H. and Lim, B. J. (2017): Effect of screw spacing on behavior of axially loaded back-to-back cold-formed steel built-up channel sections. Advances in Structural Engineering, 21(3), 474-487.

Tovar, J. and Sputo, T. (2005): Application of direct strength method to axially loaded perforated cold-formed steel studs: Distortional and local buckling. Thin-Walled Structures, 43(12), 1882-1912.

Von Karman, T., Sechler, E. E. and Donnel, L. H. (1932): The strength of thin plates in compression, Transactions ASME 54, 53-57.

Wang, L. P. and Young, B. (2015a): Behaviour of cold-formed steel built-up sections with intermediate stiffeners under bending. I: Test and numerical validation. Journal of Structural Engineering, 142(3), 04015150.

Wang, L. P. and Young, B. (2015b): Behaviour of cold-formed steel built-up sections with intermediate stiffeners under bending. II: Parametric study and design. Journal of Structural Engineering, 142(3), 04015151.

Wang, L. P. and Young, B. (2015c): Beam tests of cold-formed steel built-up sections with web perforations. Journal of Constructional Steel Research, 115, 18-33.

Wang, L. P. and Young, B. (2017): Design of cold-formed steel built-up sections with web perforations subjected to bending. Thin-Walled Structures, 120, 458-469.

Wang, L. P. and Young, B. (2018): Behaviour and design of cold-formed steel built-up section beams with different screw arrangements. Thin-walled Structures, 131, 16-32.

Whittle, J. and Ramseyer, C. (2009): Buckling capacities of axially loaded, cold-formed, built-up C-channels. Thin-Walled Structures, 47(2), 190-201.

Winter, G. (1968): Thin-walled structures theoretical solutions and test results. Preliminary Publications 8th Congress IABSE, 101-112.

Xu, L., Sultana, P. and Zhou, X. (2009): Flexural strength of cold-formed steel built-up box sections. Thin-Walled Structures, 47(6-7), 807-815.

Yao, X. Y., Guo, Y. L. and Li, Y. Q. (2016): Effective width method for distortional buckling design of cold-formed lipped channel sections. Thin-walled Structures, 109, 344-351.

Yao, Z. and Rasmussen, K. J. R. (2011a): Material and geometric nonlinear isoparametric spline finite strip analysis of perforated thin-walled steel structures—Analytical developments. Thin-Walled Structures, 49(11), 1359-1373.

Yao, Z. and Rasmussen, K. J. R. (2011b): Material and geometric nonlinear isoparametric spline finite strip analysis of perforated thin-walled steel structures—Numerical investigations. Thin-Walled Structures, 49(11), 1374-1391.

Yan, Z. and Rasmussen, K. J. R. (2012): Inelastic local buckling behaviour of perforated plates and sections under compression. Thin-Walled Structures, 61, 49-70.

Yoo, C. H. and Lee, S. C. (2011): Stability of structures, principles and applications. Oxford: Elsevier, UK.

Ye, J., Hajirasouliha, I., Becque, J. and Piakoutas, K. (2016): Development of more efficient cold-formed steel sections in bending. Thin-Walled Structures, 101, 1-13.

Ye, J., Mojtabaei, S. M. and Hajirasouliha, I. (2018a): Local-flexural interactive buckling of standard and optimised cold-formed steel columns. Journal of Constructional Steel Research, 144, 106-118.

Ye, J., Mojtabaei, S. M., Hajirasouliha, I., Shepherd, P. and Piakoutas, K. (2018b): Strength and deflection behaviour of cold-formed steel back-to-back channels. Engineering Structures, 177, 641-654.

Young, B. and Chen, J. (2008): Design of cold-formed steel built-up closed sections with intermediate stiffeners. Journal of Structural Engineering, 134(5), 727-737.

Yu, C. and Schafer, B. W. (2003): Local buckling tests on cold-formed steel beams. Journal of Structural Engineering, 129(12), 1596-1606.

Yu, C. and Schafer, B. W. (2006): Distortional buckling tests on cold-formed steel beams. Journal of Structural Engineering, 132(4), 515-528.

Yu, C. and Schafer, B. W. (2007): Simulation of cold-formed steel beams in local and distortional buckling with applications to the direct strength method. Journal of Constructional Steel Research, 63(5), 581-590.

Yu, C. and Yan, W. M. (2011): Effective width method for determining distortional buckling strength of cold-formed steel flexural C and Z sections. Thin-Walled Structures, 49(2), 233-238.

Yuan, W. B., Kim, B. and Li, L. Y. (2014): Buckling of axially loaded castellated steel columns. Journal of Constructional Steel Research, 92, 40-45.

Yuan, W. B., Yu, N. T. and Li L. Y. (2017): Distortional buckling of perforated cold-formed steel channel-section beams with circular holes in web. International Journal of Mechanical Sciences, 126, 255-260.

Yu, N. T., Kim, B., Yuan, W. B., Li, L. Y. and Yu, F. (2019): An analytical solution of distortional buckling resistance of cold-formed steel channel-section beams with web openings. Thin-Walled Structures, 135, 446-452.

Yu, N. T., Kim, B., Li, L. Y., Hong, W. J. and Yuan, W. B. (2020): Distortional buckling of perforated cold-formed steel beams subject to uniformly distributed transverse loads. Thin-Walled Structures, 148, 106569.

Yu, N. T., Kim, B., Huang, X. H., Yuan, W. B., Ye, R., Wu, L. and Le, J. J. (2021): Analytical solution for flange/web distortional buckling of cold-formed steel beams with circular web perforations, Mechanics of Advanced Materials and Structures, DOI:10.1080/15376494.2021.1902594

Zhang, J. H. and Young, B. (2012): Compression tests of cold-formed steel I-shaped open sections with edge and web stiffeners. Thin-Walled Structures, 52, 1-11.

Zhang, J. H. and Young, B. (2015): Numerical investigation and design of cold-formed steel built-up open section columns with longitudinal stiffeners. Thin-Walled Structures, 89, 178-191.

Zhang, J. H. and Young, B. (2018): Experimental investigation of cold-formed steel built-up closed section columns with web stiffeners. Journal of Constructional Steel Research, 147, 380-392.

Zhao, J. Y., Sun, K., Cheng, Y. and Wang, J. (2019): Tests and direct strength design on cold-formed steel channel beams with web holes. Engineering Structures, 184, 434-446.

Zhou, X. H. and Shi, Y. (2011): Flexural Strength Evaluation for Cold-Formed Steel Lip-Reinforced Built-Up I-Beams. Advances in Structural Engineering, 14(4), 597-611.

Zhu, J. and Li, L. Y. (2016): A stiffened plate buckling model for calculating critical stress of distortional buckling of CFS beams. International Journal of Mechanical Sciences, 115-116, 457-464.

Zhu, J. and Li, L. Y. (2018): Effect of shear stress on distortional buckling of CFS beams subjected to uniformly distributed transverse loading. Mechanics of Advanced Materials and Structures, 26(17), 1423-1429.

Appendix A - Mesh sensitivity analysis

A.1 Mesh sensitivity study for the distortional buckling of PCFS beams subject to pure bending

Section B (*h*=200 mm, *b*=70 mm, *c*=20 mm, *t*=2.5 mm, *d*=100 mm and *l*=1256 mm)				
Label	Element type	Analysis solver	Mesh size (mm)	M_{crd} (N·mm)
D1	Shell 181	Eigenvalue buckling	3	28980506
D2	Shell 181	Eigenvalue buckling	5	28894819
D3	Shell 181	Eigenvalue buckling	10	28304607
D4	Shell 181	Eigenvalue buckling	15	28436907
D5	Shell 181	Eigenvalue buckling	20	25394254
D6	Shell 181	Eigenvalue buckling	25	25665245
D7	Shell 181	Eigenvalue buckling	30	26003153

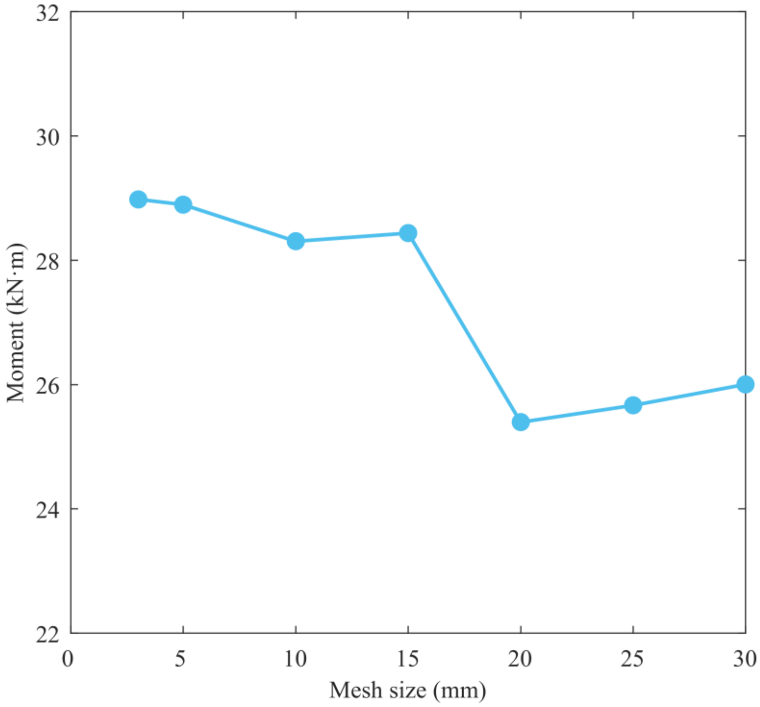

Figure A.1 Effect of mesh size on the distortional buckling of a PCFS beam (Section B: h=200 mm, b=70 mm, c=20 mm, t=2.5 mm, d=100 mm and l=1256 mm)

A.2 Mesh sensitivity study for the lateral-torsional buckling of PCFS beams subject to pure bending

Section E (*h*=200 mm, *b*=70 mm, *c*=20 mm, *t*=2 mm, *d*=100 mm and *l*=3140 mm)				
Label	Element type	Analysis solver	Mesh size (mm)	M_{crd} (N·mm)
D1	Shell 181	Eigenvalue buckling	3	9203210
D2	Shell 181	Eigenvalue buckling	5	9159739
D3	Shell 181	Eigenvalue buckling	10	9048194
D4	Shell 181	Eigenvalue buckling	15	9265247
D5	Shell 181	Eigenvalue buckling	20	9406640
D6	Shell 181	Eigenvalue buckling	25	9472125
D7	Shell 181	Eigenvalue buckling	30	8933363

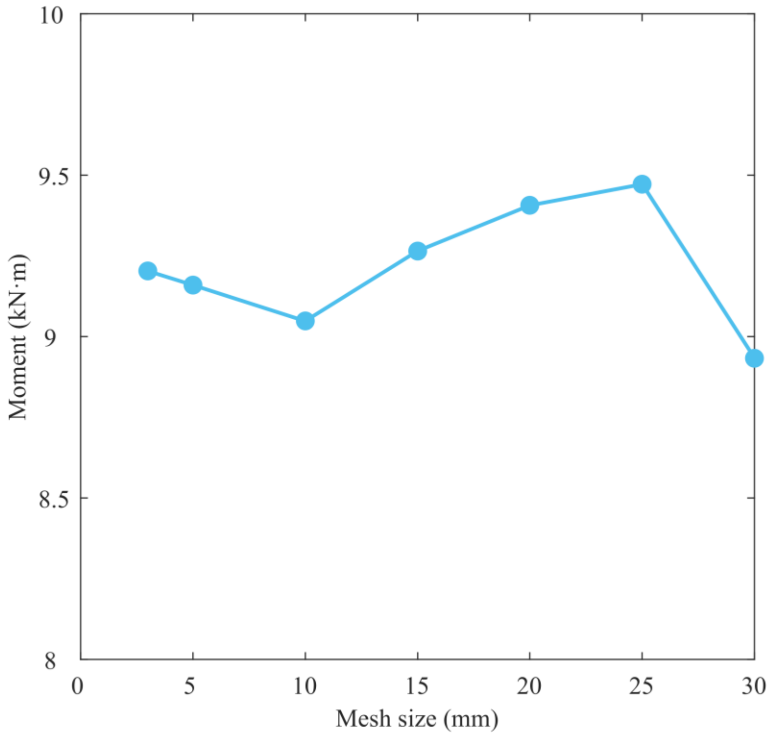

Figure A.2 Effect of mesh size on the lateral-torsional buckling of a PCFS beam (Section E: h=200 mm, b=70 mm, c=20 mm, t=2 mm, d=100 mm and l=3140 mm)

Appendix B - Distortional buckling load of PCFS beams obtained from eigenvalue buckling analysis

B.1 PCFS beams with different hole sizes subject to pure bending

Section A (h=150 mm, b=50 mm, c=15 mm, t=2 mm)							
d=43 mm		d=50 mm		d=60 mm		d=75 mm	
Length (mm)	$M_{\mathrm{crd,FEA}}$ (N·mm)	Length (mm)	$M_{\mathrm{crd,FEA}}$ (N·mm)	Length (mm)	$M_{\mathrm{crd,FEA}}$ (N·mm)	Length (mm)	$M_{\mathrm{crd,FEA}}$ (N·mm)
67	18907272	79	17078929	94	16519669	118	18968457
134	19602298	157	17906322	188	17501624	236	19040839
201	20064983	236	18390801	282	17272081	354	14431191
268	18632941	314	16208547	376	14552961	472	13933716
335	15725668	393	14731116	470	14573356	590	15530316
402	14876080	471	15007047	564	16013196	708	14560159
469	15217995	550	16294725	658	15591701	826	13893526
536	16314120	628	16343113	752	14659934	944	14005898
603	16982553	707	15286377	846	14413796	1062	14589752
670	15839439	785	14822294	940	14646338	1180	14042688
737	15206997	864	14788502	1034	15210396	1298	13887527
804	14959659	942	15077430	1128	14692926	1416	12365908
871	15007647	1021	15589102	1222	14464983	1534	10652536
938	15285978	1099	15107222	1316	14471381		
1005	15746662	1178	14852086	1410	12883778		
1072	15401149	1256	14788102	1504	11421544		
1139	15117020	1335	14594151				
1206	14989252	1413	13136315				
1273	14992051	1492	11886428				
1340	14621344	1570	10808297				
1407	13360059						
1474	12255135						
1541	11282579						

Section B (h=200 mm, b=70 mm, c=20 mm, t=2.5 mm)							
d=57.2 mm		d=66.7mm		d=80 mm		d=100 mm	
Length (mm)	$M_{\text{crd,FEA}}$ (N·mm)	Length (mm)	$M_{\text{crd,FEA}}$ (N·mm)	Length (mm)	$M_{\text{crd,FEA}}$ (N·mm)	Length (mm)	$M_{\text{crd,FEA}}$ (N·mm)
359	39472695	314	36338140	377	35491330	314	38810670
449	33384005	418	34891385	502	30395435	471	30564700
539	30572460	523	30456060	628	29199425	628	27949095
629	30410955	628	29919650	754	31145730	785	30038475
718	31896995	732	31610845	879	33247720	942	30809625
808	34500475	837	34712905	1005	30564700	1099	28578625
898	33562000	941	32218065	1130	29403125	1256	28080530
988	31705905	1046	30613685	1256	29314370	1413	28726550
1078	30704380	1151	29968150	1382	29981730	1570	29151895
1167	30354210	1255	30036050	1507	30619505	1727	28307995
1257	30513290	1360	30653455	1633	29703825	1884	28125635
1347	31079285	1464	31604540	1758	29318250	2041	26089120
1437	31979445	1569	30662185	1884	29354625		
1527	31334395	1674	30138385	2010	27864220		
1616	30747545	1778	29963785				
1706	30451210	1883	30077760				
1796	30399800	1987	28905515				
1889	30557425	2092	26291850				
1976	29675210						
2065	27351575						

Section C (h=250 mm, b=80 mm, c=25 mm, t=3 mm)							
d=71.4 mm		d=83.3 mm		d=100 mm		d=125 mm	
Length (mm)	$M_{\mathrm{crd,FEA}}$ (N·mm)	Length (mm)	$M_{\mathrm{crd,FEA}}$ (N·mm)	Length (mm)	$M_{\mathrm{crd,FEA}}$ (N·mm)	Length (mm)	$M_{\mathrm{crd,FEA}}$ (N·mm)
112	61848691	131	55906484	157	54459311	196	62882899
224	64233115	262	58755942	314	57773804	392	65342734
336	65784427	393	60376381	471	59322422	588	55982792
448	65864327	524	61344155	628	56489123	784	52690743
560	61828940	655	57029569	785	55550077	980	57234256
672	57657096	786	57122935	942	60083714	1176	56469373
784	58250509	917	61188845	1099	60534385	1372	53242859
896	61881908	1048	62310134	1256	56856303	1568	52951988
1008	66436193	1179	59665363	1413	55384891	1764	54586791
1120	62197018	1310	57362634	1570	55791572	1960	54049937
1232	59299081	1441	56748573	1727	57570912	2156	52978023
1344	57917444	1572	57406624	1884	56971215	2352	47589728
1456	57716348	1703	59044120	2041	55735013	2548	40969719
1568	58451605	1834	58781977	2198	55377709		
1680	59940074	1965	57458693	2355	48827725		
1792	60171694	2096	56890418	2512	43236538		
1904	58773897	2227	54924345				
2016	57999139	2358	49310714				
2128	57749564	2489	44511343				
2240	55018609	2620	40381693				
2352	50187816						
2464	45964800						
2576	42255297						

B.2 PCFS beams with different hole sizes subject to uniformly distributed load

Section D (h=200 mm, b=65 mm, c=20 mm, t=2.5 mm)					
d/h=0.5		d/h=0.25		d/h=0	
Length (mm)	$\sigma_{crd,FEA}$ (MPa)	Length (mm)	$\sigma_{crd,FEA}$ (MPa)	Length (mm)	$\sigma_{crd,FEA}$ (MPa)
628	114	628	152	600	170
1256	264	1256	443	1250	527
1884	375	1884	661	1800	729
2355	455	2277	732	2200	792
2512	482	2434	742	2350	770
3140	587	2983	760	2850	809
3611	633	3454	761	3400	800
4239	644	4082	757	3900	806
4710	646	4553	754	4400	795
5181	646	5024	751	4850	791
5652	646	5574	747	5350	786
6280	644	6045	745	5850	783

Appendix C - Distortional half-wave lengths of CFS beams

Cross section selected from Albion Section (unit: mm)

Section	Web depth	Flange width	Lip length	Thickness	Half-wave length
C12515	120	50	15	1.5	450
C12516	120	50	15	1.6	430
C14614	145	62.5	20	1.4	670
C14515	145	62.5	20	1.5	650
C14616	145	62.5	20	1.6	630
C14618	145	62.5	20	1.8	590
C14620	145	62.5	20	2	560
C17616	175	62.5	20	1.6	650
C17618	175	62.5	20	1.8	610
C17620	175	62.5	20	2	580
C17623	175	62.5	20	2.3	540
C17625	175	62.5	20	2.5	520
C20618	200	65	20	1.8	640
C20620	200	65	20	2	610
C20623	200	65	20	2.3	570
C20625	200	65	20	2.5	540
C22620	225	65	20	2	620
C22623	225	65	20	2.3	580
C22625	225	65	20	2.5	550
C24623	240	65	20	2.3	580
C24625	240	65	20	2.5	560
C24630	240	65	20	3	510
C26625	265	65	20	2.5	570
C26630	265	65	20	3	520
C30725	300	75	20	2.5	630
C30730	300	75	20	3	580

Appendix D - Lateral-torsional buckling load of PCFS beams obtained from eigenvalue buckling analysis

D.1 Laterally unrestrained PCFS beams with different hole sizes subject to pure bending (**k_z=0, k_ϕ=0**)

Section E (*h*=200 mm, *b*=70 mm, *c*=20 mm, *t*=2 mm)							
d=50 mm		*d*=66.7mm		*d*=80 mm		*d*=100 mm	
Length (mm)	$M_{\mathrm{cr}\lambda,\mathrm{FEA}}$ (N·mm)	Length (mm)	$M_{\mathrm{cr}\lambda,\mathrm{FEA}}$ (N·mm)	Length (mm)	$M_{\mathrm{cr}\lambda,\mathrm{FEA}}$ (N·mm)	Length (mm)	$M_{\mathrm{cr}\lambda,\mathrm{FEA}}$ (N·mm)
3062	10436214	3037	10301378	3014	10241317	3140	9159740
3533	7999621	3560	7636369	3517	7645419	3611	7022339
4004	6355352	4084	5906699	4019	5944068	4082	5567746
4553	5033819	4503	4927540	4522	4772322	4553	4535762
5024	4224783	5027	4027481	5024	3931797	5042	3777202
5495	3613725	5550	3367871	5526	3306645	5495	3201948
6045	3073319	6074	2868880	6029	2826639	5966	2754781
6516	2715329	6493	2551751	6531	2448936	6437	2400139
7065	2385563	7016	2231403	7034	2145346	7065	2031534
7536	2158564	7540	1974527	7536	1897946	7536	1812944
8007	1970438	8063	1765534	8038	1693505	8007	1631476
8557	1789401	8482	1625294	8541	1522381	8478	1479245
9028	1660302	9006	1475864	9043	1377886	8949	1349970
9499	1550765	9529	1348464	9546	1254899	9420	1238803
10048	1443260	10053	1237593	10048	1149450	10048	1112687
10519	1365413	10577	1140707	10550	1057887	10519	1031243
10990	1298971	10995	1072138	11053	977981	10990	959023
11540	1233261	11519	996150	11555	907830	11461	894537
12011	1185646	12043	929172	12058	845951	11932	836669
12482	1145058	12566	869358	12560	791114	12560	768126
13031	1105412	13090	815724	13062	742217	13031	722167
13502	1077052	13509	776713	13565	698449	13502	680345
14052	1049418	14032	731887	14067	659093	14130	630556

D.2 Laterally restrained PCFS beams with different hole sizes subject to pure bending ($k_z=\infty$, $k_\phi=0$)

Section E (h=200 mm, b=70 mm, c=20 mm, t=2 mm)							
d=50 mm		d=66.7mm		d=80 mm		d=100 mm	
Length (mm)	$M_{cr\lambda,FEA}$ (N·mm)	Length (mm)	$M_{cr\lambda,FEA}$ (N·mm)	Length (mm)	$M_{cr\lambda,FEA}$ (N·mm)	Length (mm)	$M_{cr\lambda,FEA}$ (N·mm)
3062	10444145	3037	10308078	3014	10251967	3140	9181325
3533	8002207	3560	7639713	3517	7653393	3611	7041488
4004	6355917	4084	5909741	4019	5951799	4082	5585880
4553	5033899	4503	4931297	4522	4780963	4553	4553826
5024	4225323	5027	4032821	5024	3942238	5042	3795869
5495	3615310	5550	3375507	5526	3319464	5495	3221716
6045	3076532	6074	2879174	6029	2841876	5966	2776158
6516	2720158	6493	2564609	6531	2467225	6437	2423431
7065	2392441	7016	2247294	7034	2166874	7065	2057720
7536	2167278	7540	1993835	7536	1922912	7536	1841715
8007	1981149	8063	1788465	8038	1722150	8007	1662845
8557	1802410	8482	1651210	8541	1554648	8478	1513289
9028	1675352	9006	1505630	9043	1413901	8949	1386773
9499	1567689	9529	1382135	9546	1294751	9420	1278464
10048	1462328	10053	1275242	10048	1193000	10048	1156217
10519	1386301	10577	1182303	10550	1105297	10519	1077771
10990	1321266	10995	1116831	11053	1029150	10990	1008541
11540	1257097	11519	1044632	11555	962713	11461	947128
12011	1210654	12043	981385	12058	904505	11932	892332
12482	1170864	12566	925359	12560	853294	12560	827838
13031	1131975	13090	875398	13062	807982	13031	784867
13502	1103967	13509	839292	13565	767725	13502	745990
14052	1076541	14032	798043	14067	731825	14130	699998

D.3 Laterally unrestrained PCFS beams with different hole sizes subject to uniformly distributed uplift load (k_z=0, k_ϕ=0)

Section E (h=200 mm, b=70 mm, c=20 mm, t=2 mm)							
d=50 mm		d=66.7mm		d=80 mm		d=100 mm	
Length (mm)	$M_{cr\lambda,FEA}$ (N·mm)	Length (mm)	$M_{cr\lambda,FEA}$ (N·mm)	Length (mm)	$M_{cr\lambda,FEA}$ (N·mm)	Length (mm)	$M_{cr\lambda,FEA}$ (N·mm)
3062	6973576	3037	6917786	3014	6866571	3140	6249833
3533	5509547	3560	5329344	3517	5337146	3611	4960282
4004	4456655	4084	4216435	4019	4247988	4082	4016740
4553	3578803	4503	3563169	4522	3465772	4553	3321021
5024	3029384	5027	2949408	5024	2892053	5042	2799155
5495	2608955	5550	2492981	5526	2460322	5495	2398978
6045	2233390	6074	2144881	6029	2126232	5966	2085580
6516	1982495	6493	1922398	6531	1861680	6437	1835516
7065	1750154	7016	1696360	7034	1648198	7065	1573520
7536	1589499	7540	1514353	7536	1473046	7536	1416693
8007	1455724	8063	1365613	8038	1327735	8007	1285572
8557	1326120	8482	1265399	8541	1205587	8478	1174897
9028	1233056	9006	1158439	9043	1101991	8949	1080717
9499	1153448	9529	1067435	9546	1013418	9420	999806
10048	1074486	10053	988700	10048	937044	10048	908238
10519	1016653	10577	919472	10550	870665	10519	849285
10990	966403	10995	869755	11053	812449	10990	796999
11540	915859	11519	813753	11555	761127	11461	750265
12011	878407	12043	763779	12058	715508	11932	708192
12482	845614	12566	719137	12560	674880	12560	658159
13031	812421	13090	678931	13062	638331	13031	624445
13502	787739	13509	649603	13565	605484	13502	593495
14052	762667	14032	616004	14067	575610	14130	555982

D.4 Laterally restrained PCFS beams with different hole sizes subject to uniformly distributed uplift load ($k_z=\infty$, $k_\phi=0$)

Section E (h=200 mm, b=70 mm, c=20 mm, t=2 mm)							
d=50 mm		d=66.7mm		d=80 mm		d=100 mm	
Length (mm)	$M_{\mathrm{cr}\lambda,\mathrm{FEA}}$ (N·mm)	Length (mm)	$M_{\mathrm{cr}\lambda,\mathrm{FEA}}$ (N·mm)	Length (mm)	$M_{\mathrm{cr}\lambda,\mathrm{FEA}}$ (N·mm)	Length (mm)	$M_{\mathrm{cr}\lambda,\mathrm{FEA}}$ (N·mm)
3062	6224789	3037	7646161	3014	7558300	3140	6814388
3533	6051031	3560	5806569	3517	5788867	3611	5342061
4004	4850321	4084	4544943	4019	4558137	4082	4285385
4553	3859136	4503	3812840	4522	3686348	4553	3515770
5024	3243970	5027	3130306	5024	3052889	5042	2943241
5495	2776182	5550	2626182	5526	2579244	5495	2506848
6045	2360472	6074	2243732	6029	2214364	5966	2166677
6516	2084207	6493	2000385	6531	1926653	6437	1896604
7065	1829335	7016	1754321	7034	1695790	7065	1615033
7536	1653718	7540	1557140	7536	1507352	7536	1447644
8007	1507848	8063	1397058	8038	1352093	8007	1308422
8557	1366988	8482	1289818	8541	1222566	8478	1191685
9028	1266306	9006	1175991	9043	1113637	8949	1093018
9499	1180640	9529	1079826	9546	1021345	9420	1008854
10048	1096189	10053	997283	10048	942552	10048	914409
10519	1034738	10577	925383	10550	874751	10519	854164
10990	981662	10995	874216	11053	816012	10990	801195
11540	928584	11519	817194	11555	764739	11461	754276
12011	889511	12043	766925	12058	719814	11932	712477
12482	855484	12566	722548	12560	680153	12560	663395
13031	821211	13090	683114	13062	645070	13031	630756
13502	795953	13509	654691	13565	613895	13502	601177
14052	770437	14032	622478	14067	586054	14130	565806

Appendix E - Comparison of ultimate moment obtained from FEA with original and modified DSM prediction for CFS built-up beams with web perforations

E.1 Comparison of ultimate moment obtained from FEA with original and modified DSM prediction for CFS built-up beams with web perforations failed by local buckling

Specimen	FEA		Yield moment		DSM		Comparison	
	M_{FEA} (kN·mm)	Failure mode	M_y (kN·mm)	M_{ynet} (kN·mm)	$M_{DSM,o}$ (kN·mm)	$M_{DSM,m}$ (kN·mm)	$M_{FEA}/M_{DSM,o}$	$M_{FEA}/M_{DSM,m}$
H200-L1200-T1.4-S50-A0(d/h0)	20021	L+D	27213	27213	18991	18991	1.05	1.05
H200-L1200-T1.4-S100-A0(d/h0)	19993	L+D	27213	27213	18991	18991	1.05	1.05
H200-L1200-T1.4-S200-A0(d/h0)	19950	L+D	27213	27213	18991	18991	1.05	1.05
H200-L1200-T1.4-S400-A0(d/h0)	19881	L+D	27213	27213	18991	18991	1.05	1.05
H200-L1200-T1.4-S800-A0(d/h0)	19793	L+D	27213	27213	18991	18991	1.04	1.04
H200-L1200-T1.4-S1200-A0(d/h0)	19606	L+D	27213	27213	18991	18991	1.03	1.03
H200-L1200-T1.4-S200-A300(d/h0.25)	19895	L+D	27213	27099	18991	18991	1.05	1.05
H200-L1200-T1.4-S50-A300(d/h0.5)	19714	L+D	27213	26303	15568	18240	1.27	1.08
H200-L1200-T1.4-S100-A300(d/h0.5)	19695	L+D	27213	26303	15568	18240	1.27	1.08
H200-L1200-T1.4-S200-A300(d/h0.5)	19622	L+D	27213	26303	15568	18240	1.26	1.08
H200-L1200-T1.4-S400-A300(d/h0.5)	19554	L+D	27213	26303	15568	18240	1.26	1.07
H200-L1200-T1.4-S800-A300(d/h0.5)	19432	L+D	27213	26303	15568	18240	1.25	1.07
H200-L1200-T1.4-S1200-A300(d/h0.5)	19290	L+D	27213	26303	15568	18240	1.24	1.06
H200-L1200-T1.4-S200-A300(d/h0.65)	18292	L+D	27213	25213	15350	17917	1.19	1.02
H200-L1800-T1.4-S200-A150(d/h0.5)	19357	L+D	27213	26303	15568	18240	1.24	1.06
H200-L1800-T1.4-S200-A200(d/h0.5)	19423	L+D	27213	26303	15568	18240	1.25	1.06
H200-L1800-T1.4-S200-A250(d/h0.5)	19427	L+D	27213	26303	15568	18240	1.25	1.07
H200-L1800-T1.4-S200-A300(d/h0.5)	19379	L+D	27213	26303	15568	18240	1.24	1.06

H200-L1800-T1.4-S200-A350(d/h0.5)	19374	L+D	27213	26303	15568	18240	1.24	1.06
H200-L1800-T1.4-S200-A400(d/h0.5)	19492	L+D	27213	26303	15568	18240	1.25	1.07
H200-L1800-T1.4-S200-A450(d/h0.5)	19681	L+D	27213	26303	15568	18240	1.26	1.08
H200-L1200-T1.6-S200-A0(d/h0)	25353	L+D	31100	31100	23784	23784	1.07	1.07
H200-L1200-T1.6-S200-A300(d/h0.25)	25280	L+D	31100	30970	23784	23784	1.06	1.06
H200-L1200-T1.6-S200-A300(d/h0.5)	24930	L+D	31100	30060	19564	23509	1.27	1.06
H200-L1200-T1.6-S200-A300(d/h0.65)	23174	L+D	31100	28815	19295	23100	1.20	1.00
H200-L1200-T1.8-S200-A0(d/h0)	30701	L+D	34988	34988	28958	28958	1.06	1.06
H200-L1200-T1.8-S200-A300(d/h0.25)	30598	L+D	34988	34841	28958	28958	1.06	1.06
H200-L1200-T1.8-S200-A300(d/h0.5)	30149	L+D	34988	33818	23902	29356	1.26	1.03
H200-L1200-T1.8-S200-A300(d/h0.65)	28129	L+D	34988	32417	23578	28854	1.19	0.97
H200-L1200-T2.0-S200-A0(d/h0)	35500	L+D	38875	38875	34482	34482	1.03	1.03
H200-L1200-T2.0-S200-A300(d/h0.25)	35437	L+D	38875	38713	34482	34482	1.03	1.03
H200-L1200-T2.0-S200-A300(d/h0.5)	34959	L+D	38875	37575	28560	35751	1.22	0.98
H200-L1200-T2.0-S200-A300(d/h0.65)	33337	L+D	38875	36019	28179	35150	1.18	0.95
H300-L1200-T1.4-S50-D0(d0)	29010	L+D	54857	54857	28711	28711	1.01	1.01
H300-L1200-T1.4-S100-D0(d0)	28952	L+D	54857	54857	28711	28711	1.01	1.01
H300-L1200-T1.4-S200-D0(d0)	28787	L+D	54857	54857	28711	28711	1.00	1.00
H300-L1200-T1.4-S300-D0(d0)	28503	L+D	54857	54857	28711	28711	0.99	0.99
H300-L1200-T1.4-S400-D0(d0)	28488	L+D	54857	54857	28711	28711	0.99	0.99
H300-L1200-T1.4-S800-D0(d0)	28390	L+D	54857	54857	28711	28711	0.99	0.99
H300-L1200-T1.4-S1200-D0(d0)	28292	L+D	54857	54857	28711	28711	0.99	0.99
H300-L1200-T1.4-S300-D300(d0.25)	27683	L+D	54857	54601	28711	28711	0.96	0.96
H300-L1200-T1.4-S50-D300(d0.5)	26707	L+D	54857	52810	23347	25267	1.14	1.06
H300-L1200-T1.4-S100-D300(d0.5)	26629	L+D	54857	52810	23347	25267	1.14	1.05
H300-L1200-T1.4-S200-D300(d0.5)	26500	L+D	54857	52810	23347	25267	1.14	1.05
H300-L1200-T1.4-S300-D300(d0.5)	26225	L+D	54857	52810	23347	25267	1.12	1.04
H300-L1200-T1.4-S400-D300(d0.5)	26189	L+D	54857	52810	23347	25267	1.12	1.04
H300-L1200-T1.4-S800-D300(d0.5)	26032	L+D	54857	52810	23347	25267	1.11	1.03
H300-L1200-T1.4-S1200-D300(d0.5)	25876	L+D	54857	52810	23347	25267	1.11	1.02
H300-L1200-T1.4-S300-D300(d0.65)	24089	L+D	54857	50359	23010	24805	1.05	0.97

H300-L1800-T1.4-S300-D200(d0.5)	23837	L+D	54857	52810	23347	25267	1.02	0.94
H300-L1800-T1.4-S300-D250(d0.5)	24039	L+D	54857	52810	23347	25267	1.03	0.95
H300-L1800-T1.4-S300-D300(d0.5)	24853	L+D	54857	52810	23347	25267	1.06	0.98
H300-L1800-T1.4-S300-D350(d0.5)	24880	L+D	54857	52810	23347	25267	1.07	0.98
H300-L1800-T1.4-S300-D400(d0.5)	24324	L+D	54857	52810	23347	25267	1.04	0.96
H300-L1800-T1.4-S300-D450(d0.5)	24974	L+D	54857	52810	23347	25267	1.07	0.99
H300-L1200-T1.6-S300-D0(d0)	35621	L+D	62694	62694	36126	36126	0.99	0.99
H300-L1200-T1.6-S300-D300(d0.25)	35319	L+D	62694	62401	36126	36126	0.98	0.98
H300-L1200-T1.6-S300-D300(d0.5)	34244	L+D	62694	60354	29444	32720	1.16	1.05
H300-L1200-T1.6-S300-D300(d0.65)	31471	L+D	62694	57553	29023	32127	1.08	0.98
H300-L1200-T1.8-S300-D0(d0)	44767	L+D	70531	70531	44191	44191	1.01	1.01
H300-L1200-T1.8-S300-D300(d0.25)	44175	L+D	70531	70202	44191	44191	1.00	1.00
H300-L1200-T1.8-S300-D300(d0.5)	42427	L+D	70531	67898	36101	41055	1.18	1.03
H300-L1200-T1.8-S300-D300(d0.65)	39677	L+D	70531	64747	35590	40319	1.11	0.98
H300-L1200-T2.0-S300-D0(d0)	53804	L+D	78367	78367	52868	52868	1.02	1.02
H300-L1200-T2.0-S300-D300(d0.25)	53708	L+D	78367	78002	52868	52868	1.02	1.02
H300-L1200-T2.0-S300-D300(d0.5)	51370	L+D	78367	75442	43289	50245	1.19	1.02
H300-L1200-T2.0-S300-D300(d0.65)	49154	L+D	78367	71940	42682	49353	1.15	1.00
Mean							1.11	1.02
COV							0.088	0.038
Φ_b =0.9, Reliability index (β_1)							2.849	2.668

E.2 Comparison of ultimate moment obtained from FEA with original and modified DSM prediction for CFS built-up beams with web perforations failed by distortional buckling

Specimen	FEA		Yield moment		DSM		Comparison	
	M_{FEA} (kN·mm)	Failure mode	M_{y} (kN·mm)	M_{ynet} (kN·mm)	$M_{\mathrm{DSM,o}}$ (kN·mm)	$M_{\mathrm{DSM,m}}$ (kN·mm)	$M_{\mathrm{FEA}}/M_{\mathrm{DSM,o}}$	$M_{\mathrm{FEA}}/M_{\mathrm{DSM,m}}$
H150-L1200-T1.4-S50-A0(d/h0)	13131	D	16740	16740	11748	12183	1.12	1.08
H150-L1200-T1.4-S100-A0(d/h0)	13037	D	16740	16740	11748	12183	1.11	1.07
H150-L1200-T1.4-S150-A0(d/h0)	12950	D	16740	16740	11748	12183	1.10	1.06
H150-L1200-T1.4-S200-A0(d/h0)	12954	D	16740	16740	11748	12183	1.10	1.06
H150-L1200-T1.4-S400-A0(d/h0)	12854	D	16740	16740	11748	12183	1.09	1.06
H150-L1200-T1.4-S800-A0(d/h0)	12842	D	16740	16740	11748	12183	1.09	1.05
H150-L1200-T1.4-S1200-A0(d/h0)	12820	D	16740	16740	11748	12183	1.09	1.05
H150-L1200-T1.4-S150-A300(d/h0.25)	12828	D	16740	16676	11691	12114	1.10	1.06
H150-L1200-T1.4-S50-A300(d/h0.5)	12476	D+L	16740	16228	11433	11809	1.09	1.06
H150-L1200-T1.4-S100-A300(d/h0.5)	12400	D+L	16740	16228	11433	11809	1.08	1.05
H150-L1200-T1.4-S150-A300(d/h0.5)	12356	D+L	16740	16228	11433	11809	1.08	1.05
H150-L1200-T1.4-S200-A300(d/h0.5)	12388	D+L	16740	16228	11433	11809	1.08	1.05
H150-L1200-T1.4-S400-A300(d/h0.5)	12350	D+L	16740	16228	11433	11809	1.08	1.05
H150-L1200-T1.4-S800-A300(d/h0.5)	12347	D+L	16740	16228	11433	11809	1.08	1.05
H150-L1200-T1.4-S1200-A300(d/h0.5)	12342	D+L	16740	16228	11433	11809	1.08	1.05
H150-L1200-T1.4-S150-A300(d/h0.65)	12125	D+L	16740	15616	11123	11459	1.09	1.06
H150-L1200-T1.4-S150-A300(d/h0.8)	11740	D+L	16740	14644	10661	10971	1.10	1.07
H150-L1800-T1.4-S150-A150(d/h0.5)	11170	D+L	16740	16228	11193	11517	1.00	0.97
H150-L1800-T1.4-S150-A200(d/h0.5)	11331	D+L	16740	16228	11323	11676	1.00	0.97
H150-L1800-T1.4-S150-A250(d/h0.5)	11465	D+L	16740	16228	11392	11758	1.01	0.98
H150-L1800-T1.4-S150-A300(d/h0.5)	11451	D+L	16740	16228	11433	11809	1.00	0.97

H150-L1800-T1.4-S150-A350(d/h0.5)	11498	D+L	16740	16228	11462	11844	1.00	0.97
H150-L1800-T1.4-S150-A400(d/h0.5)	11490	D+L	16740	16228	11482	11868	1.00	0.97
H150-L1800-T1.4-S150-A450(d/h0.5)	11501	D+L	16740	16228	11498	11887	1.00	0.97
H150-L1200-T1.6-S150-A0(d/h0)	15475	D	19132	19132	14221	14911	1.09	1.04
H150-L1200-T1.6-S150-A300(d/h0.25)	15368	D	19132	19059	14154	14828	1.09	1.04
H150-L1200-T1.6-S150-A300(d/h0.5)	14816	D+L	19132	18547	13853	14453	1.07	1.03
H150-L1200-T1.6-S150-A300(d/h0.65)	14473	D+L	19132	17847	13488	14019	1.07	1.03
H150-L1200-T1.6-S150-A300(d/h0.8)	13886	D+L	19132	16736	12944	13408	1.07	1.04
H150-L1200-T1.8-S150-A0(d/h0)	18069	D	21523	21523	16812	17792	1.07	1.02
H150-L1200-T1.8-S150-A300(d/h0.25)	17952	D	21523	21441	16737	17695	1.07	1.01
H150-L1200-T1.8-S150-A300(d/h0.5)	17447	D+L	21523	20865	16392	17250	1.06	1.01
H150-L1200-T1.8-S150-A300(d/h0.65)	16828	D+L	21523	20077	15975	16728	1.05	1.01
H150-L1200-T1.8-S150-A300(d/h0.8)	15973	D+L	21523	18828	15155	15989	1.05	1.00
H150-L1200-T2.0-S150-A0(d/h0)	20895	D	23915	23915	19510	20808	1.07	1.00
H150-L1200-T2.0-S150-A300(d/h0.25)	20809	D	23915	23823	19426	20697	1.07	1.01
H150-L1200-T2.0-S150-A300(d/h0.5)	20262	D+L	23915	23184	19040	20181	1.06	1.00
H150-L1200-T2.0-S150-A300(d/h0.65)	19527	D+L	23915	22308	18571	19571	1.05	1.00
H150-L1200-T2.0-S150-A300(d/h0.8)	18118	D+L	23915	20920	17247	18688	1.05	0.97
H150-L1800-T2.0-S150-A0(d/h0)	20306	D	23915	23915	19510	20808	1.04	0.98
H150-L1800-T2.0-S150-A300(d/h0.25)	20108	D	23915	23823	19426	20697	1.04	0.97
H150-L1800-T2.0-S150-A300(d/h0.5)	19479	D	23915	23184	19040	20181	1.02	0.97
H150-L1800-T2.0-S150-A300(d/h0.65)	18810	D	23915	22308	18571	19571	1.01	0.96
H150-L1800-T2.0-S150-A300(d/h0.8)	17542	D	23915	20920	17247	18688	1.02	0.94
H150-L1200-T2.2-S150-A0(d/h0)	23660	D	26306	26306	22301	23942	1.06	0.99
H150-L1200-T2.2-S150-A300(d/h0.25)	23568	D	26306	26206	22209	23818	1.06	0.99
H150-L1200-T2.2-S150-A300(d/h0.5)	23022	D+L	26306	25502	21783	23232	1.06	0.99
H150-L1200-T2.2-S150-A300(d/h0.65)	22177	D+L	26306	24539	21266	22535	1.04	0.98
H150-L1200-T2.2-S150-A300(d/h0.8)	20454	D+L	26306	23012	19360	20824	1.06	0.98
H150-L1200-T2.4-S50-A0(d/h0)	26586	D	28698	28698	25175	27176	1.06	0.98
H150-L1200-T2.4-S100-A0(d/h0)	26456	D	28698	28698	25175	27176	1.05	0.97
H150-L1200-T2.4-S150-A0(d/h0)	26374	D	28698	28698	25175	27176	1.05	0.97

H150-L1200-T2.4-S200-A0(d/h0)	26317	D	28698	28698	25175	27176	1.05	0.97
H150-L1200-T2.4-S400-A0(d/h0)	26189	D	28698	28698	25175	27176	1.04	0.96
H150-L1200-T2.4-S800-A0(d/h0)	26165	D	28698	28698	25175	27176	1.04	0.96
H150-L1200-T2.4-S1200-A0(d/h0)	26143	D	28698	28698	25175	27176	1.04	0.96
H150-L1200-T2.4-S150-A300(d/h0.25)	26281	D	28698	28588	25076	27040	1.05	0.97
H150-L1200-T2.4-S50-A300(d/h0.5)	25952	D+L	28698	27820	24613	26388	1.05	0.98
H150-L1200-T2.4-S100-A300(d/h0.5)	25811	D+L	28698	27820	24613	26388	1.05	0.98
H150-L1200-T2.4-S150-A300(d/h0.5)	25703	D+L	28698	27820	24613	26388	1.04	0.97
H150-L1200-T2.4-S200-A300(d/h0.5)	25663	D+L	28698	27820	24613	26388	1.04	0.97
H150-L1200-T2.4-S400-A300(d/h0.5)	25512	D+L	28698	27820	24613	26388	1.04	0.97
H150-L1200-T2.4-S800-A300(d/h0.5)	25493	D+L	28698	27820	24613	26388	1.04	0.97
H150-L1200-T2.4-S1200-A300(d/h0.5)	25476	D+L	28698	27820	24613	26388	1.04	0.97
H150-L1200-T2.4-S150-A300(d/h0.65)	24704	D+L	28698	26770	23978	25319	1.03	0.98
H150-L1200-T2.4-S150-A300(d/h0.8)	22610	D+L	28698	25104	21489	22972	1.05	0.98
H150-L1800-T2.4-S150-A150(d/h0.5)	25830	D+L	28698	27820	24186	25864	1.07	1.00
H150-L1800-T2.4-S150-A200(d/h0.5)	25871	D+L	28698	27820	24418	26149	1.06	0.99
H150-L1800-T2.4-S150-A250(d/h0.5)	25927	D+L	28698	27820	24539	26297	1.06	0.99
H150-L1800-T2.4-S150-A300(d/h0.5)	25975	D+L	28698	27820	24613	26388	1.06	0.98
H150-L1800-T2.4-S150-A350(d/h0.5)	25990	D+L	28698	27820	24663	26450	1.05	0.98
H150-L1800-T2.4-S150-A400(d/h0.5)	25993	D+L	28698	27820	24699	26494	1.05	0.98
H150-L1800-T2.4-S150-A450(d/h0.5)	26028	D+L	28698	27820	24726	26527	1.05	0.98
H200-L1200-T1.4-S200-A300(d/h0.8)	16872	D+L	27213	23485	15956	16301	1.06	1.04
H200-L1200-T1.6-S200-A300(d/h0.8)	22203	D+L	31100	26840	19385	19928	1.15	1.11
H200-L1200-T1.8-S200-A300(d/h0.8)	27275	D+L	34988	30195	23004	23774	1.19	1.15
H200-L1200-T2.0-S200-A300(d/h0.8)	31175	D+L	38875	33550	26413	27821	1.18	1.12
H200-L1800-T2.0-S200-A0(d/h0)	31691	D	38875	38875	30022	31705	1.06	1.00
H200-L1800-T2.0-S200-A300(d/h0.25)	31466	D+L	38875	38713	29850	31485	1.05	1.00
H200-L1800-T2.0-S200-A300(d/h0.5)	30288	D+L	38875	37575	29076	30502	1.04	0.99
H200-L1800-T2.0-S200-A300(d/h0.65)	29212	D+L	38875	36019	28153	29376	1.04	0.99
H200-L1800-T2.0-S200-A300(d/h0.8)	27762	D+L	38875	33550	26413	27821	1.05	1.00
H200-L1200-T2.2-S200-A0(d/h0)	39181	D	42763	42763	34339	36522	1.14	1.07

H200-L1200-T2.2-S200-A300(d/h0.25)	39142	D	42763	42584	34149	36274	1.15	1.08
H200-L1200-T2.2-S200-A300(d/h0.5)	38830	D+L	42763	41333	33290	35153	1.17	1.10
H200-L1200-T2.2-S200-A300(d/h0.65)	37564	D+L	42763	39621	32263	33857	1.16	1.11
H200-L1200-T2.2-S200-A300(d/h0.8)	34678	D+L	42763	36905	29721	32054	1.17	1.08
H200-L1200-T2.4-S50-A0(d/h0)	42922	D	46650	46650	38792	41511	1.11	1.03
H200-L1200-T2.4-S100-A0(d/h0)	42805	D	46650	46650	38792	41511	1.10	1.03
H200-L1200-T2.4-S200-A0(d/h0)	42798	D	46650	46650	38792	41511	1.10	1.03
H200-L1200-T2.4-S400-A0(d/h0)	42643	D	46650	46650	38792	41511	1.10	1.03
H200-L1200-T2.4-S800-A0(d/h0)	42605	D	46650	46650	38792	41511	1.10	1.03
H200-L1200-T2.4-S1200-A0(d/h0)	42568	D	46650	46650	38792	41511	1.10	1.03
H200-L1200-T2.4-S200-A300(d/h0.25)	42674	D	46650	46455	38585	41236	1.11	1.03
H200-L1200-T2.4-S50-A300(d/h0.5)	42831	D+L	46650	45090	37644	39979	1.14	1.07
H200-L1200-T2.4-S100-A300(d/h0.5)	42730	D+L	46650	45090	37644	39979	1.14	1.07
H200-L1200-T2.4-S200-A300(d/h0.5)	42607	D+L	46650	45090	37644	39979	1.13	1.07
H200-L1200-T2.4-S400-A300(d/h0.5)	42370	D+L	46650	45090	37644	39979	1.13	1.06
H200-L1200-T2.4-S800-A300(d/h0.5)	42265	D+L	46650	45090	37644	39979	1.12	1.06
H200-L1200-T2.4-S1200-A300(d/h0.5)	42160	D+L	46650	45090	37644	39979	1.12	1.05
H200-L1200-T2.4-S200-A300(d/h0.65)	41492	D+L	46650	43223	36516	38513	1.14	1.08
H200-L1200-T2.4-S200-A300(d/h0.8)	38048	D+L	46650	40260	33059	35834	1.15	1.06
H200-L1800-T2.4-S200-A150(d/h0.5)	38378	D+L	46650	45090	36538	38621	1.05	0.99
H200-L1800-T2.4-S200-A200(d/h0.5)	38539	D+L	46650	45090	37161	39385	1.04	0.98
H200-L1800-T2.4-S200-A250(d/h0.5)	38764	D+L	46650	45090	37463	39757	1.03	0.98
H200-L1800-T2.4-S200-A300(d/h0.5)	38748	D+L	46650	45090	37644	39979	1.03	0.97
H200-L1800-T2.4-S200-A350(d/h0.5)	38825	D+L	46650	45090	37762	40124	1.03	0.97
H200-L1800-T2.4-S200-A400(d/h0.5)	38700	D+L	46650	45090	37846	40227	1.02	0.96
H200-L1800-T2.4-S200-A450(d/h0.5)	38771	D+L	46650	45090	37910	40304	1.02	0.96
H300-L1200-T1.4-S300-A300(d/h0.8)	22144	D+L	54857	46471	23650	23561	0.94	0.94
H300-L1200-T1.6-S300-A300(d/h0.8)	28792	D+L	62694	53109	28895	28960	1.00	0.99
H300-L1200-T1.8-S300-A300(d/h0.8)	36522	D+L	70531	59748	34477	34739	1.06	1.05
H300-L1200-T2.0-S300-A300(d/h0.8)	44918	D+L	78367	66386	40381	40881	1.11	1.10
H300-L1800-T2.0-S300-A0(d/h0)	46642	D+L	78367	78367	47816	48228	0.98	0.97

H300-L1800-T2.0-S300-A300(d/h0.25)	46452	D+L	78367	78002	47407	47761	0.98	0.97
H300-L1800-T2.0-S300-A300(d/h0.5)	45916	D+L	78367	75442	45552	45764	1.01	1.00
H300-L1800-T2.0-S300-A300(d/h0.65)	42381	D+L	78367	71940	43398	43607	0.98	0.97
H300-L1800-T2.0-S300-A300(d/h0.8)	39722	D+L	78367	66386	40381	40881	0.98	0.97
H300-L2400-T2.0-S300-A0(d/h0)	46001	D+L	78367	78367	47816	48228	0.96	0.95
H300-L2400-T2.0-S300-A300(d/h0.25)	45774	D+L	78367	78002	47407	47761	0.97	0.96
H300-L2400-T2.0-S300-A300(d/h0.5)	45199	D+L	78367	75442	45552	45764	0.99	0.99
H300-L2400-T2.0-S300-A300(d/h0.65)	41604	D+L	78367	71940	43398	43607	0.96	0.95
H300-L2400-T2.0-S300-A300(d/h0.8)	39345	D+L	78367	66386	40381	40881	0.97	0.96
H300-L1200-T2.2-S300-A0(d/h0)	63213	D	86204	86204	54990	55961	1.15	1.13
H300-L1200-T2.2-S300-A300(d/h0.25)	62798	D	86204	85802	54530	55425	1.15	1.13
H300-L1200-T2.2-S300-A300(d/h0.5)	60713	D+L	86204	82987	52439	53104	1.16	1.14
H300-L1200-T2.2-S300-A300(d/h0.65)	57166	D+L	86204	79135	50004	50579	1.14	1.13
H300-L1200-T2.2-S300-A300(d/h0.8)	52216	D+L	86204	73024	46587	47367	1.12	1.10
H300-L1200-T2.4-S50-A0(d/h0)	72403	D	94041	94041	62459	64075	1.16	1.13
H300-L1200-T2.4-S100-A0(d/h0)	72106	D	94041	94041	62459	64075	1.15	1.13
H300-L1200-T2.4-S200-A0(d/h0)	71721	D	94041	94041	62459	64075	1.15	1.12
H300-L1200-T2.4-S300-A0(d/h0)	71657	D	94041	94041	62459	64075	1.15	1.12
H300-L1200-T2.4-S400-A0(d/h0)	70585	D	94041	94041	62459	64075	1.13	1.10
H300-L1200-T2.4-S800-A0(d/h0)	70289	D	94041	94041	62459	64075	1.13	1.10
H300-L1200-T2.4-S1200-A0(d/h0)	70093	D	94041	94041	62459	64075	1.12	1.09
H300-L1200-T2.4-S300-A300(d/h0.25)	70518	D	94041	93602	61948	63467	1.14	1.11
H300-L1200-T2.4-S50-A300(d/h0.5)	70814	D+L	94041	92531	59619	60689	1.19	1.17
H300-L1200-T2.4-S100-A300(d/h0.5)	70798	D+L	94041	92531	59619	60689	1.19	1.17
H300-L1200-T2.4-S200-A300(d/h0.5)	70377	D+L	94041	92531	59619	60689	1.18	1.16
H300-L1200-T2.4-S300-A300(d/h0.5)	69873	D+L	94041	92531	59619	60689	1.17	1.15
H300-L1200-T2.4-S400-A300(d/h0.5)	69116	D+L	94041	92531	59619	60689	1.16	1.14
H300-L1200-T2.4-S800-A300(d/h0.5)	68876	D+L	94041	92531	59619	60689	1.16	1.13
H300-L1200-T2.4-S1200-A300(d/h0.5)	68637	D+L	94041	92531	59619	60689	1.15	1.13
H300-L1200-T2.4-S300-A300(d/h0.65)	65161	D+L	94041	86329	56903	57905	1.15	1.13
H300-L1200-T2.4-S300-A300(d/h0.8)	59261	D+L	94041	79664	53081	54180	1.12	1.09

H300-L1800-T2.4-S300-A200(d/h0.5)	57233	D+L	94041	92531	57999	58733	0.99	0.97
H300-L1800-T2.4-S300-A250(d/h0.5)	57789	D+L	94041	92531	59051	60002	0.98	0.96
H300-L1800-T2.4-S300-A300(d/h0.5)	58091	D+L	94041	92531	59619	60689	0.97	0.96
H300-L1800-T2.4-S300-A350(d/h0.5)	58230	D+L	94041	92531	59976	61121	0.97	0.95
H300-L1800-T2.4-S300-A400(d/h0.5)	58769	D+L	94041	92531	60221	61418	0.98	0.96
H300-L1800-T2.4-S300-A450(d/h0.5)	59027	D+L	94041	92531	60400	61635	0.98	0.96
Mean							1.07	1.02
COV							0.054	0.06
Φ_b =0.9, Reliability index (β_1)							2.823	2.627

E.3 Comparison of ultimate moment obtained from FEA with original and modified DSM prediction for CFS built-up beams with web perforations failed by lateral-torsional buckling

Specimen	FEA		Yield moment		DSM		Comparison	
	M_{FEA} (kN·mm)	Failure mode	M_{y} (kN·mm)	M_{ynet} (kN·mm)	$M_{\mathrm{DSM,o}}$ (kN·mm)	$M_{\mathrm{DSM,m}}$ (kN·mm)	$M_{\mathrm{FEA}}/M_{\mathrm{DSM,o}}$	$M_{\mathrm{FEA}}/M_{\mathrm{DSM,m}}$
H150-L4000-T1.4-S200-A0(d/h0)	8843	LTB	16740	16740	4792	8997	1.85	0.98
H150-L4000-T1.4-S200-A300(d/h0.25)	8842	LTB	16740	16672	4562	8652	1.94	1.02
H150-L4000-T1.4-S200-A300(d/h0.5)	8810	LTB	16740	16228	4326	8668	2.04	1.02
H150-L4000-T1.4-S200-A300(d/h0.65)	8760	LTB	16740	15616	4180	8774	2.10	1.00
H150-L4000-T1.4-S200-A300(d/h0.8)	8673	LTB	16740	14644	4032	8570	2.15	1.01
H150-L4000-T1.6-S200-A0(d/h0)	10246	LTB	19132	19132	5584	10483	1.83	0.98
H150-L4000-T1.6-S200-A300(d/h0.25)	10229	LTB	19132	19058	5304	10055	1.93	1.02
H150-L4000-T1.6-S200-A300(d/h0.5)	10186	LTB	19132	18546	5020	10060	2.03	1.01
H150-L4000-T1.6-S200-A300(d/h0.65)	10139	LTB	19132	17846	4844	10168	2.09	1.00
H150-L4000-T1.6-S200-A300(d/h0.8)	10098	LTB	19132	16736	4668	9921	2.16	1.02
H150-L4000-T1.8-S200-A0(d/h0)	11644	LTB	21522	21522	6416	12045	1.81	0.97
H150-L4000-T1.8-S200-A300(d/h0.25)	11627	LTB	21522	21440	6082	11528	1.91	1.01
H150-L4000-T1.8-S200-A300(d/h0.5)	11612	LTB	21522	20864	5742	11505	2.02	1.01
H150-L4000-T1.8-S200-A300(d/h0.65)	11554	LTB	21522	20076	5534	11616	2.09	0.99
H150-L4000-T1.8-S200-A300(d/h0.8)	11509	LTB	21522	18828	5324	11316	2.16	1.02
H150-L4000-T2.0-S200-A0(d/h0)	13143	LTB	23914	23914	7292	13690	1.80	0.96
H150-L4000-T2.0-S200-A300(d/h0.25)	13136	LTB	23914	23822	6896	13072	1.90	1.00
H150-L4000-T2.0-S200-A300(d/h0.5)	13130	LTB	23914	23184	6496	13015	2.02	1.01
H150-L4000-T2.0-S200-A300(d/h0.65)	13020	LTB	23914	22308	6252	13123	2.08	0.99
H150-L4000-T2.0-S200-A300(d/h0.8)	12944	LTB	23914	20920	6006	12765	2.16	1.01
H150-L4000-T2.2-S200-A0(d/h0)	14692	LTB	26306	26306	8214	15420	1.79	0.95
H150-L4000-T2.2-S200-A300(d/h0.25)	14646	LTB	26306	26206	7750	14689	1.89	1.00
H150-L4000-T2.2-S200-A300(d/h0.5)	14608	LTB	26306	25502	7284	14594	2.01	1.00

H150-L4000-T2.2-S200-A300(d/h0.65)	14548	LTB	26306	24538	7000	14693	2.08	0.99
H150-L4000-T2.2-S200-A300(d/h0.8)	14426	LTB	26306	23012	6712	14265	2.15	1.01
H150-L4000-T2.4-S200-A0(d/h0)	16287	LTB	28688	28688	9184	17241	1.77	0.94
H150-L4000-T2.4-S200-A300(d/h0.25)	16313	LTB	28688	28588	8648	16378	1.89	1.00
H150-L4000-T2.4-S200-A300(d/h0.5)	16229	LTB	28688	27820	8108	16236	2.00	1.00
H150-L4000-T2.4-S200-A300(d/h0.65)	16141	LTB	28688	26770	7780	16325	2.07	0.99
H150-L4000-T2.4-S200-A300(d/h0.8)	16016	LTB	28688	25104	7450	15835	2.15	1.01
H150-L4000-T1.4-S200-A150(d/h0.5)	8756	LTB	16740	16228	4326	8668	2.02	1.01
H150-L4000-T1.4-S200-A200(d/h0.5)	8793	LTB	16740	16228	4326	8668	2.03	1.01
H150-L4000-T1.4-S200-A250(d/h0.5)	8807	LTB	16740	16228	4326	8668	2.04	1.02
H150-L4000-T1.4-S200-A300(d/h0.5)	8810	LTB	16740	16228	4326	8668	2.04	1.02
H150-L4000-T1.4-S200-A350(d/h0.5)	8820	LTB	16740	16228	4326	8668	2.04	1.02
H150-L4000-T1.4-S200-A400(d/h0.5)	8814	LTB	16740	16228	4326	8668	2.04	1.02
H150-L4000-T1.4-S200-A450(d/h0.5)	8826	LTB	16740	16228	4326	8668	2.04	1.02
H150-L4000-T2.4-S200-A150(d/h0.5)	16112	LTB	28688	27820	8108	16236	1.99	0.99
H150-L4000-T2.4-S200-A200(d/h0.5)	16218	LTB	28688	27820	8108	16236	2.00	1.00
H150-L4000-T2.4-S200-A250(d/h0.5)	16221	LTB	28688	27820	8108	16236	2.00	1.00
H150-L4000-T2.4-S200-A300(d/h0.5)	16261	LTB	28688	27820	8108	16236	2.01	1.00
H150-L4000-T2.4-S200-A350(d/h0.5)	16268	LTB	28688	27820	8108	16236	2.01	1.00
H150-L4000-T2.4-S200-A400(d/h0.5)	16308	LTB	28688	27820	8108	16236	2.01	1.00
H150-L4000-T2.4-S200-A450(d/h0.5)	16302	LTB	28688	27820	8108	16236	2.01	1.00
H150-L4000-T1.6-S200-A150(d/h0.5)	10089	LTB	19132	18546	5020	10060	2.01	1.00
H150-L4000-T1.6-S200-A200(d/h0.5)	10103	LTB	19132	18546	5020	10060	2.01	1.00
H150-L4000-T1.6-S200-A250(d/h0.5)	10134	LTB	19132	18546	5020	10060	2.02	1.01
H150-L4000-T1.6-S200-A300(d/h0.5)	10186	LTB	19132	18546	5020	10060	2.03	1.01
H150-L4000-T1.6-S200-A350(d/h0.5)	10204	LTB	19132	18546	5020	10060	2.03	1.01
H150-L4000-T1.6-S200-A400(d/h0.5)	10234	LTB	19132	18546	5020	10060	2.04	1.02
H150-L4000-T1.6-S200-A450(d/h0.5)	10278	LTB	19132	18546	5020	10060	2.05	1.02
H150-L4000-T1.4-S50-A0(d/h0)	9079	LTB	16740	16740	4792	9240	1.89	0.98
H150-L4000-T1.4-S100-A0(d/h0)	8962	LTB	16740	16740	4792	9155	1.87	0.98
H150-L4000-T1.4-S200-A0(d/h0)	8843	LTB	16740	16740	4792	8997	1.85	0.98

H150-L4000-T1.4-S400-A0(d/h0)	8694	LTB	16740	16740	4792	8720	1.81	1.00
H150-L4000-T1.4-S800-A0(d/h0)	8045	LTB	16740	16740	4792	8306	1.68	0.97
H150-L4000-T1.4-S1600-A0(d/h0)	7580	LTB	16740	16740	4792	7833	1.58	0.97
H150-L4000-T1.4-S4000-A0(d/h0)	5148	LTB	16740	16740	4792	5203	1.07	0.99
H150-L4000-T1.4-S50-A300(d/h0.5)	9011	LTB	16740	16228	4326	8902	2.08	1.01
H150-L4000-T1.4-S100-A300(d/h0.5)	8912	LTB	16740	16228	4326	8821	2.06	1.01
H150-L4000-T1.4-S200-A300(d/h0.5)	8810	LTB	16740	16228	4326	8668	2.04	1.02
H150-L4000-T1.4-S400-A300(d/h0.5)	8622	LTB	16740	16228	4326	8402	1.99	1.03
H150-L4000-T1.4-S800-A300(d/h0.5)	7852	LTB	16740	16228	4326	8003	1.82	0.98
H150-L4000-T1.4-S1600-A300(d/h0.5)	7285	LTB	16740	16228	4326	7548	1.68	0.97
H150-L4000-T1.4-S4000-A300(d/h0.5)	4805	LTB	16740	16228	4326	5014	1.11	0.96
H150-L4000-T2.4-S50-A0(d/h0)	17046	LTB	28688	28688	9184	17707	1.86	0.96
H150-L4000-T2.4-S100-A0(d/h0)	16653	LTB	28688	28688	9184	17544	1.81	0.95
H150-L4000-T2.4-S200-A0(d/h0)	16287	LTB	28688	28688	9184	17241	1.77	0.94
H150-L4000-T2.4-S400-A0(d/h0)	15904	LTB	28688	28688	9184	16712	1.73	0.95
H150-L4000-T2.4-S800-A0(d/h0)	14907	LTB	28688	28688	9184	15918	1.62	0.94
H150-L4000-T2.4-S1600-A0(d/h0)	13896	LTB	28688	28688	9184	15012	1.51	0.93
H150-L4000-T2.4-S4000-A0(d/h0)	10062	LTB	28688	28688	9184	9972	1.10	1.01
H150-L4000-T2.4-S50-A300(d/h0.5)	16890	LTB	28688	27820	8108	16675	2.08	1.01
H150-L4000-T2.4-S100-A300(d/h0.5)	16522	LTB	28688	27820	8108	16522	2.04	1.00
H150-L4000-T2.4-S200-A300(d/h0.5)	16229	LTB	28688	27820	8108	16236	2.00	1.00
H150-L4000-T2.4-S400-A300(d/h0.5)	15826	LTB	28688	27820	8108	15738	1.95	1.01
H150-L4000-T2.4-S800-A300(d/h0.5)	14708	LTB	28688	27820	8108	14990	1.81	0.98
H150-L4000-T2.4-S1600-A300(d/h0.5)	13587	LTB	28688	27820	8108	14137	1.68	0.96
H150-L4000-T2.4-S4000-A300(d/h0.5)	9441	LTB	28688	27820	8108	9391	1.16	1.01
H150-L4000-T1.6-S50-A0(d/h0)	10512	LTB	19132	19132	5584	10767	1.88	0.98
H150-L4000-T1.6-S100-A0(d/h0)	10392	LTB	19132	19132	5584	10668	1.86	0.97
H150-L4000-T1.6-S200-A0(d/h0)	10246	LTB	19132	19132	5584	10483	1.83	0.98
H150-L4000-T1.6-S400-A0(d/h0)	9916	LTB	19132	19132	5584	10162	1.78	0.98
H150-L4000-T1.6-S800-A0(d/h0)	9301	LTB	19132	19132	5584	9679	1.67	0.96
H150-L4000-T1.6-S1600-A0(d/h0)	8733	LTB	19132	19132	5584	9128	1.56	0.96

H150-L4000-T1.6-S4000-A0(d/h0)	6063	LTB	19132	19132	5584	6063	1.09	1.00
H150-L4000-T1.6-S50-A300(d/h0.5)	10499	LTB	19132	18546	5020	10331	2.09	1.02
H150-L4000-T1.6-S100-A300(d/h0.5)	10337	LTB	19132	18546	5020	10237	2.06	1.01
H150-L4000-T1.6-S200-A300(d/h0.5)	10186	LTB	19132	18546	5020	10060	2.03	1.01
H150-L4000-T1.6-S400-A300(d/h0.5)	9885	LTB	19132	18546	5020	9751	1.97	1.01
H150-L4000-T1.6-S800-A300(d/h0.5)	9283	LTB	19132	18546	5020	9288	1.85	1.00
H150-L4000-T1.6-S1600-A300(d/h0.5)	8627	LTB	19132	18546	5020	8759	1.72	0.98
H150-L4000-T1.6-S4000-A300(d/h0.5)	5671	LTB	19132	18546	5020	5818	1.13	0.97
H150-L3200-T2.0-S200-A300(d/h0.25)	17249	LTB	23914	23822	10360	17158	1.66	1.01
H150-L3200-T2.0-S200-A300(d/h0.5)	17227	LTB	23914	23184	9802	17283	1.76	1.00
H150-L3200-T2.0-S200-A300(d/h0.65)	16692	LTB	23914	22308	9462	17579	1.76	0.95
H150-L3200-T2.0-S200-A300(d/h0.8)	16630	LTB	23914	20920	9116	17175	1.82	0.97
H150-L5000-T2.0-S200-A300(d/h0.25)	9787	LTB	23914	23822	4666	9980	2.10	0.98
H150-L5000-T2.0-S200-A300(d/h0.5)	9724	LTB	23914	23184	4370	9822	2.23	0.99
H150-L5000-T2.0-S200-A300(d/h0.65)	9638	LTB	23914	22308	4190	9820	2.30	0.98
H150-L5000-T2.0-S200-A300(d/h0.8)	9554	LTB	23914	20920	4008	9500	2.38	1.01
H150-L6000-T2.0-S200-A300(d/h0.25)	7800	LTB	23914	23822	3444	7992	2.26	0.98
H150-L6000-T2.0-S200-A300(d/h0.5)	7701	LTB	23914	23184	3206	7789	2.40	0.99
H150-L6000-T2.0-S200-A300(d/h0.65)	7612	LTB	23914	22308	3062	7735	2.49	0.98
H150-L6000-T2.0-S200-A300(d/h0.8)	7562	LTB	23914	20920	2918	7449	2.59	1.02
H200-L4000-T1.6-S200-A0(d/h0)	19352	LTB	31100	31100	12012	19272	1.61	1.00
H200-L4000-T1.6-S200-A300(d/h0.25)	19378	LTB	31100	30970	11482	18649	1.69	1.04
H200-L4000-T1.6-S200-A300(d/h0.5)	19111	LTB	31100	30060	10936	19033	1.75	1.00
H200-L4000-T1.6-S200-A300(d/h0.65)	18703	LTB	31100	28814	10600	19466	1.76	0.96
H200-L4000-T1.6-S200-A300(d/h0.8)	18606	LTB	31100	26840	10256	18862	1.81	0.99
H200-L4000-T1.8-S200-A0(d/h0)	21956	LTB	34998	34998	13646	21893	1.61	1.00
H200-L4000-T1.8-S200-A300(d/h0.25)	21920	LTB	34998	34840	13028	21180	1.68	1.03
H200-L4000-T1.8-S200-A300(d/h0.5)	21868	LTB	34998	33818	12394	21581	1.76	1.01
H200-L4000-T1.8-S200-A300(d/h0.65)	21771	LTB	34998	32416	12004	22048	1.81	0.99
H200-L4000-T1.8-S200-A300(d/h0.8)	21274	LTB	34998	30194	11606	21340	1.83	1.00
H200-L4000-T2.0-S200-A0(d/h0)	24595	LTB	38874	38874	15324	24585	1.60	1.00

H200-L4000-T2.0-S200-A300(d/h0.25)	24559	LTB	38874	38712	14614	23734	1.68	1.03
H200-L4000-T2.0-S200-A300(d/h0.5)	24412	LTB	38874	37574	13884	24163	1.76	1.01
H200-L4000-T2.0-S200-A300(d/h0.65)	24308	LTB	38874	36018	13436	24672	1.81	0.99
H200-L4000-T2.0-S200-A300(d/h0.8)	23832	LTB	38874	33550	12982	23876	1.84	1.00
H200-L4000-T2.2-S200-A0(d/h0)	27281	LTB	42762	42762	17052	27357	1.60	1.00
H200-L4000-T2.2-S200-A300(d/h0.25)	27239	LTB	42762	42584	16240	26375	1.68	1.03
H200-L4000-T2.2-S200-A300(d/h0.5)	27175	LTB	42762	41332	15408	26815	1.76	1.01
H200-L4000-T2.2-S200-A300(d/h0.65)	26928	LTB	42762	39620	14900	27361	1.81	0.98
H200-L4000-T2.2-S200-A300(d/h0.8)	26449	LTB	42762	36904	14382	26450	1.84	1.00
H200-L4000-T2.4-S200-A0(d/h0)	30008	LTB	46700	46700	18834	30216	1.59	0.99
H200-L4000-T2.4-S200-A300(d/h0.25)	29939	LTB	46700	46454	17912	29181	1.67	1.03
H200-L4000-T2.4-S200-A300(d/h0.5)	29746	LTB	46700	45090	16970	29591	1.75	1.01
H200-L4000-T2.4-S200-A300(d/h0.65)	29586	LTB	46700	43222	16396	30131	1.80	0.98
H200-L4000-T2.4-S200-A300(d/h0.8)	29022	LTB	46700	40260	15812	29059	1.84	1.00
H200-L4000-T2.4-S200-A150(d/h0.5)	29724	LTB	46700	45090	16970	29591	1.75	1.00
H200-L4000-T2.4-S200-A200(d/h0.5)	29813	LTB	46700	45090	16970	29591	1.76	1.01
H200-L4000-T2.4-S200-A250(d/h0.5)	29658	LTB	46700	45090	16970	29591	1.75	1.00
H200-L4000-T2.4-S200-A300(d/h0.5)	29746	LTB	46700	45090	16970	29591	1.75	1.01
H200-L4000-T2.4-S200-A350(d/h0.5)	29852	LTB	46700	45090	16970	29591	1.76	1.01
H200-L4000-T2.4-S200-A400(d/h0.5)	29857	LTB	46700	45090	16970	29591	1.76	1.01
H200-L4000-T2.4-S200-A450(d/h0.5)	29859	LTB	46700	45090	16970	29591	1.76	1.01
H200-L4000-T1.6-S200-A150(d/h0.5)	19002	LTB	31100	30060	10936	19033	1.74	1.00
H200-L4000-T1.6-S200-A200(d/h0.5)	19032	LTB	31100	30060	10936	19033	1.74	1.00
H200-L4000-T1.6-S200-A250(d/h0.5)	19067	LTB	31100	30060	10936	19033	1.74	1.00
H200-L4000-T1.6-S200-A300(d/h0.5)	19111	LTB	31100	30060	10936	19033	1.75	1.00
H200-L4000-T1.6-S200-A350(d/h0.5)	19176	LTB	31100	30060	10936	19033	1.75	1.01
H200-L4000-T1.6-S200-A400(d/h0.5)	19203	LTB	31100	30060	10936	19033	1.76	1.01
H200-L4000-T1.6-S200-A450(d/h0.5)	19234	LTB	31100	30060	10936	19033	1.76	1.01
H200-L4000-T2.4-S50-A0(d/h0)	30860	LTB	46700	46700	18834	31032	1.64	0.99
H200-L4000-T2.4-S100-A0(d/h0)	30450	LTB	46700	46700	18834	30748	1.62	0.99
H200-L4000-T2.4-S200-A0(d/h0)	29994	LTB	46700	46700	18834	30216	1.59	0.99

H200-L4000-T2.4-S400-A0(d/h0)	29475	LTB	46700	46700	18834	29289	1.56	1.01
H200-L4000-T2.4-S800-A0(d/h0)	27808	LTB	46700	46700	18834	27898	1.48	1.00
H200-L4000-T2.4-S1600-A0(d/h0)	26514	LTB	46700	46700	18834	26309	1.41	1.01
H200-L4000-T2.4-S4000-A0(d/h0)	19090	LTB	46700	46700	18834	17476	1.01	1.09
H200-L4000-T2.4-S50-A300(d/h0.5)	30238	LTB	46700	45090	16970	30390	1.78	0.99
H200-L4000-T2.4-S100-A300(d/h0.5)	30032	LTB	46700	45090	16970	30112	1.77	1.00
H200-L4000-T2.4-S200-A300(d/h0.5)	29834	LTB	46700	45090	16970	29591	1.76	1.01
H200-L4000-T2.4-S400-A300(d/h0.5)	28752	LTB	46700	45090	16970	28683	1.69	1.00
H200-L4000-T2.4-S800-A300(d/h0.5)	27390	LTB	46700	45090	16970	27320	1.61	1.00
H200-L4000-T2.4-S1600-A300(d/h0.5)	26115	LTB	46700	45090	16970	25765	1.54	1.01
H200-L4000-T2.4-S4000-A300(d/h0.5)	17791	LTB	46700	45090	16970	17114	1.05	1.04
H200-L4000-T1.6-S50-A0(d/h0)	19789	LTB	31100	31100	12012	19793	1.65	1.00
H200-L4000-T1.6-S100-A0(d/h0)	19597	LTB	31100	31100	12012	19611	1.63	1.00
H200-L4000-T1.6-S200-A0(d/h0)	19352	LTB	31100	31100	12012	19272	1.61	1.00
H200-L4000-T1.6-S400-A0(d/h0)	19082	LTB	31100	31100	12012	18681	1.59	1.02
H200-L4000-T1.6-S800-A0(d/h0)	18108	LTB	31100	31100	12012	17793	1.51	1.02
H200-L4000-T1.6-S1600-A0(d/h0)	17071	LTB	31100	31100	12012	16780	1.42	1.02
H200-L4000-T1.6-S4000-A0(d/h0)	11839	LTB	31100	31100	12012	11146	0.99	1.06
H200-L4000-T1.6-S50-A300(d/h0.5)	19619	LTB	31100	30060	10936	19547	1.79	1.00
H200-L4000-T1.6-S100-A300(d/h0.5)	19297	LTB	31100	30060	10936	19368	1.76	1.00
H200-L4000-T1.6-S200-A300(d/h0.5)	19111	LTB	31100	30060	10936	19033	1.75	1.00
H200-L4000-T1.6-S400-A300(d/h0.5)	18670	LTB	31100	30060	10936	18449	1.71	1.01
H200-L4000-T1.6-S800-A300(d/h0.5)	17617	LTB	31100	30060	10936	17573	1.61	1.00
H200-L4000-T1.6-S1600-A300(d/h0.5)	16824	LTB	31100	30060	10936	16572	1.54	1.02
H200-L4000-T1.6-S4000-A300(d/h0.5)	11278	LTB	31100	30060	10936	11008	1.03	1.02
H200-L5000-T2.0-S200-A300(d/h0.25)	17984	LTB	38874	38712	9608	17865	1.87	1.01
H200-L5000-T2.0-S200-A300(d/h0.5)	17881	LTB	38874	37574	9096	17978	1.97	0.99
H200-L5000-T2.0-S200-A300(d/h0.65)	17783	LTB	38874	36018	8784	18210	2.02	0.98
H200-L5000-T2.0-S200-A300(d/h0.8)	17614	LTB	38874	33550	8468	17579	2.08	1.00
H200-L6000-T2.0-S200-A300(d/h0.25)	13817	LTB	38874	38712	6884	14172	2.01	0.97
H200-L6000-T2.0-S200-A300(d/h0.5)	13684	LTB	38874	37574	6492	14128	2.11	0.97

H200-L6000-T2.0-S200-A300(d/h0.65)	13535	LTB	38874	36018	6254	14217	2.16	0.95
H200-L6000-T2.0-S200-A300(d/h0.8)	13475	LTB	38874	33550	6012	13684	2.24	0.98
Mean							1.826	1
COV							0.15	0.022
Φ_b =0.9, Reliability index (β_1)							4.32	2.592

Publications

Yu, N. T., Kim, B., Huang, X. H., Yuan, W. B., Ye, R., Wu, L. and Le, J. J. (2021): Analytical solution for flange/web distortional buckling of cold-formed steel beams with circular web perforations, Mechanics of Advanced Materials and Structures, DOI:10.1080/15376494.2021.1902594

Yu, N. T., Kim, B., Li, L. Y., Hong, W. J. and Yuan, W. B. (2020): Distortional buckling of perforated cold-formed steel beams subject to uniformly distributed transverse loads. Thin-Walled Structures, 148, 106569.

Yu, N. T., Kim, B., Yuan, W. B., Li, L. Y. and Yu, F. (2019): An analytical solution of distortional buckling resistance of cold-formed steel channel-section beams with web openings. Thin-Walled Structures, 135, 446-452.